

AD-A280 596



9



DTIC
SELECTE
JUN 24 1994
S B D

COMPUTATIONAL INVESTIGATION OF AN
IMPROVED COWL CONCEPT FOR
HYPERSONIC PROPULSIVE NOZZLES

THESIS

Mark C. Butler

AFTT/GAE/ENY/94J-1

DISTRIBUTION STATEMENT A
Approved for public release
Distribution Unlimited

DTIC QUALITY INSPECTED

DEPARTMENT OF THE AIR FORCE
AIR UNIVERSITY

AIR FORCE INSTITUTE OF TECHNOLOGY

Wright-Patterson Air Force Base, Ohio

94 6 24 008

AFTT/GAE/ENY/94J-1

**COMPUTATIONAL INVESTIGATION OF AN
IMPROVED COWL CONCEPT FOR
HYPERSONIC PROPULSIVE NOZZLES
THESIS**

Mark C. Butler

AFTT/GAE/ENY/94J-1

94-19379



Approved for public release; distribution unlimited

AFTT/GAE/ENY/94J-1

**COMPUTATIONAL INVESTIGATION OF AN IMPROVED COWL CONCEPT
FOR HYPERSONIC PROPULSIVE NOZZLES**

THESIS

**Presented to the Faculty of the School of Engineering
of the Air Force Institute of Technology**

Air University

**In Partial Fulfillment of the
Requirements for the Degree of
Master of Science in Aeronautical Engineering**

Mark C. Butler, B.A.E.

June 1994

Accession For	
NTIS GRA&I	<input checked="checked" type="checkbox"/>
DTIC TAB	<input type="checkbox"/>
Unannounced	<input type="checkbox"/>
Justification	
By _____	
Distribution/_____	
Availability Codes	
Dist	Avail and/or Special
A1	

Approved for public release; distribution unlimited

Acknowledgements

This thesis could not have been completed without the support of my family and the help of many friends. A special thanks to Capt John H. Doty, my thesis advisor, for his patience, support and guidance given generously throughout this process.

Many additional friends deserve recognition for their help and contributions to this analysis effort. Maj Yonghee Hyun, ROKAF, made a heroic effort to provide me with a complete understanding of his research methodology before his return to Korea. Dr Datta Gaitonde and Lt John Soe provided critical guidance on the computational code and the GRIDGEN software. Capt John Riehl guided me through the code optimization procedure and, in general, helped me tame the National Air Intelligence Center (NAIC) computers used for the computational analysis. I would also like to thank Dr. William Elrod and Dr. R. Bowersox, the members of my thesis committee, for their thoughtful suggestions. In addition to serving on my thesis committee, Dr. Elrod also provided continual support, guidance and motivation throughout my AFTT experience.

Most importantly, I would like to thank my family for their support, patience and understanding during this effort. This research effort is dedicated to my wife Susan, my daughter Caroline, and my son Kevin. Thank you.

Mark C. Butler, June 1994

Table of Contents

Acknowledgements	ii
List of Figures	v
List of Tables	xi
List of Symbols	xii
Abstract	xv
I. INTRODUCTION	1
1.1 Background	1
1.2 Purpose	2
1.3 Scope	3
1.4 Approach	6
II. GOVERNING EQUATIONS AND NUMERICAL METHODS	13
2.1 Governing Equations	13
2.2 Numerical Methods	15
2.2.1 Coordinate Transformation	15
2.2.2 Discretization	16
2.3 Boundary and Initial Conditions	20
2.4 Computer Code Description	28
2.5 Solution Procedure	30
2.6 Computer Code Modifications	32
2.6.1 Addition of a Gas Generator Flowfield	33
2.6.2 Code Optimization	34
III. ANALYSIS OF NOZZLE COWL FLOWFIELDS	37
3.1 An Experimentally Validated Nozzle/Cowl Geometry	37
3.2 A Generic Hypersonic Vehicle Configuration	40
3.2.1 Nozzle/Cowl Model	40
3.2.2 Grid Generation	43
3.2.3 The Trajectory	45
3.3 The Gas Generator Model	46
IV. RESULTS AND DISCUSSIONS	58
4.1 Grid Resolution Effects	59
4.2 Application of a Cowl Gas Generator Flowfield to an Experimentally Validated Off-Design Configuration	66
4.2.1 Gas Generator Mass Flow Effects	70
4.2.2 Gas Generator Deflection Angle Effects	72

4.2.3 Gas Generator Comparison to Nozzle/Cowl Geometry Effects	73
4.2.4 Nozzle Pressure Ratio Effects	74
4.3 Application of a Cowl Gas Generator Flow to a Generic Hypersonic Vehicle Configuration Over a Typical On-Design Trajectory	92
4.3.1 Gas Generator Mass Flow Effects	97
4.3.2 Gas Generator Deflection Angle Effects	98
4.3.3 Trajectory Performance Analysis	99
 V. CONCLUSIONS AND RECOMMENDATIONS	122
5.1 Summary	122
5.2 Conclusions	123
5.3 Recommendations	126
 Bibliography	127
 Appendix A: Code Inputs	130
 Appendix B: Code Parallelization	133
B.1 Profile of Non Parallelized Code	133
B.2 Profile of Parallelized Code	135
B.3 Parallelization of Subroutine <i>Lf</i>	143
 Appendix C: Pressure and Mach Number Contours	145
 Vita	170

List of Figures

Figure 1-1 Typical Hypersonic Vehicle (9)	10
Figure 1-2 Experimental Nozzle/Cowl/Afterbody Model (4)	10
Figure 1-3 Diagram of the Hypersonic Nozzle/Cowl/Afterbody Experiment (4) . . .	11
Figure 1-4 Expanded View of a Generic Hypersonic Nozzle/Cowl Configuration (9)	12
Figure 2-1 Addition of Ghost Points to a Grid	21
Figure 3-1 Experimental Nozzle Geometry (1)	51
Figure 3-2 Experimental Nozzle/Cowl Final Cell Centered Grid (101x71)	52
Figure 3-3 Generic Nozzle Wall Definition (9)	53
Figure 3-4 Generic Nozzle/Cowl Coarse Cell Centered Grid (101x71)	54
Figure 3-5 Generic Nozzle/Cowl Medium Cell Centered Grid (151x101)	55
Figure 3-6 Generic Nozzle/Cowl Fine Cell Centered Grid (201x151)	56
Figure 3-7 Generic Nozzle Trajectory	57
Figure 4-1 Schematic of Over and Underexpanded Exhaust at Supersonic Freestream Mach Number (1)	63
Figure 4-2 Grid Resolution Effects, Gas Generator On 100%	64
Figure 4-3 Gas Generator Effects, Mach 15, Coarse Grid	64
Figure 4-4 Explicit Stability Check, Mach 15, Coarse Grid (101x71)	65
Figure 4-5 Gas Generator Effects, Mach 1.9, NPR=7.0	78
Figure 4-6 Gas Generator Effects, Mach 3.0, NPR=16.0	78
Figure 4-7 Constant Axial Location Flow Profile, Mach 1.9, NPR=7.0, I=52	79
Figure 4-8 Constant Axial Location Flow Profile, Mach 3.0, NPR=16.0, I=52	80

Figure 4-9 Gas Generator Mass Flow Effects, Mach 1.9, NPR=7.0 Nozzle Wall Pressure Distribution, No Gas Generator Deflection	81
Figure 4-10 Gas Generator Mass Flow Effects, Mach 1.9, NPR=7.0 Nozzle Wall Pressure Thrust, No Gas Generator Deflection	81
Figure 4-11 Gas Generator Mass Flow Effects, Mach 3.0, NPR=16.0 Nozzle Wall Pressure Distribution, No Gas Generator Deflection	82
Figure 4-12 Gas Generator Mass Flow Effects, Mach 3.0, NPR=16.0 Nozzle Wall Pressure Thrust, No Gas Generator Deflection	82
Figure 4-13 Gas Generator Deflection Effects, Mach 1.9, NPR=7.0 Nozzle Wall Pressure Distribution	83
Figure 4-14 Gas Generator Deflection Effects, Mach 1.9, NPR=7.0 Nozzle Wall Pressure Thrust	83
Figure 4-15 Gas Generator Deflection Effects, Mach 3.0, NPR=16.0 Nozzle Wall Pressure Distribution	84
Figure 4-16 Gas Generator Deflection Effects, Mach 3.0, NPR=16.0 Nozzle Wall Pressure Thrust	84
Figure 4-17 Experimental Nozzle/Cowl Geometry Effects, Mach 1.9, NPR=7.0 . . .	85
Figure 4-18 Experimental Nozzle/Cowl Geometry Effects, Mach 3.0, NPR=16.0 . .	86
Figure 4-19 Nozzle Pressure Ratio Effects, Mach 1.9, Gas Generator Off	87
Figure 4-20 Nozzle Pressure Ratio Effects, Mach 1.9, Gas Generator On 100% . .	88
Figure 4-21 Nozzle Pressure Ratio Effects, Mach 3.0, Gas Generator Off	89
Figure 4-22 Nozzle Pressure Ratio Effects, Mach 3.0, Gas Generator On 100% . .	90
Figure 4-23 Nozzle Pressure Ratio Effects, Nozzle Wall Pressure Thrust	91
Figure 4-24 Nozzle Pressure Ratio Effects, Percent Change in Thrust	91
Figure 4-25 Generic Nozzle/Cowl Pressure Distribution, Gas Generator Off	102
Figure 4-26 Constant Axial Location Flow Profile, Mach 10.0, I=52	103
Figure 4-27 Constant Axial Location Flow Profile, Mach 15.0, I=52	104

Figure 4-28 Constant Axial Location Flow Profile, Mach 20.0, I=52	105
Figure 4-29 Constant Axial Location Flow Profile, Mach 25.0, I=52	106
Figure 4-30 Gas Generator Mass Flow Effects, Mach 10 Nozzle Wall Pressure Distribution, No Gas Generator Deflection	107
Figure 4-31 Gas Generator Mass Flow Effects, Mach 10 Nozzle Wall Pressure Thrust, No Gas Generator Deflection	107
Figure 4-32 Gas Generator Mass Flow Effects, Mach 15 Nozzle Wall Pressure Distribution, No Gas Generator Deflection	108
Figure 4-33 Gas Generator Mass Flow Effects, Mach 15 Nozzle Wall Pressure Thrust, No Gas Generator Deflection	108
Figure 4-34 Gas Generator Mass Flow Effects, Mach 20 Nozzle Wall Pressure Distribution, No Gas Generator Deflection	109
Figure 4-35 Gas Generator Mass Flow Effects, Mach 20 Nozzle Wall Pressure Thrust, No Gas Generator Deflection	109
Figure 4-36 Gas Generator Mass Flow Effects, Mach 25 Nozzle Wall Pressure Distribution, No Gas Generator Deflection	110
Figure 4-37 Gas Generator Mass Flow Effects, Mach 25 Nozzle Wall Pressure Thrust, No Gas Generator Deflection	110
Figure 4-38 Gas Generator Deflection Effects, Mach 10 Nozzle Wall Pressure Distribution	111
Figure 4-39 Gas Generator Deflection Effects, Mach 10 Nozzle Wall Pressure Thrust	111
Figure 4-40 Gas Generator Deflection Effects, Mach 15 Nozzle Wall Pressure Distribution	112
Figure 4-41 Gas Generator Deflection Effects, Mach 15 Nozzle Wall Pressure Thrust	112
Figure 4-42 Gas Generator Deflection Effects, Mach 20 Nozzle Wall Pressure Distribution	113
Figure 4-43 Gas Generator Deflection Effects, Mach 20 Nozzle Wall Pressure Thrust	113

Figure 4-44 Gas Generator Deflection Effects, Mach 25 Nozzle Wall Pressure Distribution	114
Figure 4-45 Gas Generator Deflection Effects, Mach 25 Nozzle Wall Pressure Thrust	114
Figure 4-46 Gas Generator Mass Flow Effects, Percent Change in Nozzle Wall Lift, No Gas Generator Deflection	115
Figure 4-47 Gas Generator Deflection Effects, Nozzle Wall Pressure Contribution to Lift, Gas Generator Throttle 100%	116
Figure 4-48 Gas Generator Deflection Effects, Nozzle Wall Pressure and Direct Gas Generator Contribution to Lift, Gas Generator Throttle 100%	117
Figure 4-49 Gas Generator Mass Flow Effects, Nozzle Wall Pressure Contribution to Net Thrust, No Gas Generator Deflection	118
Figure 4-50 Gas Generator Mass Flow Effects, Nozzle Wall Pressure and Direct Gas Generator Contribution to Net Thrust, No Gas Generator Deflection	119
Figure 4-51 Gas Generator Deflection Effects, Nozzle Wall Pressure Contribution to Net Thrust, Gas Generator Throttle 100%	120
Figure 4-52 Gas Generator Deflection Effects, Nozzle Wall Pressure, Direct Gas Generator, and Nozzle Exhaust Contributions to Net Thrust, Gas Generator Throttle 100%	121
Figure C-1 Pressure Contours, Mach 1.9, Gas Generator Off	146
Figure C-2 Mach Number Contours, Mach 1.9, Gas Generator Off	147
Figure C-3 Pressure Contours, Mach 1.9, Gas Generator 100%	148
Figure C-4 Mach Number Contours, Mach 1.9, Gas Generator 100%	149
Figure C-5 Pressure Contours, Mach 3.0, Gas Generator Off	150
Figure C-6 Mach Number Contours, Mach 3.0, Gas Generator Off	151
Figure C-7 Pressure Contours, Mach 3.0, Gas Generator 100%	152
Figure C-8 Mach Number Contours, Mach 3.0, Gas Generator 100%	153

Figure C-9 Pressure Contours, Mach 10, Gas Generator Off	154
Figure C-10 Mach Number Contours, Mach 10, Gas Generator Off	155
Figure C-11 Pressure Contours, Mach 10, Gas Generator 100%	156
Figure C-12 Mach Number Contours, Mach 10, Gas Generator 100%	157
Figure C-13 Pressure Contours, Mach 15, Gas Generator Off	158
Figure C-14 Mach Number Contours, Mach 15, Gas Generator Off	159
Figure C-15 Pressure Contours, Mach 15, Gas Generator 100%	160
Figure C-16 Mach Number Contours, Mach 15, Gas Generator 100%	161
Figure C-17 Pressure Contours, Mach 20, Gas Generator Off	162
Figure C-18 Mach Number Contours, Mach 20, Gas Generator Off	163
Figure C-19 Pressure Contours, Mach 20, Gas generator 100%	164
Figure C-20 Mach Number Contours, Mach 20, Gas Generator 100%	165
Figure C-21 Pressure Contours, Mach 25, Gas Generator Off	166
Figure C-22 Mach Number Contours, Mach 25, Gas Generator Off	167
Figure C-23 Pressure Contours, Mach 25, Gas Generator 100%	168
Figure C-24 Mach Number Contours, Mach 25, Gas Generator 100%	169

List of Tables

Table 1-1 Experimental Nozzle, Mass Flow Cases	8
Table 1-2 Experimental Nozzle, Thrust Vector Deflection Cases	8
Table 1-3 Experimental Nozzle, Nozzle Pressure Ratio Cases	8
Table 1-4 Generic Nozzle, Mass Flow Cases	9
Table 1-5 Generic Nozzle, Thrust Vector Deflection Cases	9
Table 3-1 Generic Nozzle Configuration Definition	43
Table 3-2 Experimental Nozzle, Mach 1.9 Flow Definition	48
Table 3-3 Experimental Nozzle, Mach 3.0 Flow Definition	48
Table 3-4 Generic Nozzle Flow Definition	49
Table 3-5 Gas Generator Flow Definition	50
Table A-1 Algorithm Control Parameters	130
Table A-2 Geometric Parameters	130
Table A-3 Flowfield Conditions	131
Table A-4 Basic Control Parameters	131

List of Symbols

a	Speed of Sound [ft/s]
A	Flux Vector Jacobian Matrix
B	Flux Vector Jacobian Matrix
C_p	Coefficient of Pressure [-]
c_p	Specific Heat at Constant Pressure [ft ² /(s ² °R)]
c_v	Specific Heat at Constant Volume [ft ² /(s ² °R)]
D	Difference Operator, $Df = f_{i+1/2} - f_{i-1/2}$
e	Specific Internal Energy [ft ² /s ²]
E_t	Total Energy [lbm/(ft s ²)]
F	Inviscid Flux Vector
F_v	Viscous Flux Vector
G	Inviscid Flux Vector
G_v	Viscous Flux Vector
h	Nozzle Height [in]
J	Jacobian Matrix
k	Thermal Conductivity [BTU/(ft s °R)]
M	Mach Number [-]
p	Static Pressure [lbf/ft ²]
P_T	Total Pressure [lbf/ft ²]
p_i	Local Pressure [lbf/ft ²]
q	Heat Transfer Rate per Unit Area [BTU/(s ft ²)] or Dynamic Pressure [lbf/ft ²]

Q	Heat Flow Rate [BTU/s]
R	Gas Constant per Unit Mass [$\text{ft}^2/(\text{s}^2 \text{ } ^\circ\text{R})$]
r_o	Adiabatic Recovery Factor [-]
Re	Reynolds Number [-]
T	Static Temperature [$^\circ\text{R}$]
T_{wall}	Wall Temperature [$^\circ\text{R}$]
u	Velocity in the Cartesian Coordinate x-Direction [ft/s]
v	Velocity in the Cartesian Coordinate y-Direction [ft/s]
U	Vector of Conserved Variables, Density, Momentum, and Energy
U	Velocity Magnitude [ft/s]

Greek

θ	Thrust Vector Deflection Angle [degrees]
α	Angle of Attack [degrees]
δ	Difference Operator, $\delta f = f^{n+1} - f^n$
γ	Ratio of Specific Heats, C_p/C_v [-]
λ	Second Coefficient of Viscosity [lbf s/ft ²]
λ_1	Eigenvalue
μ	First Coefficient of Viscosity [lbf s/ft ²]
ρ	Density [lbm/ft ³]
τ_{ij}	Stress Tensor
ξ	Computational Streamwise Axis
η	Computational Normal Axis

Subscripts

i	Streamwise Direction Index
injected	Value at Gas Generator Injector
j	Normal Direction Index
n	Nozzle Internal Flow Value
x	Cartesian Coordinate Streamwise Direction
y	Cartesian Coordinate Normal Direction
∞	Freestream Flow Value

Superscripts

L	Finite Volume Left Interface
n	Time Index
R	Finite Volume Right Interface
\pm	Upwinding Notation

Abstract

An improved propulsive nozzle/cowl concept has been proposed which may have some potential for increasing the overall performance of hypersonic flight vehicles. The concept consists of placing a gas generator into the cowl to supply a relatively high pressure boundary condition to the main exhaust plume. This computational study investigated two nozzle/cowl geometries; an experimentally validated nozzle/cowl configuration evaluated at off-design conditions and a generic hypersonic propulsive nozzle evaluated at more realistic on-design conditions. The flowfields were analyzed using a combination of Van Leer flux-vector splitting (FVS) and Roe flux-difference splitting (FDS) finite volume computational algorithms implemented in a code developed by Wright Laboratory (WL/FIMC). The two-dimensional Navier-Stokes equations were solved assuming laminar flow and a perfect gas equation of state. This investigation highlighted the effect of the gas generator on the nozzle wall pressure distribution and its effect on overall nozzle performance. The analysis emphasized the effect of gas generator mass flow and deflection angle effects. In general, the gas generator tended to show a larger improvement in nozzle performance at lower Mach number and nozzle pressure ratio (NPR) off-design conditions where the flow is significantly underexpanded. For the very high Mach, high NPR on-design configuration analyzed, the overall system performance increased with the addition of the gas generator but the nozzle wall pressure recovery actually tended to decrease slightly. This unexpected decrease occurred because the gas generator exit pressure was relatively low compared to the very high recompression pressure experienced

behind the blunt cowl at these high speed trajectory points. Simply placing a nominal gas generator into the flowfield tended to have a much larger effect on nozzle wall pressure than varying its mass flow even though nozzle performance did tend to increase with increased mass flow. Deflecting the gas generator flow towards the nozzle wall provided a dramatic improvement in pressure recovery and only a small penalty was paid for deflecting it away from the wall. For the experimentally validated off-design cases analyzed, the gas generator successfully acted as an aerodynamic cowl extension. Gas generator effects on nozzle wall pressure recovery were very similar to cowl geometry extension and deflection effects previously analyzed for this configuration. Nozzle operating condition had a significant impact on the gas generator performance. As the nozzle exit pressure and trajectory Mach number increased, the flow became increasingly dominated by the large initial expansions. The increased initial expansion combined with higher internal nozzle flow Mach numbers decreased the overall effects of the gas generator and tended to push the propagation of the gas generator effects to the nozzle wall further downstream. Grid refinement effects were limited to the region near the peak of the initial recompression where the finer grids captured slightly higher peak pressures.

COMPUTATIONAL INVESTIGATION OF AN IMPROVED COWL CONCEPT FOR HYPERSONIC PROPULSIVE NOZZLES

I. INTRODUCTION

1.1 Background

A fundamental desire to design aircraft that fly higher and faster has been evident in flight vehicle design since the earliest days of manned flight. The ability to develop and build manned hypersonic flight vehicles was proven with experimental flight vehicles such as the X-15 which exceeded Mach 7 and 350,000 ft. in 1963 (3). A series of manned hypersonic experimental aircraft developed in the 1960's led to the development of the first reusable manned hypersonic vehicle--the Space Shuttle, which regularly achieves Mach 25 flight during its reentry glide. The next major step is to design a reusable manned single stage to orbit (SSTO) flight vehicle such as the proposed National AeroSpace Plane (NASP). Unlike the X-15 which was rocket powered or the Space Shuttle which is unpowered, a reusable SSTO vehicle must have an integrated propulsion system that is capable of accelerating the vehicle to orbital speeds in excess of Mach 25. These hypersonic flight vehicle designs will be dominated by the air-breathing supersonic combustion ramjet (SCRAMjet) engines which will be integrated into a single airframe-engine propulsion system (3).

Figure 1-1 shows a typical hypersonic vehicle with its airframe-integrated propulsion system. The vehicle forebody behaves as a compression ramp for the

engine inlet flow. Further compression of the flow and combustion take place in the modular chambers below the vehicle. The flow is then expanded along the vehicle afterbody which acts like a nozzle wall.

At hypersonic speeds, the integrated propulsion system is designed to operate at very high pressure ratios. The nozzle pressure ratio (NPR) is defined as the SCRAMjet total exit pressure divided by the ambient freestream static pressure, $NPR = P_T/P_\infty$. For hypersonic flight conditions, the combustor exit flow is typically underexpanded and some of the excess pressure can be recovered along the nozzle wall to increase net thrust and lift. At low Mach numbers, once the flow exits the combustor, the flow typically overexpands resulting in a pressure just downstream of the combustor that is less than the ambient pressure which results in increased drag and decreased net thrust.

Any net performance improvements to hypersonic propulsive nozzles could have a significant impact on hypersonic flight vehicle designs like the NASP or NASP-derived vehicles. An improved cowl concept has been proposed which may have some potential for increasing the overall performance of these vehicles. This concept consists of placing a rocket or gas generator into the cowl to supply a relatively high pressure boundary condition to the main exhaust plume.

1.2 Purpose

There are many potential benefits for placing a throttleable, vectorable gas generator into the cowl of a hypersonic vehicle. The gas generator could potentially provide weight reduction due to a decreased cowl length, increased direct thrust from

the gas generator, and a potential increase in nozzle performance due to higher pressure on the nozzle wall. In addition, the offset location of the gas generator in the cowl may make it well suited for providing direct stability and control moment control to the vehicle.

This computational analysis investigates the effect of inserting a gas generator flow into a nozzle/cowl flowfield.

1.3 Scope

The scope of this research effort included implementing a gas generator flow model into an existing computational fluid dynamics (CFD) code and evaluating the potential on-design and off-design performance of this concept.

The effect of a gas generator on nozzle performance was investigated for two different nozzle/cowl geometries. An experimentally validated hypersonic nozzle/cowl configuration was analyzed at relatively low speed, off-design conditions of Mach 1.9 and 3.0. A more realistic generic nozzle/cowl configuration was analyzed over a typical trajectory which maintained a constant dynamic pressure, q , of 1000 psf through on-design flight conditions ranging between Mach 10 and 25.

The first nozzle was based on an experimental hypersonic nozzle/afterbody model developed by Cochran (4). This is also the same geometry used by Hyun (1) to validate the computational code used for this research. Figure 1-2 shows the experimental model and Figure 1-3 shows the experimental apparatus that this configuration was based on.

The second nozzle/cowl geometry analyzed represents a more realistic generic hypersonic vehicle afterbody configuration which was analyzed over a typical flight trajectory. Figure 1-3 shows the generic nozzle/cowl geometry developed by Doty (9) that was used for this portion of the study. The generic nozzle/cowl geometry was optimized by Bonaparte (2) over this typical trajectory. The nozzle configuration chosen for this analysis corresponds to Bonaparte's optimized generic nozzle geometry evaluated at a design Mach number of 15.

Realistic gas generator exhaust conditions were obtained using a code developed to determine the equilibrium flow solution for a liquid hydrogen-oxygen rocket motor. The gas generator configuration was based on a scaled down Space Shuttle Main Engine (SSME) geometry (22).

The gas generator flowfield was applied to both of the nozzle/cowl configurations and the flow solution was evaluated at a variety of gas generator operating conditions. Not only were the effects of gas generator mass flow and exit pressure analyzed, but the effects of gas generator thrust vector deflection angle were also investigated.

For the experimental nozzle/cowl configuration, the gas generator effects were evaluated over a range of NPR at two low speed off-design Mach numbers, Mach 1.9 and Mach 3.0. Tables 1-1 through 1-3 describe the initial conditions analyzed computationally. For each Mach number, the gas generator mass flow was varied from the baseline gas generator off condition (0% throttle setting) to a 200% of design operating condition throttle setting in 25% increments. The gas generator deflection effects were analyzed at a 100% throttle setting over a range of ± 10 degrees in 2.5

degree increments. A negative gas generator deflection angle is defined as a deflection towards the nozzle wall and a positive deflection is defined as a deflection away from the nozzle wall. The baseline gas generator off cases were compared to the flow solution using a non-deflected 100% throttle gas generator flow over a range of operating NPR. A total of 48 final flow solutions were calculated for this experimental nozzle/cowl geometry.

The gas generator effects are also compared to the effects of varying the cowl wall geometry. Cowl wall trailing edge extensions (+0.5 inch) and deflections (± 5 degrees) were analyzed experimentally by Cochran and numerically by Hyun. Gas generator effects are compared directly to these results.

For the generic nozzle/cowl configuration, the results were analyzed over a typical trajectory. Tables 1-4 and 1-5 describe the cases evaluated for this analysis. The gas generator effects were analyzed over 4 points spanning a typical trajectory. Mach 10, 15, 20 and 25 flight conditions were evaluated over a constant 1000 psf dynamic pressure trajectory. Gas generator throttle setting was increased from 0% to 200% of the design operating condition in 50% increments. The gas generator deflection angles covered ± 10 degrees in 5 degree increments. Excursions were also made to analyze the trends associated with relatively large gas generator deflection angles of ± 20 degrees. A total of 44 final flow solutions were calculated for this generic nozzle/cowl geometry.

The effects of the gas generator are presented in terms of overall nozzle performance. Since a significant percentage of total thrust is generated through pressure recovery along the airframe-integrated nozzle wall, the effects of the gas

generator are presented in terms of the pressure distribution along the nozzle wall.

The net effect of these pressure recovery changes are presented in terms of the integrated nozzle wall pressure contributions to lift and thrust. For the trajectory analysis of the generic nozzle/cowl configuration, the pressure contributions to lift and thrust are also presented relative to the overall vehicle afterbody performance.

1.4 Approach

Hypersonic vehicle afterbody flowfields contain a complex interaction of flowfield phenomena including expansion waves, shock waves, viscous contact surfaces, and solid surface boundaries including the cowl and nozzle walls. The flowfield is complicated with the strong interaction of all of these components.

The literature shows that many computational fluid dynamics (CFD) codes have been developed to analyze the complex flowfield of hypersonic propulsive nozzles. Any CFD code used to analyze this type of complicated flow must be validated against experimental data to ensure that it can accurately capture the effects of all of the complicated flowfield interactions. One such code, developed by Wright Laboratory, solves the unsteady, two-dimensional Navier-Stokes equations based on perfect gas laminar flow assumptions using several explicit flux-splitting finite volume schemes. Hyun (1) compared the Wright Laboratory code to the experimental data of Cochran (4). Hyun demonstrated that this code captured the complicated flowfield phenomena quite well for high speed freestream flow conditions. Hyun also showed that as NPR and freestream Mach number increased, the general correlation between experimental and computational results improved. For these reasons, this code was

chosen to analyze the effects of placing an additional gas generator into this complicated flowfield.

The flux-vector splitting (FVS) approach of Van Leer and the flux-difference splitting (FDS) approach of Roe were incorporated into the Wright Laboratory code by Gaitonde (7). These robust algorithms are second-order accurate in space and time.

The Van Leer method was initially used to achieve a steady state solution since it requires no more than two internal cells to capture internal shock structures. Hyun (1) discovered that the Roe method should not be used for the initial steady state solution because it may violate the entropy condition near sonic or stagnation points. When the Van Leer solution converged to a steady state solution, the flowfield calculations were then completed using the Roe approach, which more accurately captures wave interactions between cell interfaces (1).

Several grid densities were evaluated to perform a grid resolution study on the generic nozzle/cowl configuration investigated. Once a suitable grid was chosen, complete flow solutions were calculated for each desired flow condition.

Table 1-1 Experimental Nozzle, Mass Flow Cases

Mach	Gas Generator Throttle Setting [%]								
1.9	0	25	50	75	100	125	150	175	200
3.0	0	25	50	75	100	125	150	175	200

Table 1-2 Experimental Nozzle, Thrust Vector Deflection Cases

Mach	Gas Generator Thrust Vector Deflection Angle [deg]								
1.9	-10.0	-7.5	-5.0	-2.5	0.0	2.5	5.0	7.5	10.0
3.0	-10.0	-7.5	-5.0	-2.5	0.0	2.5	5.0	7.5	10.0

Table 1-3 Experimental Nozzle, Nozzle Pressure Ratio Cases

Mach	Nozzle Pressure Ratio (NPR)				
1.9	3.0	5.0	7.0	12.0	N/A
3.0	5.0	7.0	9.0	12.0	16.0

Table 1-4 Generic Nozzle, Mass Flow Cases

Mach	Gas Generator Throttle Setting [%]				
10	0	50	100	150	200
15	0	50	100	150	200
20	0	50	100	150	200
25	0	50	100	150	200

Table 1-5 Generic Nozzle, Thrust Vector Deflection Cases

Mach	Gas Generator Thrust Vector Deflection Angle [deg]						
10	-20	-10	-5	0	5	10	20
15	-20	-10	-5	0	5	10	20
20	-20	-10	-5	0	5	10	20
25	-20	-10	-5	0	5	10	20

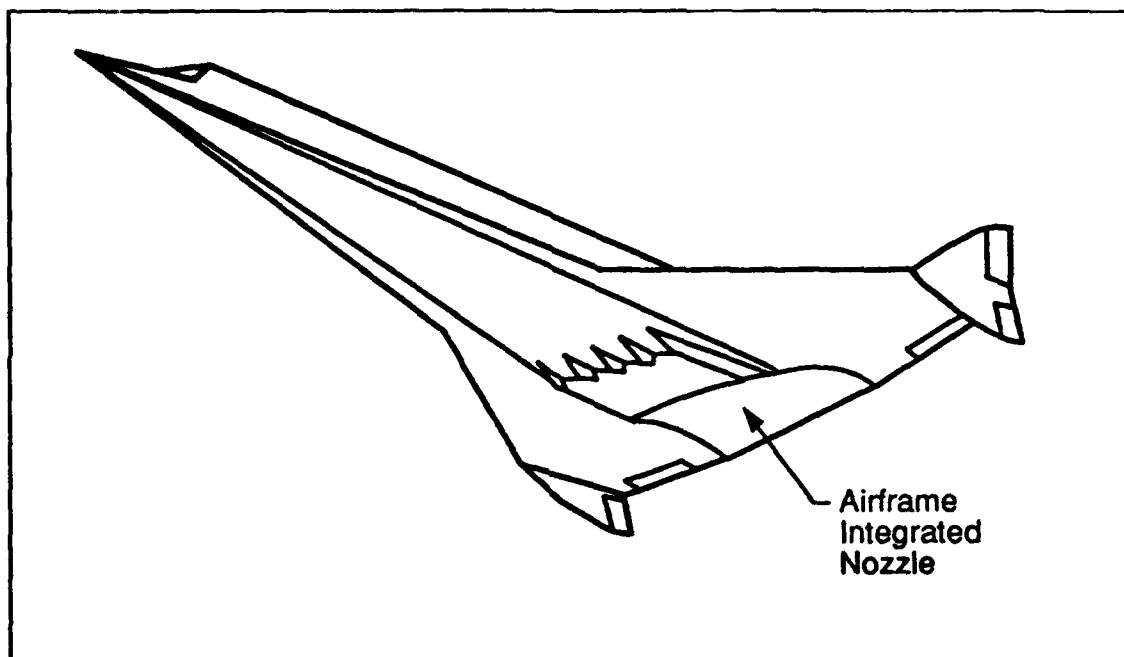


Figure 1-1 Typical Hypersonic Vehicle (9)

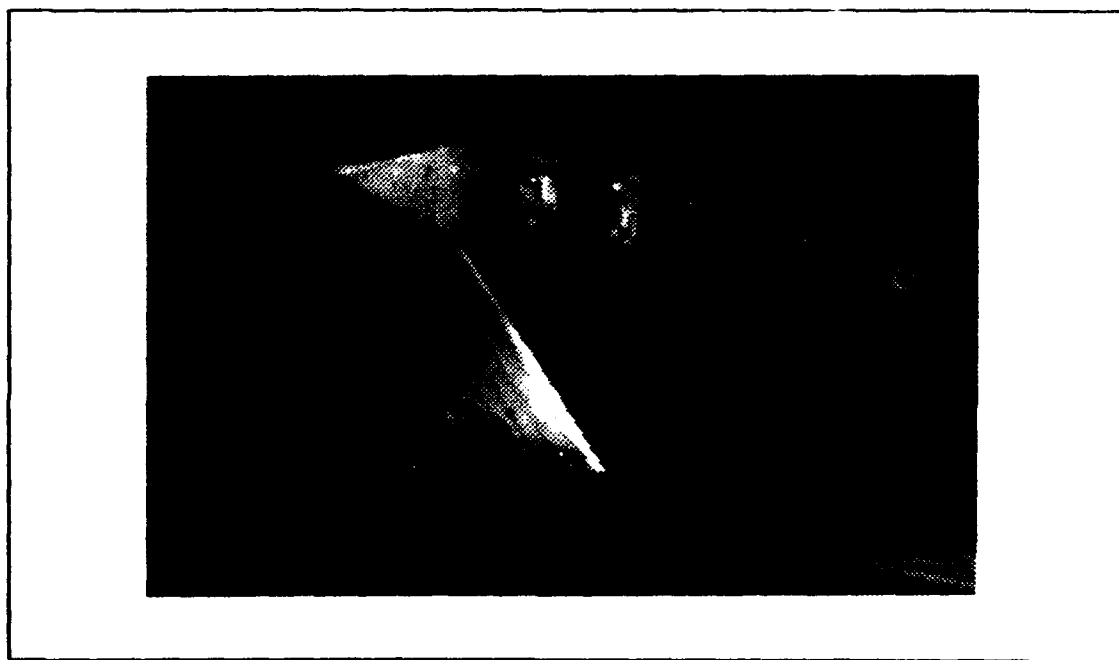


Figure 1-2 Experimental Nozzle/Cowl/Afterbody Model (4)

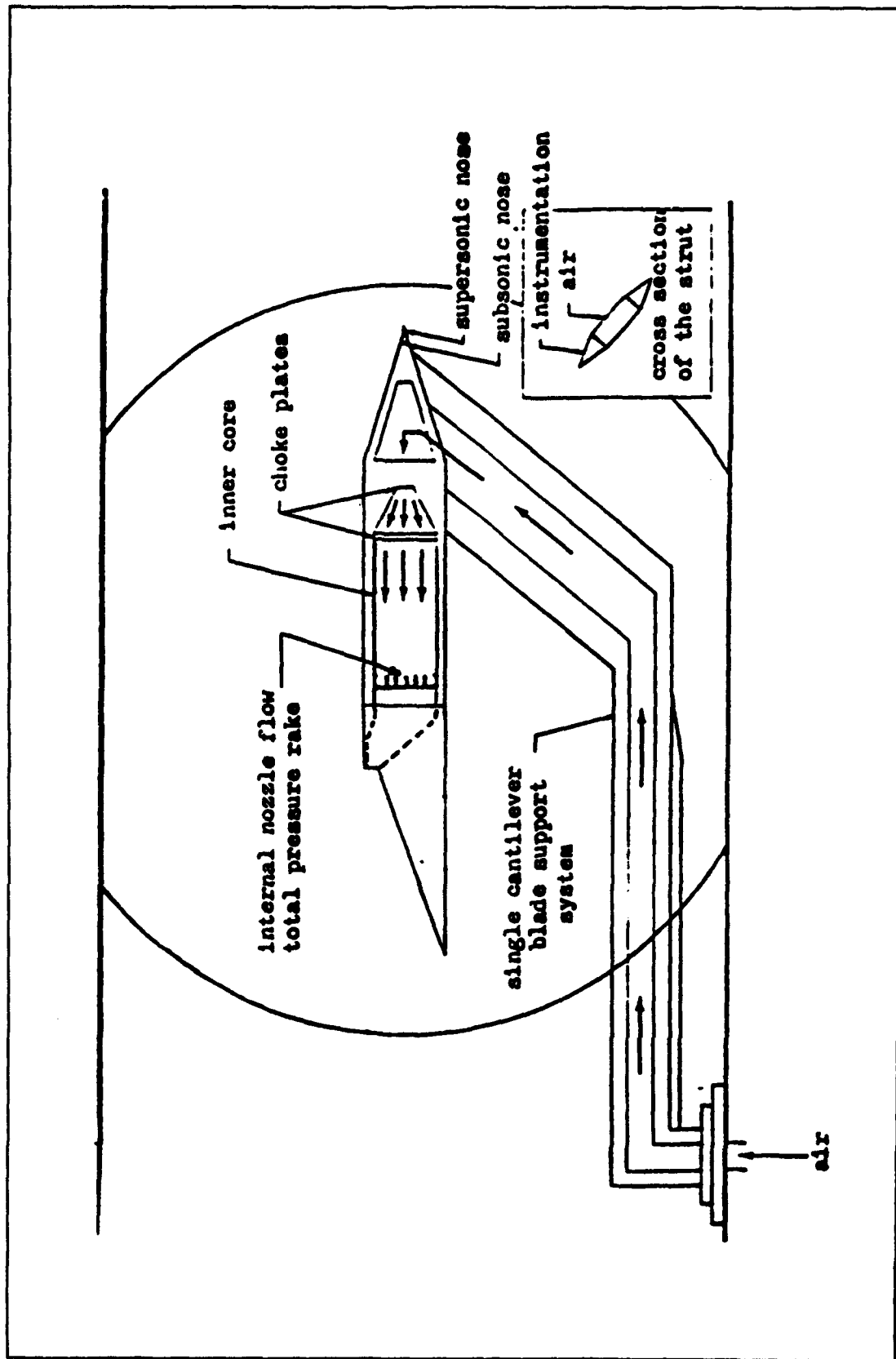


Figure 1-3 Diagram of the Hypersonic Nozzle/Cow/Afterbody Experiment (4)

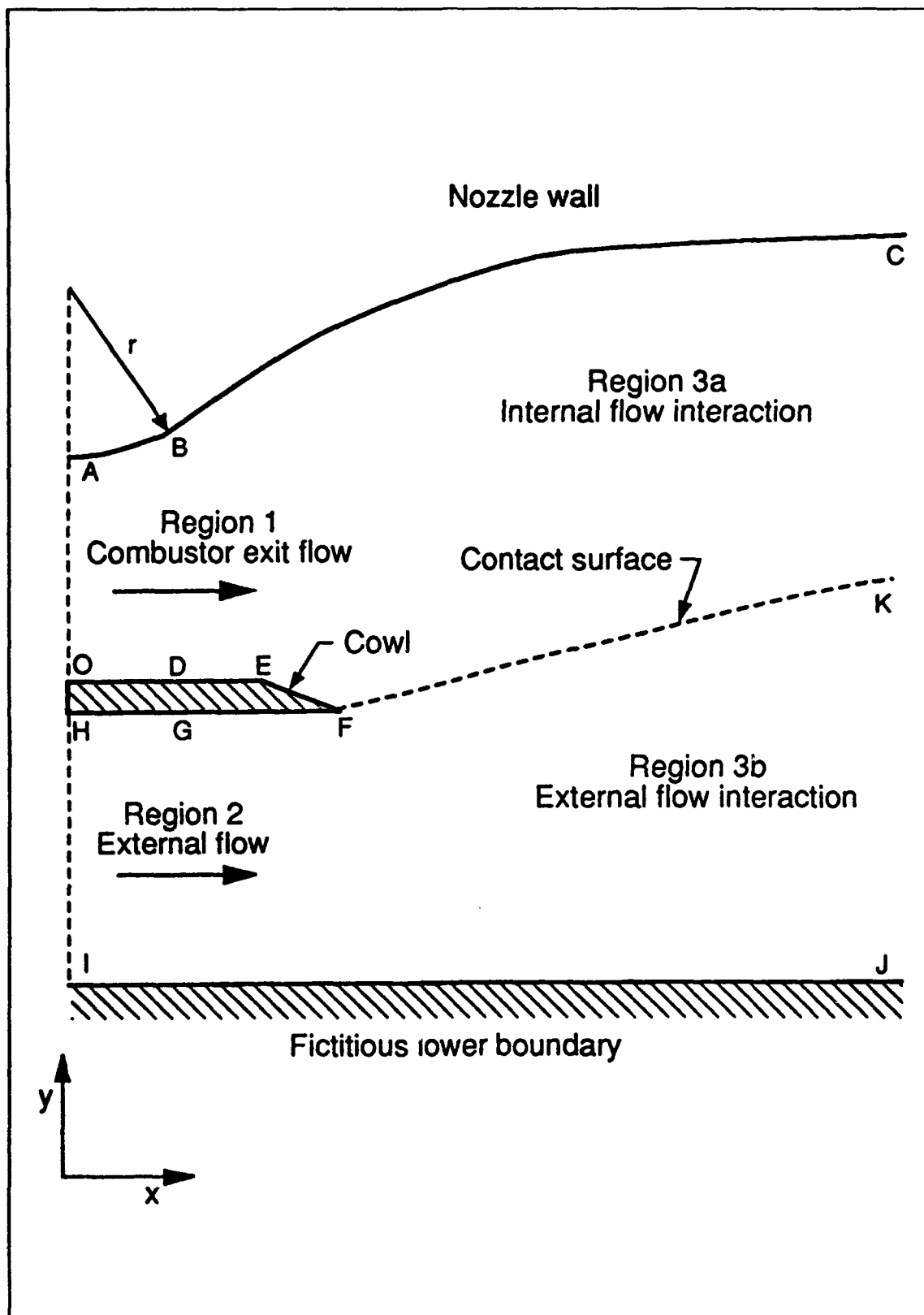


Figure 1-4 Expanded View of a Generic Hypersonic Nozzle/Cowl Configuration (9)

II. GOVERNING EQUATIONS AND NUMERICAL METHODS

2.1 Governing Equations

The governing equations of motion for the planar, unsteady, viscous flow of a compressible fluid which account for viscous stresses and thermal conduction are the Navier-Stokes equations. By neglecting body forces and heat sources, the Navier-Stokes equations may be written (10):

$$\frac{\partial \rho}{\partial t} + \frac{\partial \rho u_j}{\partial x_j} = 0 \quad (\text{Continuity}) \quad (2-1)$$

$$\frac{\partial \rho u_i}{\partial t} + \frac{\partial \rho u_i u_j}{\partial x_j} + \frac{\partial p}{\partial x_i} - \frac{\partial \tau_{ij}}{\partial x_j} = 0 \quad (\text{Momentum}) \quad (2-2)$$

$$\frac{\partial e}{\partial t} + \frac{\partial (E_i + p)}{\partial x_j} - \frac{\partial (u_i \tau_{ij} - q_j)}{\partial x_j} = 0 \quad (\text{Energy}) \quad (2-3)$$

$$p = f(e, \rho) = f\left(\frac{E_i}{\rho} - \frac{|\bar{u}|^2}{2}, \rho\right) \quad (\text{Equation of state}) \quad (2-4)$$

where indicial notation has been used (repeated indices are summed) and

u_i = component of velocity in x_i direction

τ_{ij} = viscous stress

$$\tau_{ij} = \lambda \delta_{ij} \frac{\partial u_k}{\partial x_k} + \mu \left(\frac{\partial u_i}{\partial x_j} + \frac{\partial u_j}{\partial x_i} \right) \quad (2-5)$$

where δ_{ij} = the Kronecker delta

μ, λ = first and second coefficients of viscosity, respectively

$$q_j = -k(\partial T / \partial x_j)$$

where k is the coefficient of thermal conductivity.

The coefficient of viscosity is related to the thermodynamic variables using Sutherlands Law (10):

$$\mu = C_1 \frac{T^{\frac{3}{2}}}{T + C_2} \quad (2-6)$$

where C_1 and C_2 are constants for a given gas. For air at standard temperatures, $C_1 = 2.27E-08 \text{ lb}_m / (\text{ft-sec } ^\circ\text{R}^{1/2})$ and $C_2 = 198.9 \text{ R}$.

The two-dimensional Navier-Stokes equations presented in Equations (2-1) through (2-4) can be rewritten in vector divergence form. The vector divergence form of these equations simplifies their implementation into finite volume computational fluid dynamics algorithms. In vector divergence form, these equations may be written:

$$\frac{\partial \mathbf{U}}{\partial t} + \frac{\partial \mathbf{F}}{\partial x} + \frac{\partial \mathbf{G}}{\partial y} = 0 \quad (2-7)$$

where the conserved variables are given by:

$$U = \begin{bmatrix} \rho \\ \rho u \\ \rho v \\ E_t \end{bmatrix} \quad (2-8)$$

and the flux vectors are separated into their inviscid (F, G) and viscous terms (F_v, G_v).

$$F = \begin{bmatrix} \rho u \\ \rho u^2 + p \\ \rho uv \\ (E_t + p)u \end{bmatrix} \quad G = \begin{bmatrix} \rho v \\ \rho uv \\ \rho v^2 + p \\ (E_t + p)v \end{bmatrix} \quad (2-9)$$

$$F_v = \begin{bmatrix} 0 \\ \tau_{xx} \\ \tau_{yx} \\ u_j \tau_{xj} + k \frac{\partial T}{\partial x} \end{bmatrix} \quad G_v = \begin{bmatrix} 0 \\ \tau_{xy} \\ \tau_{yy} \\ u_j \tau_{yj} + k \frac{\partial T}{\partial y} \end{bmatrix} \quad (2-10)$$

The final equation required to define the flow field is the perfect gas equation-of-state.

$$p = (\gamma - 1) \rho e \quad e = \frac{E_t}{\rho} - \frac{1}{2}(u^2 + v^2) \quad (2-11)$$

2.2 Numerical Methods

2.2.1 Coordinate Transformation. The Navier-Stokes equations are transformed from the physical space coordinate system to a computational space coordinate system in order to generate a suitable computational grid for the application

of the numerical method. The coordinate transformation simplifies the process of applying boundary conditions, clustering grid points, and providing orthogonality for application of numerical solutions to the Navier-Stokes equations (10). Equation (2-7) can be transformed into a general coordinate system (ξ, η) :

$$\frac{\partial U}{\partial \xi} + \frac{\partial F}{\partial \xi} + \frac{\partial G}{\partial \eta} = 0 \quad (2-12)$$

The details of this transformation can be found in (6) and (12). The general transformed form of the Navier-Stokes equations can be written (1):

$$\begin{aligned} \frac{\partial}{\partial \xi} \left(\frac{U}{J} \right) + \frac{\partial}{\partial \xi} \left(\frac{1}{J} [\xi_x (F - F_v) + \xi_y (G - G_v)] \right) \\ + \frac{\partial}{\partial \eta} \left(\frac{1}{J} [\eta_x (F - F_v) + \eta_y (G - G_v)] \right) = 0 \end{aligned} \quad (2-13)$$

where the Jacobian of the transformation is given by:

$$J^{-1} = x_\xi y_\eta - x_\eta y_\xi \quad (2-14)$$

2.2.2 Discretization. This study uses a modified version of a code that was developed by Wright Laboratory (WL/FIMC). The code has three options available for the discretization of the Navier-Stokes equations; Steger and Warming flux-vector splitting, Van Leer flux-vector splitting, and Roe flux-difference splitting. The viscous flux vector terms (F_v, G_v) are discretized using simple central differences. The inviscid flux vector terms (F, G) may be discretized using either of the flux-vector splitting or flux-difference splitting methods. A detailed discussion and examples of these three discretizations can be found in Hyun (1).

The numerical approach is second-order accurate in time and space. The solution is marched in time using a two-stage Runge-Kutta scheme. The formulation is finite volume and second-order accuracy is obtained through the use of the MUSCL (Monotonic Upstream Schemes for Conservation Laws) approach in conjunction with a *minmod* limiter to prevent oscillations. Details of the MUSCL approach and the *minmod* limiter applied to a one-dimensional example can also be found in Hyun (1).

The basic concept of the flux-vector and flux difference splitting can be illustrated using the following one-dimensional, inviscid model:

$$\frac{\partial U}{\partial t} + \frac{\partial F(U)}{\partial x} = 0 \quad (2-15)$$

A first-order explicit discretization of Equation (2-15) using the forward Euler method gives:

$$\frac{(\delta U^n)_i}{\Delta t} = - \frac{F_{i+\frac{1}{2}}^n - F_{i-\frac{1}{2}}^n}{\Delta x} \quad (2-16)$$

where

$$\delta U^n = U^{n+1} - U^n \quad (2-17)$$

and where $F_{i+1/2}$ is based on some combination of F at the adjacent grid points. For example, a simple average value could be used where $F_{i+1/2} = (F_i + F_{i+1})/2$.

The two-dimensional Navier-Stokes Equation (2-7) can be discretized in a similar manner. A successive balancing of the fluxes in each direction is used to

compute the right hand side, or residual, of the two-dimensional version of Equation (2-16):

$$LHS_1 = \frac{F_{i+\frac{1}{2}}(U^n) - F_{i-\frac{1}{2}}(U^n)}{\Delta x} \quad (2-18)$$

$$LHS_2 = LHS_1 + \frac{G_{i+\frac{1}{2}}(U^n) - G_{i-\frac{1}{2}}(U^n)}{\Delta y}$$

where LHS_1 is the left hand side of the two-dimensional version of Equation (2-16).

The left hand side of Equation (2-16) is calculated using a two stage Runge-Kutta scheme known as Heun's method. The details of this Runge-Kutta application can be found in (24).

The right hand side of Equation (2-16) can be evaluated using either the flux-vector splitting approach of Steger and Warming or Van Leer or the flux-difference splitting approach of Roe. The Van Leer approach is essentially an improvement over the earlier Steger and Warming flux-vector splitting approach. Inaccuracies arise in the Steger and Warming scheme when the eigenvalues of the flux Jacobians change sign. The flux Jacobians, A and B are given by:

$$F = AU ; A = \frac{\partial F}{\partial U} \quad G = BU ; B = \frac{\partial G}{\partial U} \quad (2-19)$$

Eigenvalue sign changes will occur near shock structures or stagnation points in the flowfield. In the Steger and Warming scheme, the split-flux derivatives are discontinuous at these eigenvalue sign changes giving rise to inaccuracies and instabilities in these regions. Van Leer's improvement over the Steger and Warming

scheme was to split the fluxes so that the forward and backward flux contributions transitioned smoothly at the eigenvalue sign changes. A comparison of these two methods is presented in Hyun (1).

The Van Leer approach was chosen as the initial flow solver for this study since it is more robust than the Steger and Warming approach. Van Leer's approach to solving the right hand side of Equation (2-16) consists of splitting the flux into positive and negative components for appropriate upwind differencing:

$$F_{i+\frac{1}{2}} = F^+(U^L) + F^-(U^R) \quad (2-20)$$

where U^R and U^L are vectors of the conserved flow variables at each interface. The Van Leer flux-vector splitting approach is designed to make computational schemes more robust and to improve computational efficiency. The goal of a flux-vector splitting scheme is to split the flux vectors in such a way that an upwind finite-difference scheme may be used throughout the entire flowfield. This is accomplished by splitting the flux vectors into upwind and downwind parts. For second-order accuracy, U^R and U^L are obtained using Van Leer's MUSCL approach to extrapolate the conserved variables to the cell surface. Van Leer's approach also incorporates a *minmod* limiter based on local conditions to avoid oscillations in shock regions. The addition of the *minmod* limiter causes the solution to locally revert back to first-order accuracy in the vicinity of the shock in order to preserve monotonicity within the solution.

The Van Leer approach is also very robust in regions of supersonic expansion. This method is useful for starting the flow solution when there is a significant amount of expansion from the initial conditions in the steady state flow solution (1).

Roe's scheme is used to achieve a final solution after the Van Leer solution has achieved a steady state solution through the initial flowfield expansions. Roe's approach to solving the right hand side of Equation (2-16) is:

$$F_{i+\frac{1}{2}} = \frac{1}{2} \left[F(U^L) + F(U^R) - \frac{1}{2} \hat{A} (U^R - U^L) \right] \quad (2-21)$$

where \hat{A} is the Roe-averaged flux vector Jacobian matrix. The " $\hat{\cdot}$ " refers to Roe averaging given by:

$$\hat{x} = \frac{\sqrt{\rho_L} x_L + \sqrt{\rho_R} x_R}{\sqrt{\rho_L} + \sqrt{\rho_R}} \quad x = \rho, u, v, \text{ and } h \quad (2-22)$$

where the R and the L subscripts refer to the components of U^R and U^L respectively.

The Roe approach also uses a MUSCL approach and a minmod limiter to achieve second-order accuracy.

2.3 Boundary and Initial Conditions

Since the finite-volume computational schemes used for this study are cell centered methods which solve for fluxes across the cell surfaces, ghost points must be added to the grid in order to apply boundary conditions. Ghost points are required at all internal and external boundaries. Figure 2-1 demonstrates the application of ghost points to a simplified grid and it helps highlight the necessity of ghost points. For example, if the surface boundary depicted in Figure 2-1 requires a no-slip boundary

condition there is no way to specify zero velocity on this surface with the basic cell centered grid. Ghost grid point nodes are applied such that a row of new fictitious cells are created as extrapolations of the original grid. The extrapolated grid has an associated row of fictitious cell centers that are outside of the original surface boundary as shown in Figure 2-1. Flow variables can then be specified at the ghost cell centers such that the desired boundary conditions are enforced on the surface boundary. For this simplified example, where the internal and external cell centers are the same distance from the edge of the grid, a no-slip boundary condition can be

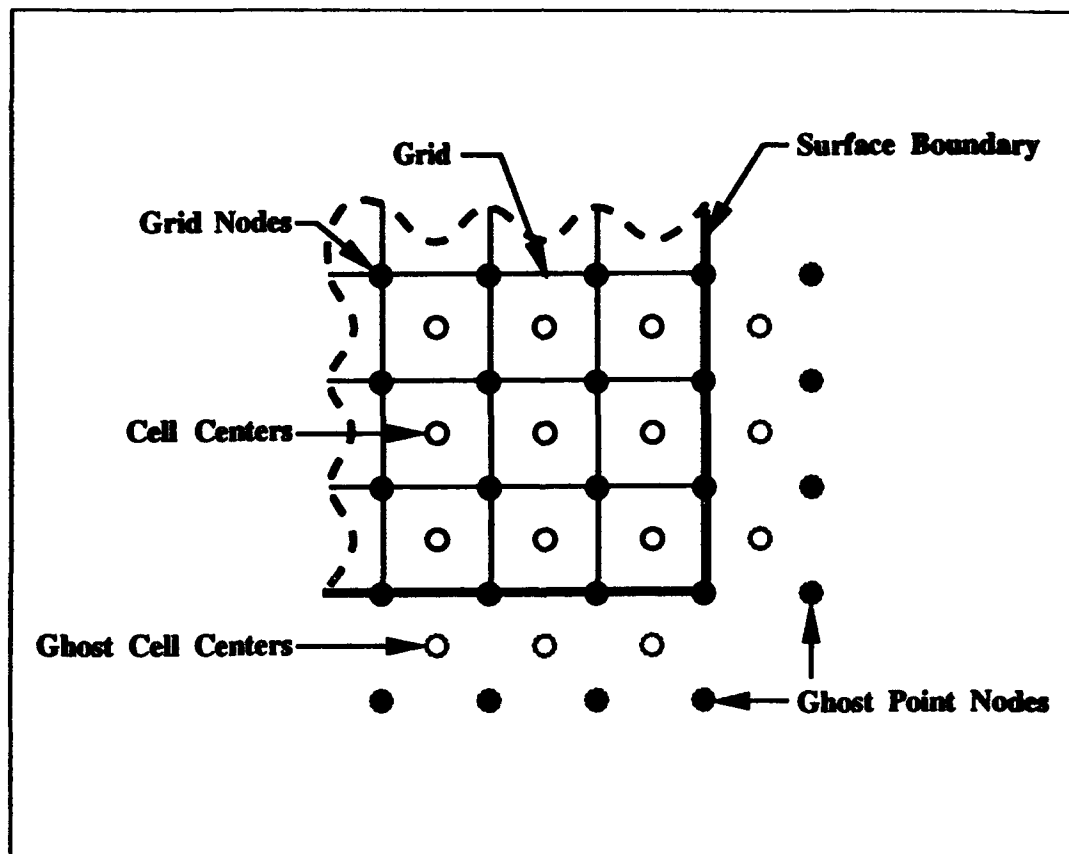


Figure 2-1 Addition of Ghost Points to a Grid

applied on the edge of the grid by simply setting the velocity components in the new fictitious cells equal to and opposite from the velocity components specified in their neighboring internal edge cells. This approach creates a velocity gradient from the last internal cell to the fictitious ghost cell such that the velocity is zero on the surface boundary.

Boundary conditions must be applied at all of the edges and surface boundaries associated with the physical problem being modelled. The nozzle/cowl flowfield requires inflow, freestream, outflow, and surface boundaries conditions to be applied.

The inflow boundary conditions must be specified for several different flowfields for the hypersonic vehicle aft body problem. The internal flowfield corresponding to the main combustion chamber exhaust, the external flowfield that the vehicle aft body is exposed to, and the new gas generator flowfield added to the code for this study all require inflow boundary conditions to be specified. At these inflow boundaries, the flowfield is specified according to given initial conditions. The required flow variables, U , are calculated from the inflow initial conditions. On the inflow faces, corresponding to lines AO and HI in Figure 1-4 for the internal and external flowfields respectively, the boundary conditions are applied by setting the flow vector in the boundary cells equal to the input flow vector:

$$U_{i,j} = U_{\infty} \quad (2-23)$$

For the freestream boundary corresponding to line IJ in figure 1-4, the initial conditions are specified as the freestream values:

$$U_{i,jmax} = U_{\infty} \quad (2-24)$$

The zero gradient boundary condition is then applied by simply setting the flow vector in the boundary cell equal to the flow vector in the last cell of the flow solution:

$$U_{i,jmax+1} = U_{i,jmax} \quad (2-25)$$

The outflow boundary condition corresponding to line CJ in Figure 1-4 also has a similar no-change boundary condition applied:

$$U_{imax+1,j} = U_{imax,j} \quad (2-26)$$

The solid boundaries of the nozzle wall corresponding to curve ABC in Figure 1-4 and all of the cowl lip surfaces corresponding to line OEPH in Figure 1-4 must have the no-slip boundary condition applied. For example, on the nozzle wall:

$$\begin{aligned} u_{i,2} &= -u_{i,1} \\ v_{i,2} &= -v_{i,1} \end{aligned} \quad (2-27)$$

The pressure gradient also goes to zero on the wall:

$$\frac{\partial p}{\partial \eta} = 0 \quad (2-28)$$

For a zeroth-order implementation, this gives:

$$p_{i,1} = p_{i,2} \quad (2-29)$$

The Wright Laboratory code used for this analysis also requires a definition of the wall temperature. An adiabatic wall temperature assumption was briefly investigated for the generic nozzle configuration analyzed in this research. An

approximation for adiabatic wall temperature for compressible boundary layers is given by (13):

$$T_{aw} = T_\infty \left(1 + r_c \frac{\gamma - 1}{2} M_\infty^2 \right) \quad (2-30)$$

where r_c is the adiabatic recovery factor which, for laminar compressible boundary layers, is approximately equal to the square root of the Prandtl number, Pr. The Prandtl number for air up to moderately high temperature is $Pr = 0.72$.

For air at the conditions specified for Mach 15 flow in Table 3-4, the adiabatic wall temperature would be approximately 16610 °R for the internal nozzle wall at the inlet and approximately 18280 °R on the external cowl wall. These temperatures are much higher than the melting temperature of most advanced materials. Therefore, the vehicle requires active cooling on the upstream nozzle wall and the cowl wall. Active cooling was assumed such that the wall temperature could be maintained below a reasonable target design temperature. A typical upper limit on nozzle wall temperature for a NASP-type vehicle is on the order of 2000 °R (21). Although this temperature would vary due to an increase in convective heat transfer as the flow expanded down the nozzle wall, a constant 2000 °R was applied as a reasonable approximation over the entire nozzle. The errors associated with the uniform temperature non-adiabatic wall assumption manifest themselves primarily in the calculation of viscous wall forces. Since the primary objective of this study was to investigate the pressure contribution to the vehicle performance, the errors associated with the viscous drag and lift terms were not considered to be critical.

The non-adiabatic wall temperature is specified as T_{wall} . The specific internal energy can then be specified for the boundary cell such that the wall is maintained at the given temperature. Again, a zeroth-order implementation gives:

$$e_{i,1} = 2c_v T_{wall} - e_{i,2} \quad (2-31)$$

Not only does the flow vector have to be specified on the boundary cell, but the fluxes on the edge cell must also be specified for the finite volume applications used in this study. The no-slip condition on the wall forces the inviscid mass and energy fluxes on the wall surface to go to zero. An examination of Equations (2-9) and (2-10) show that the only terms remaining in the inviscid flux vectors (F , G) are the pressure terms. The inviscid fluxes on the wall are then specified by:

$$U_{i,wall} = \begin{bmatrix} 0 \\ p\eta_x \\ p\eta_y \\ 0 \end{bmatrix} \quad (2-32)$$

The viscous fluxes on the wall (F_v , G_v) are simply calculated based on the given wall temperatures and the zero velocity no-slip condition. The same approach described above for the nozzle wall is also applied to the solid boundaries of the cowl.

The initial conditions required to start the solution procedure are applied such that the entire grid is initially at the input freestream conditions except at the inflow boundaries where the appropriate inflow boundary conditions are applied. The nozzle internal and external inflow boundary conditions and freestream conditions for the nozzle configuration analyzed in Section 3.1 were chosen by Hyun (1) to match the experimental results of Cochran (4). A similar set of initial conditions for the nozzle

configuration analyzed in Section 3.2 were developed by Bonaparte (2) for a generic flight vehicle over a typical trajectory. Details of the initial conditions used in these studies can be found in Section 3.1 and 3.2, respectively.

The inflow boundary conditions are specified by the Reynolds number, Mach number and temperature of the flow. For a calorically perfect gas, all of the required flow variables and fluxes can be calculated given the gas constant R , and specific heat ratio γ . For air at standard conditions, $R = 1716 \text{ ft}^2/(\text{s}^2 \text{ } ^\circ\text{R})$ and $\gamma=1.4$.

One disadvantage of the Wright Laboratory code used for this research is that it currently has no provisions for flowfield mixing. A hypersonic propulsive nozzle will typically have different internal and external flow gas properties which will mix along a contact surface as illustrated in Figure 1-4. The current computational code is designed to run only a single calorically perfect gas mixture throughout the entire flowfield. This was considered an acceptable source of error since this study is parametric in nature and the primary objective is to determine the trends associated with the incorporation of a gas generator into the cowl. Slight modifications were made to the code, however, to improve the consistency of the results. Separate values for R and γ can now be input for each of the three inflow boundary conditions (internal combustor flow, external freestream flow, and the gas generator flow) analyzed in this study. This modification uses the input Reynolds number, Mach number, temperature, R and γ to calculate the correct pressures and fluxes at the inflow boundaries. These new inflow pressures and fluxes are then used in the code assuming a single calorically perfect gas.

The following procedure is used to convert the input variables to the appropriate pressure and flux terms. First, the speed of sound and velocity are calculated using the input variables.

$$a = \sqrt{\gamma RT} \quad (2-33)$$

$$U = a \cdot M \quad (2-34)$$

The components of the input velocity are then calculated using the input flow deflection angle, θ .

$$u = U \cdot \cos\theta \quad (2-35)$$

$$v = U \cdot \sin\theta \quad (2-36)$$

Next, coefficient of viscosity, μ , is calculated using Sutherlands formula, Equation (2-6). Density is then calculated using the definition of Reynolds number.

$$\rho = \frac{Re \mu}{Ul} \quad (2-37)$$

Next, specific internal energy can be calculated.

$$e = \rho \left(c_v T + \frac{|U|^2}{2} \right) \quad (2-38)$$

The final term that is required before the inviscid flux vectors (F,G) given in Equation (2-9) can be determined is the static pressure. The perfect gas equation of state is used to calculate pressure.

$$p = \rho RT$$

(2-39)

These updated flow variables and flux vectors are then used as the inflow boundary conditions for the rest of the solution which assumes a single calorically perfect gas throughout the nozzle.

2.4 Computer Code Description

The baseline code used to solve the nozzle/cowl flowfields analyzed in this study was developed by Wright Laboratory (WL/FIMC). This second-order accurate code was developed to solve the two-dimensional, viscous Navier-Stokes equations based on a laminar flow assumption.

The original code was developed to study uniform flow through a channel. Wright Laboratory modified the code in order to solve the hypersonic vehicle aft body problem analyzed by Hyun (1). The primary code modifications required for Hyun's study included adding a second flow stream to represent the external flow, adding a freestream outer boundary condition, and inserting a cowl solid boundary. One goal of the present study was to further modify the code to incorporate a third flow stream in order to model the effects of a gas generator inserted into the cowl lip. A description of the required gas generator code modifications is presented in Section 2.6.1.

A validation of the flux-splitting algorithms was completed by Hyun (1). Hyun's study compared the computational results of this code to the experimental data of Cochran (4) using the same baseline geometry and grid presented in Section 3.1 of this study. Hyun showed that as Mach number and nozzle pressure ratio (NPR)

increased, the correlation between the computational results and the experimental data generally improved. The computations based on the assumption of planar laminar flow tended to be more consistent with the experimental data as the Mach and NPR approached their on-design conditions. The promising results for the supersonic flow conditions and the trend towards increased correlation at higher Mach and NPR provided the required justification for using this code in the present study.

The Wright Laboratory code provides many options for solving the given flow problem. The code can be used to solve the inviscid Euler equations as well as the viscous Navier-Stokes equations. The code also allows the user to choose which type of flux-splitting algorithm to use; Steger and Warming flux-vector splitting, Van Leer flux-vector splitting, or Roe flux-difference splitting can be selected. The code also has a restart feature which allows any combination of these solutions to be run in series. For example, the present study uses the steady-state Van Leer solution as the initial conditions for the final Roe solution. A general discussion of the solution procedure used is presented in Section 2.5.

In addition to choosing the type of flow solver, the code allows the user to control other aspects of the problem including; control of the CFL stability criteria, input of flowfield and boundary conditions, and control of miscellaneous format and run parameters. A sample input file and a description of the inputs for can be found in Appendix A.

The code is written entirely in FORTRAN and it was run on a network of Silicon Graphics Iris 4D/240 and Indigo series workstations.

2.5 Solution Procedure

The explicit formulation of the numerical problem was used for this computational analysis. This approach is second-order accurate in space and time. The explicit formulation was desired because it is well suited for optimization on parallel processing machines. Section 2.6.2 and Appendix B highlight the code optimization that was completed for this research.

The approach taken to solve the nozzle/cowl problem uses a combination of the Van Leer flux-vector splitting method and the Roe flux-difference splitting method. The initial conditions required to start the iterative solution algorithm are initially set to the input freestream conditions. As the flow solution is marched in time, the initial perturbations are very large. The initial conditions for the numerical solution are significantly underexpanded and as the solution marches towards steady-state, the code must overcome this initial underexpansion. The code provides the user with direct control over the Courant-Friedrichs and Lewy (CFL) stability criterion defined as (1):

$$CFL = \frac{\Delta t}{\lambda_{\max}} \quad (2-40)$$

where λ_{\max} is the largest eigenvalue of the flux Jacobian matrix.

An initial CFL of 0.01 is used to force very small initial steps in time through the initial expansion of the flow. The CFL is then gradually increased to a maximum of 0.9 as the solution is marched towards steady-state.

The Roe approach has demonstrated convergence problems when trying to start extremely underexpanded initial conditions for the numerical solution (1). For this reason, the Van Leer approach was chosen to generate an initial steady-state solution

because it has demonstrated robustness through these initial supersonic expansion regions. Once a steady solution was achieved using the Van Leer approach, a final solution was generated using the Roe flux-difference splitting approach to accurately capture the wave interactions.

Convergence to the steady-state solution was determined explicitly for each run in this study. The explicit criteria used to determine the convergence are the root mean square (RMS) heat transfer and pressure values along the nozzle wall:

$$Q_{RMS} = \frac{1}{IL} \sqrt{\sum_{i=1}^{IL} (Q_{ij-surface})^2} \quad (2-41)$$

$$P_{RMS} = \frac{1}{IL} \sqrt{\sum_{i=1}^{IL} (P_{ij-surface})^2} \quad (2-42)$$

Convergence is determined when Q_{RMS} and P_{RMS} do not fluctuate more than 0.01% over a large number of iterations. The typical number of iterations required for a converged Van Leer solution ranged from 750 to 2000. An additional 500 to 4000 Roe iterations were then required on top of this to achieve a final steady-state solution. As freestream Mach number and NPR were increased, the number of iterations required for a steady state solution tended to decrease. This trend also tends to support the notion that the viscous laminar flow assumption used in this code is well suited for the hypersonic nozzle/cowl problem.

Since one of the primary goals of this research was to evaluate the effect of gas generator flowfield on the pressure distribution along the nozzle wall, several representative measures of performance are presented. The coefficient of pressure (C_p) and the pressure contribution to lift and thrust were calculated along the nozzle wall.

The pressure coefficient along the nozzle wall is calculated locally using:

$$C_{pi} = \frac{p_i - p_\infty}{q_\infty} \quad (2-43)$$

where p_∞ and q_∞ are the freestream static and dynamic pressure, respectively.

The pressure contribution to thrust along the nozzle wall is given by:

$$Thrust_{p_{wall}} = \sum_{i=1}^{IL} (\Delta y_i) p_i \quad (2-44)$$

where Δy_i is calculated from the wall grid spacing and p_i is calculated at the cell center.

The pressure contribution to lift along the nozzle wall is calculated in a similar manner:

$$Lift_{p_{wall}} = \sum_{i=1}^{IL} (\Delta x_i) p_i \quad (2-45)$$

where Δx_i is also calculated based on the wall grid spacing.

2.6 Computer Code Modifications

In addition to the small change in the inflow boundary conditions described in Section 2.3, several more significant changes were made to the Wright Laboratory code for the incorporation of a vectorable gas generator flowfield into the cowl and

the optimization of the code for use on parallel processing machines. The following sections highlight these code changes.

2.6.1 Addition of a Gas Generator Flowfield. The data input subroutine, *DATIN.f*, and the common block routine, *gcommon.f*, were modified to read in the required gas generator flow definition from the input file *cnldat* found in Appendix A. The new variables are Reynolds number, Mach number, temperature, R , γ , and thrust vector deflection angle θ . The variables are then converted to the desired flow variables as described in Section 2.3.

The initial condition subroutine, *INITL.f*, was modified to set the flow variables and the conserved variables, U , to the proper initial conditions on the gas generator boundary.

The boundary condition subroutine, *BC.f*, required the most extensive modifications. The solid surface boundary condition at the cowl lip was replaced with an inflow boundary condition as described in Section 2.3.

The main calculation subroutine, *L.f*, also required a slight modification. In the baseline code (no gas generator) the cowl lip was treated as a solid boundary. This required that the inviscid flux terms on the surface be specified as shown in Equation (2-31) where the mass and energy terms are set to zero and only the pressure contribution to the momentum terms remain. In the modified code, the cowl lip is no longer modelled as a solid boundary and the flux vectors are not reset. These terms are now set equal to the flux terms associated with the gas generator flowfield initial conditions.

2.6.2 Code Optimization. The steady-state solution of a typical nozzle/cowl configuration required on the order of 4 to 20 hours of computer run time using the baseline code. A significant reduction in run time was required in order to complete the large number of runs required for this research in a timely manner. The run time could be reduced because the explicit formulation of the numerical problem is well suited for optimization using parallel processing machines such as the Silicon Graphics 4D/240 used for most of this research.

The Silicon Graphics Power Series comes equipped with extensive support for parallel applications at both the operating system level and the compilers and tools level. Moving the applications from the operating system level to the compiler or tool level greatly enhances the ease of developing parallel applications.

Code can be parallelized relatively easily using compilers such as the Silicon Graphics Power FORTRAN compiler. This compiler has a scheme for homoparallelization of DO loops through in-line comments that provide multiprocessing directives to the compiler. Interpretation of these directives is enabled through the use of the `-mp` option with this compiler. The basic construct is the `c$doacross` directive which informs the Power FORTRAN compiler that the DO loop immediately following is to be parallelized.

Since the `c$doacross` directive can be cumbersome to insert manually, Power FORTRAN is equipped with code analyzer tools which helps the user identify opportunities for parallelization. These tools are called `pfa` and `pca` respectively. Both are source-to-source optimizing processors that discover blocks of code that can be made parallel and actually insert the directives necessary to implement parallelism.

The pfa tool was used for this task. The pfa tool is generally very good at identifying which loops can be parallelized and which have data dependencies or too few iterations to be considered. It generates a listing that shows which portion of the code were parallelized and why it could not parallelize the others. This listing helps the developer by highlighting any dependencies which require further attention.

Another tool that helps the developer parallelize applications is an execution profiler. An execution profiler such as pixie counts the number of CPU cycles a section of code takes to execute and keeps track of the total use by that section of the code. By accumulating these statistics during a run of an application, this tool can generate detailed reports on the execution of the code. An example of the pixie profiler results accumulated from a run of the baseline code applied to a typical solution is presented in Appendix B.1.

For the baseline profile example in Appendix B.1, the solution of 1000 Roe iterations for a typical nozzle/cowl configuration requires 86.82 minutes of CPU time. The routines *sqrt* and *r_sign* are math library routines and can not be parallelized. The remaining routines which were parallelized are *FSIROE*, *FSJROE*, *LMTRI*, *LMTRJ*, *WISEUL*, *VJSEUL*, and *L*. Between them, these subroutines took approximately 80% of the total application run time.

The pfa tool was then used to analyze and parallelize the code for each of these subroutines. All of the subroutines except *L* were parallelized without any manual intervention. With the help of pfa, the problem areas in *L* were highlighted and several minor changes were then made to further parallelize this subroutine. Details of these minor changes in *L* and an example of the `c$doacross` structures can

be found in Appendix B.3. Since the other subroutines were successfully parallelized by pfa without any manual code changes, their listings were not included.

The execution profile for the parallelized code running this same nozzle/cowl example is presented in Appendix B.2. The limiting CPU time required for the most heavily used processor was reduced to 33.85 minutes. The speedup ratio in terms of CPU cycles was 2.56. This particular test case took 158 minutes with no parallelization and 69 minutes with parallelization, which corresponds to a time speedup factor of 2.29. The numbers associated with time are subject to some amount of variation due to the competition for CPU time with the operating system.

III. ANALYSIS OF NOZZLE COWL FLOWFIELDS

3.1 An Experimentally Validated Nozzle/Cowl Geometry

The first nozzle/cowl geometry analyzed in this study is based on the experimental hypersonic vehicle afterbody configuration analyzed by Cochran (4). The two-dimensional nozzle/cowl model was designed to be representative of the external geometry of a hypersonic vehicle. Figure 3-1 presents a cross-sectional view of this experimental nozzle/cowl assembly. In order to facilitate fabrication, the internal nozzle consisted of a 50 degree straight convergent ramp. At the throat, the flow is turned at a sharp corner and allowed to expand along a 20 degree external expansion ramp. Four different cowl configurations were analyzed in Cochran's experimental study: a baseline short cowl, a long cowl, a long cowl deflected towards the body 5 degrees, and a long cowl deflected away from the body 5 degrees.

Cochran analyzed these hypersonic vehicle afterbody configurations in the Wright Laboratory two-foot trisonic gasdynamic tunnel at subsonic, transonic, and supersonic off-design operating conditions. The testing was limited to relatively slow speed off-design operating conditions due to the operating limitations of the gasdynamic tunnel facility. For the subsonic flow cases the maximum dynamic pressure was limited to 350 pounds per square foot (psf) and the maximum Reynolds number was limited to 2.5 million per foot. For the supersonic cases the maximum dynamic pressure increased to 1000 psf and the maximum Reynolds number increased to 5.0 million per foot. The total stagnation temperature was maintained at

approximately 559.7 °R for all of the analysis. The nozzle/cowl wall temperatures were maintained at a nearly constant 400.6 °R for this analysis.

Cochran's goal was to experimentally analyze the nozzle/afterbody drag force on these models by integrating the pressure distribution on the external ramp. Pressure distributions on the external ramp were obtained for each cowl configuration over a range of NPR, freestream Mach number, and Reynolds number. The maximum errors reported for the experimental tests were 0.20% for the freestream total pressure, 0.12% for the freestream static pressure, 0.57% for the static pressure probes, and 0.43% for the internal nozzle total pressure.

Hyun, (1), compared these data to the results of the Wright Laboratory finite volume computational code described in Chapter 2. The goal of Hyun's research was to attempt to validate the numerical method using the experimental data gathered from this very practical experimental example. In general, the two-dimensional flux-splitting algorithms performed very well for the supersonic external flow cases. Three-dimensional effects in the experimental data were the primary reasons for most of the small discrepancies. For the supersonic external flow cases, small differences occurred at the far downstream locations on the expansion ramp where the thickening boundary layer tended to interact with the external flowfield. Hyun demonstrated that as NPR and freestream Mach increased, the correlation between the experimental data and the computational results generally increased.

The two-dimensional Wright Laboratory code could not be validated for the subsonic flow case because of very strong three-dimensional effects on the nozzle/cowl experimental data. The experimental data contained significant three-

dimensional effects due to the interaction between the exhaust plume, the expansion ramp subsonic boundary layer, and the subsonic external flow. For these reasons, the scope of the current analysis is limited to the validated supersonic off-design conditions analyzed by Hyun and Cochran.

The initial conditions used for this analysis were chosen to match the experimental conditions reported by Cochran and used by Hyun. Table 3-2 describes the Mach 1.9 flowfields analyzed at nozzle pressure ratios of approximately 3, 5, 7, and 12. Table 3-3 describes the Mach 3.0 flowfields analyzed at nozzle pressure ratios of 5, 7, 9, 12, and 16. The test point number (TPN) presented in these tables corresponds to Cochran's original test points. For this experimental nozzle configuration, the high pressure internal nozzle flow is subsonic and it is accelerated to supersonic speeds through the converging-diverging nozzle section.

The computational grid developed by Hyun was used as a baseline for the current analysis. Hyun used an approach that is very similar to the approach taken for the generic nozzle grid generation described in Section 3.2.2. Figure 3-2 shows the final grid that was used for the baseline experimental nozzle analysis. This grid has dimensions of 101 (ξ) by 71 (η). An algebraic distribution of grid points was used along each edge and a combination of algebraic and elliptic grid generators were used to distribute the internal nozzle grid points.

The primary objective of the first part of this research was to insert a gas generator flowfield into the cowl lip. Using Hyun's grid definition and Cochran's initial conditions, the overall effects of the gas generator could be compared to the experimentally validated baseline flow solutions. This also allows for a direct

comparison of gas generator mass flow and deflection angle effects to the effects of nozzle cowl length extensions and deflections.

3.2 A Generic Hypersonic Vehicle Configuration

For the second part of the current research effort, a generic hypersonic vehicle nozzle/cowl geometry was evaluated at more realistic on-design flight conditions.

Since the Wright Laboratory code showed good correlation to the experimental data and a trend towards increasing accuracy with increasing freestream Mach number and NPR, it was determined that the same code could be used to determine trends at more realistic on-design flight conditions.

The generic nozzle design used for this study was developed by Doty (9). This same nozzle definition was used in the nozzle geometry optimization research of Bonaparte (2). The purpose of Bonaparte's study was to implement a two parameter optimization for nozzle attachment angle and cowl deflection angle using an inviscid flux-difference splitting code developed by Doty. Doty's nozzle definition and Bonaparte's trajectory were used for the present analysis. Trends associated with a gas generator flowfield were evaluated for the generic nozzle/afterbody over a this typical flight trajectory corresponding to a constant dynamic pressure, q , of 1000 psf through flight Mach numbers ranging between 10 and 25.

3.2.1 Nozzle/Cowl Model. There are many options available for defining a generic nozzle/cowl assembly. Doty, (9), defined a family of generic nozzles consisting of a circular arc section extending from the combustor exit to the nozzle wall and a parabolic arc section which defines the nozzle wall. Figure 3-3 (not drawn

to scale) defines this generic configuration. An internal height, h_{in} , an external height, h_{ext} , a nozzle length, and a nozzle wall attachment angle (θ_B) are all that is required to parametrically describe this family of nozzles. The circular arc is defined relative to the origin, O, by the following relationships:

$$x = x_O + r[\sin(\theta)] \quad (3-1)$$

$$y = y_O + r[1 - \cos(\theta)] \quad (3-2)$$

where θ extends from 0 to θ_B .

The general form of the parabolic wall is given by:

$$y^2 + c_1x + c_2y + c_3 = 0 \quad (3-3)$$

where the three unknowns, c_1 , c_2 , and c_3 can be evaluated using known information.

The following relationships define the nozzle wall:

$$c_2 = \frac{-[(y_C)^2 - (y_B)^2] + 2(y_B)(\dot{y}_B)(x_C - x_B)}{(y_C - y_B) - (x_C - x_B)(\dot{y}_B)} \quad (3-4)$$

$$c_1 = -2(y_B)(\dot{y}_B) - (\dot{y}_B)^2 c_2 \quad (3-5)$$

$$c_3 = -(y_B)^2 + 2(y_B)(\dot{y}_B)(x_B) + (\dot{y}_B^2 x_B - y_B) c_2 \quad (3-6)$$

where,

$$\dot{y} \equiv (dy/dx)_B = \tan(\theta_B) \quad (3-7)$$

and the x and y locations are known at points A and C. For a given nozzle inlet

height, nozzle exit height, and nozzle length, a complete family of nozzle configurations is defined by the nozzle attachment angle, θ_n .

Bonaparte's optimization effort showed that the nozzle performance is fairly sensitive to the nozzle attachment angle. For this generic nozzle configuration analyzed over the typical trajectory presented in Section 3.2.3, the optimum nozzle attachment angle, θ_n , varied from nearly 36 degrees at a trajectory Mach number of 10 down to almost 16 degrees at a trajectory Mach number of 25. The nozzle configuration chosen for the current analysis was based on a design trajectory Mach number of 15 where the optimum nozzle attachment angle is approximately 24 degrees. The Mach 15 design condition and the 24 degree nozzle attachment angle represent a reasonable design trade-off over the Mach 10 to Mach 25 flight trajectory since the 24 degree nozzle attachment angle falls just less than half way between the optimum values for Mach 10 and Mach 25.

Table 3-1 completely defines the generic nozzle/cowl geometry used in this investigation. The total expansion ratio is 25:1, the overall nozzle length is 100 times the combustion chamber exit height, and the cowl wall spans $1/10^{\text{th}}$ of the overall nozzle length. The cowl wall is modelled as a flat plate with a blunt trailing edge.

Table 3-1 Generic Nozzle Configuration Definition

Nozzle Data	Value
Nozzle Length, L (in)	100
Inlet Height, h_{in} (in)	1
Exit Height, h_{ex} (in)	25
Circular Arc Radius of Curvature, r (in)	1
Circular Arc/Nozzle Attachment Angle, θ_b (deg)	24
Cowl Length (in)	10
Cowl Thickness (in)	0.25

3.2.2 Grid Generation. Successful grid generation is a very meticulous iterative procedure. The process of developing the grids used in this research was simplified using the GRIDGEN software package developed under contract by the Fort Worth Division of the Lockheed Corporation (formerly General Dynamics) for the Flight Dynamics Laboratory, Aeromechanics Division, Wright Laboratory (WL/FIM) (16,17).

A quasi two-dimensional surface grid is required to define the generic nozzle/afterbody configuration investigated in this research. The final grid with dimensions of (101x71) used for this analysis is presented in Figure 3-4. The grids used for the grid resolution study are shown in Figures 3-5 and 3-6 corresponding to grid dimensions of (151x101) and (201x151) respectively. Details of the grid resolution study can be found in Section 4.1.

Only the two-dimensional grid generation portion of GRIDGEN called GRIDGEN2D was required for this effort. GRIDGEN2D is designed for use on the Silicon Graphics, Inc. (SGI) 3000 and 4D series IRIS workstations and the IBM RISC 6000 workstations. The GRIDGEN software was installed on a NAIC SGI network for this effort.

For this problem, a single block was defined with the desired dimensions (ξ_{\max} , η_{\max} , ζ_{\max}). ζ_{\max} was set to 1 since only a two-dimensional surface grid was required. ξ_{\max} and η_{\max} were set to the overall grid dimensions of 101x71 respectively. The generic nozzle/cowl definition is well suited for grid generation in Cartesian coordinates.

The edges were defined by importing a high resolution edge definition file which contained the nozzle geometry definition as specified in Equations 3-1 through 3-7 and Table 3-1. The grid points were then distributed along the edges using algebraic distributions.

The main domain was broken down into several subunits in order to help cluster grid points and control the grid definition. Grid clustering was provided in the regions near the solid boundaries to provide sufficient resolution of the boundary layer flow and in the regions where strong expansions and shocks were expected.

The external flow grid was calculated algebraically using the spacing defined on the edges. The algebraic solver used transfinite interpolation (TFI) with arclength based interpolants to generate the external flow grid. This method tended to keep the internal grid clustering proportional to the defined edge clustering as was desired.

The internal flow grid was calculated using an elliptic partial differential equation (PDE) grid solver. Thomas-Middlecoff control functions, with a relaxation factor of 0.3, were used for smoothing since they appeared to give the best results. The elliptic solver was set up to force the grid to be perpendicular to the solid boundaries and the freestream inflow boundary and was set up to force a constant gradient geometry at the downstream outflow boundary. Approximately 400 iterations were run to generate the final grid.

Once the surface grid was created, a small FORTRAN routine was used to add the required boundary ghost points as described in Section 2.3. This routine also converted the grid to a cell centered grid and it inverted the grid for evaluation with the Wright Laboratory code.

3.2.3 The Trajectory. A hypersonic vehicle will typically travel along a design trajectory. A constant dynamic pressure, q , trajectory can be used to represent typical aerodynamic and structural loads on a hypersonic vehicle. A typical value of dynamic pressure for a NASP type vehicle is $q=1000$ psf (2). The trajectory is then specified by the definition of dynamic pressure:

$$q = \frac{1}{2} \gamma p_{\infty} M_{\infty}^2 \quad (3-8)$$

A pressure altitude corresponding to p_{∞} is determined as a function of design dynamic pressure and vehicle Mach number. Figure 3-7 defines the trajectory associated with a constant 1000 psf dynamic pressure flight path. The pressure altitude was based on the 1976 standard atmosphere.

Table 3-4 defines the internal and external flowfields used for this analysis.

The internal flow parameters were based on the engine analysis conducted by Bonaparte, (2). Bonaparte obtained the engine exhaust parameters by analyzing a generic scramjet configuration over this trajectory using the Johns Hopkins RamJet Performance Analysis (RJPA) program (24).

The external flowfield presented in Table 3-4 was based on another set of simplifying assumptions. Since the forebody of a hypersonic vehicle typically acts as a large compression ramp, assumptions had to be made regarding the effect of this flowfield compression on the afterbody freestream flow. Bonaparte assumed a total of eight degrees of flowfield turning was accomplished by passing the external flow through an oblique shock. The oblique shock solution was calculated using an iterative solution which accounted for temperature changes in the caloric models used for enthalpy, h , and specific heat capacity at constant pressure, c_p . Although the Wright Laboratory code used for this research is not capable of mixing dissimilar flowfields, a realistic freestream boundary condition is desired. The trajectory analysis completed using the caloric model provided more realistic freestream inflow pressure and flux terms which were then used in the Wright Laboratory code as described in Section 2.3.

3.3 The Gas Generator Model

The primary goal of the current research was to determine the effects of inserting a vectorable, throttleable gas generator flow into the cowl lip. The gas generator flowfield was obtained using a computer program developed by the author to

determine the equilibrium flow solution for a liquid hydrogen-oxygen rocket motor (22). The exit stage solution from this model was used as the input initial conditions for the improved cowl concept gas generator.

Table 3-5 defines the gas generator flow used for this analysis. The baseline nozzle geometry and operating conditions were based largely on a scaled down Space Shuttle Main Engine (SSME). The oxygen to fuel mixture ratio was 6.026:1, the combustion chamber inlet pressure at 100% throttle was 204.55 atm, and the exit to throat area ratio was 77.5 for the baseline gas generator. In order to analyze the effects of varying mass flows and exit pressures, this engine configuration was analyzed operating at a range of throttle settings varying from 25% to 200%. Engine throttling is accomplished by increasing or decreasing the combustor chamber pressure. In addition to throttling, the gas generator flow was also vectored through a range of +20 to -20 degrees using the approach described in Section 2.3.

Table 3-2 Experimental Nozzle, Mach 1.9 Flow Definition

Test Point	NPR [-]	M_a [-]	U_a [ft/s]	Re_d/ft [$10^6/ft$]	P_a [psf]	T_a [°R]	M_a [-]	Re_d/ft [$10^6/ft$]	P_a [psf]	T_a [°R]
150	2.98720	1.89880	1668.96	2.04680	170.31	321.58	0.31067	0.54214	475.840	483.92
149	4.99910	1.89900	1667.81	2.04307	169.61	321.07	0.31782	0.91714	790.550	485.67
148	7.31330	1.89930	1658.05	2.00984	164.06	317.22	0.31849	1.30696	1118.40	483.73
147	12.1210	1.89920	1654.09	2.09328	169.78	315.74	0.31526	2.24468	1920.90	479.94

Note: $R_a = R_a = 1716.0 \text{ ft}^2/(\text{s}^2 \cdot \text{°R})$, and $\gamma_a = \gamma_a = 1.4$

Table 3-3 Experimental Nozzle, Mach 3.0 Flow Definition

Test Point	NPR [-]	M_a [-]	U_a [ft/s]	Re_d/ft [$10^6/ft$]	P_a [psf]	T_a [°R]	M_a [-]	Re_d/ft [$10^6/ft$]	P_a [psf]	T_a [°R]
179	5.05230	3.00200	2066.01	2.03391	53.060	197.59	0.25863	0.24678	255.890	477.72
180	6.95610	2.99900	2073.66	2.02096	53.345	199.01	0.27252	0.35733	352.410	478.54
181	8.9958	2.99480	2079.94	2.00542	53.717	200.78	0.28331	0.47941	457.030	480.35
183	12.1850	2.99040	2070.41	2.03679	54.129	199.53	0.29093	0.67467	621.930	477.74
184	15.9730	2.98640	2070.28	1.99574	54.430	200.04	0.29333	0.89706	819.010	477.22

Note: $R_a = R_a = 1716.0 \text{ ft}^2/(\text{s}^2 \cdot \text{°R})$, and $\gamma_a = \gamma_a = 1.4$

Table 3-4 Generic Nozzle Flow Definition

Flight Mach	NPR [-]	M_∞ [-]	U_∞ [ft/s]	Re_∞ /ft [10^6 /ft]	P_∞ [psf]	T_∞ [°R]	M_a [-]	Re_η /ft [10^6 /ft]	P_η [psf]	T_η [°R]
10	961.5	7.4301	9871.5	1.1312	74.116	756.81	2.0062	3.3173	8269.13	5375.70
15	5080.4	9.5347	15363.4	0.73728	59.319	1113.21	3.4445	2.8701	4276.35	5511.96
20	20481.8	10.9740	21003.4	0.52098	53.752	1570.61	4.7575	2.4751	2774.07	5719.50
25	64290.2	12.0221	26748.7	0.38703	50.742	2122.58	6.0497	2.1530	1963.87	5912.64

Note: $R_\infty = 1716.3 \text{ ft}^2/(\text{s}^2 \text{ } ^\circ\text{R})$ and $\gamma_\infty = 1.35$ for the external freestream flow.

$R_\eta = 2242.5 \text{ ft}^2/(\text{s}^2 \text{ } ^\circ\text{R})$ and $\gamma_\eta = 1.25$ for the internal nozzle flow.

Table 3-5 Gas Generator Flow Definition

Throttle [%]	P_{injected} [atm]	M_{in} [-]	U_{in} [ft/s]	Re_d/ft [$10^6/\text{ft}$]	P_{in} [psf]	T_{in} [°R]	γ [-]
25	51.14	4.628	14406.8	0.1891	99.22	2203.57	1.2535
50	102.27	4.663	14436.6	0.3784	194.58	2178.79	1.2535
75	153.41	4.682	14451.7	0.5676	288.91	2166.25	1.2535
100	204.55	4.680	14461.3	0.7572	382.94	2158.29	1.2606
125	255.68	4.687	14467.9	0.9467	476.41	2152.58	1.2614
150	306.82	4.694	14473.0	1.1356	569.58	2148.23	1.2614
175	358.96	4.699	14477.1	1.3246	662.51	2144.76	1.2614
200	409.09	4.703	14480.4	1.5136	755.25	2141.90	1.2614

Note: $Re_d = 3509.0 \text{ ft}^2/(\text{s}^2 \text{ °R})$ for all gas generator flow conditions.

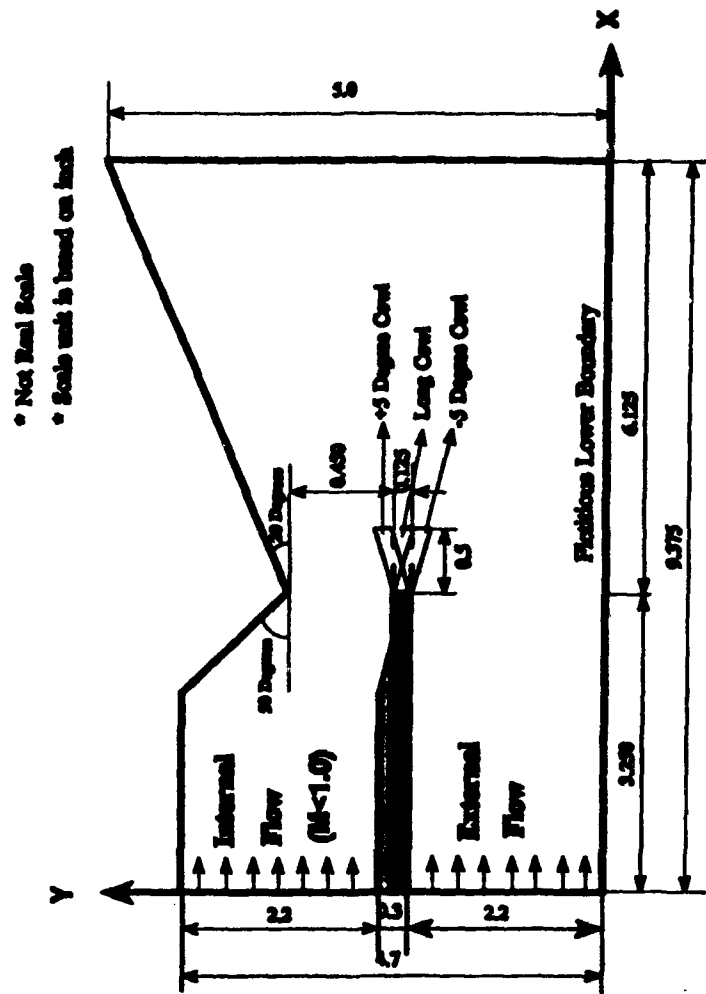


Figure 3-1 Experimental Nozzle Geometry (1)

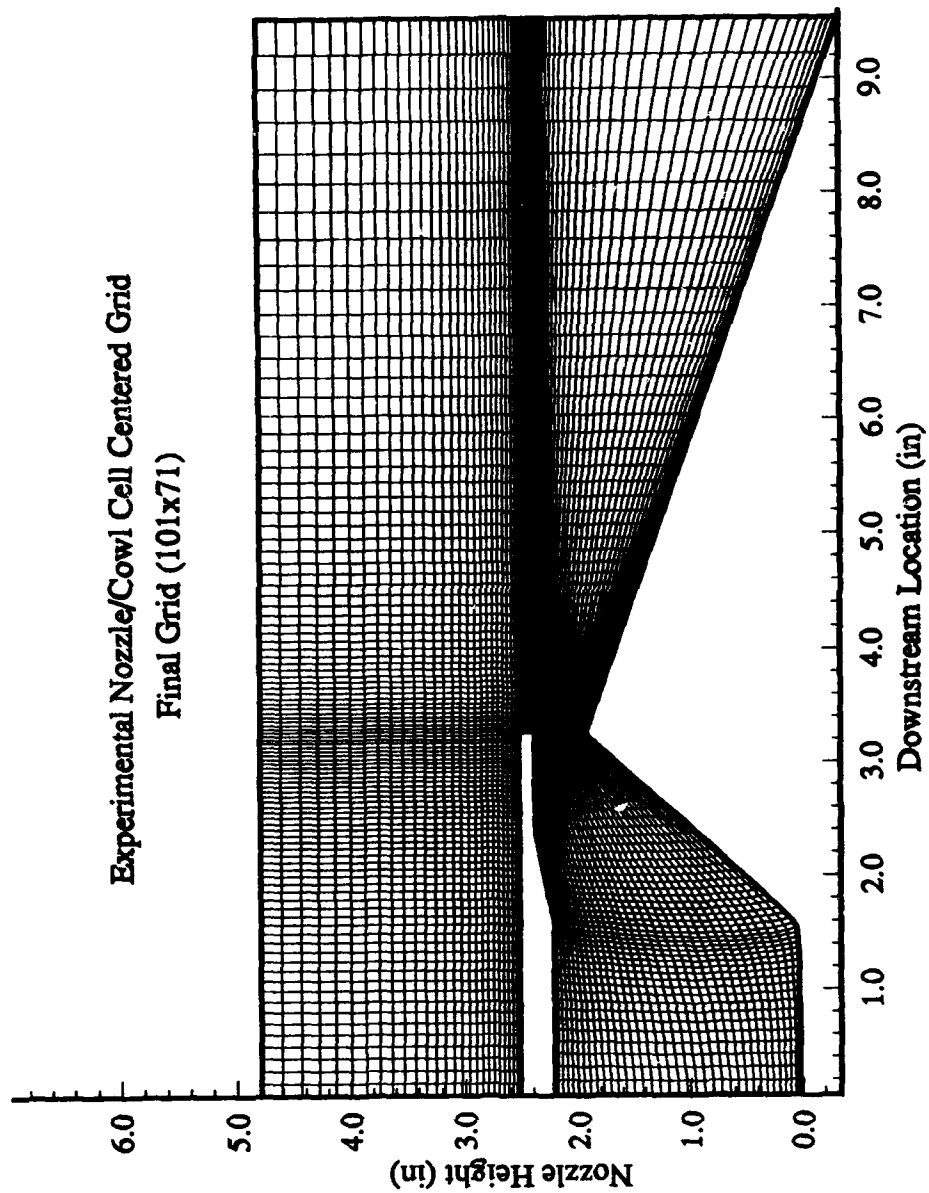


Figure 3-2 Experimental Nozzle/Cowl Final Cell Centered Grid (101x71)

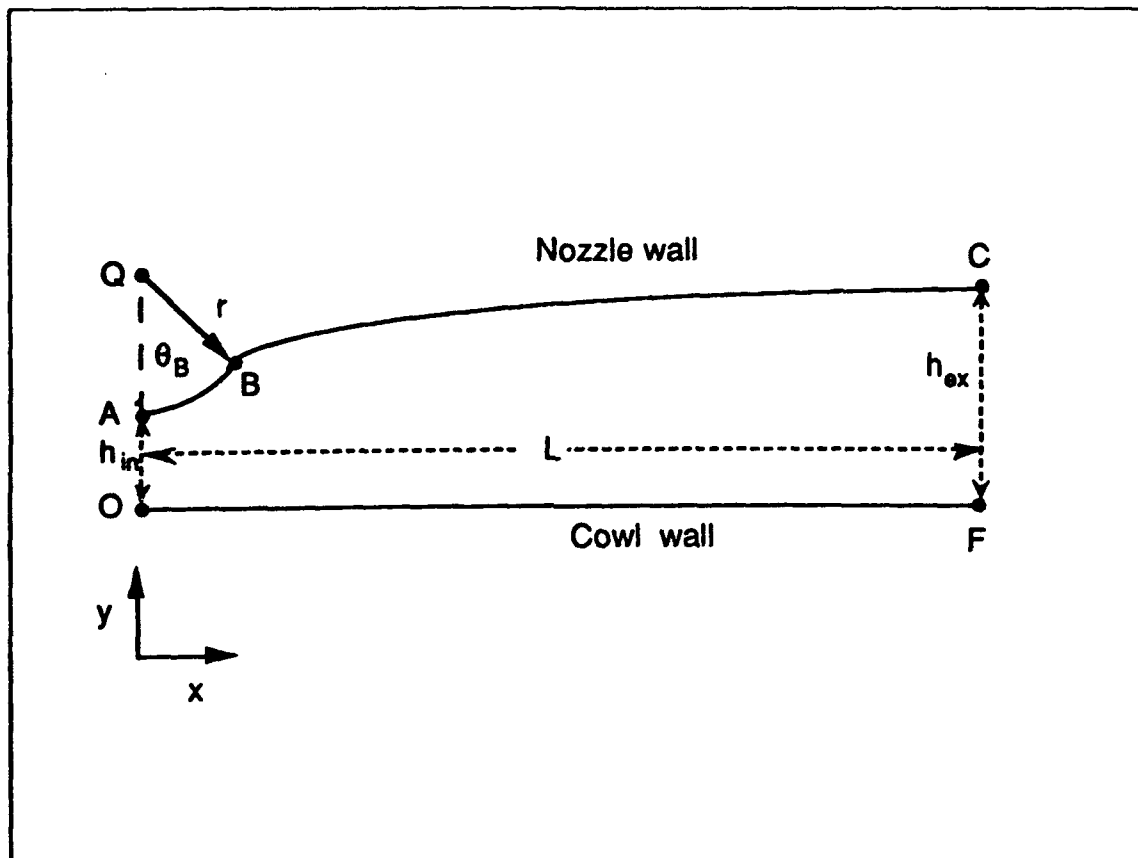


Figure 3-3 Generic Nozzle Wall Definition (9)

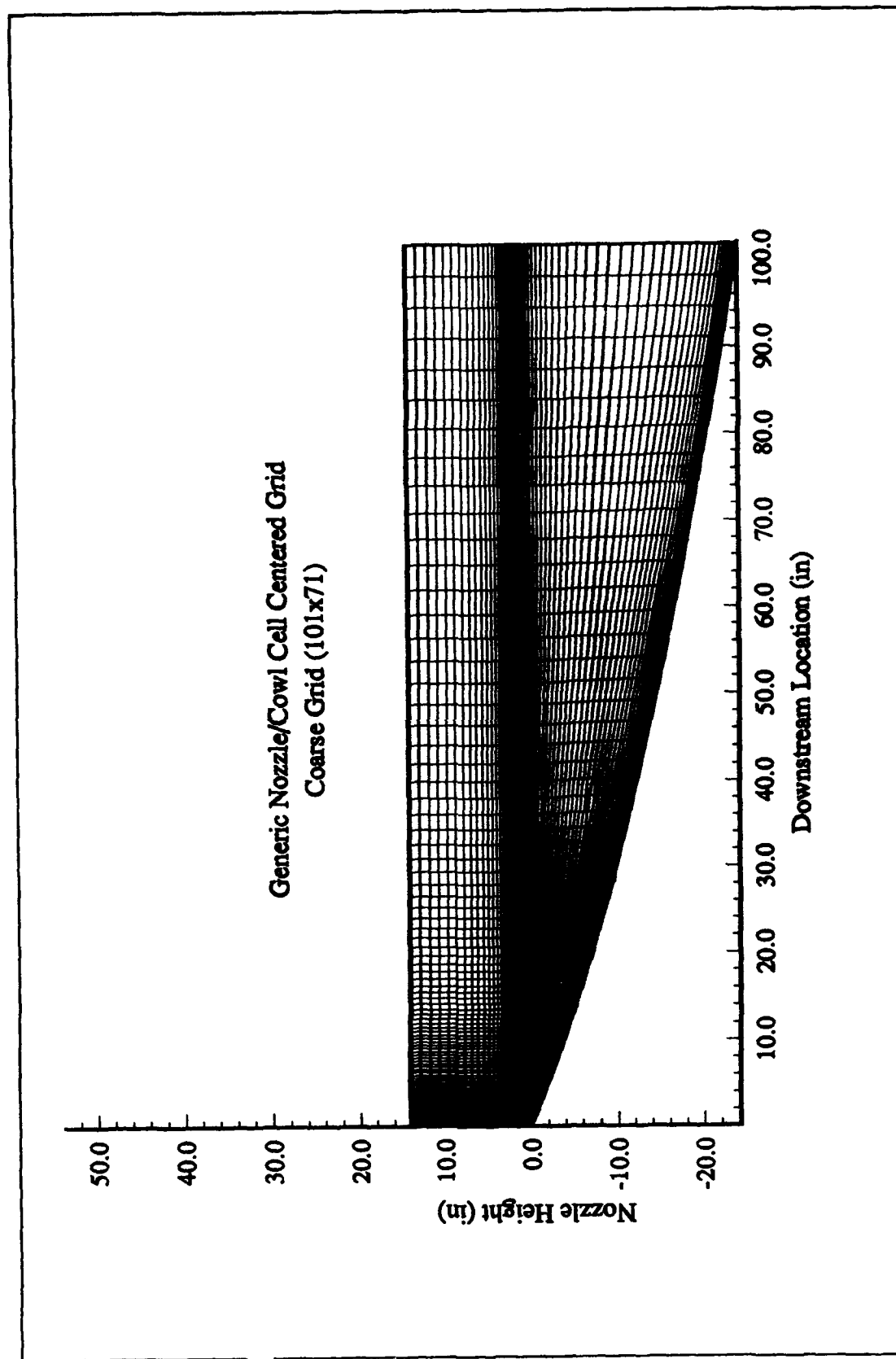


Figure 3-4 Generic Nozzle/Cowl Coarse Cell Centered Grid (101x71)

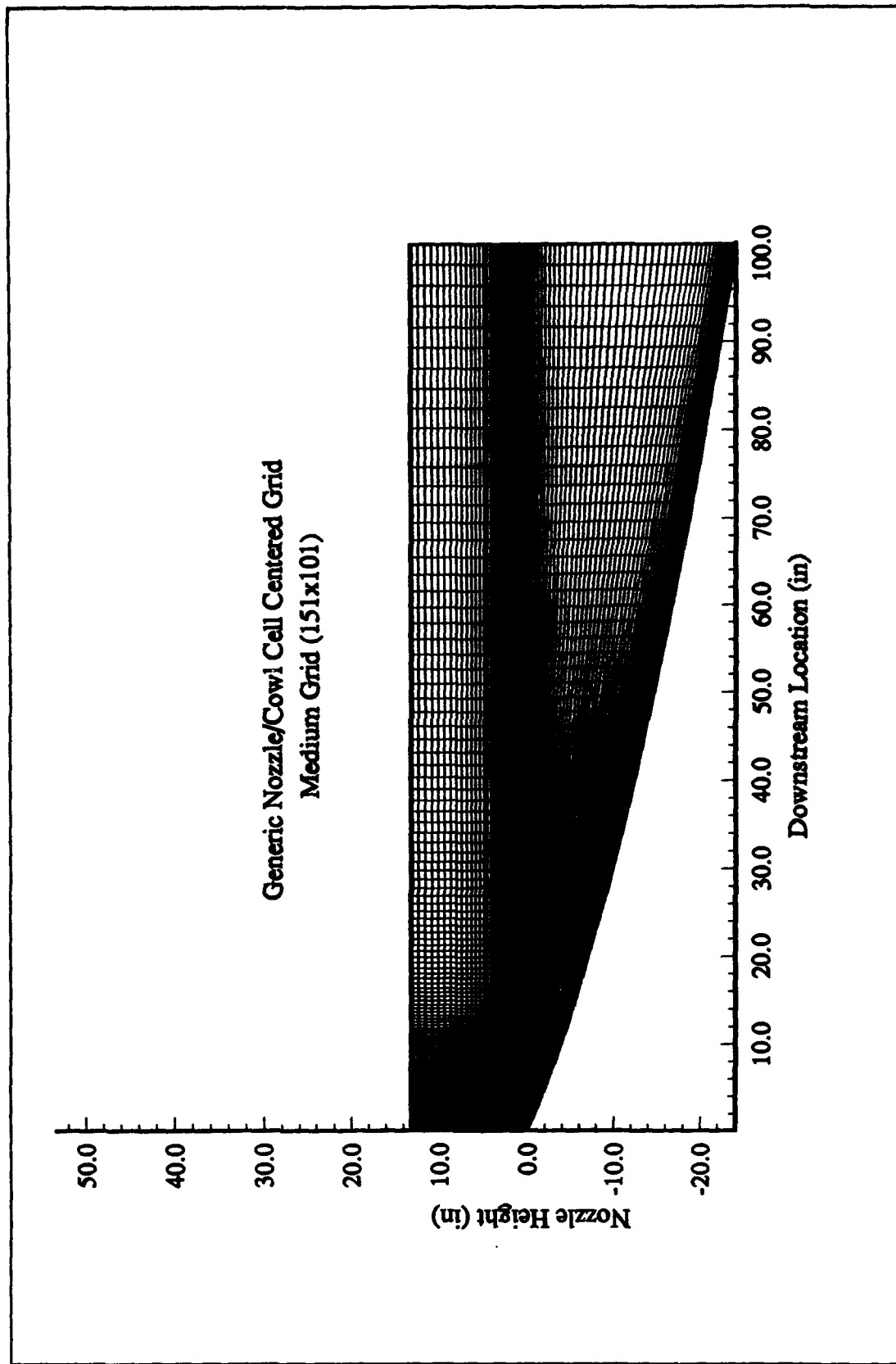


Figure 3-5 Generic Nozzle/Cowl Medium Cell Centered Grid (151x101)

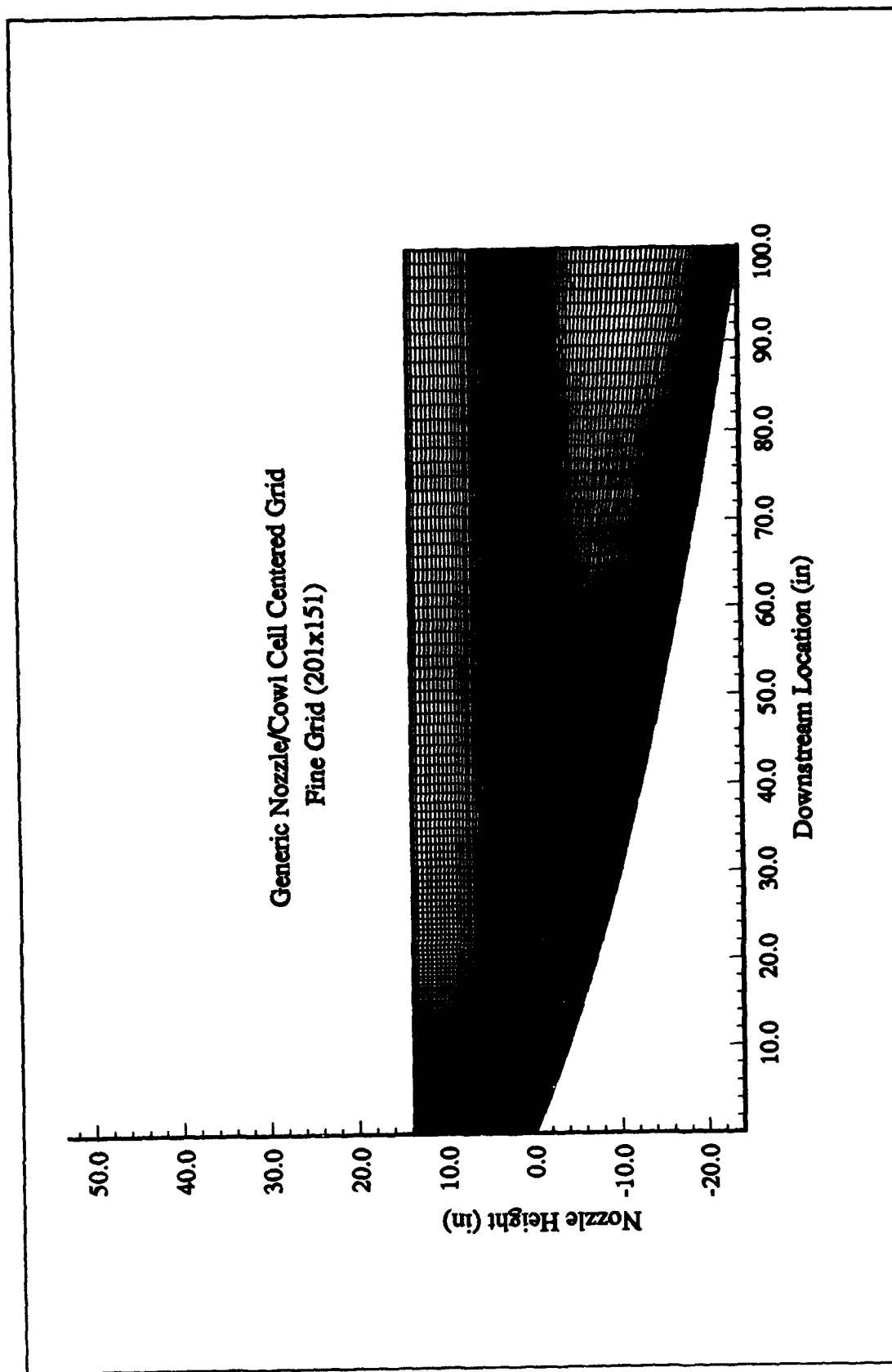


Figure 3-6 Generic Nozzle/Cowl Fine Cell Centered Grid (201x151)

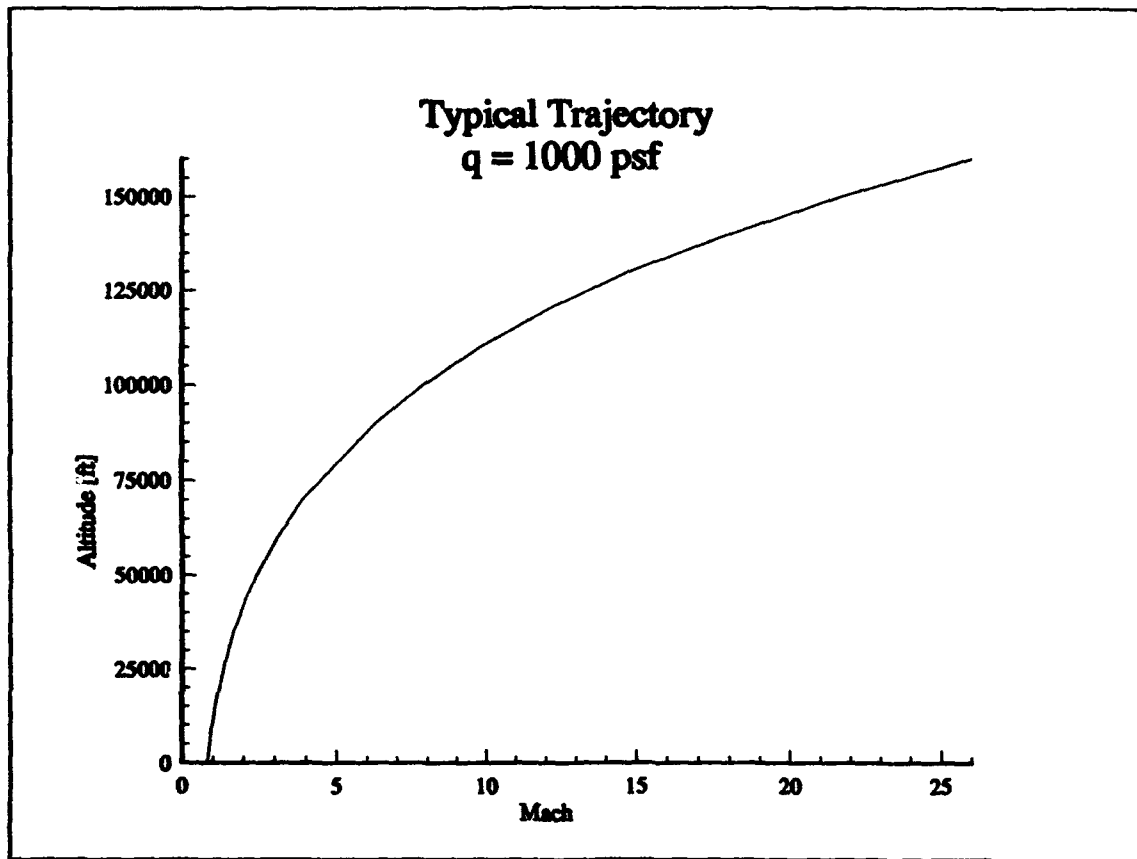


Figure 3-7 Generic Nozzle Trajectory

IV. RESULTS AND DISCUSSIONS

The two-dimensional Navier Stokes equations were evaluated using the Wright Laboratory flux-splitting finite volume code for two separate geometries over a wide range of operating conditions. The nozzle operating conditions analyzed were all initially underexpanded since the total nozzle exit pressure, P_{T_e} , was always significantly higher than the ambient static pressure, P_∞ . The flowfield was dominated by the initial expansion of the flow from this underexpanded state.

A schematic of a typical overexpanded and underexpanded exhaust is presented in Figure 4-1. The wall pressure distribution is typically dominated by two separation regions. The first and largest separation bubble occurs just past the nozzle throat where the flow undergoes a dramatic initial expansion. The second separation region may appear after the shock wave associated with an overexpanded flow impinges on the nozzle wall boundary layer. These separation regions are characterized by a recompression of the flow and a subsequent increase in nozzle wall pressure followed by a re-expansion of the flow downstream.

For the experimental nozzle evaluated at the relatively low speed off-design conditions, the flow was initially underexpanded. The dramatic initial expansion caused by the sudden increase in nozzle area typically resulted in an overexpanded flow just downstream of the nozzle throat. The location of the second separation region associated with the large overexpansion and its associated recompression shock is highly dependent on the freestream Mach number, the NPR, and gas generator setting.

For the generic nozzle evaluated over the more realistic trajectory, the initial flow was also significantly underexpanded. For this nozzle, the sudden initial expansion was also very severe but the flow did not overexpand to a pressure less than ambient and the flow typically remained underexpanded throughout the nozzle. There was typically no characteristic downstream separation bubble associated with an overexpansion shock wave.

Assessing the impact of a gas generator on these characteristic flow solutions was the primary objective of this research. The overall impact of adding a gas generator flowfield, increasing the gas generator mass flow, and deflecting the gas generator thrust are presented in the following sections. Section 4.2 discusses the effects of the gas generator flowfield on the experimentally validated nozzle/cowl geometry presented in Figure 3-1 and Section 4.3 presents the effects of the gas generator on the generic nozzle/cowl configuration presented in Figure 3-2.

The flow solutions were evaluated with the Flow Analysis Software Toolkit (FAST) developed by NASA Ames Research Center (15). This software was also installed on the NAIC SGI network for this research.

4.1 Grid Resolution Effects

The effects of grid density must be evaluated before the flowfield can be analyzed with confidence. Any finite difference or finite volume scheme will be affected by the truncation errors associated with the chosen numerical method (10). A grid resolution study must be completed to assure that the truncation errors do not build up and dominate the flow solution. Furthermore, the grid must be dense enough

to capture all of the critical flow structures. For the configurations analyzed in this study, a series of grid refinements was made. The effects of a coarse grid (101x71), a medium grid (151x101), and a fine grid (201x151) were evaluated at several operating conditions.

Hyun (1) completed this grid resolution study for the experimental nozzle/cowl configuration presented in Section 3.1 and Figure 3-1 at the $M_{\infty}=1.9$, $NPR=7.0$, and $M_{\infty}=3.0$, $NPR=16.0$ test conditions. Hyun showed that the dominant effects of grid resolution occurred in the region of the first separation bubble just downstream of the sharp throat. As grid density increased, the flow characteristics in the initial recompression region were resolved. Grid refinement did not significantly change the magnitude of the peak recompression and it had almost no effect on the re-expansion of the flow past the first separation bubble. Even as the grid resolution was increased and the recompression structure was resolved, there was still a noticeable difference between the overall recompression calculated numerically and the experimental measurements. The primary reason for the small difference between the experimental and numerical solution was attributed to the laminar flow assumption used in the numerical method. Overall, the agreement between the experimental data and the numerical solution was very good. Since the results were not significantly improved and the penalty paid in overall computation time was so large for the finer grids, the coarse grid was determined to be acceptable for this analysis.

A similar study was done for the generic nozzle/cowl configuration presented in Section 3.2, and Figure 3-2 at the design Mach 15 condition with the gas generator operating at 100% throttle with no deflection. The three grids used for this analysis

were presented in Figures 3-3 through 3-5. Figure 4-2 shows the effects of grid resolution. As with the previous geometry, the largest differences occur in the region of the initial recompression. For this case, the most significant changes occur near the peak of the recompression and they tend to disappear during the subsequent downstream expansion. The effect of the compression waves associated with the wall curvature were resolved with the finer grids in this region.

Since there is no experimental data to compare to, the grid resolution effects had to be evaluated in terms of their relative impact on this gas generator study. Figure 4-3 shows the net effect of turning off the gas generator on the nozzle wall pressure distribution at this same Mach 15 trajectory point using the coarse (101x71) grid. Note that the gas generator is located in the cowl at a downstream location of 10 inches. Since the flow is supersonic, there is no upstream effect of the gas generator. Furthermore, any pressure differences associated with the gas generator must propagate through the internal nozzle flowfield before they can have an impact on the nozzle wall. Since the internal nozzle flow is expanded to fairly high Mach numbers for this geometry, the propagation of the gas generator effects are limited to the downstream nozzle wall locations.

The convergence of the final solution is determined by achieving a steady RMS heat transfer and pressure along the nozzle wall as defined in Section 2.5 and Equations 2-41 and 2-42. Figure 4-4 shows the explicit convergence history of the Mach 15 trajectory point using the coarse 101x71 grid. For this example, convergence for the Van Leer solution was achieved in a relatively quick 500 iterations and an acceptable convergence for the Roe solution was achieved by 920 iterations.

For this same example, convergence was achieved in 1120 iterations for the medium grid and 1300 iterations for the fine grid. The code required approximately 787.9 microseconds per iteration per node for the coarse grid, 954.43 microseconds per iteration per node for the medium grid and 929.6 microseconds per iteration per node for the fine grid. Using a Silicon Graphics Iris Indigo workstation, the total CPU time required for this example solution was 1.444 hours with the coarse grid, 4.529 hours with the medium grid and 10.188 hours with the fine grid.

As illustrated in Figure 4-2, the initial recompression was not accurately captured with the coarse grid. The magnitude of the peak recompression tends to increase slightly with increased grid resolution. However, Hyun (1) noted that the numerical vs. experimental discrepancy in this region was due as much to the laminar flow assumption as it was to grid resolution. Note from Figure 4-3 that the cowl and gas generator effects are not evident in the flowfield nor nozzle pressure until significantly downstream of the initial expansion region. Additionally, since the downstream influence of the cowl is not affected significantly by the grid resolution, the computational time penalty associated with the increased grid density was not justified. Therefore, the coarse grid (101x71) was used for the remainder of this analysis.

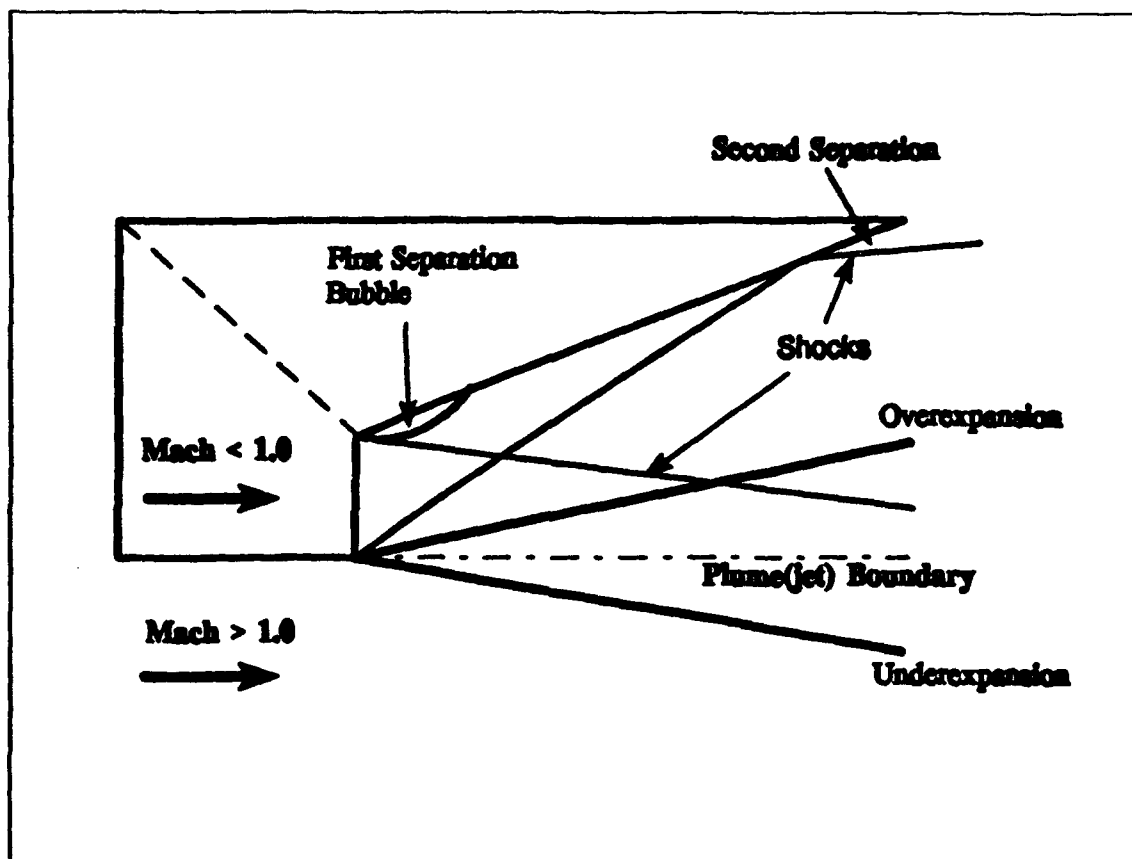


Figure 4-1 Schematic of Over and Underexpanded Exhaust at Supersonic Freestream Mach Number (1)

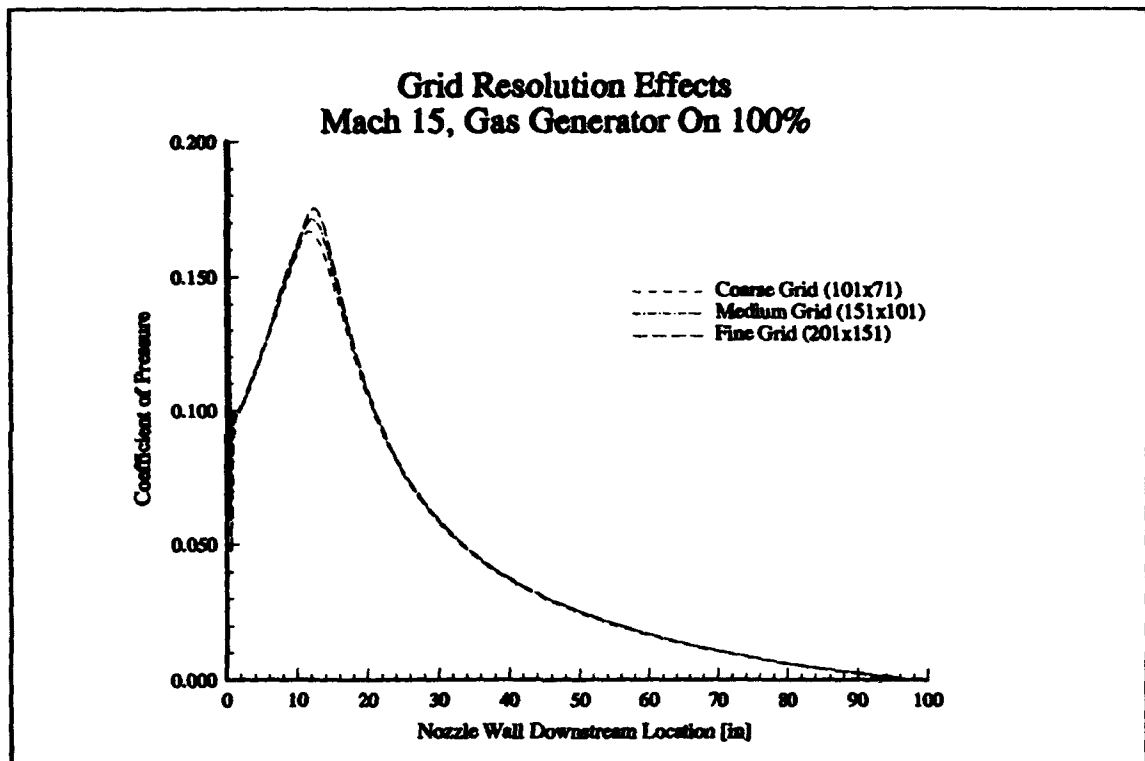


Figure 4-2 Grid Resolution Effects, Gas Generator On 100%

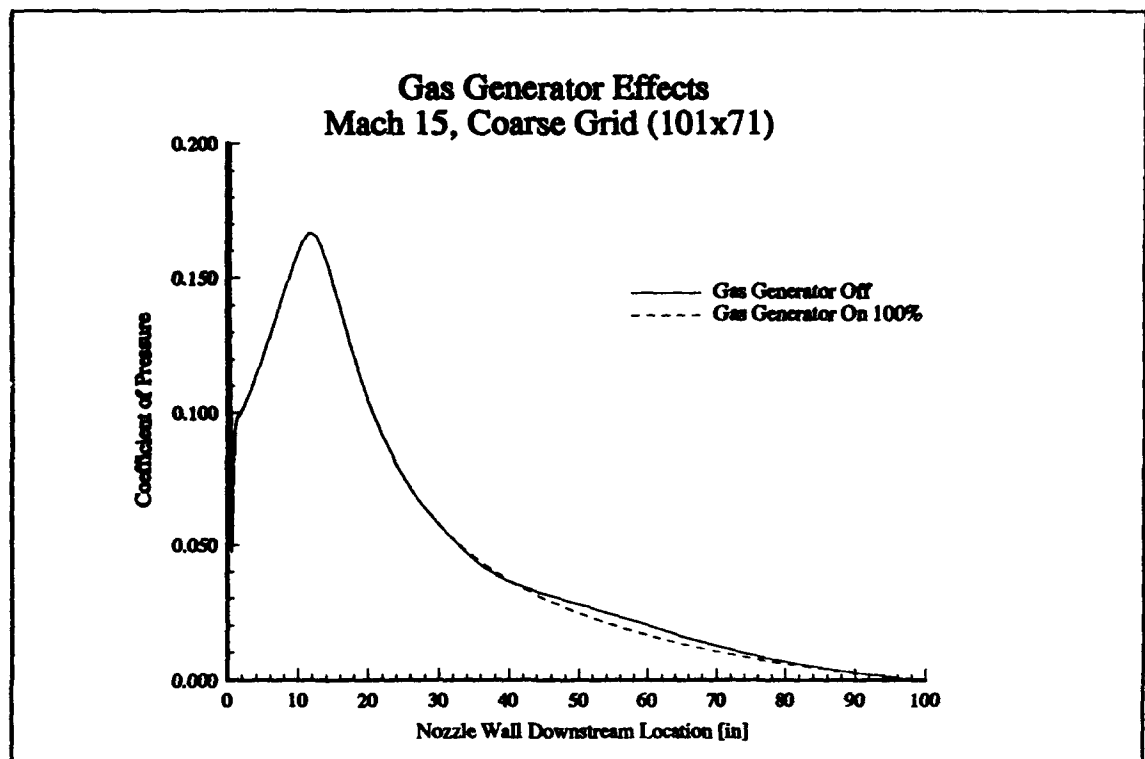


Figure 4-3 Gas Generator Effects, Mach 15, Coarse Grid

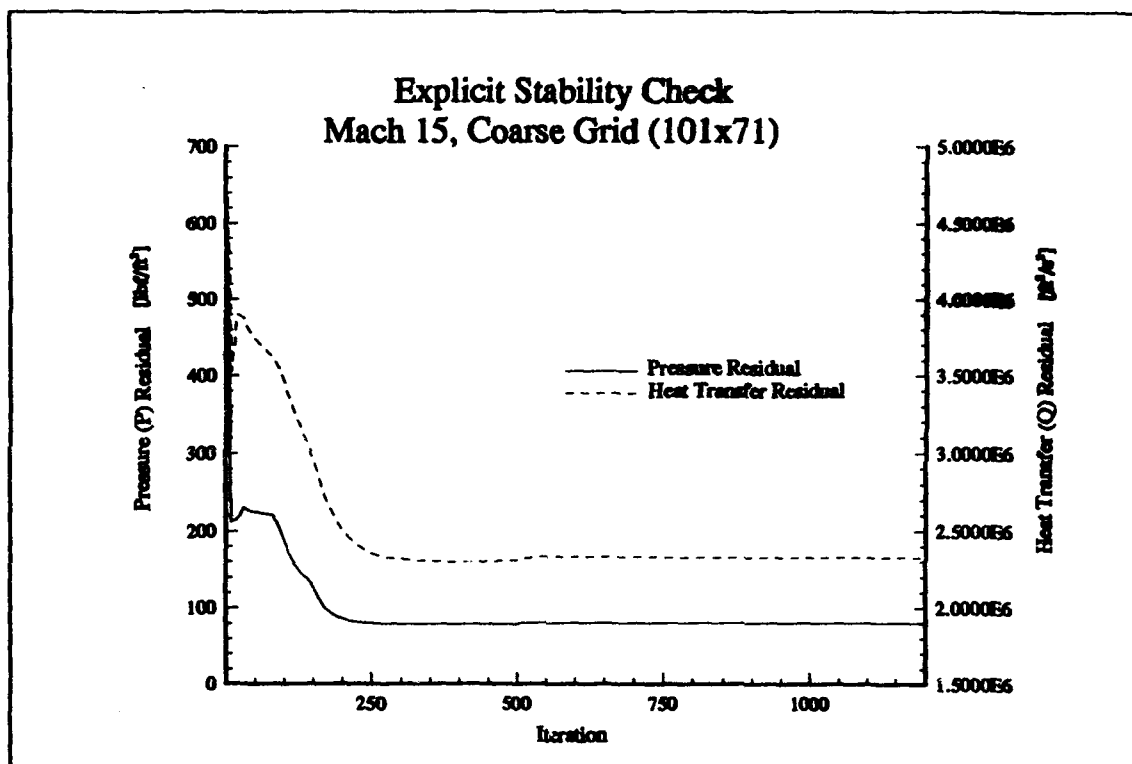


Figure 4-4 Explicit Stability Check, Mach 15, Coarse Grid (101x71)

4.2 Application of a Cowl Gas Generator Flowfield to an Experimentally Validated Off-Design Configuration

The experimental hypersonic nozzle/cowl geometry presented in Figure 3-1 was evaluated with and without the gas generator for two off-design supersonic flow conditions; Mach 1.9 and Mach 3.0. The basic gas generator effects were analyzed over a range of NPR at these two Mach numbers. The gas generator mass flow and deflection angle effects were evaluated for two typical configurations, Mach 1.9, NPR=7, and Mach 3.0, NPR=16 since these were the same conditions analyzed by Cochran (4) and Hyun (1) for their cowl geometry studies described in Section 3.1. These baseline flow conditions correspond to Cochran's test point numbers 148 and 184, respectively.

The nozzle wall pressure distributions for the Mach 1.9, NPR=7, TPN 148 case are presented in Figure 4-5 for both the baseline gas generator off condition and the gas generator 100%/no deflection operating condition. The nozzle throat is located at a downstream location of 3.25 inches. It is obvious that the internal flow upstream of the throat is significantly underexpanded. As the flow passes the sharp corner at the throat, it experiences a significant increase in flow area resulting in a dramatic expansion. The flow actually overexpands to a pressure less than ambient. Both with and without the gas generator, the flow immediately begins to recompress due to the presence of the first separation bubble past the sharp throat. For the baseline case with the gas generator off, the recompression is not very strong and the flow remains overexpanded along the entire nozzle wall downstream of the throat. With the gas generator on, the size of the first separation bubble increases significantly as indicated

by the increased region of recompression along the nozzle wall. The gas generator not only increases the magnitude of the recompression, but it also moves the location of the peak magnitude and the subsequent re-expansion downstream. The relatively high pressure gas generator acts like an aerodynamic cowl extension. The relatively high pressure boundary between the internal and external flowfields created by the gas generator reduces the expansion of the high pressure internal nozzle flow near the cowl wall to the relatively low pressure external freestream flow. The effects of this increased pressure then propagate through the relatively low speed supersonic flow just downstream of the nozzle throat where it appears as an increase in pressure along the nozzle wall.

The shock wave associated with the overexpanded baseline case impinges the nozzle wall downstream of the first separation bubble. This shock impingement causes a second smaller separation region to form and the flow is again recompressed. This flow does not reattach to the nozzle wall and the flow remains separated to the end of the nozzle. With the gas generator on, the second separation does not form. For both cases, the flow overexpands and never recovers to ambient pressure.

The nozzle wall pressure distribution for the Mach 3.0, NPR=16, TPN 184 case is presented in Figure 4-6. For this increased nozzle pressure ratio and external flow Mach number case, the initial expansion past the sharp throat is not as strong as the previous case and the flow does not overexpand past the throat. The magnitude of the first separation bubble increases for both the gas generator on and off as indicated by the increased pressure recovery along the nozzle wall. Again, the gas generator tends to increase the overall size of the first separation bubble resulting in a delayed re-

expansion. The second separation does not form until the very end of the nozzle wall for the gas generator off case and therefore, the downstream pressure for the gas generator on case remains higher than the gas generator off case throughout the entire length of the nozzle. As with the previous case neither of these flows recover to ambient pressure.

Appendix C presents the pressure and Mach number contours for these two baseline configurations with the gas generator operating at 100% throttle with no deflection and with the gas generator off. Figures C-1 and C-2 present the flowfield solution for the baseline Mach 1.9, NPR=7.0, gas generator off case. In addition to the nozzle wall expansion and recompression associated with the separation regions, the other flow phenomena can be seen. Figure C-1 clearly demonstrates how the internal nozzle flow is dominated by the initial expansion just downstream of the throat. As the high pressure internal flow expands past the cowl, a plume shock appears as a pressure rise in the external flowfield. The boundary between the internal and external flowfield can also be seen as large Mach number gradients in Figure C-2. In addition, the internal shock extending from the cowl wall and the impingement of this shock on the nozzle wall is also evident in Figure C-2. At approximately 6.5 inches downstream, the internal shock impinges on the wall and the adverse pressure gradient acting on the viscous boundary layer causes a flow separation which can also be seen in figure C-2.

Figures C-3 and C-4 show this same cases with the gas generator operating at 100% throttle with no deflection. The interaction of the nozzle flow structures with the gas generator flow can now be seen. Figure C-3 shows how the gas generator acts

as an aerodynamic cowl extension by delaying the large initial expansion just downstream of the cowl wall. The increased pressure recovery along the nozzle wall is also evident in this figure. Figure C-4 clearly shows the location of the gas generator boundaries as very strong Mach number gradients. Furthermore, Figure C-4 shows how the internal nozzle shock, the shock impingement on the nozzle wall, and the subsequent flow separation associated with an initial overexpansion does not form with the gas generator on. These figures also show that there is a slight increase in the external flow plume shock strength due to the expansion of the high pressure gas generator boundary into the external flowfield.

Figures C-5 through C-8 show the same information for the Mach 3.0, NPR=16.0 case. Except for the decreased plume shock angle associated with the higher external flow Mach number, and the increased internal nozzle flow expansion associated with the higher nozzle pressure ratio operating conditions, the same basic trends are obvious. A comparison of Figures C-4 and C-8 show the effect of nozzle operating condition on the gas generator plume shape. The plume is pushed out significantly due to the higher internal nozzle pressure associated with the increased Mach number and increased nozzle pressure ratio operating condition.

An appreciation for the basic effects of the gas generator can be gained by investigating a cross section of the flowfield just downstream of the gas generator. Figures 4-7 and 4-8 show the pressure distribution across the height of the nozzle at a constant axial location, indicated by index "I", just downstream of the cowl edge. A constant location of $I=52$, corresponding to an approximate downstream location of 3.27 inches, was used to generate these profiles. For reference, note that the edge of

the cowl and the gas generator is located between 2.375 and 2.5 inches. For both of these cases, the flow along the nozzle wall ($h=1.914$ inches) has already undergone a dramatic expansion due to the rapid increase in flow area. The internal nozzle flow that was traveling along the cowl wall ($h < 2.375$) is still at relatively high pressure relative to the ambient pressure, ($h > 2.5$). For these operating conditions, the gas generator operates with an exit pressure that is higher than the expanded cowl base pressure associated with the gas generator off condition. This higher pressure behind the cowl tends to keep the internal nozzle pressure higher and delays the expansion of this flow to the external freestream conditions. This higher pressure then propagates through the nozzle resulting in a higher pressure distribution on the downstream nozzle wall.

4.2.1 Gas Generator Mass Flow Effects. The effects of varying the gas generator mass flow were investigated for the Mach 1.9 and Mach 3.0 flow conditions. The gas generator throttle was increased from 0% to 200% in 25% increments. For a fixed geometry gas generator, varying the throttle effectively changes the gas generator exhaust pressure and mass flow rate. Figure 4-9 presents the effect of varying the gas generator mass flow rate on the nozzle wall pressure distribution for the Mach 1.9, NPR=7, TPN 148 case. As the throttle setting is increased, the overall size of the initial separation bubble increases as indicated by an increase in recompression along the nozzle wall. In general, increasing the gas generator mass flow rate and exhaust pressure increases the initial rate of recompression and moves the location of the peak recompression slightly upstream. The subsequent downstream re-expansion is also

delayed by the increase in the size of the separation bubble. At the lower mass flow rates, the effect of an expansion and subsequent recompression can be seen within the first separation bubble. In general, as the gas generator mass flow is increased, the effects of the second separation region disappear resulting in a decreased pressure near the end of the nozzle wall.

The nozzle wall pressures were integrated using Equations 2-44 to calculate the nozzle wall contribution to thrust. Figure 4-10 presents the effects of varying the gas generator mass flow in terms of the nozzle wall pressure contributions to thrust. The thrust values are negative for this configuration indicating there is a net pressure drag acting on the nozzle wall for this operating condition. This is caused by the dominant high pressure on the internal 50 degree converging wall. This figure highlights that at this operating condition, simply placing a gas generator into the cowl wall gives a larger net effect than varying the mass flow. Increasing mass flow tends to increase the performance due to the rise in pressure associated with the larger initial recompression region. Decreasing mass flow does not appear to significantly decrease the performance at these operating conditions. This is caused by the slight increase in downstream nozzle wall pressure that occurs when the gas generator is operating at low throttle settings.

Figures 4-11 and 4-12 show the same information presented above for the increased Mach and NPR case; Mach 3.0, NPR=16.0, TPN 184. These figures show the same basic trends that were observed for the Mach 1.9, NPR=7.0, TPN 148 case described above. Since this case did not have a significant second separation region, the downstream recompression associated with it did not significantly affect the trends

at the low throttle settings. The change in the integrated pressure thrust contribution varies nearly linearly with changes in gas generator throttle setting at this operating condition.

4.2.2 Gas Generator Deflection Angle Effects. The effect of deflecting the gas generator flow was also investigated for the Mach 1.9 and Mach 3.0 flow conditions. The gas generator deflection angle was varied from -10 to +10 degrees in 2.5 degree increments. Figure 4-13 shows the effect of deflecting the gas generator for the Mach 1.9, NPR=7.0, TPN 148 case. The gas generator was held at a constant 100% throttle setting for all of these profiles. The overall trends associated with deflecting the gas generator flow are quite different than the trends associated with the change in mass flow. Like the increasing mass flow trends, as the flow is deflected towards the nozzle wall (negative deflection angle), the rate of recompression increases and the peak recompression increases and moves upstream. Unlike the increasing mass flow trends, as the flow is deflected towards the nozzle wall, the initial recompression occurs much faster and the magnitude of the peak compression is much larger. The effects of gas generator deflection are primarily limited to the vicinity of the first separation bubble. The downstream pressure distributions tend to converge to the same solution calculated for the non deflected gas generator.

Figure 4-14 presents the gas generator deflection angle effects on the nozzle wall pressure contribution to thrust. Sharp increases in the peak recompression with deflections towards the wall tend to increasingly improve the pressure contribution to thrust. Deflections away from the wall decrease the peak compression and decrease the performance improvement associated with the gas generator. The performance

decreases with deflections away from the wall are not as great as the performance increases associated with deflections towards the wall. This occurs because the deflections towards the wall increase both the magnitude of the peak compression and the rate at which the recompression occurs. Deflections away from the wall, on the other hand, tend to decrease the peak magnitude of the recompression but they do not significantly decrease the rate of initial recompression.

Figures 4-15 and 4-16 show the gas generator deflection angle effects for the Mach 3.0, NPR=16.0, TPN 184 case. The overall trends are similar to the trends observed for the Mach 1.9 operating condition. The gas generator deflection effects are characterized by increases in the magnitude of the peak recompression and the rate of initial recompression.

4.2.3 Gas Generator Comparison to Nozzle/Cowl Geometry Effects.

Cochran (4) and Hyun (1) evaluated the effects of modifying the cowl edge geometry for this configuration at these same two operating conditions. An extended cowl and an extended cowl with + 5 and -5 degree deflections were evaluated experimentally by Cochran and numerically by Hyun. Figure 4-17 shows the results of Hyun's numerical analysis compared to the baseline gas generator flow case for the Mach 1.9, NPR=7.0, TPN 148 case. The basic effect of a cowl wall extension is very similar to the effect of placing a gas generator into the baseline cowl. Increasing the cowl wall length increases the overall size of the first separation bubble. Unlike the gas generator, however, the effect of extending the cowl does not minimize the effects of the second separation.

Overall, the basic effects of cowl wall deflections are very similar to gas generator deflection effects. As the cowl wall extension is deflected towards the wall, the peak recompression increases and moves upstream. Like a gas generator deflection, the overall effect of the cowl extension deflection is limited to the first separation bubble and does not significantly alter the downstream flow.

For the conditions analyzed, the gas generator behaves like an aerodynamic cowl extension. In general, gas generator mass flow and exhaust pressure increases can be used to simulate the effects of cowl extensions. Furthermore, gas generator deflections can be used to simulate the effects of mechanical cowl deflections.

Figure 4-18 compares the available cowl geometry data to the baseline gas generator flow solution for the Mach 3.0, NPR=16.0, TPN 184 case. The experimental and numerical data was only available for the -5 degree deflection towards the nozzle wall. The overall trends are very similar to the previous case because the gas generator still provides a relatively high pressure boundary between the internal and external flowfields which acts like an aerodynamic cowl extension.

4.2.4 Nozzle Pressure Ratio Effects. The effect of varying nozzle pressure ratio was also investigated. Figure 4-19 presents the nozzle pressure ratio effects for the Mach 1.9 operating conditions. For this case, the nozzle pressure ratio was investigated at NPR= 3.0, 5.0, 7.0, and 12.0. As the nozzle pressure ratio increases, the magnitude of the first separation bubble increases because the higher nozzle exhaust pressure propagates downstream resulting in a delayed expansion and a higher pressure along the nozzle wall. The rate of recompression is increased and the size of

the separation bubble is lengthened, resulting in a delayed expansion. The location of the peak recompression in the first separation bubble tends to remain at a constant location (3.7 inches downstream). The location of the second separation is affected dramatically by the operating nozzle pressure ratio. As the nozzle pressure ratio is increased, the cowl shock angle associated with the initial overexpansion decreases because the magnitude of the initial overexpansion decreases. This decreased shock angle moves the location of the shock impingement on the nozzle wall downstream. Since the second separation is caused by the impingement of the cowl shock on the nozzle wall boundary layer, the resultant second separation moves downstream. The flow remains separated from the nozzle wall after the shock impingement and therefore, it maintains a relatively constant pressure downstream of the separation.

Figure 4-20 shows the Mach 1.9 flow case analyzed with the gas generator operating at 100% throttle. The gas generator shows the same basic trends throughout the range of nozzle pressure ratio. The magnitude of the first separation bubble is consistently increased. The gas generator also tends to minimize the second separation over this range of operating conditions. At the lower nozzle pressure ratios, however, a second separation does appear. The location of the second separation is typically determined by the magnitude of the recompression shock wave formed off the edge of the cowl wall. With the gas generator operating, the overexpansion past the cowl wall and its associated shock wave is eliminated. The delayed second separation region which appears at the low nozzle pressure ratio operating conditions is not caused by a cowl wall recompression shock, rather it is formed by the impingement of a reflected shock. The shock wave generated by the recompression of the first separation bubble

is reflected off the gas generator stream boundary and it impinges the nozzle wall at the far downstream locations for the low nozzle pressure ratio cases. For the higher nozzle pressure ratio cases, the internal nozzle flow expands to higher Mach numbers and therefore, the internal and reflected shocks are more oblique. Subsequently, the reflected shock does not impinge on the nozzle wall for these operating conditions.

Figures 4-21 and 4-22 show the same basic information for the Mach 3.0 freestream flow conditions. For this analysis, the nozzle pressure ratio was evaluated at $NPR = 5.0, 7.0, 9.0, 12.0, \text{ and } 16.0$. The overall nozzle pressure ratio trends are very similar to the Mach 1.9 flow trends. Since the freestream Mach was increased from 1.9 to 3.0, the overall cowl shock angle decreased, moving the second separation downstream. In addition, the overall effects of nozzle pressure ratio on the first separation bubble were not as severe as they were for the Mach 1.9 cases. Like the Mach 1.9 case, increasing the nozzle pressure ratio increased the magnitude of the first separation bubble.

The nozzle pressure ratio effects are presented in terms of the integrated pressure contribution to thrust in Figure 4-23. The overall magnitude of the integrated thrust tends to increase linearly with increases in nozzle pressure ratio.

For a given nozzle pressure ratio, the magnitude of the forces are much greater for the Mach 1.9 case than for the Mach 3.0 case. This occurs because the dominant contribution to nozzle wall pressure thrust is the high pressure acting on the internal 50 degree compression ramp. The internal nozzle pressure was significantly higher for the Mach 1.9 cases than it was for the Mach 3.0 cases and therefore, the magnitude of the overall nozzle wall pressure thrust is much larger for the Mach 1.9 case.

The magnitude of the gas generator contribution to thrust and lift increases with nozzle pressure ratio due to the increase in the size of the first separation bubble with increasing nozzle pressure ratio. Figures 4-24 presents the nozzle pressure ratio effects in terms of the percent improvement in nozzle wall pressure thrust developed by operating the gas generator at 100% throttle. Although the magnitude of the pressure contributions to thrust increased with increasing nozzle pressure ratio, the percent improvement decreased. The much larger overall increase in magnitude associated with increasing the nozzle pressure ratio overwhelmed the much smaller improvements associated with the gas generator flow. For these reasons, the net effects of the gas generator on the nozzle wall pressure recovery are much more significant at the lower nozzle pressure ratio, off-design operating conditions.

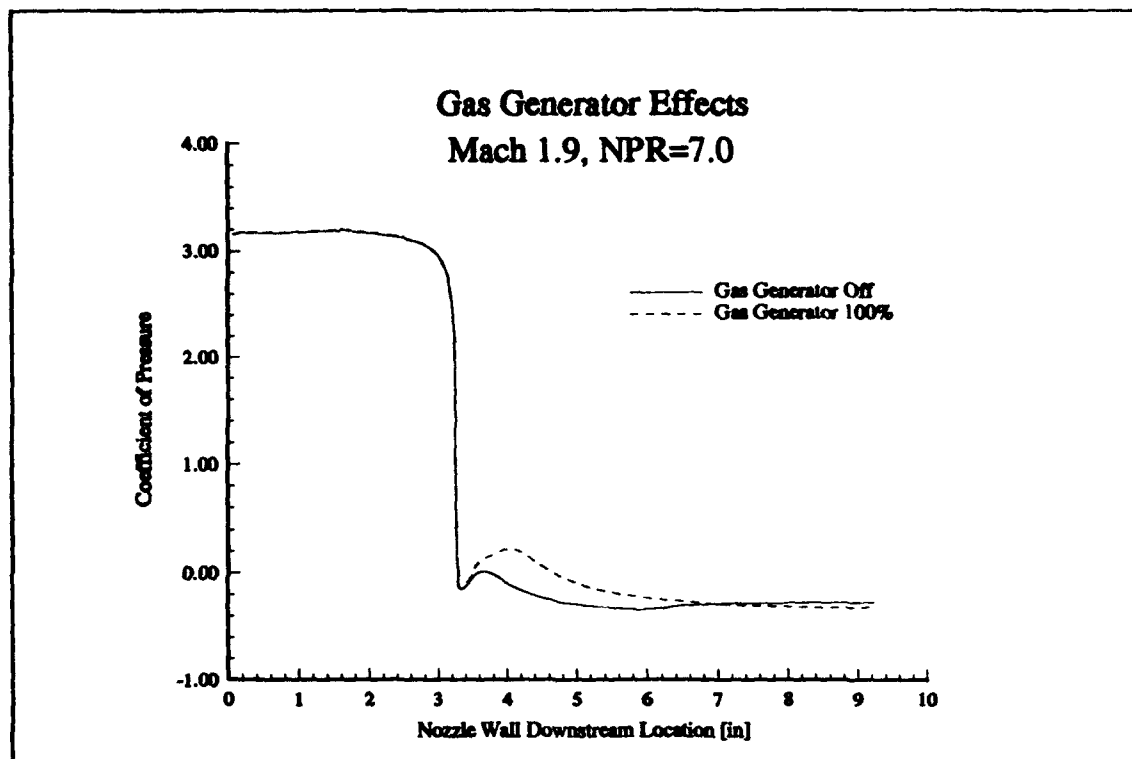


Figure 4-5 Gas Generator Effects, Mach 1.9, NPR=7.0

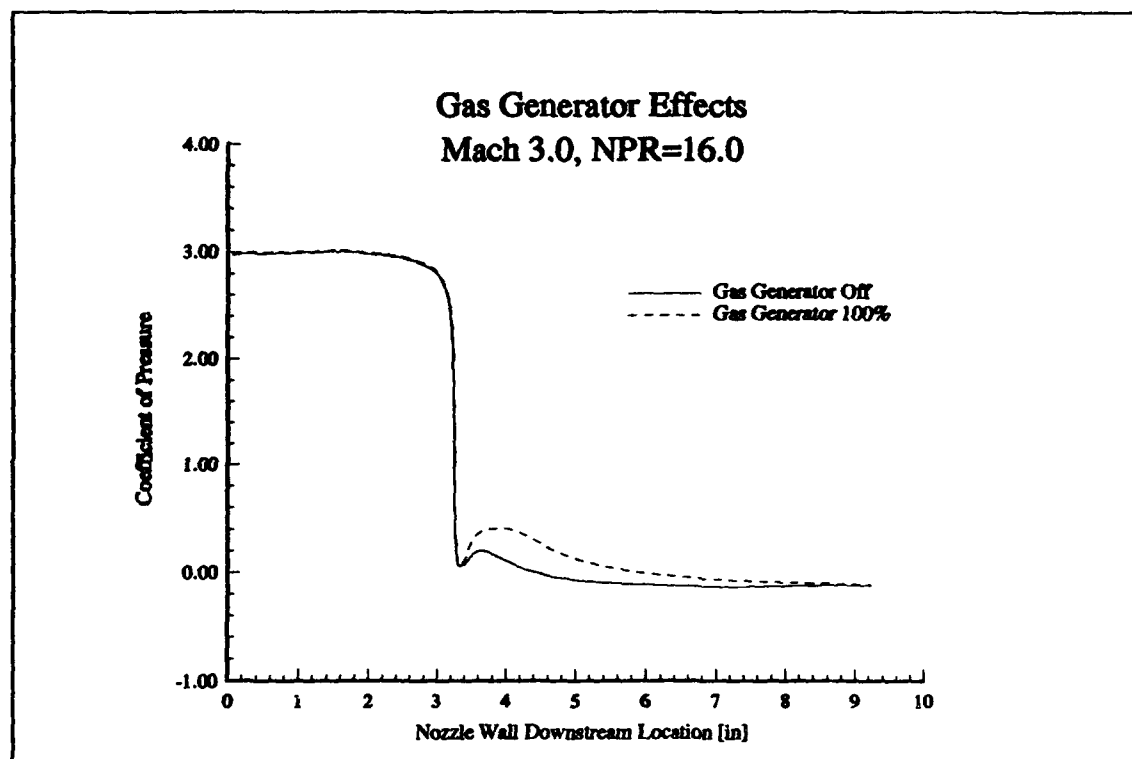


Figure 4-6 Gas Generator Effects, Mach 3.0, NPR=16.0

Constant Axial Location Flow Profile
Mach 1.9, NPR=7.0, I=52

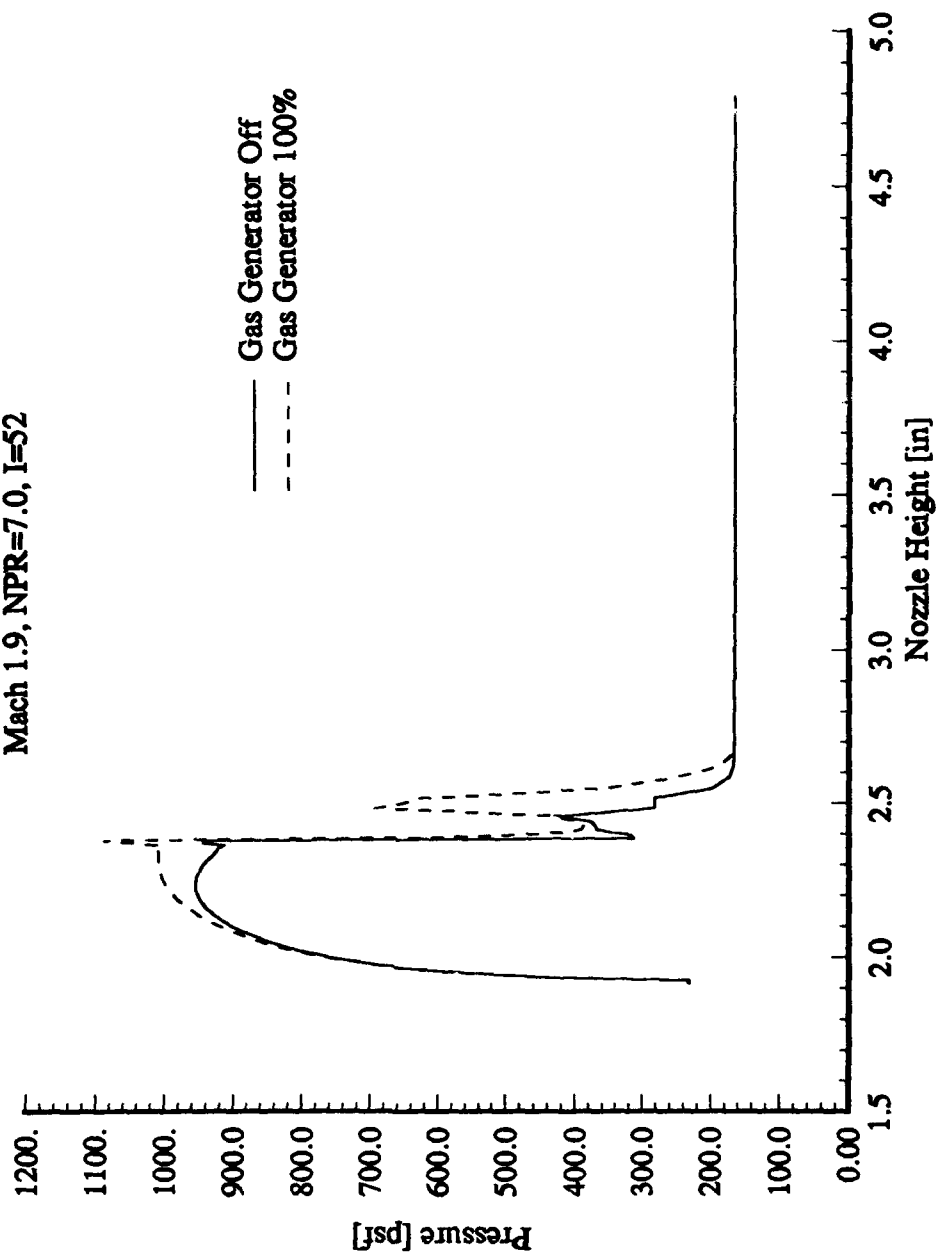


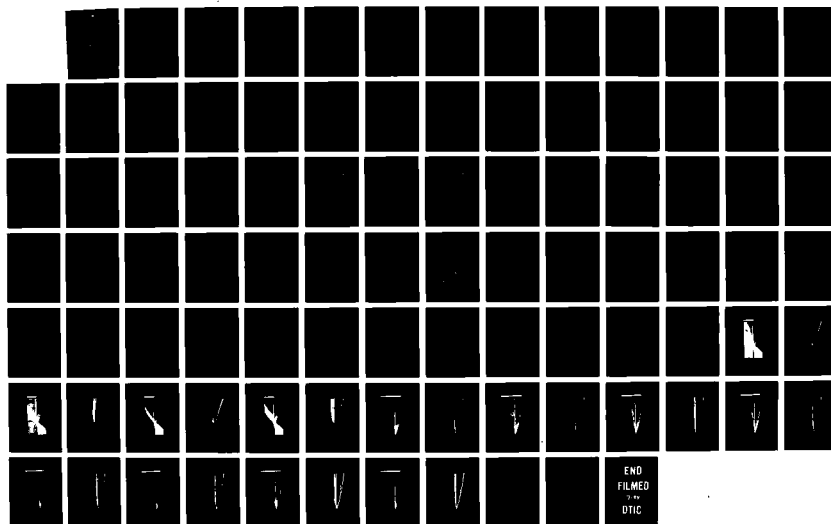
Figure 4-7 Constant Axial Location Profile, Mach 1.9, NPR=7.0, I=52

AD-A280 596

COMPUTATIONAL INVESTIGATION OF AN IMPROVED COML CONCEPT 2/2
FOR HYPERSONIC PROPULSIVE NOZZLES(U) AIR FORCE INST OF
TECH WRIGHT-PATTERSON AFB OH SCHOOL OF ENGINEERING
M C BUTLER JUN 94 AFIT/GAE/ENY/94J-1

UNCLASSIFIED

NL

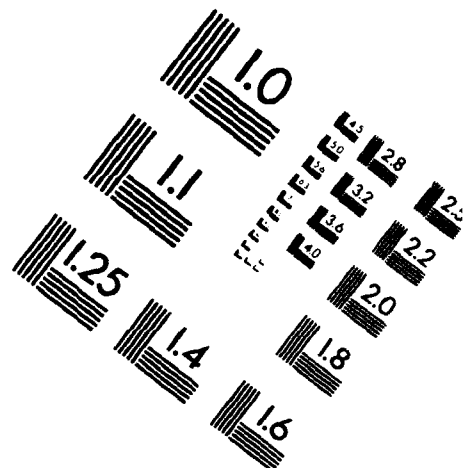
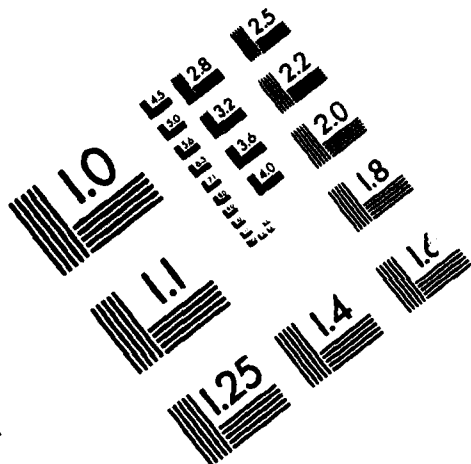




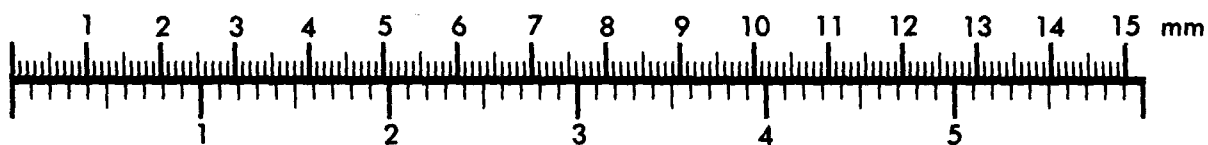
AIM

Association for Information and Image Management

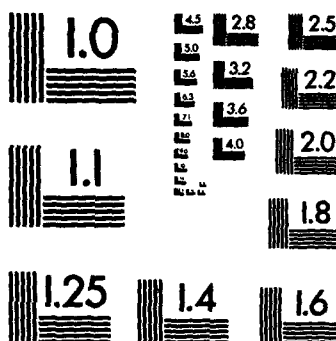
1100 Wayne Avenue, Suite 1100
Silver Spring, Maryland 20910
301/587-8202



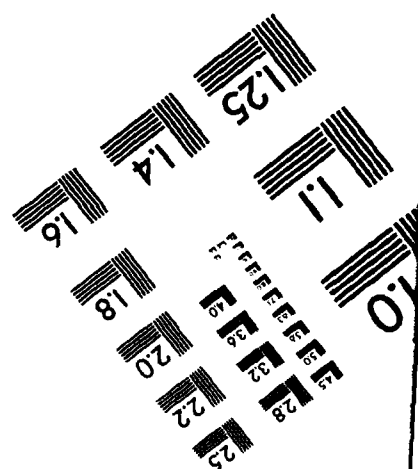
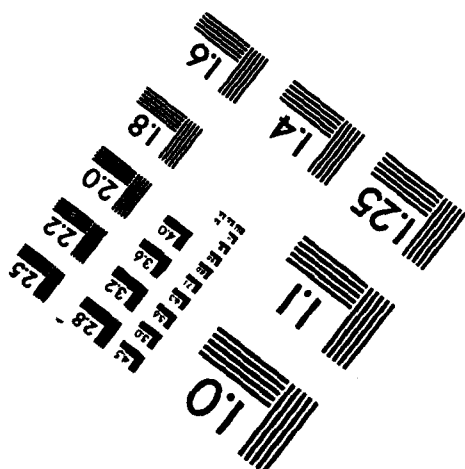
Centimeter



Inches



MANUFACTURED TO AIM STANDARDS
BY APPLIED IMAGE, INC.



Constant Axial Location Flow Profile
Mach 3.0, NPR=16.0, I=52

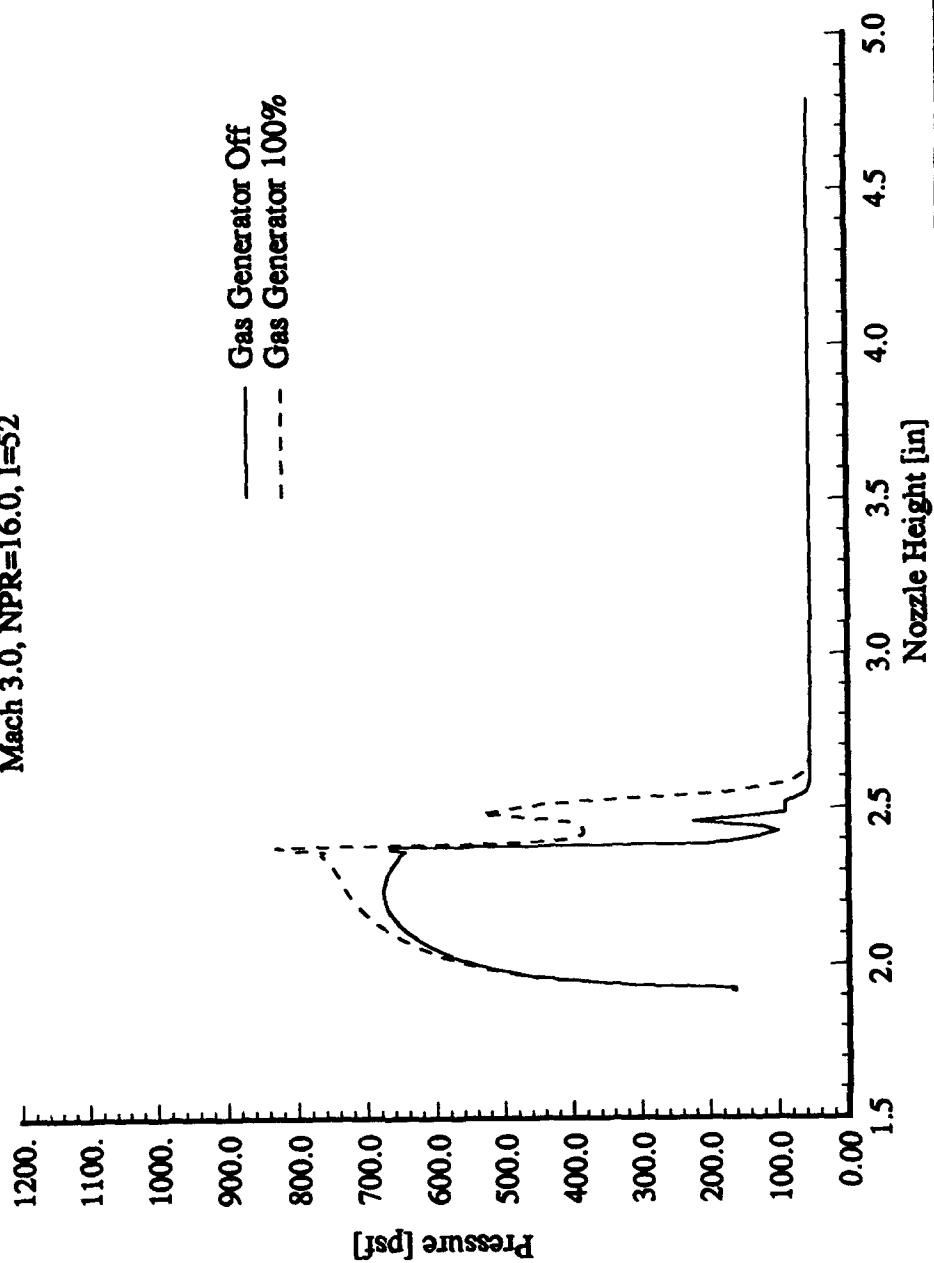


Figure 4-8 Constant Axial Location Flow Profile, Mach 3.0, NPR=16.0, I=52

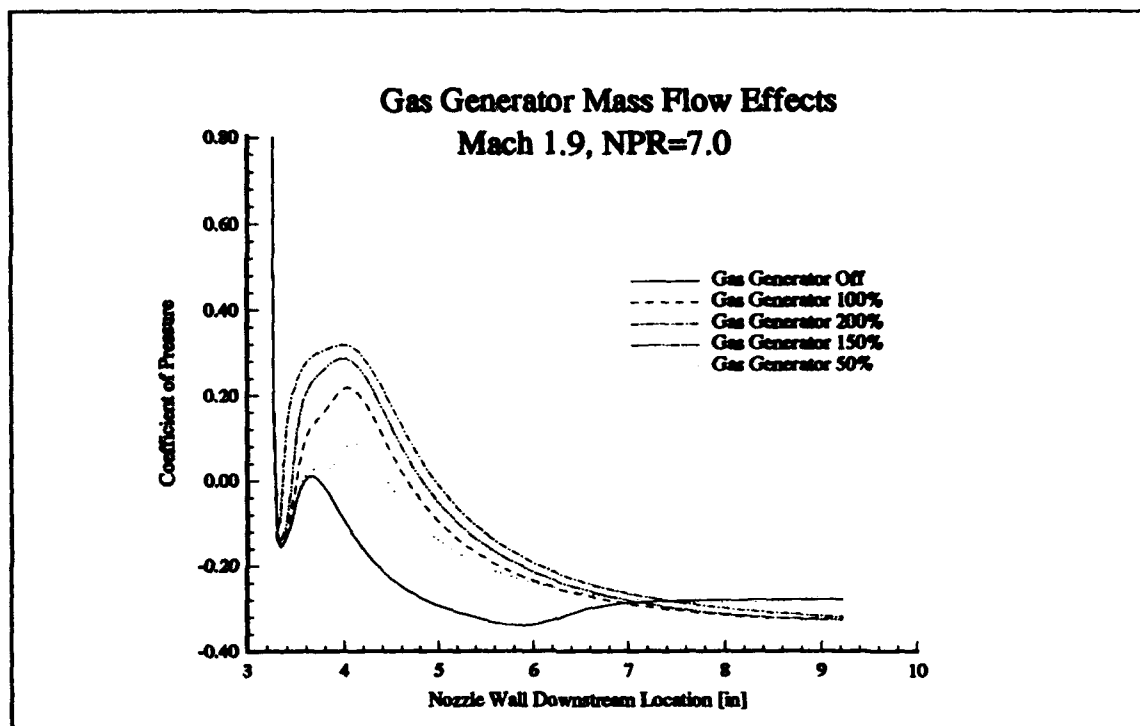


Figure 4-9 Gas Generator Mass Flow Effects, Mach 1.9, NPR=7.0 Nozzle Wall Pressure Distribution, No Gas Generator Deflection

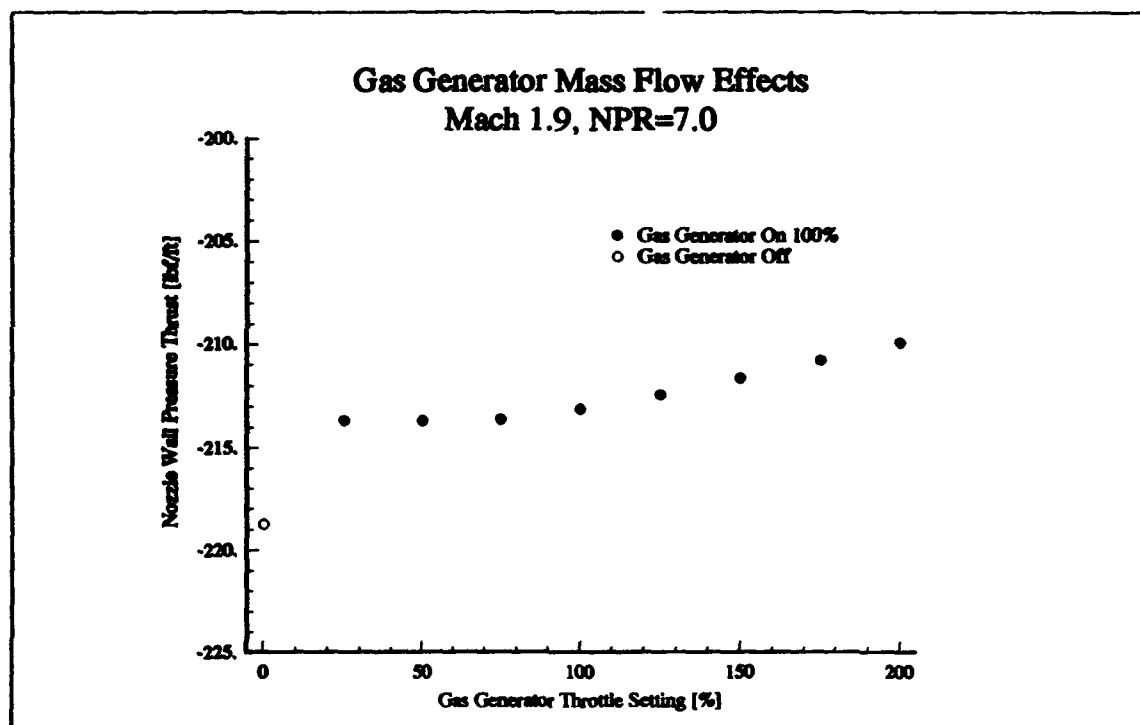


Figure 4-10 Gas Generator Mass Flow Effects, Mach 1.9, NPR=7.0 Nozzle Wall Pressure Thrust, No Gas Generator Deflection

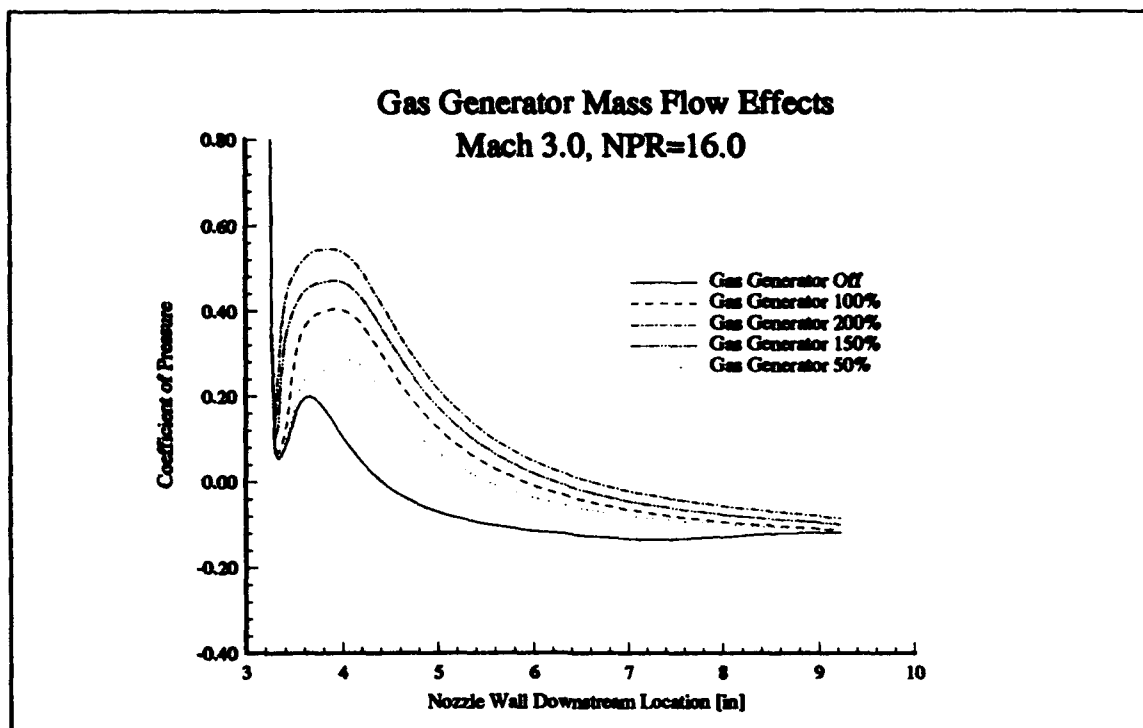


Figure 4-11 Gas Generator Mass Flow Effects, Mach 3.0, NPR=16.0 Nozzle Wall Pressure Distribution, No Gas Generator Deflection

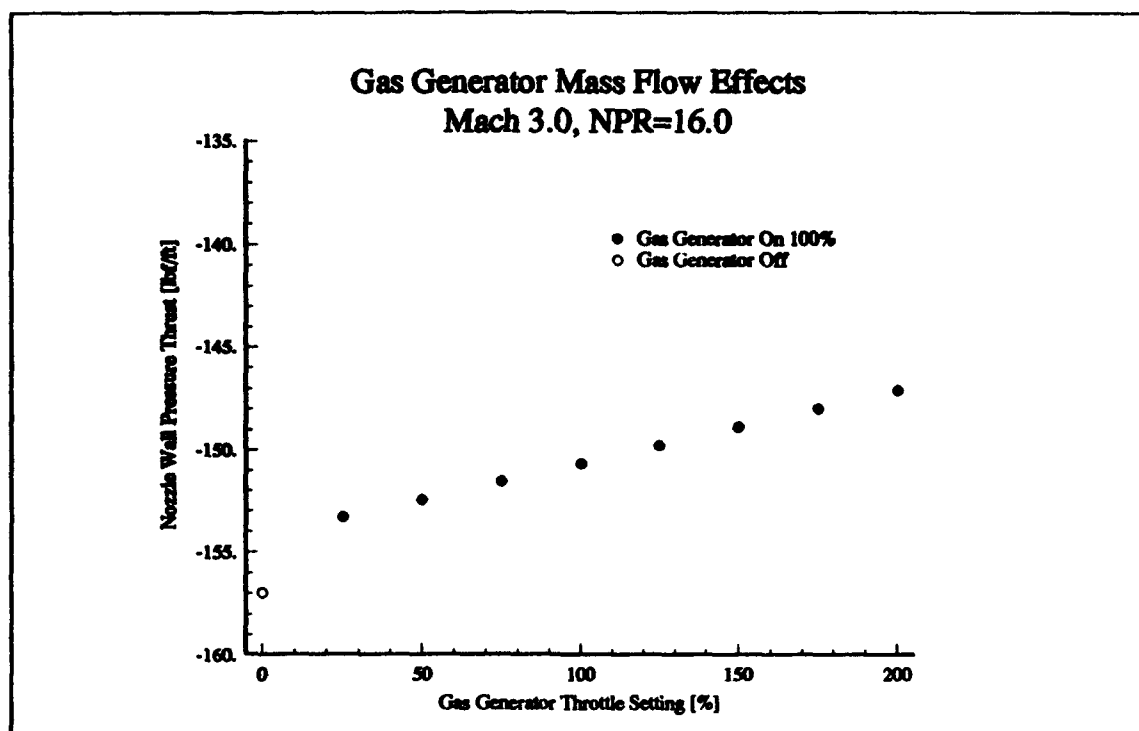


Figure 4-12 Gas Generator Mass Flow Effects, Mach 3.0, NPR=16.0 Nozzle Wall Pressure Thrust, No Gas Generator Deflection

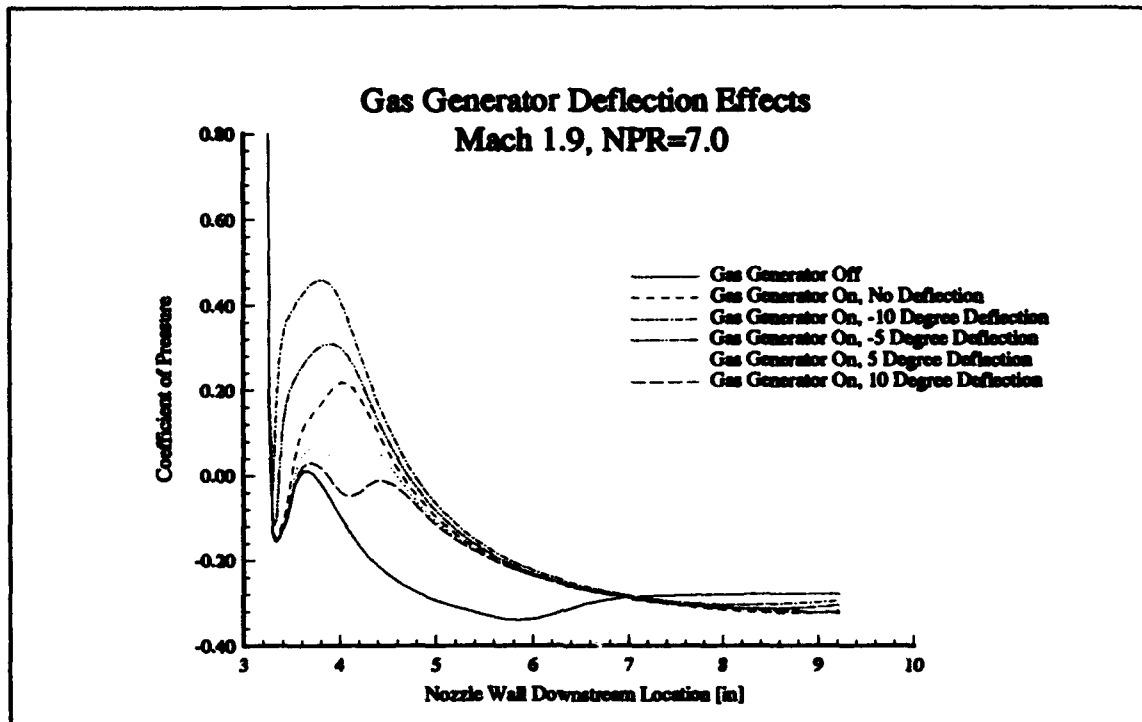


Figure 4-13 Gas Generator Deflection Effects, Mach 1.9, NPR=7.0 Nozzle Wall Pressure Distribution

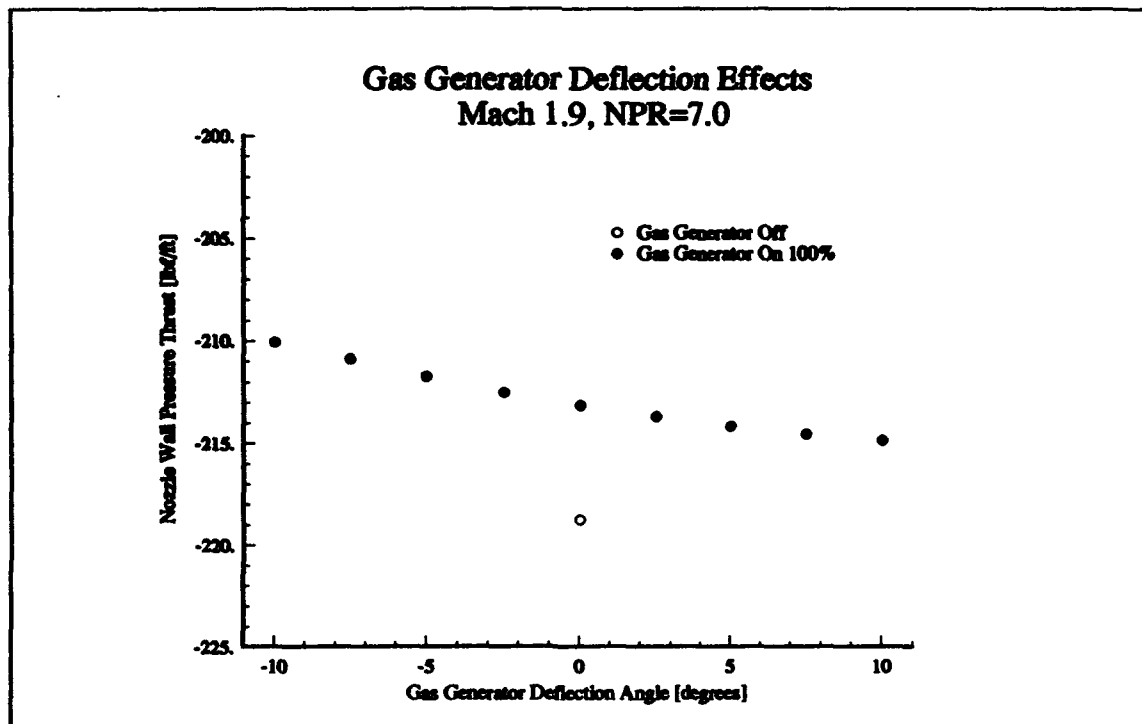


Figure 4-14 Gas Generator Deflection Effects, Mach 1.9, NPR=7.0 Nozzle Wall Pressure Thrust

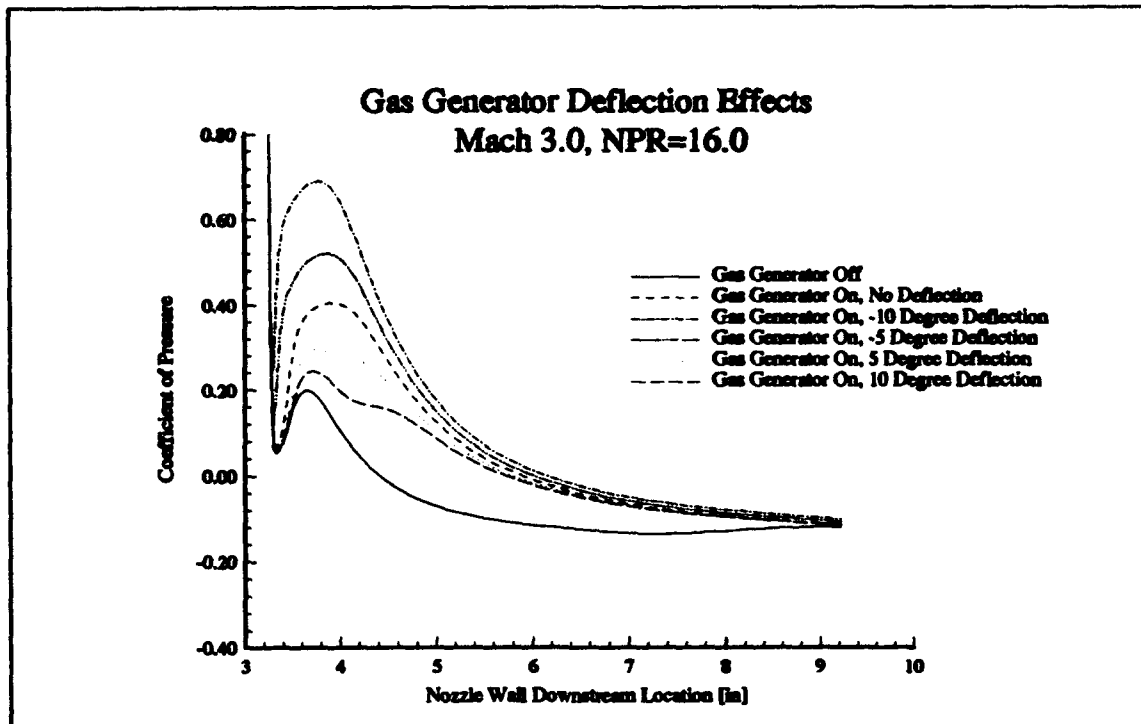


Figure 4-15 Gas Generator Deflection Effects, Mach 3.0, NPR=16.0 Nozzle Wall Pressure Distribution

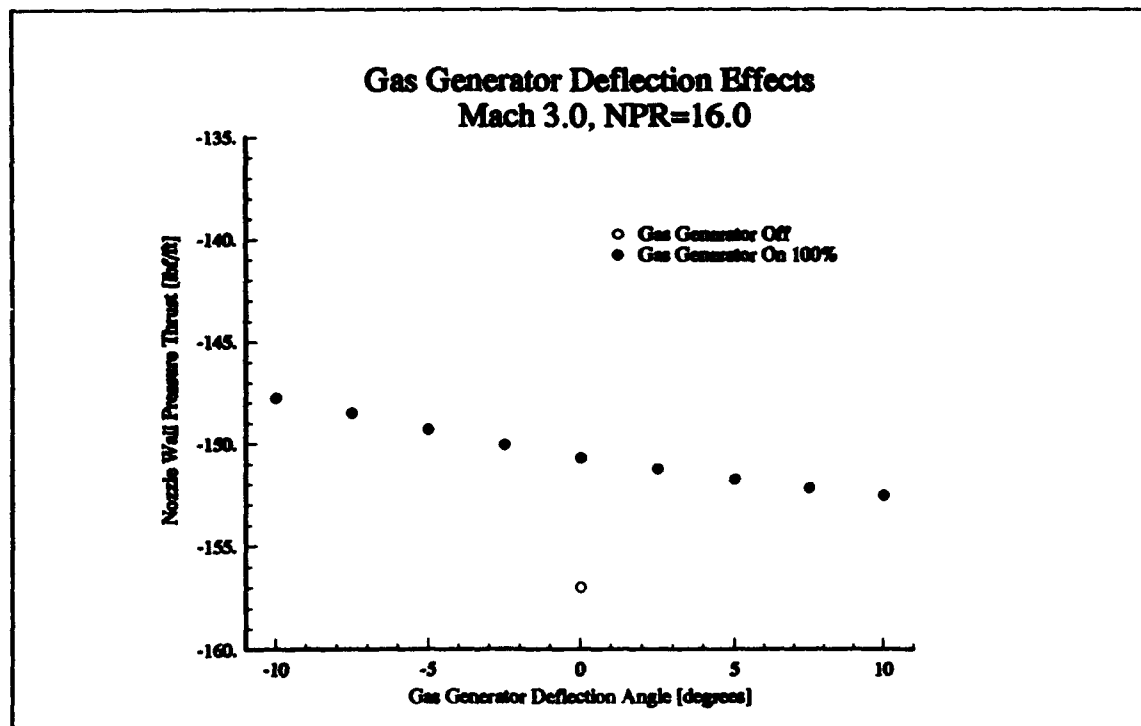


Figure 4-16 Gas Generator Deflection Effects, Mach 3.0, NPR=16.0 Nozzle Wall Pressure Thrust

Experimental Nozzle/Cowl Geometry Effects
Mach 1.9, NPR=7.0

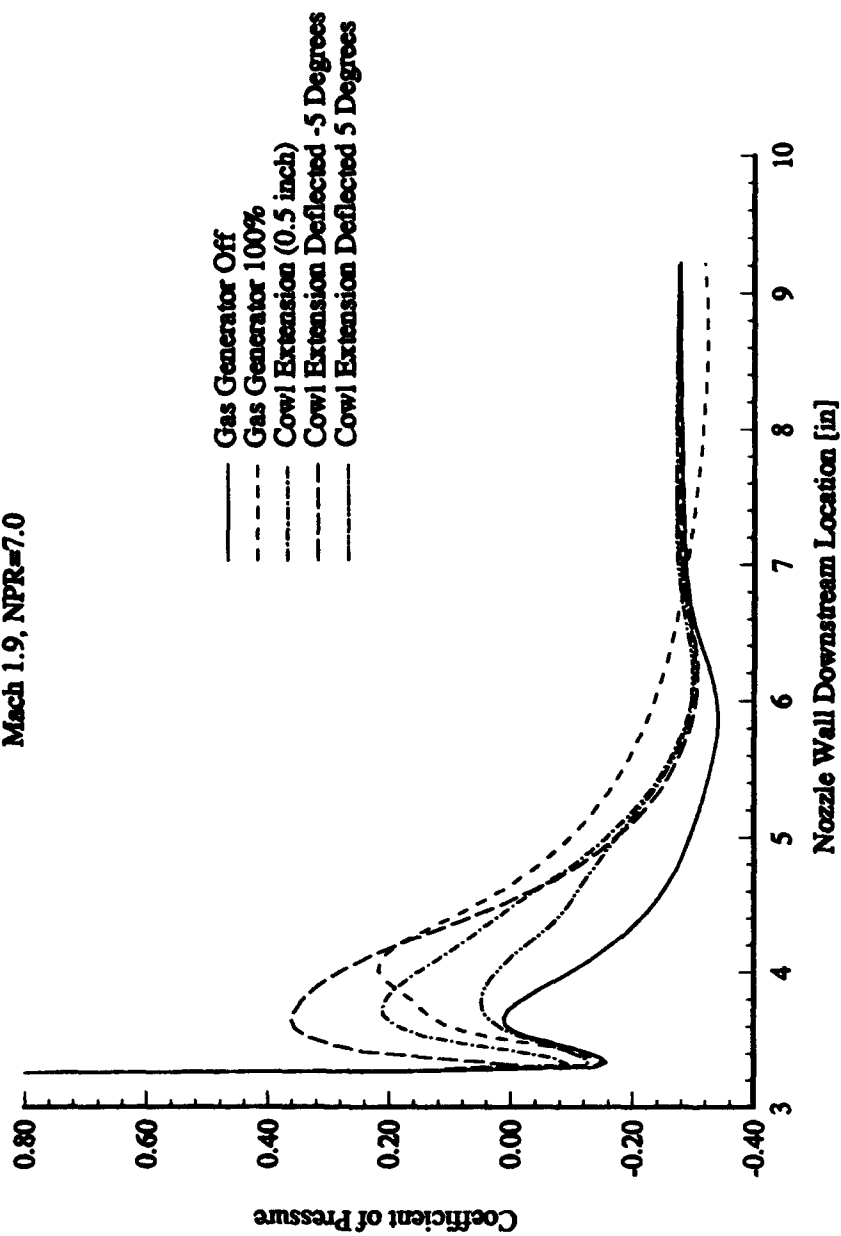


Figure 4-17 Experimental Nozzle/Cowl Geometry Effects, Mach 1.9, NPR=7.0

Experimental Nozzle/Cowl Geometry Effects
Mach 3.0, NPR=16.0

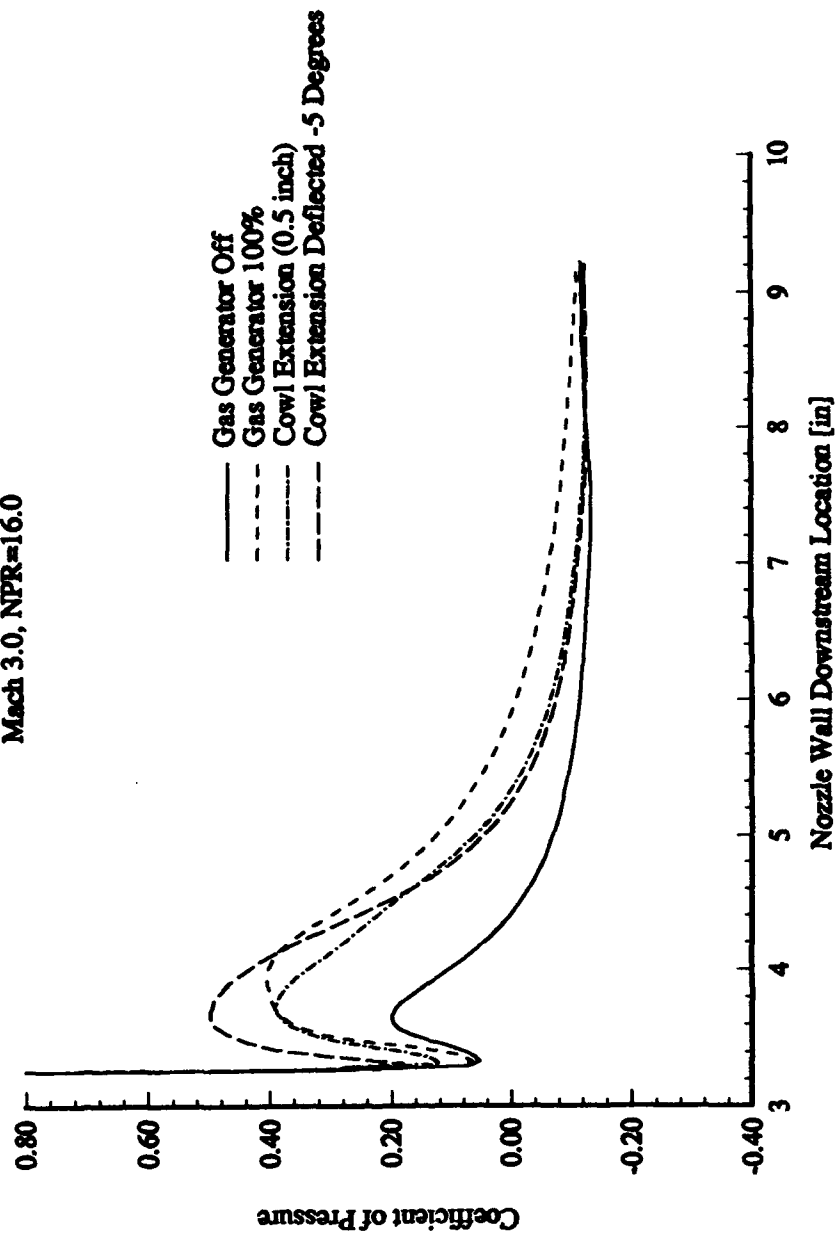


Figure 4-18 Experimental Nozzle/Cowl Geometry Effects, Mach 3.0, NPR=16.0

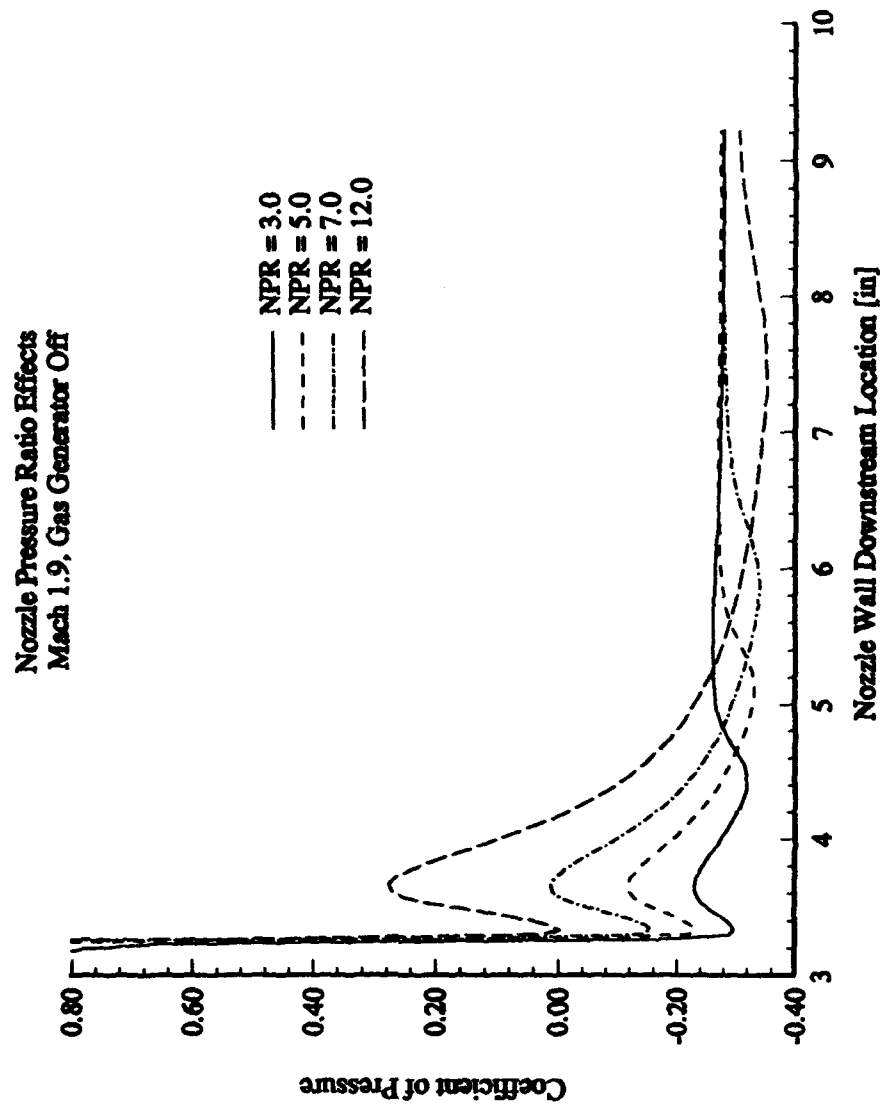


Figure 4-19 Nozzle Pressure Ratio Effects, Mach 1.9, Gas Generator Off

Nozzle Pressure Ratio Effects
Mach 1.9, Gas Generator On 100%

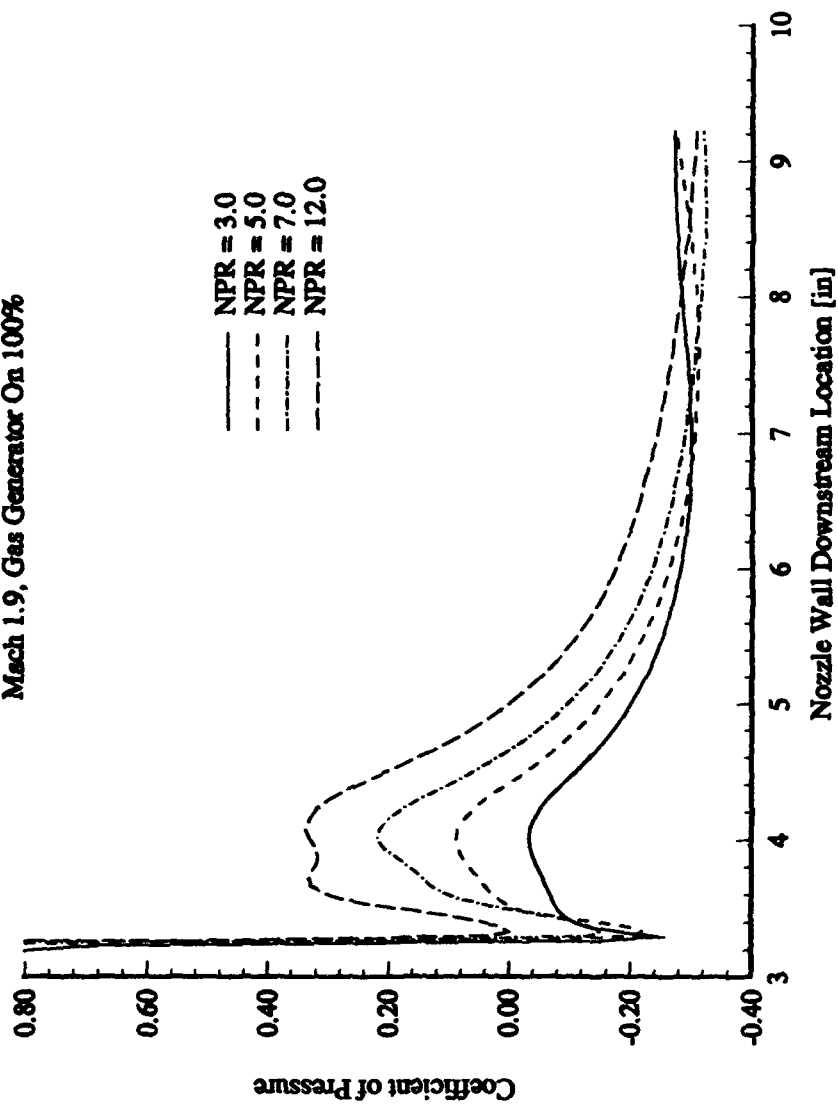


Figure 4-20 Nozzle Pressure Ratio Effects, Mach 1.9, Gas Generator On 100%

Nozzle Pressure Ratio Effects
Mach 3.0, Gas Generator Off

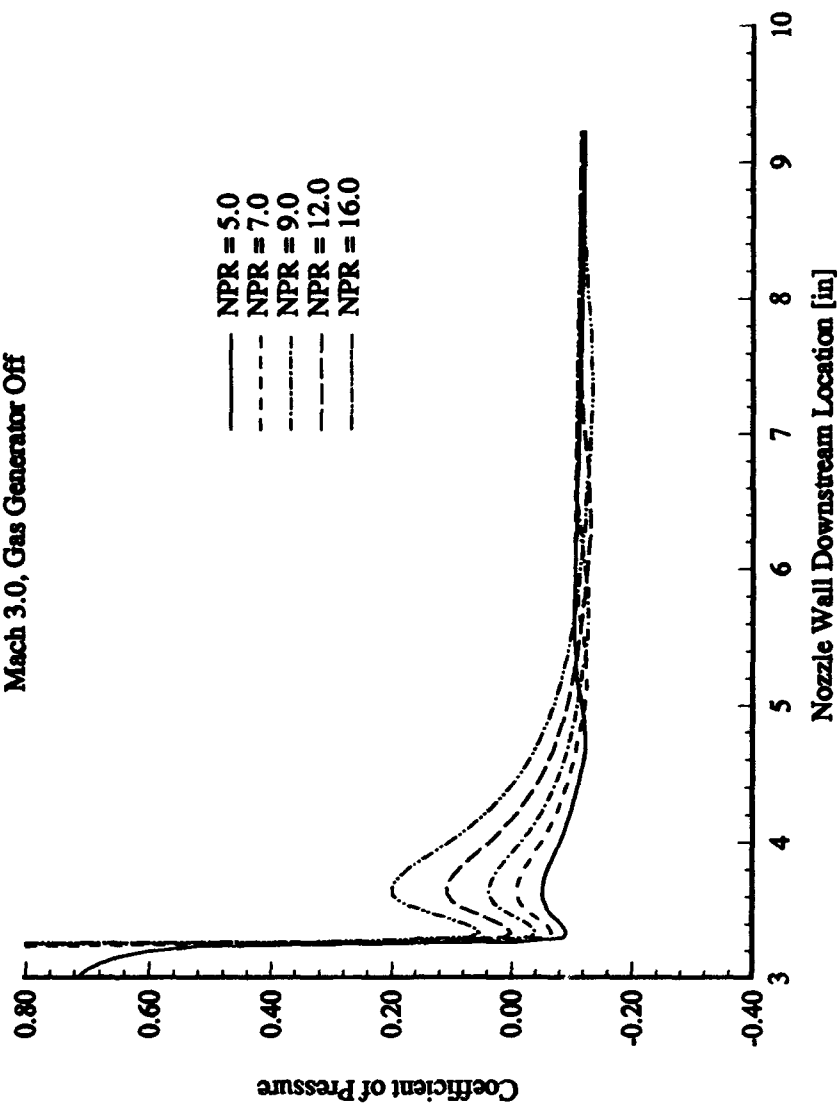


Figure 4-21 Nozzle Pressure Ratio Effects, Mach 3.0, Gas Generator Off

Nozzle Pressure Ratio Effects
Mach 3.0, Gas Generator On 100%

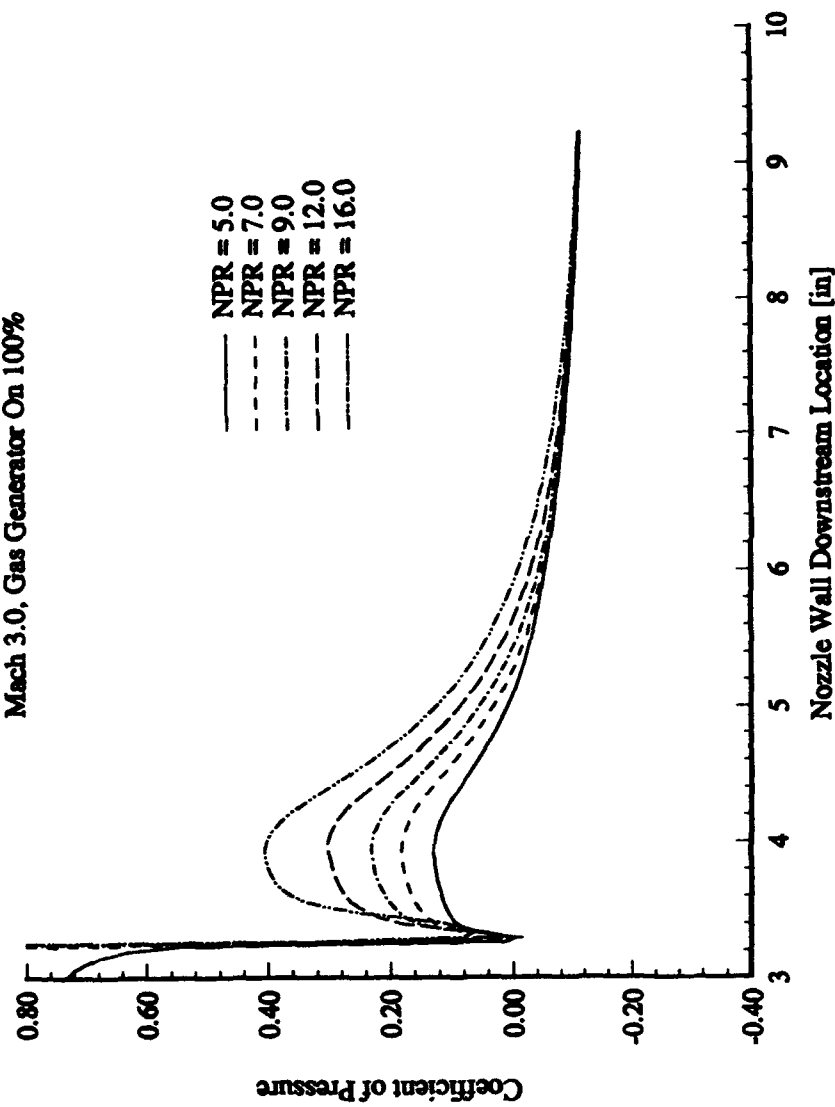


Figure 4-22 Nozzle Pressure Ratio Effects, Mach 3.0, Gas Generator On 100%

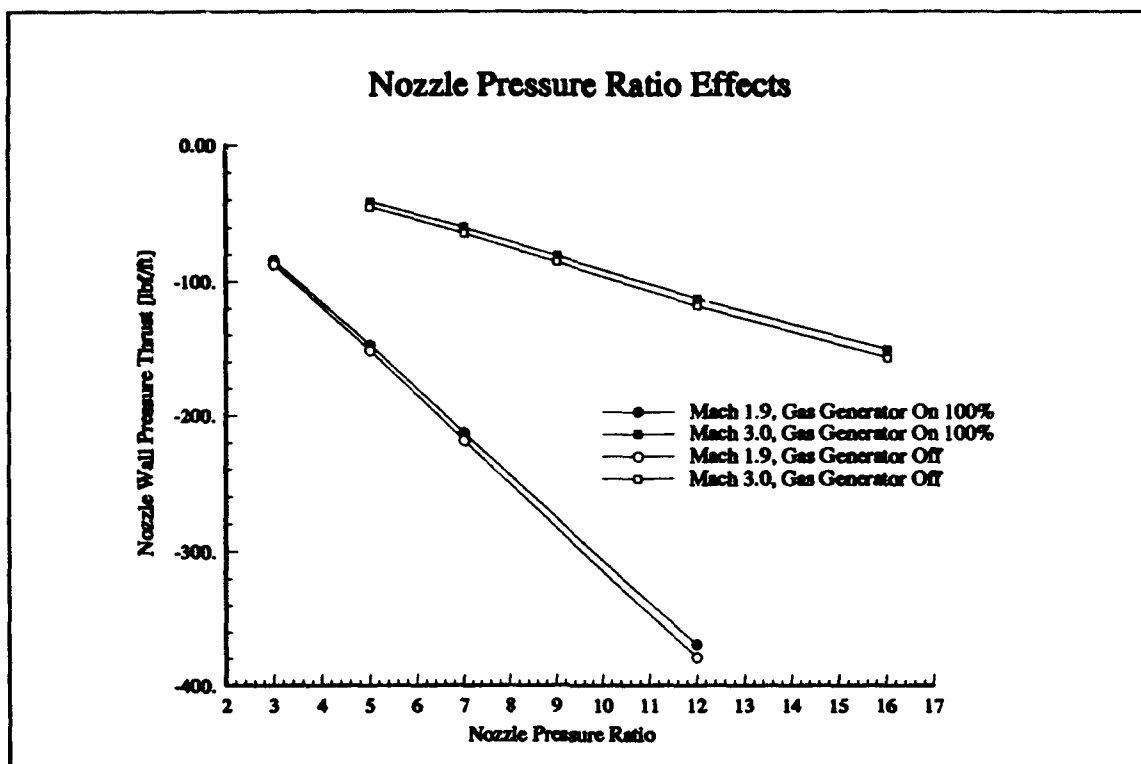


Figure 4-23 Nozzle Pressure Ratio Effects, Nozzle Wall Pressure Thrust

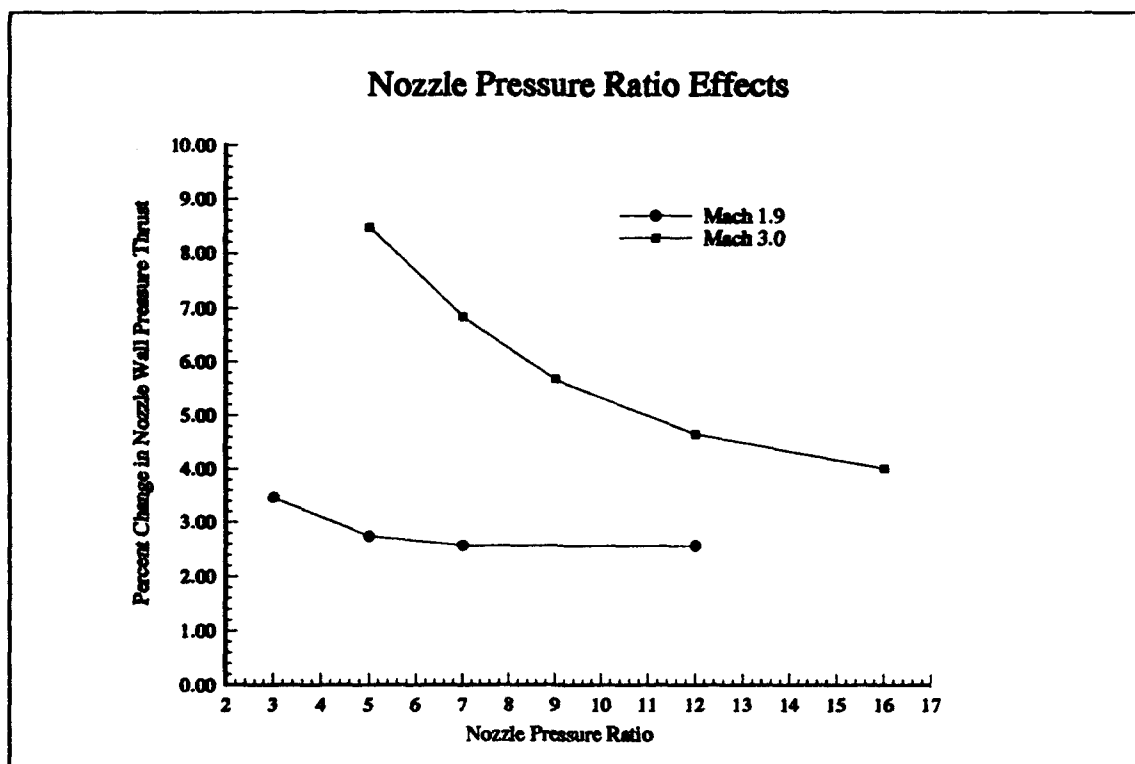


Figure 4-24 Nozzle Pressure Ratio Effects, Percent Change in Thrust

4.3 Application of a Cowl Gas Generator Flow to a Generic Hypersonic Vehicle Configuration Over a Typical On-Design Trajectory

The generic hypersonic nozzle/cowl geometry presented in Figure 1-4 was evaluated with and without the gas generator over a typical trajectory. The gas generator mass flow and deflection angle effects were analyzed at four design trajectory points; Mach 10, 15, 20, and 25.

The baseline nozzle wall pressure distributions for all four trajectory points with the gas generator off are presented in Figure 4-25. For each of these cases, the flow is initially very underexpanded. As the flow exits the combustor, it undergoes a dramatic expansion to nearly ambient conditions. As the trajectory Mach number increases, the initial expansion becomes more severe. For the Mach 20 and 25 trajectory points, the flow initially overexpands past the ambient pressure. All of the flows are characterized by a small but steep recompression immediately following the initial expansion due to a very small initial flow separation just downstream of the throat. The rapid increase in area caused by circular arc transition from the combustor exit to the nozzle wall creates an initial separation region followed by an almost immediate reattachment of the flow just downstream of the combustor exit. This flow separation has a negligible effect on the overall nozzle performance. The majority of the nozzle wall pressure distribution is dominated by the nozzle wall curvature.

At the Mach 10 trajectory point, a very significant recompression takes place along the initial curvature of the nozzle wall. As the trajectory Mach number increases, the magnitude of the recompression associated with the nozzle wall curvature decreases but the length over which the recompression occurs increases.

The location of the peak recompression also moves downstream as the trajectory Mach is increased. This occurs because the combustor exit pressure is relatively high and the combustor exit Mach number is relatively low for the lower speed trajectory points. As the trajectory Mach number increases, the combustor exit Mach number increases and the combustor exit pressure decreases significantly. Therefore, the flow entering this fixed geometry nozzle is already significantly expanded for the high Mach number trajectory points. For these reasons, a strong recompression associated with the high pressure exit conditions is not evident for the high Mach number trajectory points.

For the Mach 25 case the magnitude of the recompression is very small. The Mach 25 trajectory flow exiting the combustor initially overexpands slightly and then immediately recompresses to nearly ambient pressure just downstream of the combustor exit. A relatively weak recompression does eventually occur and it causes an increase in pressure along a fairly large portion of the nozzle wall.

For the Mach 10 trajectory point, the re-expansion past the initial recompression is fairly steep and the flow eventually ends up being slightly overexpanded at the end of the nozzle wall. Although the magnitude of the recompression decreases as the trajectory Mach number increases, the delayed re-expansion causes a slight increase in pressure along the downstream portion of the nozzle wall. The flow even becomes underexpanded at the end of the nozzle wall for the higher Mach number trajectory points.

Appendix C presents the pressure and Mach number contours for this nozzle operating over the four design trajectory points with the gas generator operating at

100% throttle with no deflection and operating with the gas generator off. Figures C-9 and C-10 present the pressure and Mach number contours for the Mach 10 trajectory point with the gas generator off. The dominance of the internal nozzle flow by the tremendous initial expansion can be seen as evidenced by the dramatic decrease in the flowfield pressure just downstream of the combustor exit. In addition, the external plume shocks, the plume flow boundaries, and the internal shocks can be seen. Figures C-11 and C-12 show the same case with the gas generator operating at 100% throttle with no deflection. The slight interaction of the flow structures with the gas generator flow can now be seen as evidenced by the elimination of the internal flow shock attached to the end of the cowl when the gas generator is on. With the gas generator operating at 100%, the internal nozzle pressure distribution decreases slightly due to the elimination of this shock. The nozzle wall pressure does not change in the upstream region near the initial recompression and the nozzle wall pressure actually decreases slightly at the downstream locations.

With the gas generator off, a very strong pressure rise occurs in the region behind the blunt trailing edge of the cowl. The flow initially undergoes a dramatic expansion as it turns around the sharp corners of the blunt cowl. As the internal and external flows meet, they are then turned back downstream through a recompression shock. The recompression shock is evidenced by a region of increased pressure just downstream of the cowl in Figures C-9, C-13, C-17, and C-21 for the Mach 10, 15, 20, and 25 trajectory points respectively. The magnitude of this recompression increases with increased trajectory Mach number. This relatively high pressure affects both sides of the flow just downstream of the cowl. For the external flow, this

increase in pressure results in a strengthening of the external plume shock attached to the external cowl wall. For the internal nozzle flow, this pressure rise propagates downstream and eventually results in a slightly increased nozzle wall pressure.

With the gas generator operating at 100%, the slight changes in the flow profile behind the cowl blunt trailing edge can be seen. For these cases, the gas generator exhaust pressure at the end of the cowl is much lower than the pressure rise associated with the recompression shock for the gas generator off cases. The decrease in pressure results in a weaker external flow plume shock and an elimination of the internal flow shock near the end of the cowl. This is evidenced by a relative decrease in pressure just downstream of the cowl in Figure C-11, C-15, C-19, and C-23 for the Mach 10, 15, 20, and 25 trajectory points respectively. This relative decrease in internal pressure shows up as a slight decrease in the downstream nozzle wall pressure.

An appreciation of the magnitude of these gas generator effects can be gained by investigating the flow profile just downstream of the gas generator. Figures 4-26 through 4-29 present the pressure distribution at a constant axial location, indicated by index "I", just downstream of the cowl blunt edge for the Mach 10, 15, 20, and 25 trajectory points respectively. A constant I location of 52, corresponding to an approximate downstream location of 10.19 inches, was used to generate these profiles. Note that the cowl edge falls between $h=1.0$ inch and $h=1.25$ inches. The internal nozzle flow is the region $h<1.0$ inch and the external plume/freestream flow is the region $h>1.25$ inches. For reference, note that the nozzle wall is located at $h=-3.903$

inches. For all of these flow cases, the internal nozzle flow has already undergone a significant initial expansion.

For the higher Mach 20 and 25 trajectory points, the internal nozzle flow is highly expanded across the entire nozzle at this location. For the lower Mach 10 and 15 trajectory points, the flow is still highly expanded but the flow along the nozzle wall is dominated by the nozzle wall curvature recompression. The internal nozzle flow along the upper cowl wall remains expanded despite the large pressure recovery along the nozzle wall.

With the gas generator off, the region just downstream of the cowl wall experiences a sharp rise in pressure. The pressure behind the blunt wall is actually higher than the gas generator exhaust pressure for all four trajectory points. As would be expected, the magnitude of this pressure rise increases significantly with the increase in operating Mach number. The internal flow recompression shock shows up as a large spike near the inner lip of the cowl at approximately 1.0 inches. The weaker external flow recompression shock shows up as a smaller spike near the outer edge of the cowl. Figures 4-26 through 4-29 show that the magnitude of these recompressions increase with increasing trajectory Mach number.

With the gas generator on, the internal flow expansion along the cowl wall results in a pressure that is almost identical to the gas generator exhaust pressure for the Mach 10 trajectory point. As the operating Mach is increased, the internal nozzle pressure along the cowl wall increases. For the higher Mach 15, 20, and 25 trajectory points, the gas generator exhaust pressure is actually lower than the internal nozzle pressure and the internal nozzle flow expands out into this region. The increased

expansion from the internal nozzle flow to the external nozzle flow shows up as a slight decrease in nozzle wall pressure as the effects propagate downstream.

4.3.1 Gas Generator Mass Flow Effects. Figure 4-30 shows the effects of the gas generator on the nozzle wall pressure recovery for the Mach 10 trajectory point. The change in pressure distribution associated with the gas generator is relatively small. The net effects are limited to small pressure changes at the downstream locations with virtually no change in pressure along the first 25 percent of the nozzle wall. For a fixed gas generator geometry, the gas generator exhaust pressure increases with increased throttle setting. The gas generator exit pressure is high enough to cause an increase in downstream nozzle wall pressure relative to the gas generator off case only when the gas generator is operating at the 150% and 200% throttle settings.

Figure 4-31 shows the magnitude of integrated pressure contribution to thrust along the nozzle wall. The nozzle performance increases slightly with increasing mass flow due to the downstream propagation of the higher gas generator exhaust pressure. The overall performance is only better than the baseline gas generator off performance for the highest throttle settings.

Figures 4-32, 4-34, and 4-36 show the gas generator mass flow effects on nozzle wall pressure distribution for the higher Mach number trajectory points. Similarly, Figures 4-33, 4-35, and 4-37 show the effects of gas generator mass flow changes on the integrated nozzle wall pressure contribution to thrust for the higher Mach 15, 20, and 25 trajectory points respectively. The overall trends associated with the gas generator are the same for each case; as the gas generator mass flow is

increased, the nozzle wall pressure recovery and subsequent performance increases slightly. Since the nozzle internal pressure along the cowl wall increases with trajectory Mach number, and the gas generator exit pressure is fixed for a given throttle setting, the gas generator contribution to nozzle wall performance decreases with increasing trajectory Mach number.

4.3.2 Gas Generator Deflection Angle Effects. Figure 4-38 shows the effects of deflecting the gas generator for the Mach 10 trajectory point. Deflecting the gas generator towards the nozzle wall causes a fairly significant increase in pressure, especially at the very large deflection angles. A 20 degree deflection towards the wall actually causes a small second separation bubble to form. This is caused by the impingement of the shock generated by the interaction of the internal nozzle flow with the sharp inward deflection of the gas generator flow. The effect of deflecting the gas generator away from the wall is very small and the net effect moves further downstream.

Figure 4-39 shows the magnitude of integrated pressure contribution to thrust along the nozzle wall. The nozzle performance increases significantly with deflections towards the wall due to the development of the small downstream separation bubble. As the gas generator is deflected away from the wall, only a small additional penalty is paid for the increased expansion near the end of the cowl.

Figures 4-40, 4-42, and 4-44 show the gas generator deflection effects on nozzle wall pressure distribution for the higher Mach number trajectory points. Similarly, Figures 4-41, 4-43, and 4-45 show the effect of gas generator deflections on

the integrated nozzle wall pressure contribution to thrust for the higher Mach 15, 20, and 25 trajectory points respectively. The overall trends associated with the gas generator deflections are the similar for each case. For the same reasons discussed above, the overall gas generator contribution to nozzle wall performance decreases with increasing trajectory Mach number.

4.3.3 Trajectory Performance Analysis. The trends discussed in previous sections need to be put into perspective. This section presents the nozzle wall pressure contributions to thrust and lift relative to the net forces acting on the generic nozzle/cowl afterbody. The nozzle wall pressure contribution to thrust and lift were calculated using Equations 2-44 and 2-45.

Figure 4-46 presents the gas generator mass flow effects and Figure 4-47 presents the gas generator deflection angle effects in terms of the percent change in the pressure contribution to the nozzle wall lift. Except for the high mass flow conditions and the large inward deflection angle cases, the gas generator results in a fairly significant decrease in the overall nozzle wall pressure contribution to lift. The overall trends are the same as discussed in the previous two sections.

The gas generator also has a direct force contribution to lift when it is deflected. This contribution must be accounted for to assess the net effect of gas generator deflections on the complete nozzle/cowl afterbody lift. Figure 4-48 shows the percent change in net lift due to both the nozzle wall pressure contribution and the direct gas generator deflection contribution to lift. Although gas generator deflections towards the wall increase the nozzle wall pressure contribution to lift, the deflections

towards the wall impart a direct thrust contribution opposing lift. The decrease in lift due to the deflected thrust component more than cancel out the increased nozzle wall pressure lift. The net lift forces increase dramatically with deflections away from the wall because the direct lift term associated with the gas generator deflection is not opposed by a very significant decrease in nozzle wall pressure lift.

Figure 4-49 presents the gas generator mass flow effects with no gas generator deflection in terms of the percent changes that the nozzle wall pressure contributions have on the net nozzle/cowl afterbody thrust. The overall magnitude of the gas generator effects on the nozzle wall pressure thrust are very small compared to the total thrust. For the worst case Mach 25 trajectory point, the net decrease in thrust is less than 0.19 percent of the total thrust.

Figure 4-50 presents the gas generator mass flow effects with no gas generator deflection in terms of percent increase in net thrust due to both the nozzle wall pressure contribution and the direct gas generator contributions to thrust. The effect of the gas generator direct thrust contribution to total thrust is nearly 2 orders of magnitude greater than the nozzle wall pressure change contributions to total thrust.

Figure 4-51 presents the gas generator deflection effects with the gas generator operating at 100% throttle in terms of the percent changes that the nozzle wall pressure contributions have on the net nozzle/cowl afterbody thrust. Again, for the best case Mach 10 trajectory point, the net increase in thrust is less than 0.26 percent of the total thrust.

Figure 4-52 presents the gas generator deflection effects with the gas generator operating at 100% throttle in terms of percent increase in net thrust due to both the

nozzle wall pressure contribution and the direct gas generator contributions to thrust. Again, the effect of the gas generator direct thrust contribution significantly dominates the nozzle wall pressure change contributions to total thrust. Obviously, the direct gas generator contribution to thrust decreases with deflections in either direction. The direct gas generator thrust more than compensates for any relative losses or gains associated with the pressure changes on the nozzle wall.

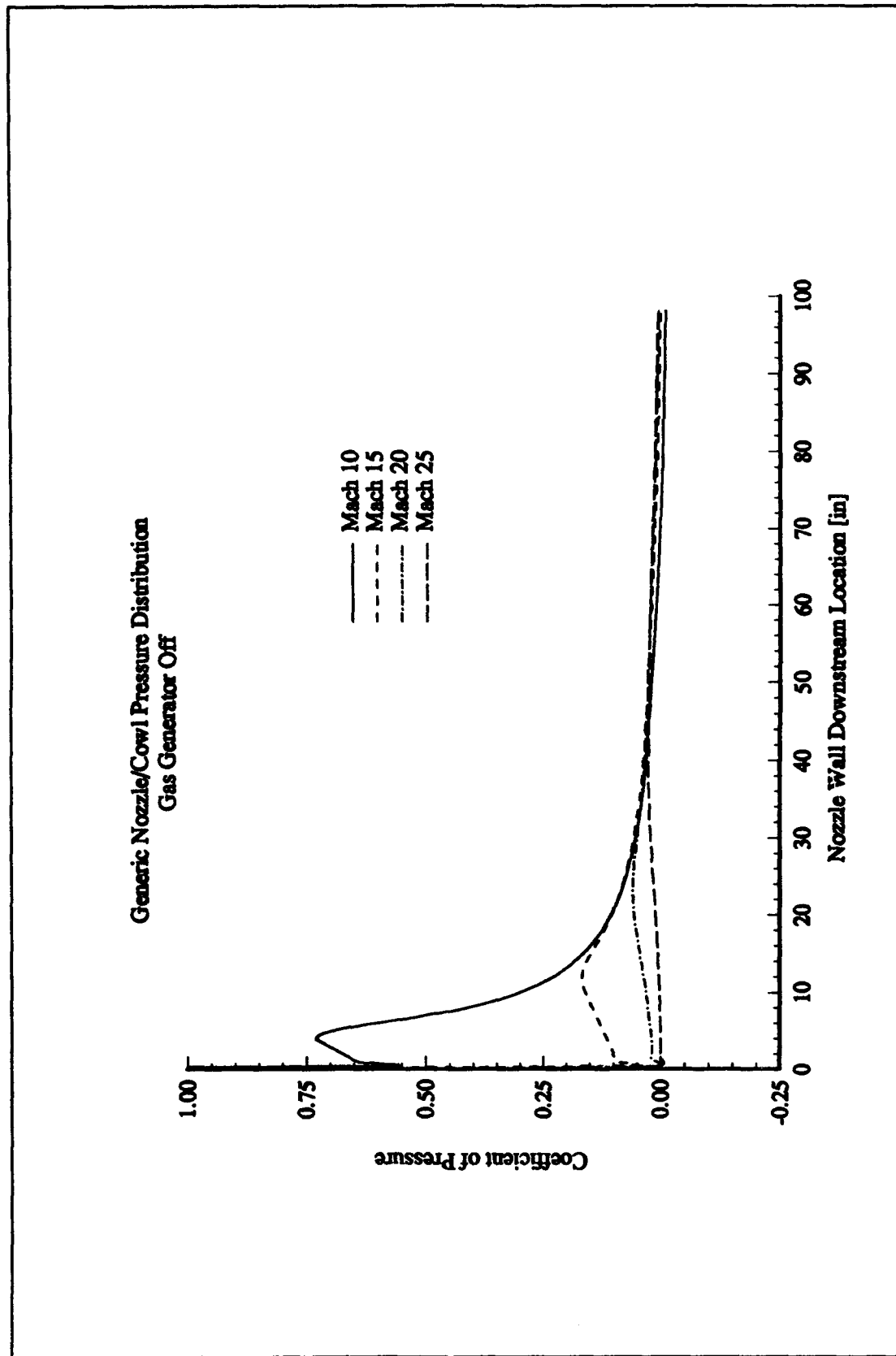


Figure 4-25 Generic Nozzle/Cowl Pressure Distribution, Gas Generator Off

Constant Axial Location Flow Profile
Mach 10.0, I=52

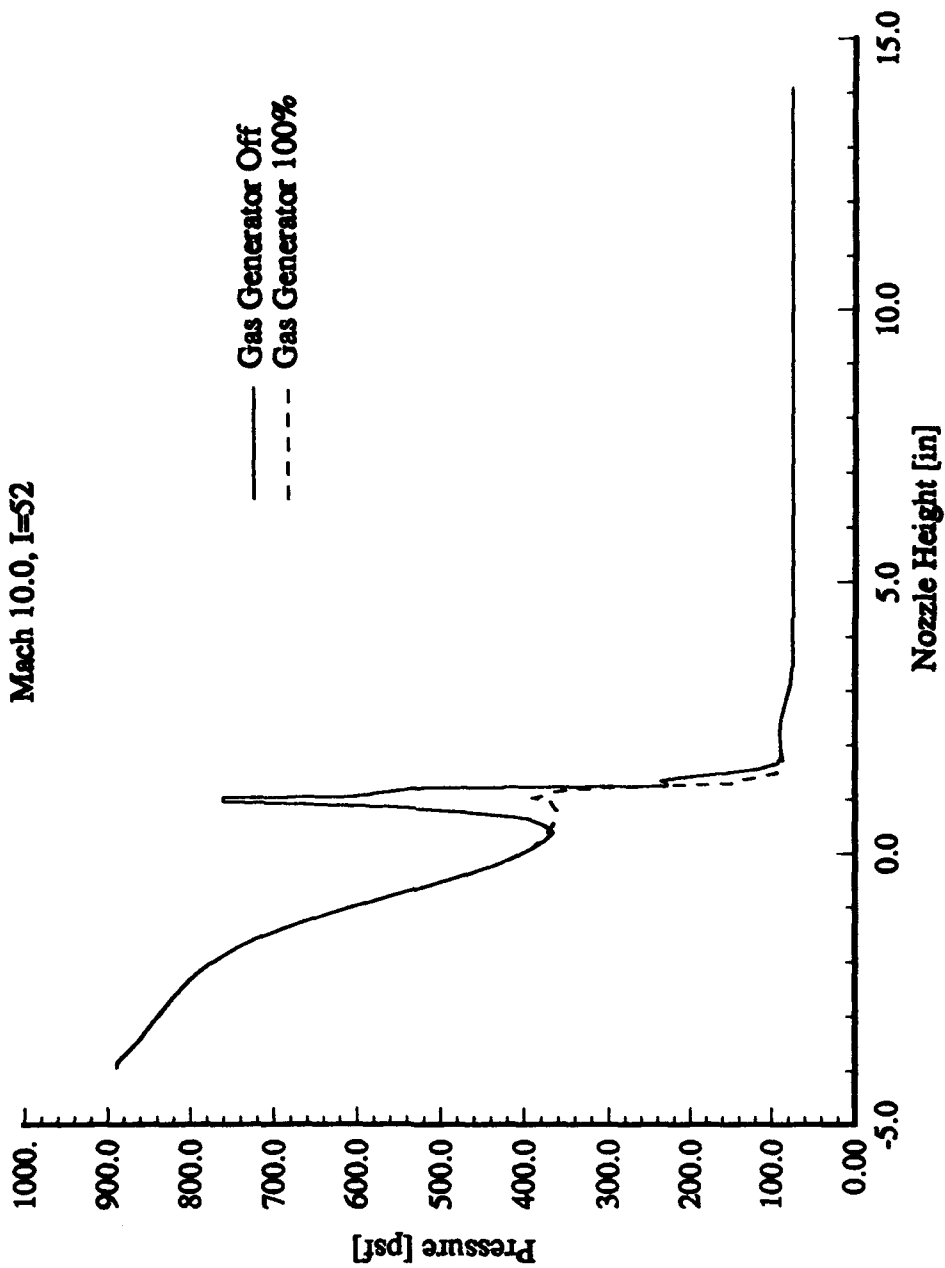


Figure 4-26 Constant Axial Location Flow Profile, Mach 10.0, I=52

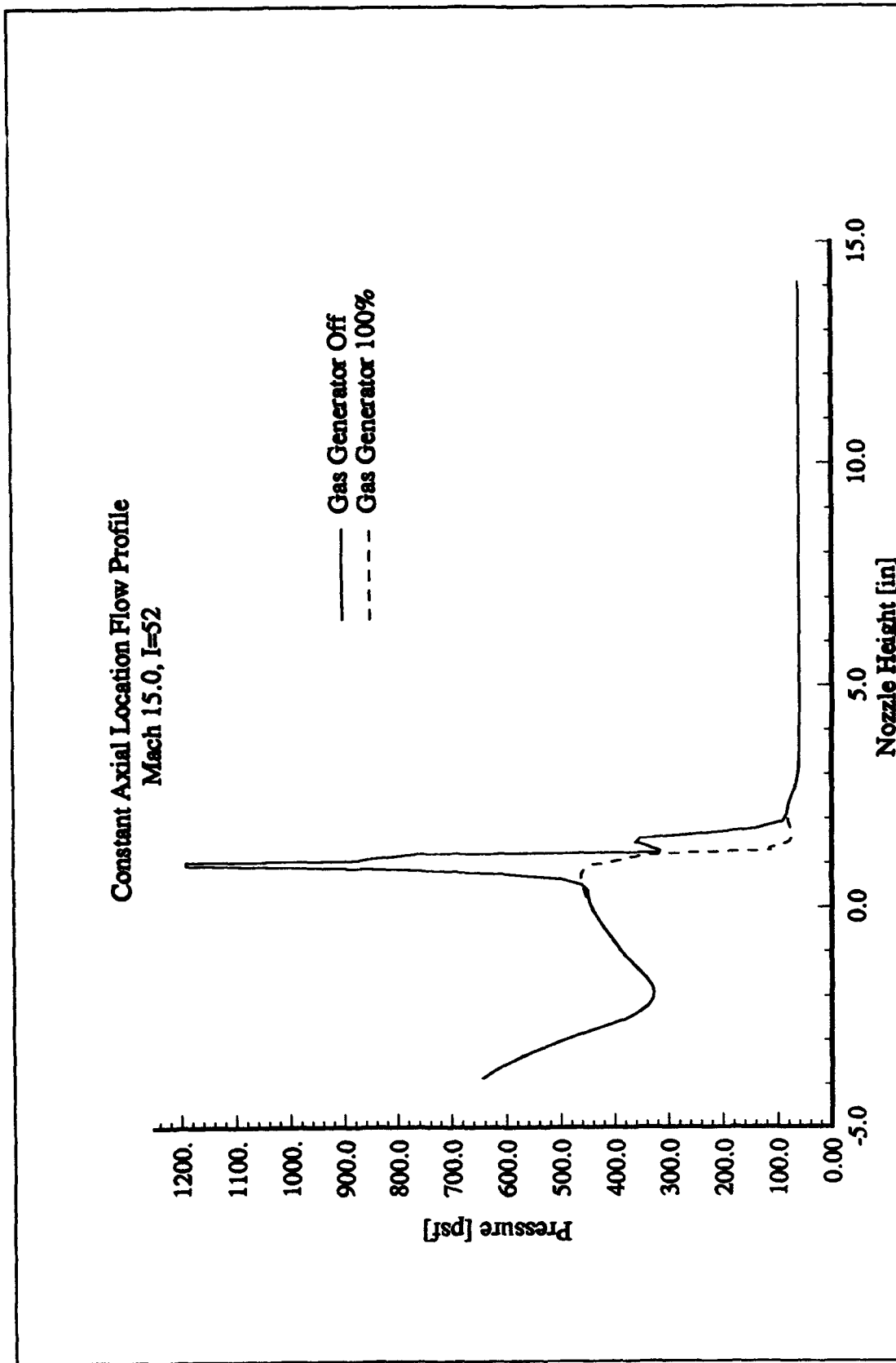


Figure 4-27 Constant Axial Location Flow Profile, Mach 15.0, I=52

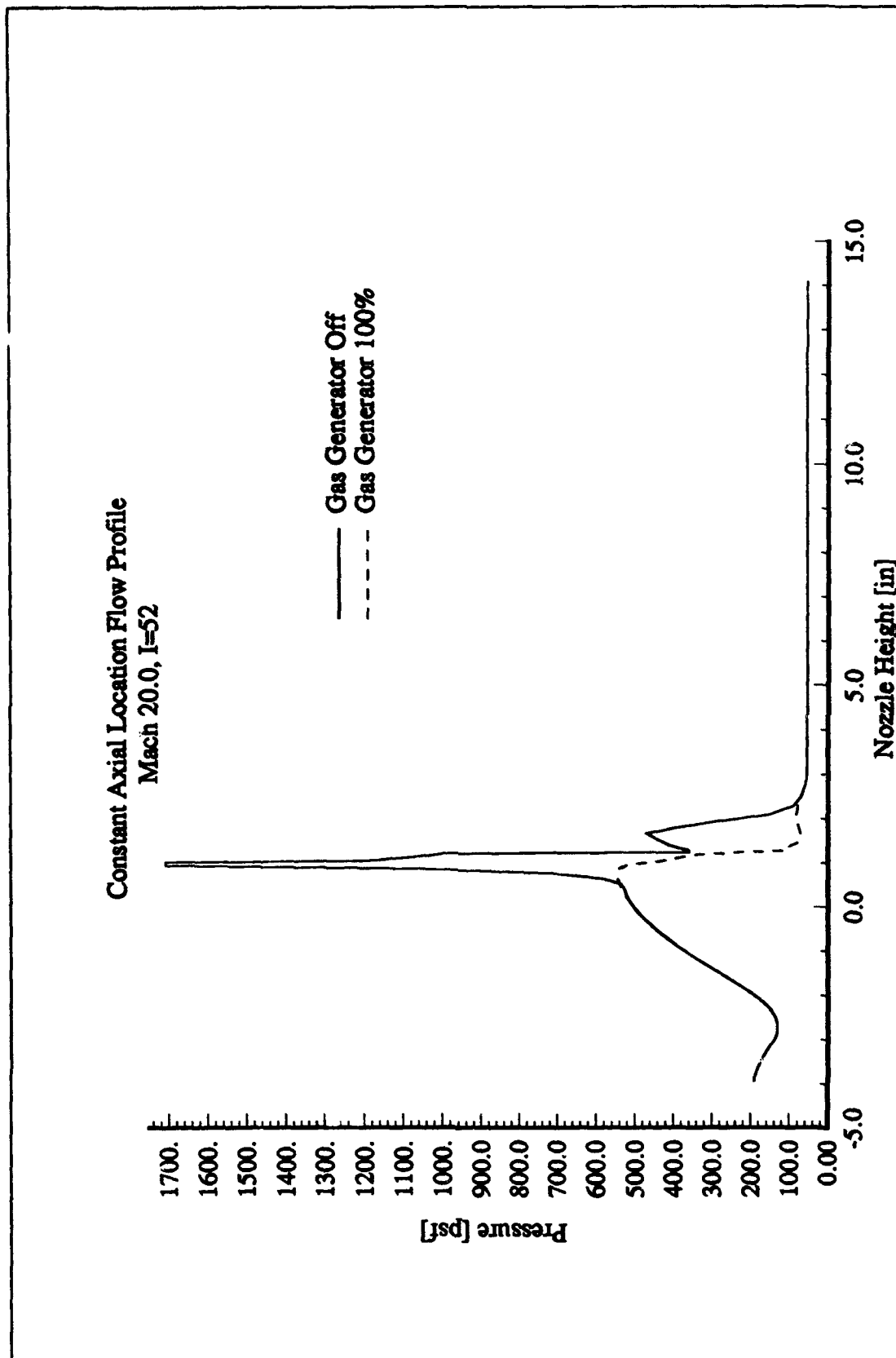


Figure 4-28 Constant Axial Location Flow Profile, Mach 20.0, I=52

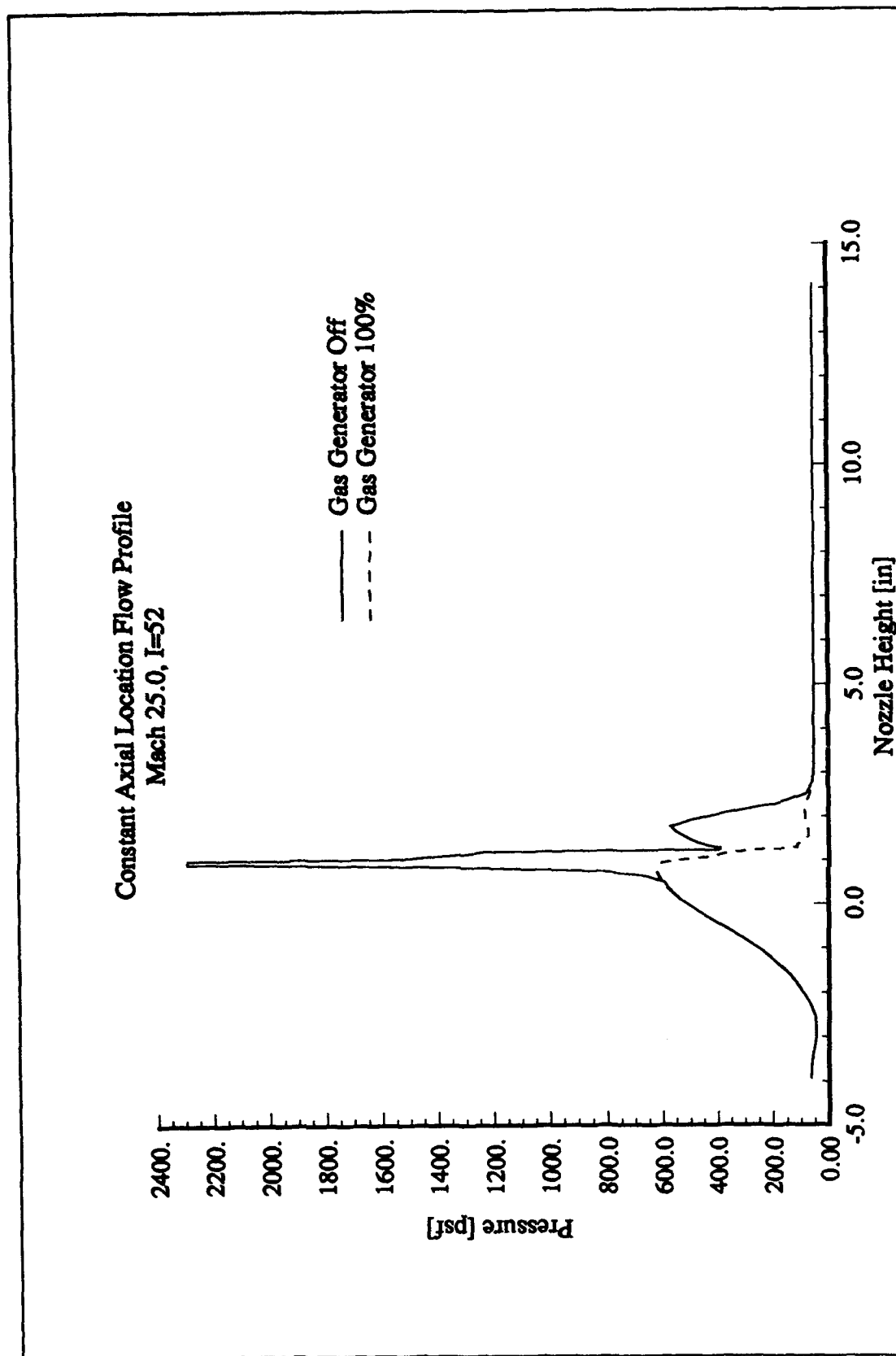


Figure 4-29 Constant Axial Location Flow Profile, Mach 25.0, I=52

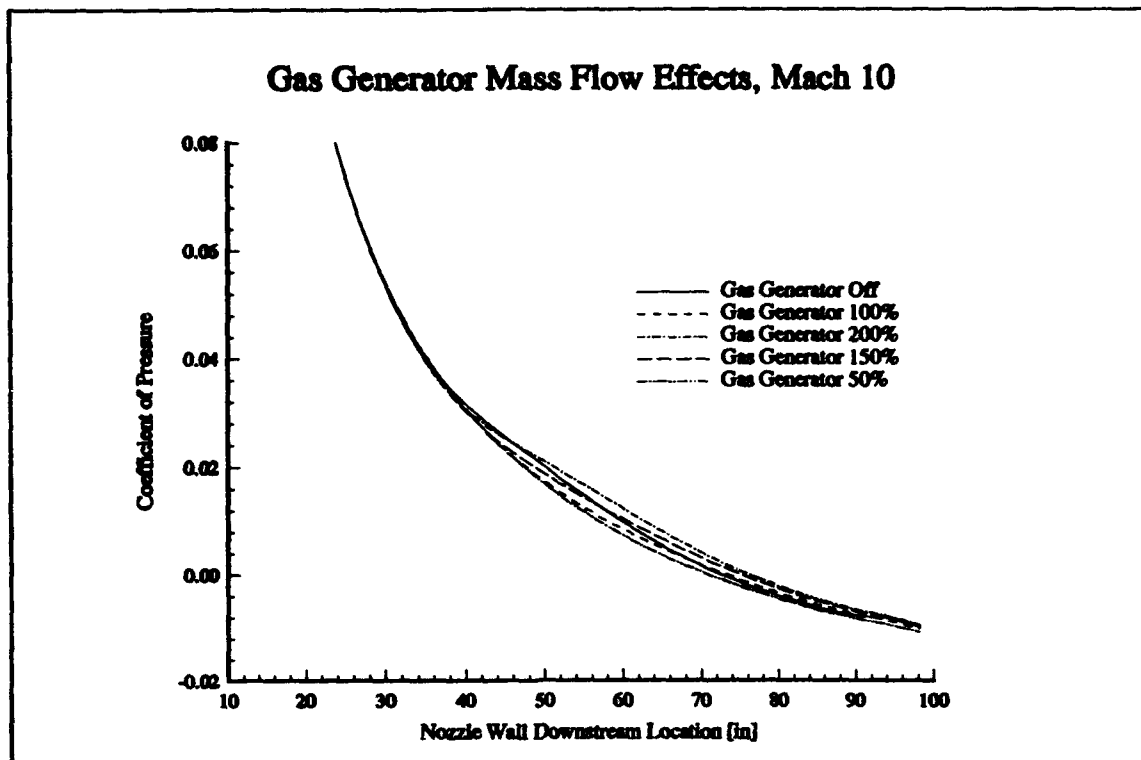


Figure 4-30 Gas Generator Mass Flow Effects, Mach 10 Nozzle Wall Pressure Distribution, No Gas Generator Deflection

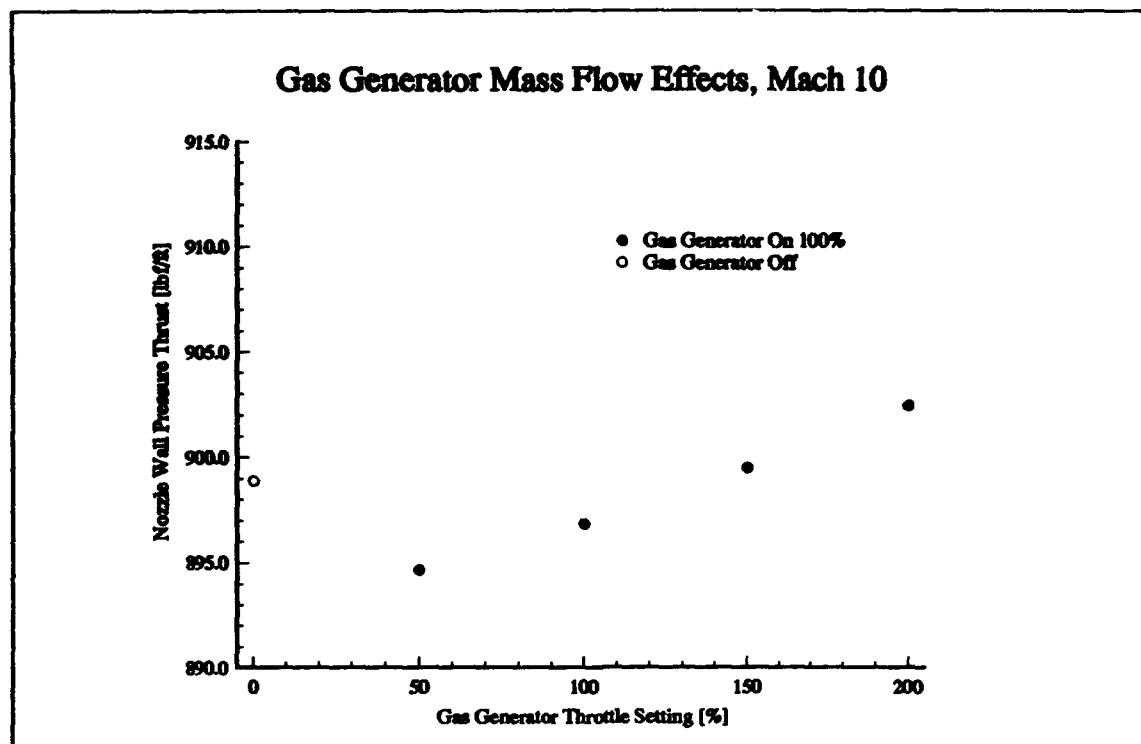


Figure 4-31 Gas Generator Mass Flow Effects, Mach 10 Nozzle Wall Pressure Thrust, No Gas Generator Deflection

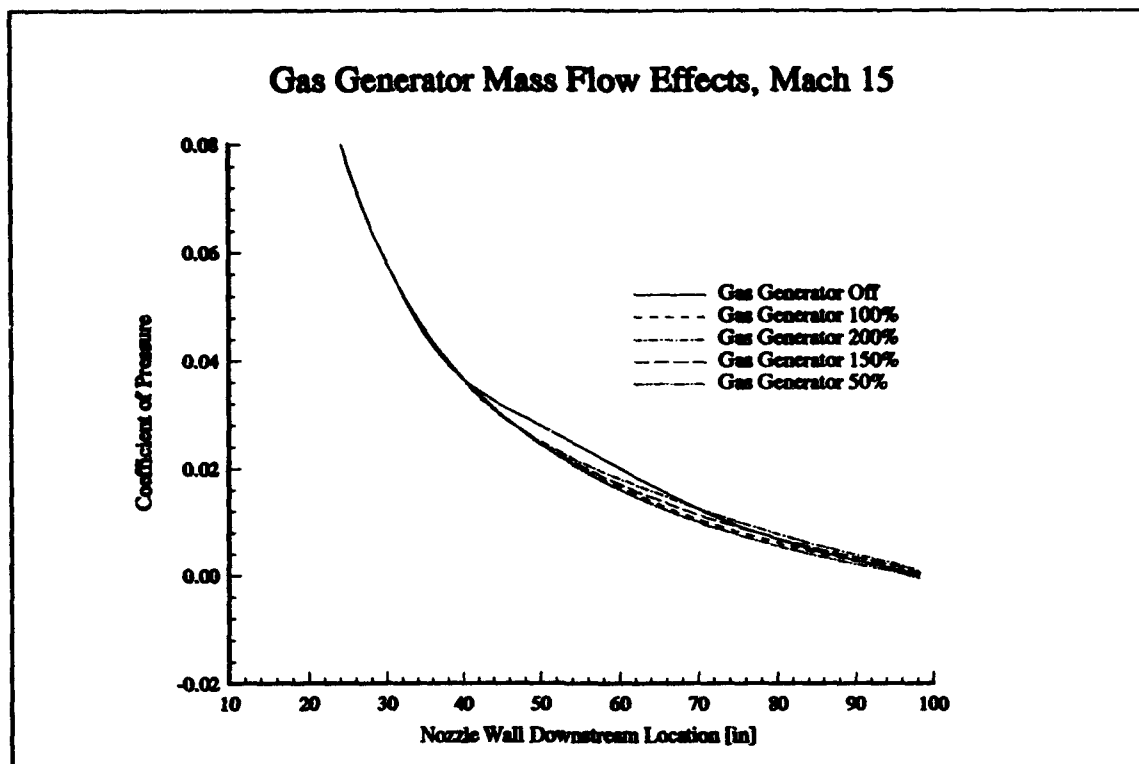


Figure 4-32 Gas Generator Mass Flow Effects, Mach 15 Nozzle Wall Pressure Distribution, No Gas Generator Deflection

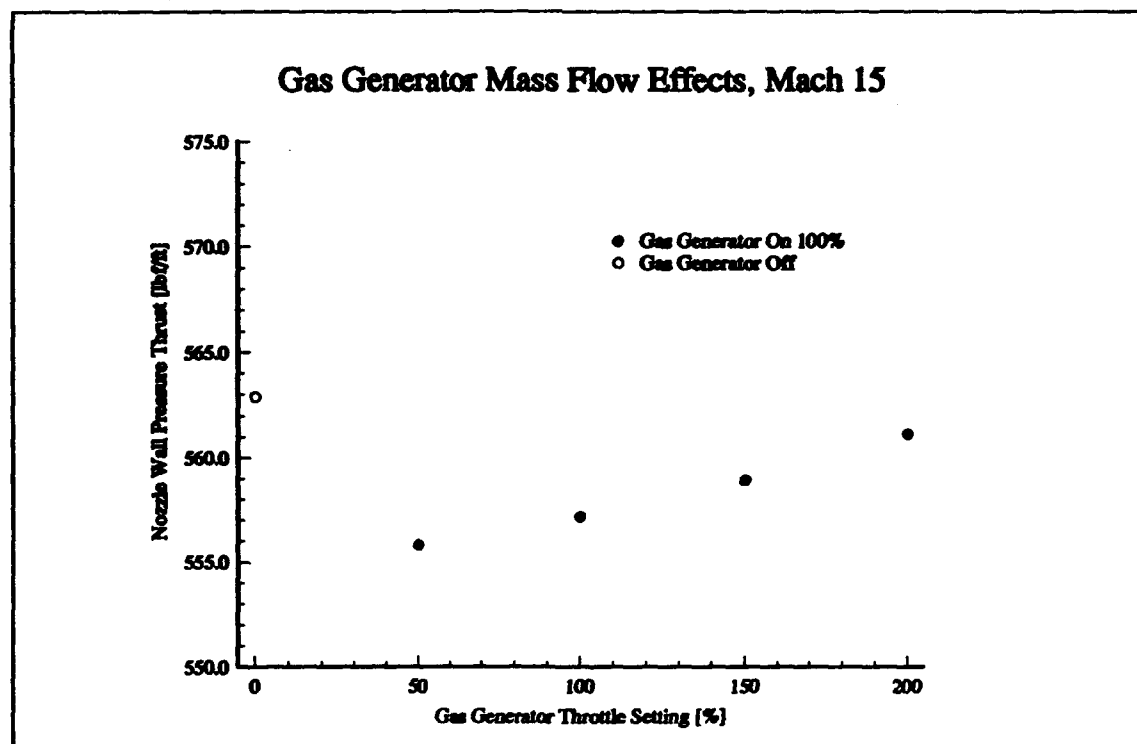


Figure 4-33 Gas Generator Mass Flow Effects, Mach 15 Nozzle Wall Pressure Thrust, No Gas Generator Deflection

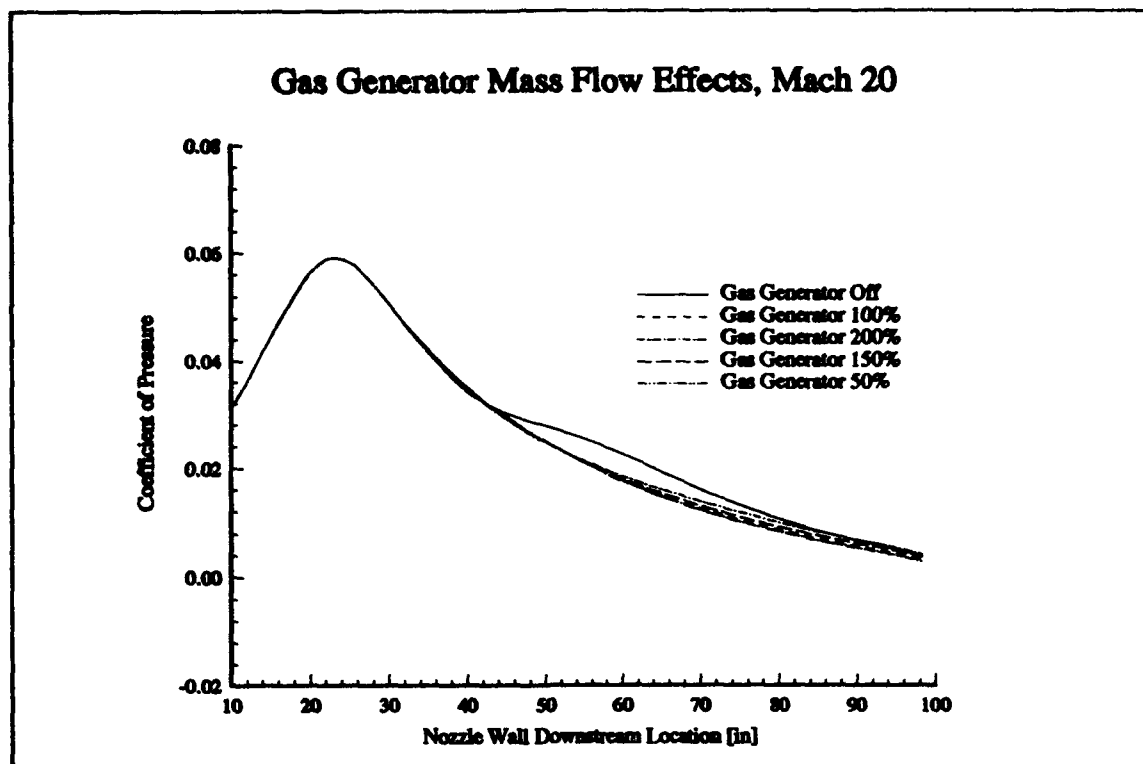


Figure 4-34 Gas Generator Mass Flow Effects, Mach 20 Nozzle Wall Pressure Distribution, No Gas Generator Deflection

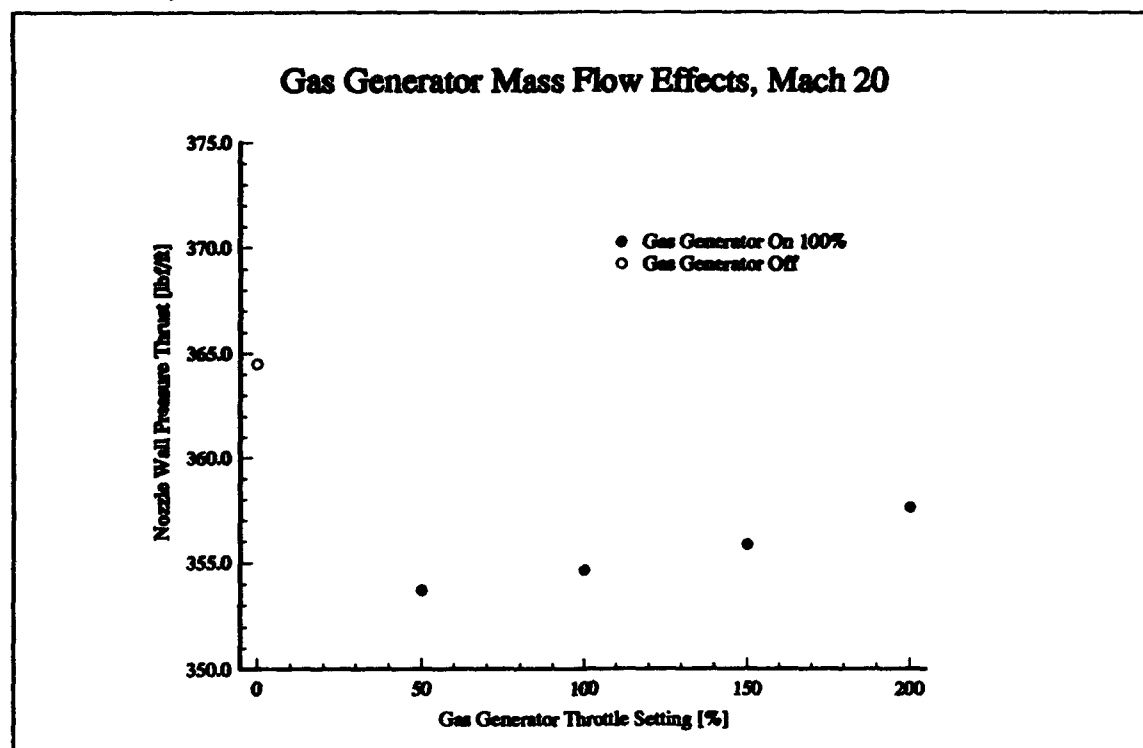


Figure 4-35 Gas Generator Mass Flow Effects, Mach 20 Nozzle Wall Pressure Thrust, No Gas Generator Deflection

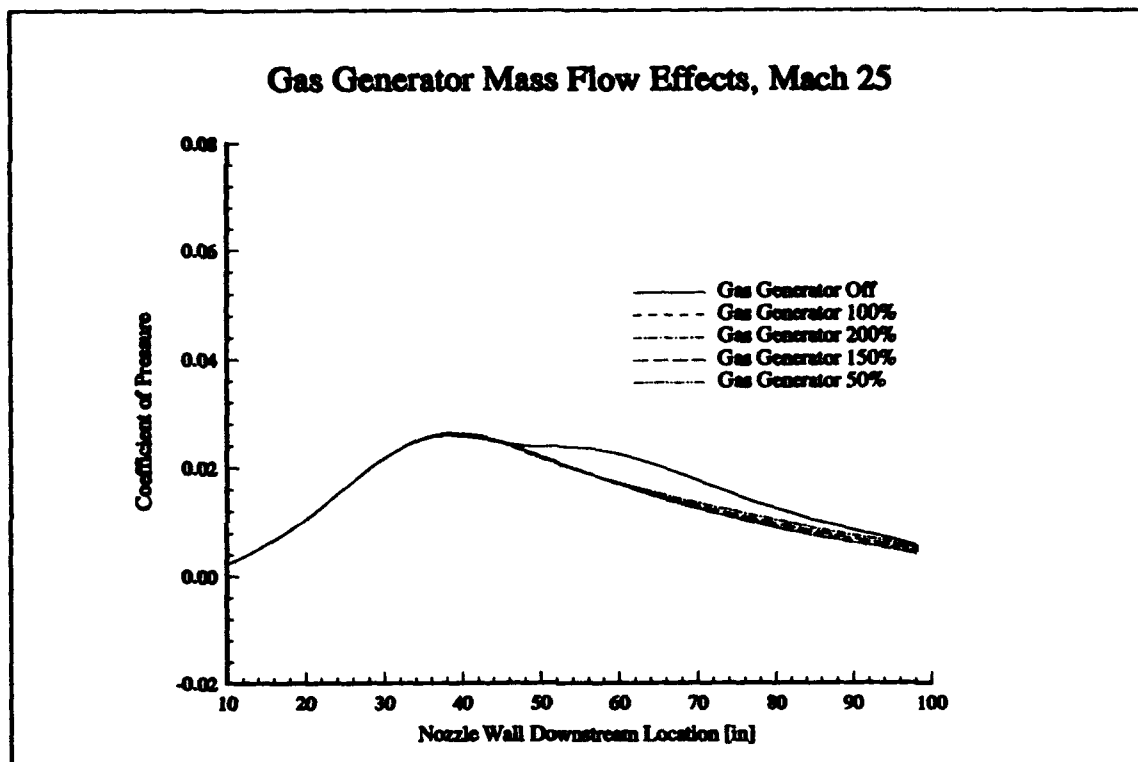


Figure 4-36 Gas Generator Mass Flow Effects, Mach 25 Nozzle Wall Pressure Distribution, No Gas Generator Deflection

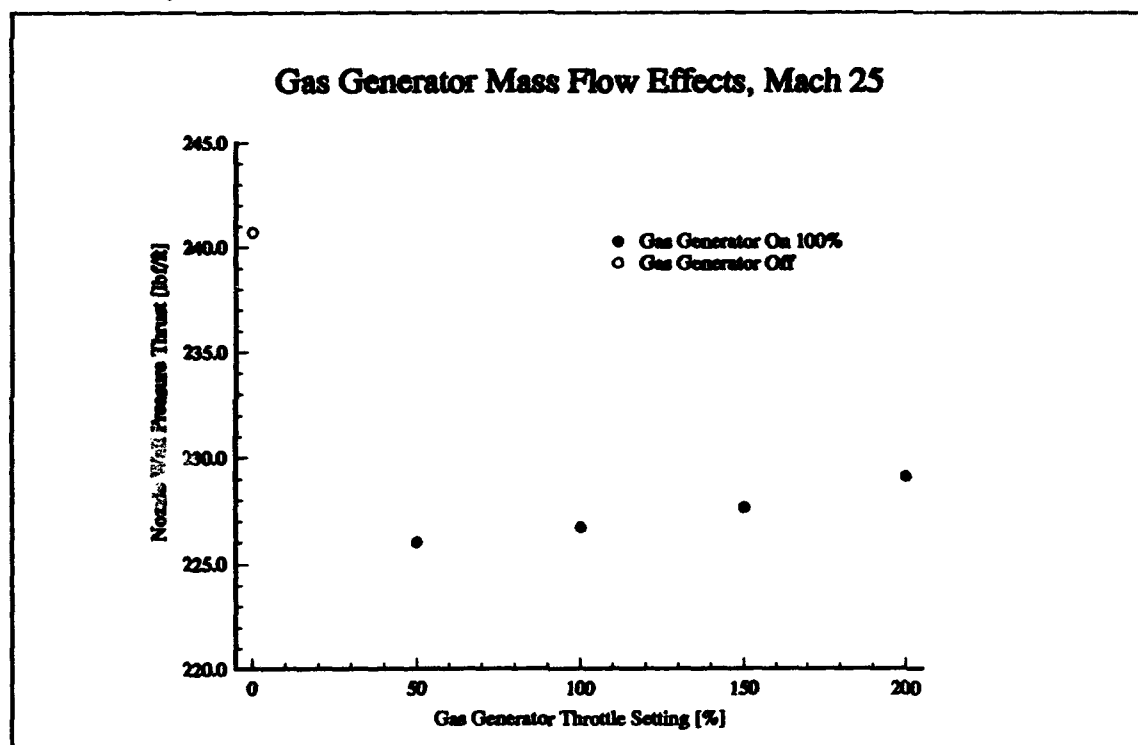


Figure 4-37 Gas Generator Mass Flow Effects, Mach 25 Nozzle Wall Pressure Thrust, No Gas Generator Deflection

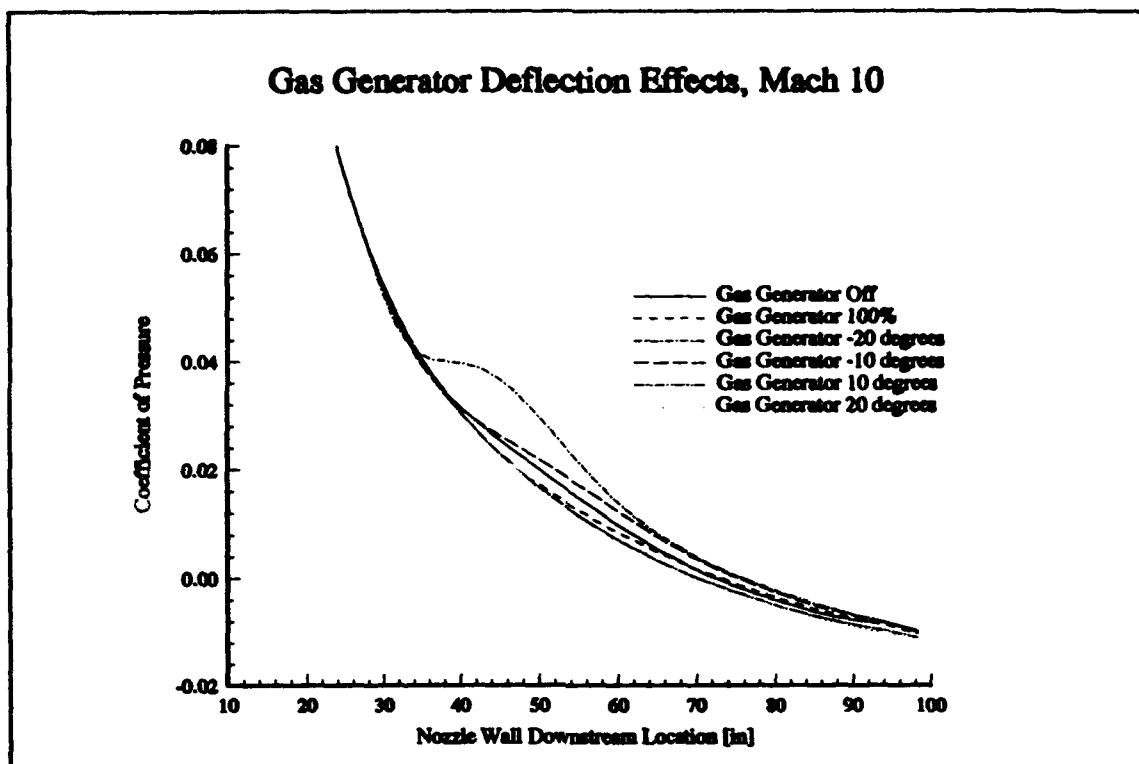


Figure 4-38 Gas Generator Deflection Effects, Mach 10 Nozzle Wall Pressure Distribution

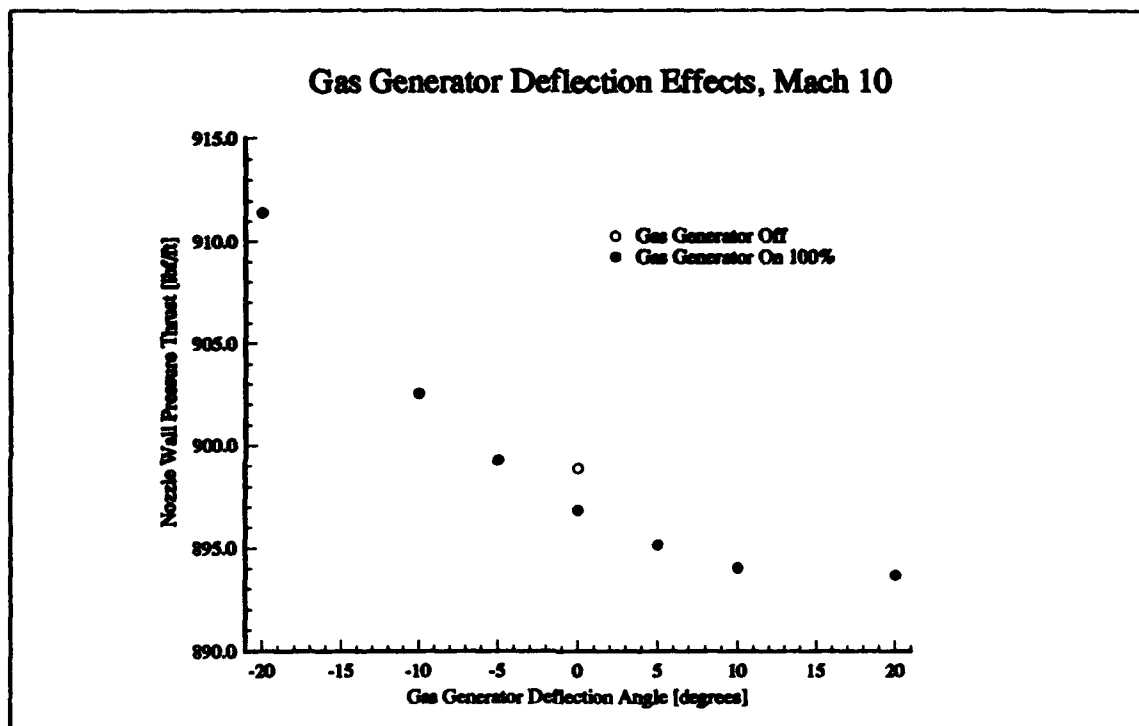


Figure 4-39 Gas Generator Deflection Effects, Mach 10 Nozzle Wall Pressure Thrust

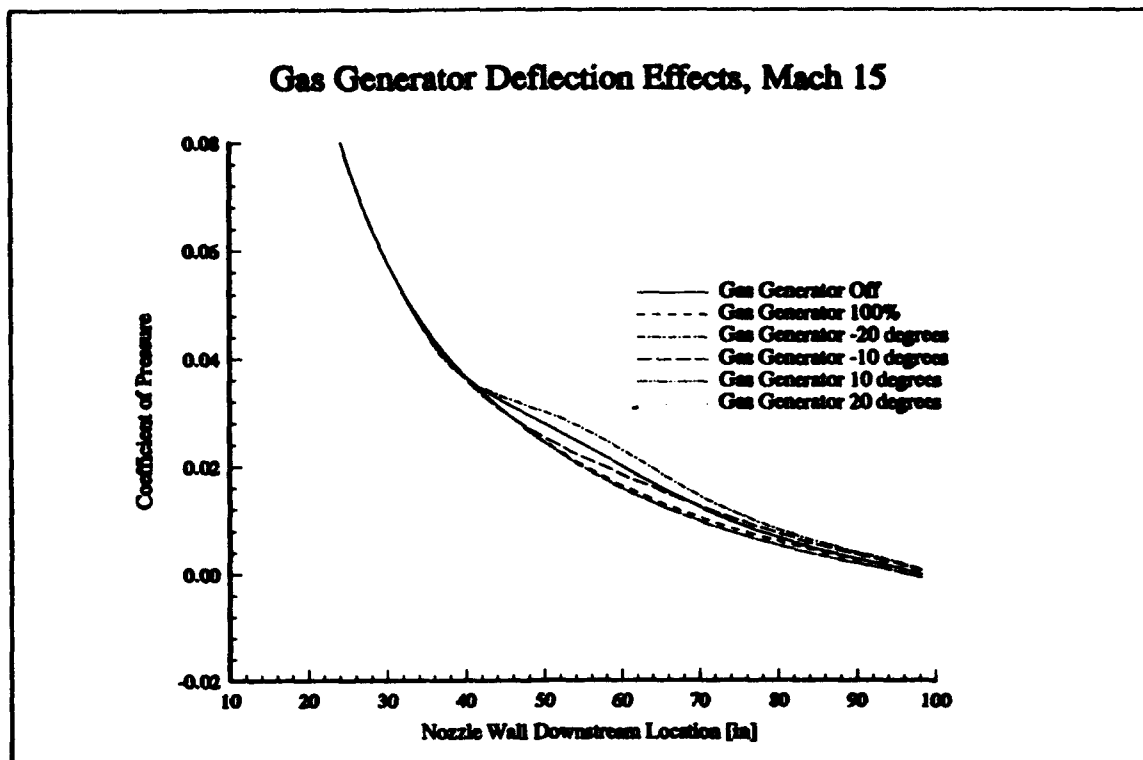


Figure 4-40 Gas Generator Deflection Effects, Mach 15 Nozzle Wall Pressure Distribution

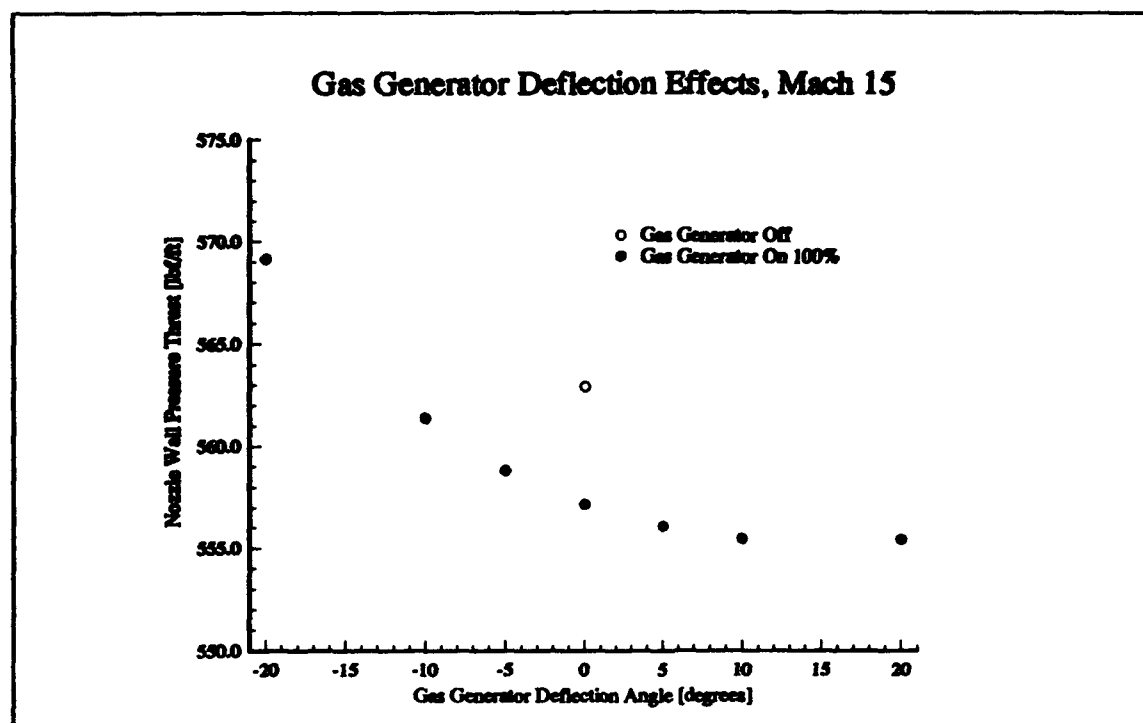


Figure 4-41 Gas Generator Deflection Effects, Mach 15 Nozzle Wall Pressure Thrust

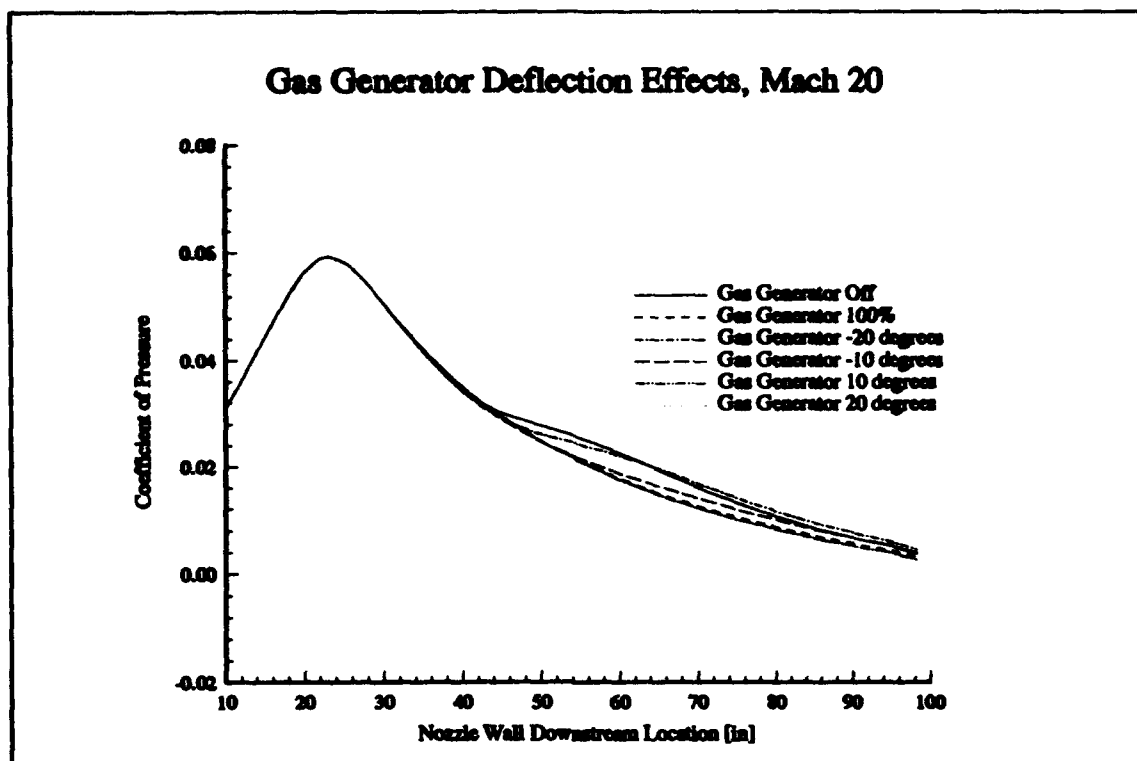


Figure 4-42 Gas Generator Deflection Effects, Mach 20 Nozzle Wall Pressure Distribution

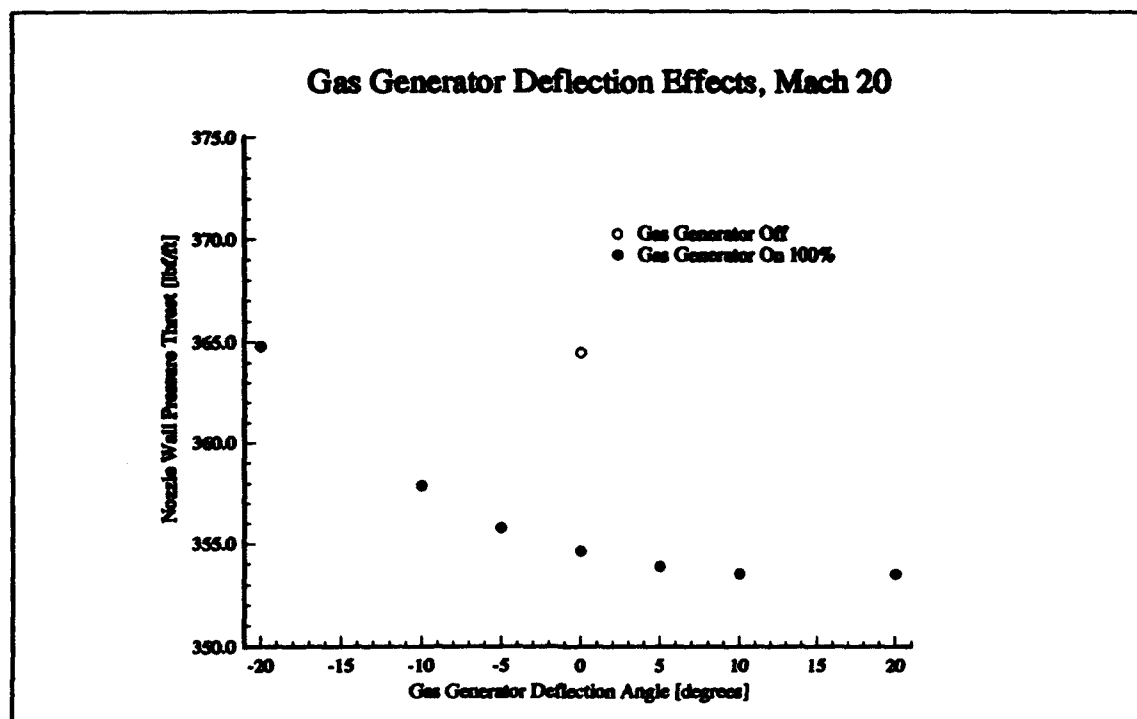


Figure 4-43 Gas Generator Deflection Effects, Mach 20 Nozzle Wall Pressure Thrust

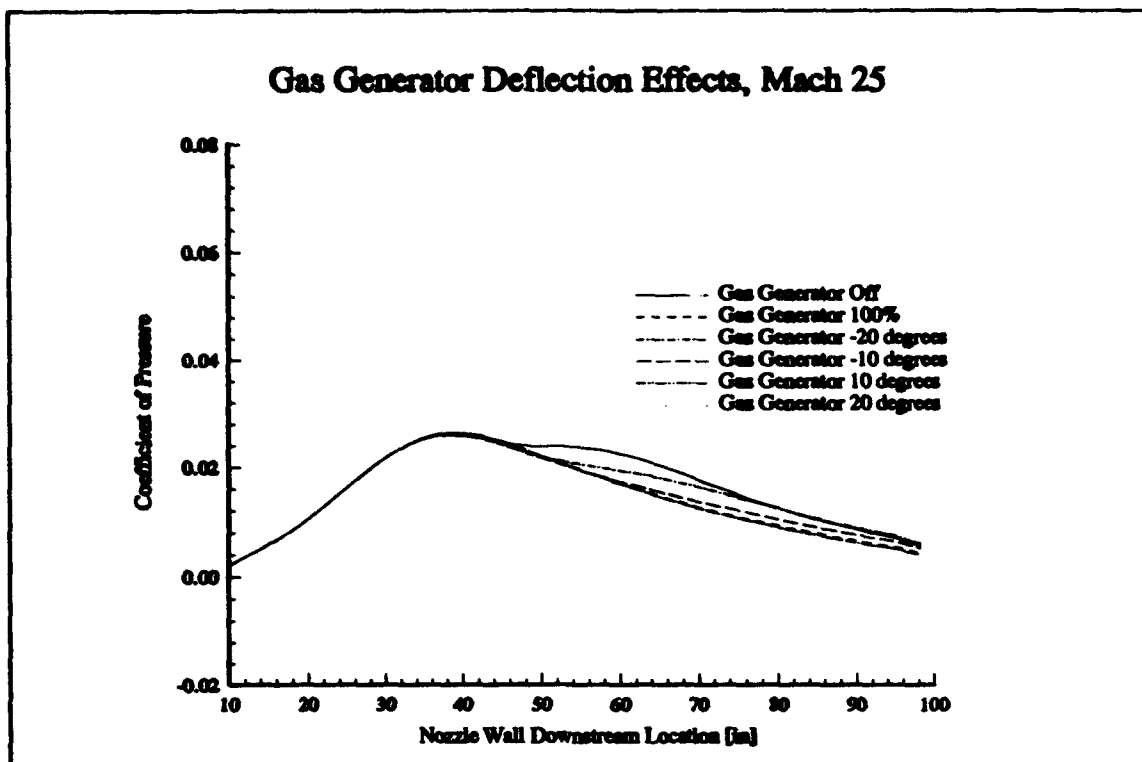


Figure 4-44 Gas Generator Deflection Effects, Mach 25 Nozzle Wall Pressure Distribution

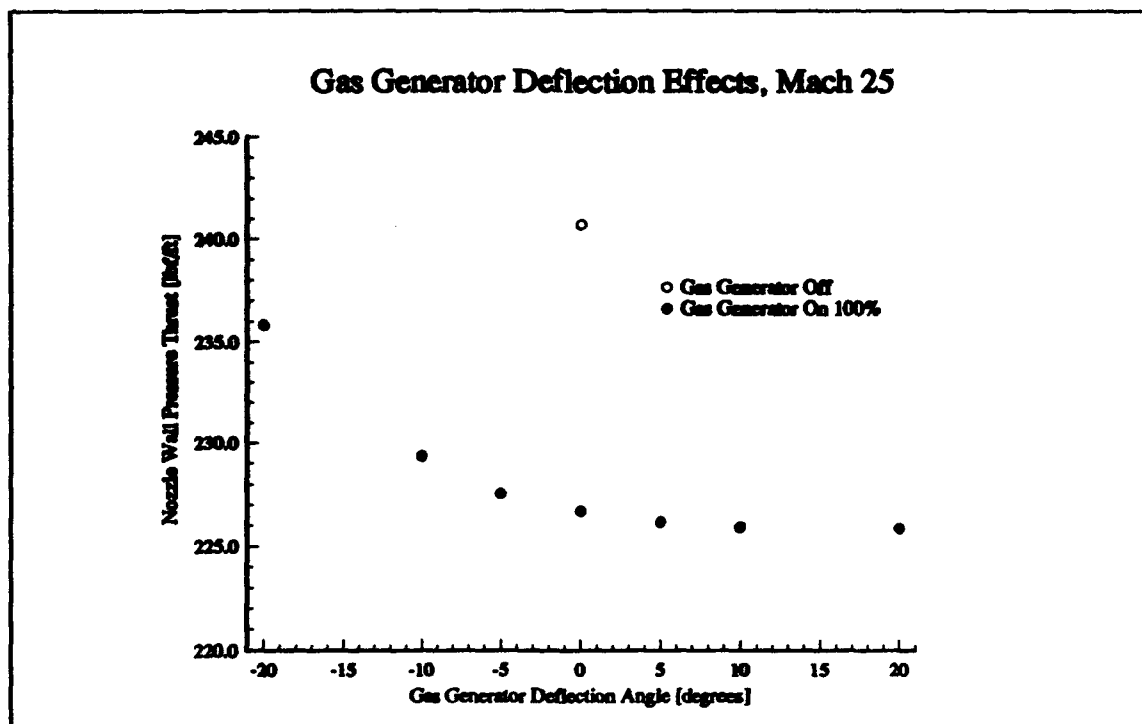


Figure 4-45 Gas Generator Deflection Effects, Mach 25 Nozzle Wall Pressure Thrust

Gas Generator Mass Flow Effects

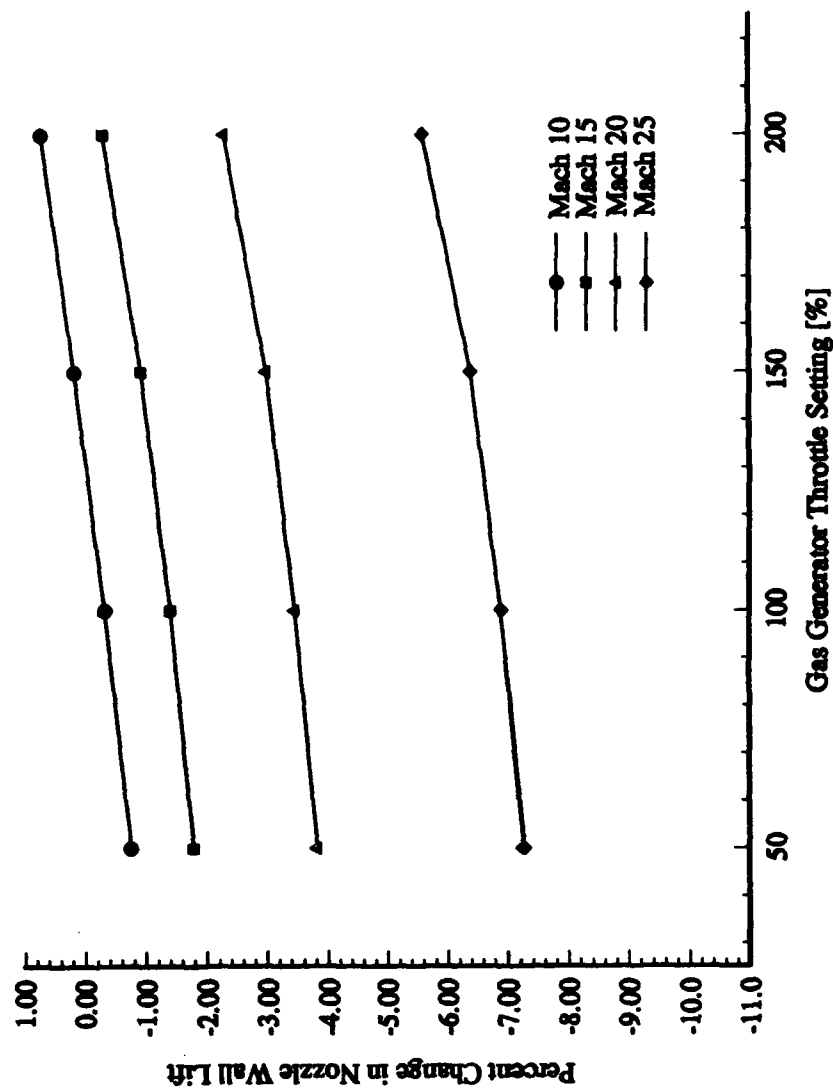


Figure 4-46 Gas Generator Mass Flow Effects, Percent Change in Nozzle Wall Lift, No Gas Generator Deflection

Gas Generator Deflection Effects
Nozzle Wall Pressure Contribution Only

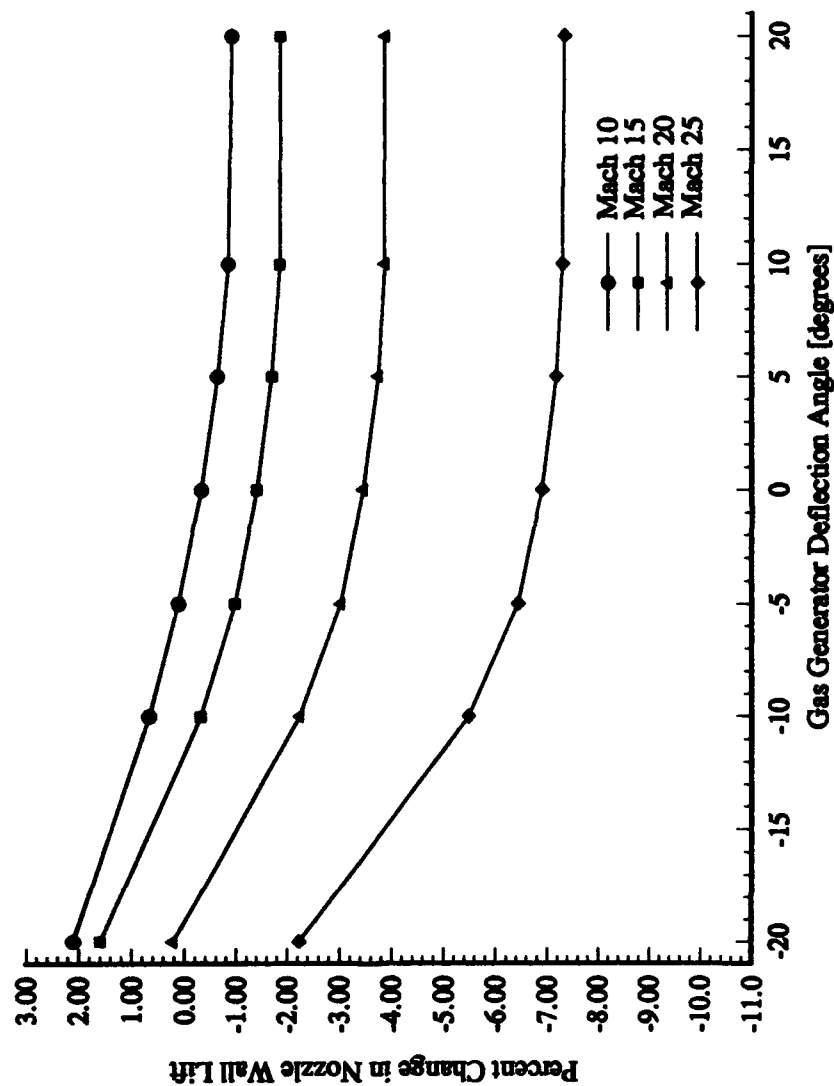


Figure 4-47 Gas Generator Deflection Effects, Nozzle Wall Pressure Contribution to Lift, Gas Generator Throttle 100%

Gas Generator Deflection Effects Nozzle Wall Pressure Lift and Direct Gas Generator Contribution to Lift

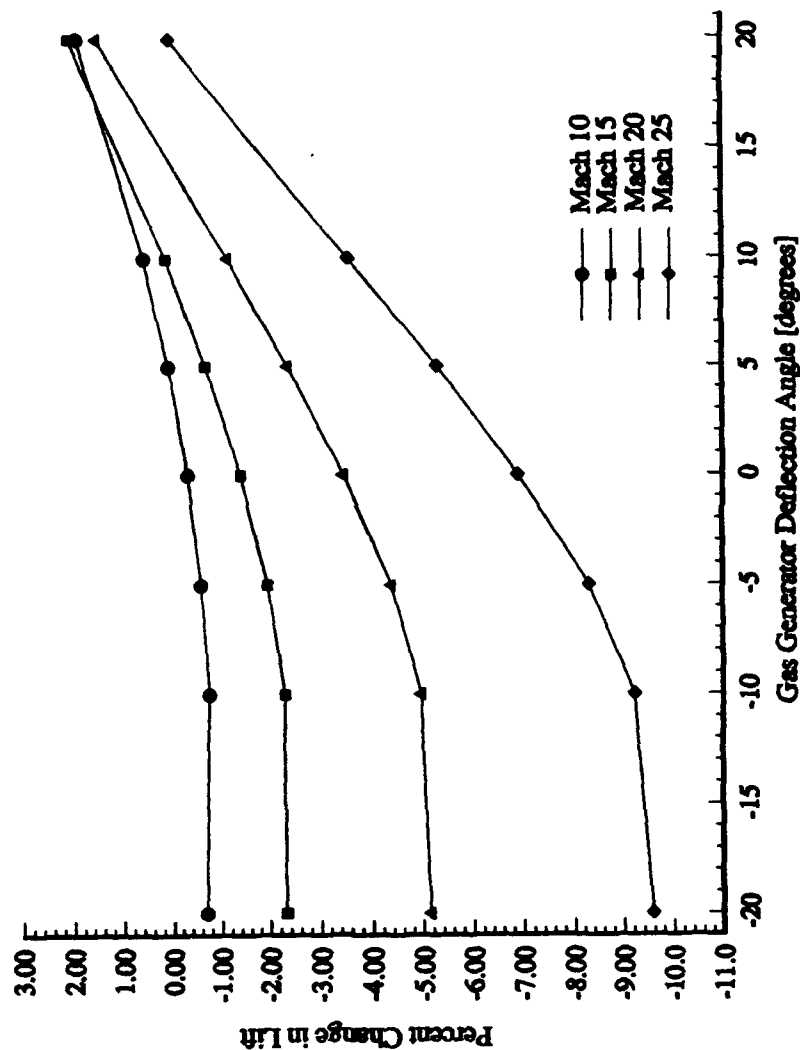


Figure 4-48 Gas Generator Deflection Effects, Nozzle Wall Pressure and Direct Gas Generator Contribution to Lift, Gas Generator Throttle 100%

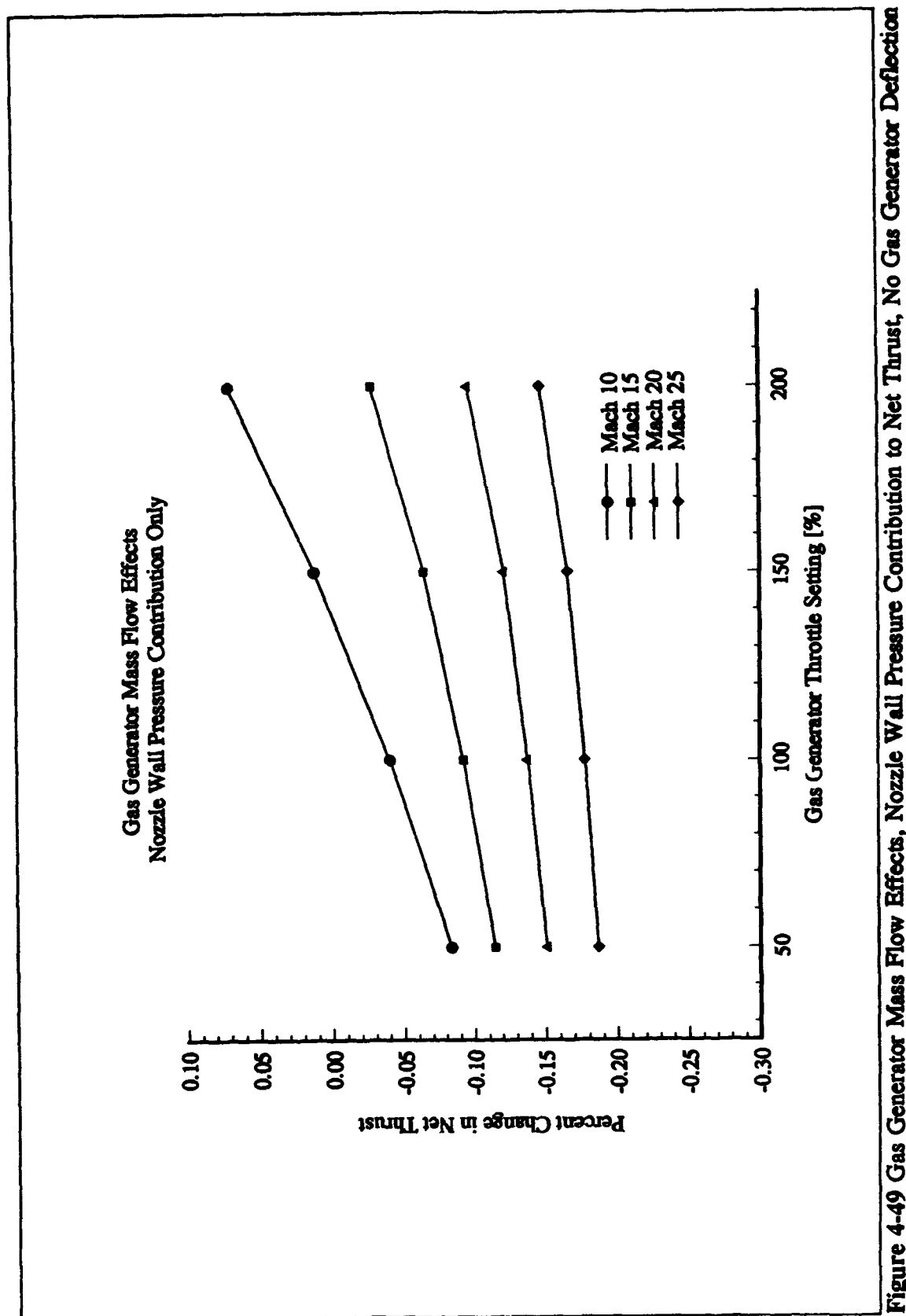


Figure 4-49 Gas Generator Mass Flow Effects, Nozzle Wall Pressure Contribution to Net Thrust, No Gas Generator Deflection

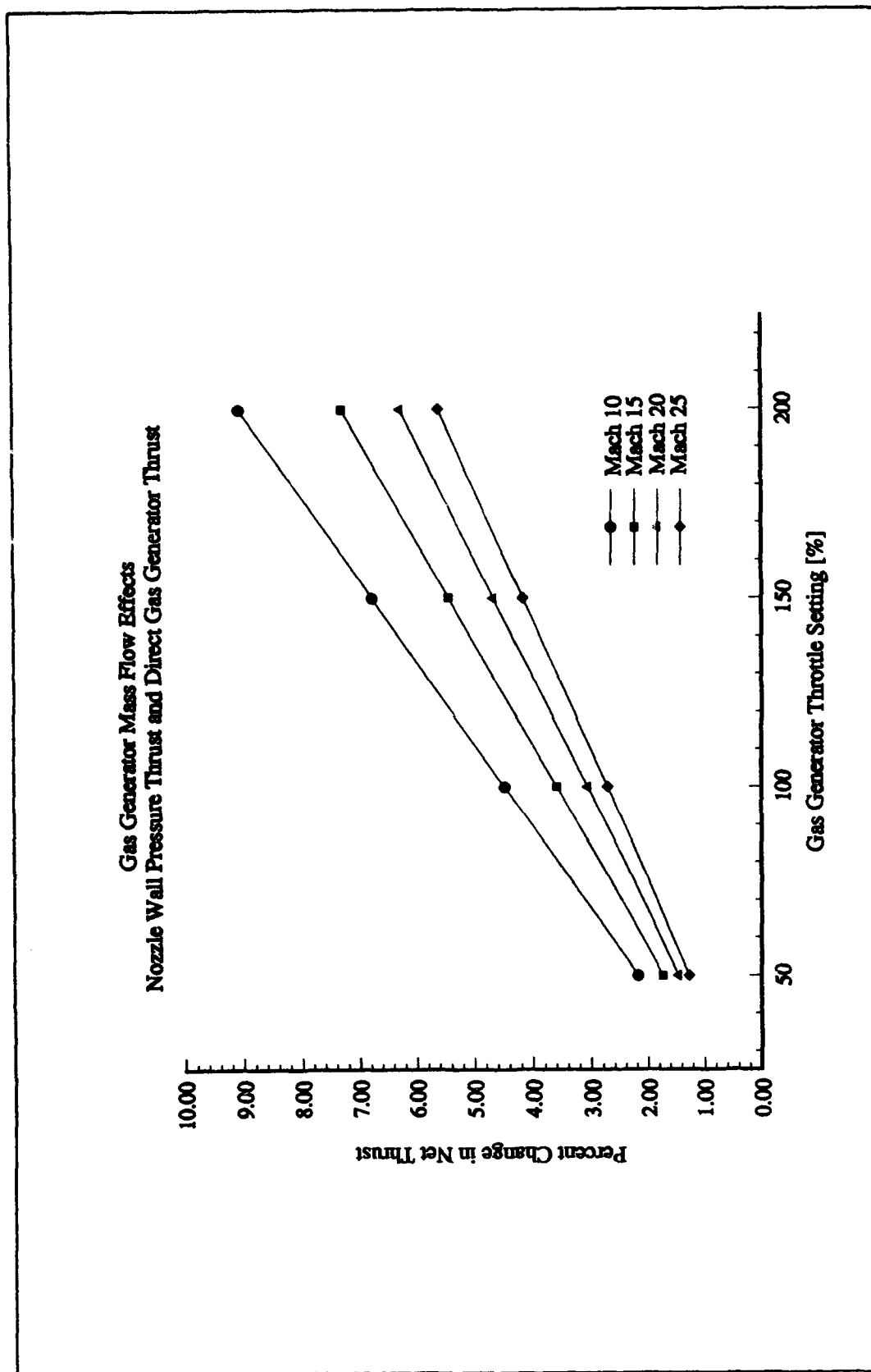


Figure 4-50 Gas Generator Mass Flow Effects, Nozzle Wall Pressure and Direct Gas Generator Contribution to Net Thrust, No Gas Generator Deflection

Gas Generator Deflection Effects
Nozzle Wall Pressure Contribution Only

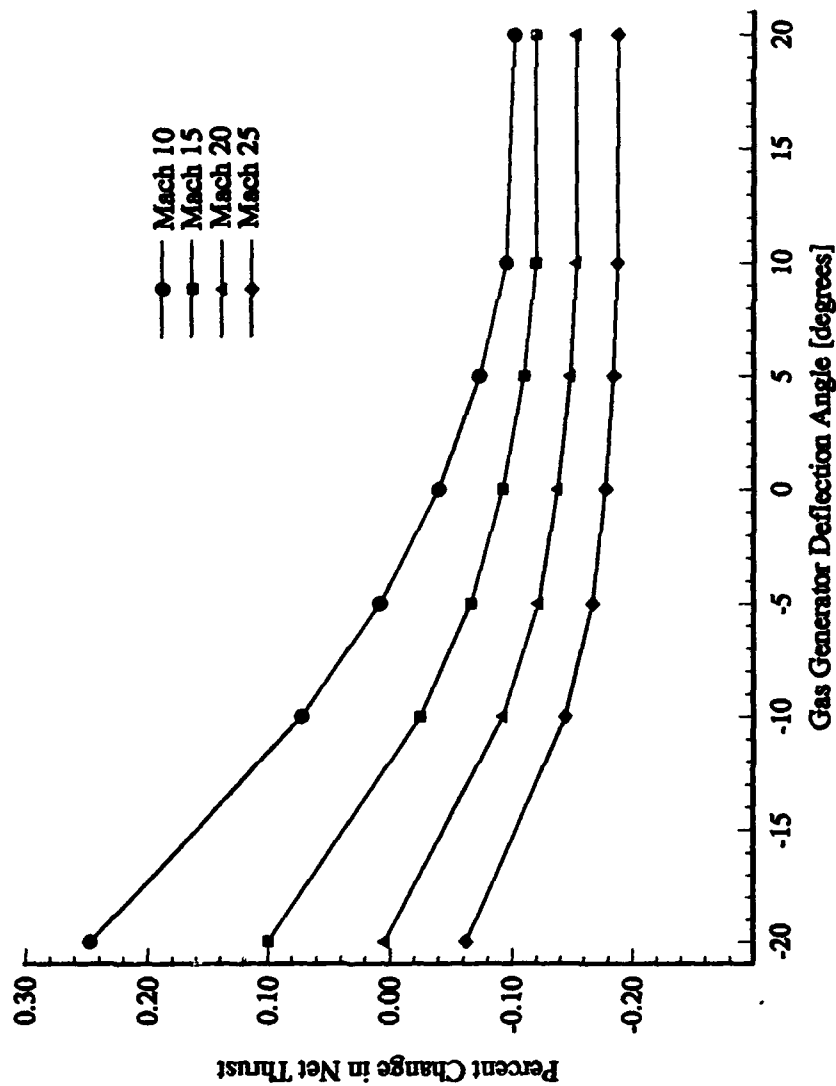


Figure 4-51 Gas Generator Deflection Effects, Nozzle Wall Pressure Contribution to Net Thrust, Gas Generator Throttle: 100%

Gas Generator Deflection Effects Nozzle Wall Pressure Thrust and Direct Gas Generator and Nozzle Exit Thrust

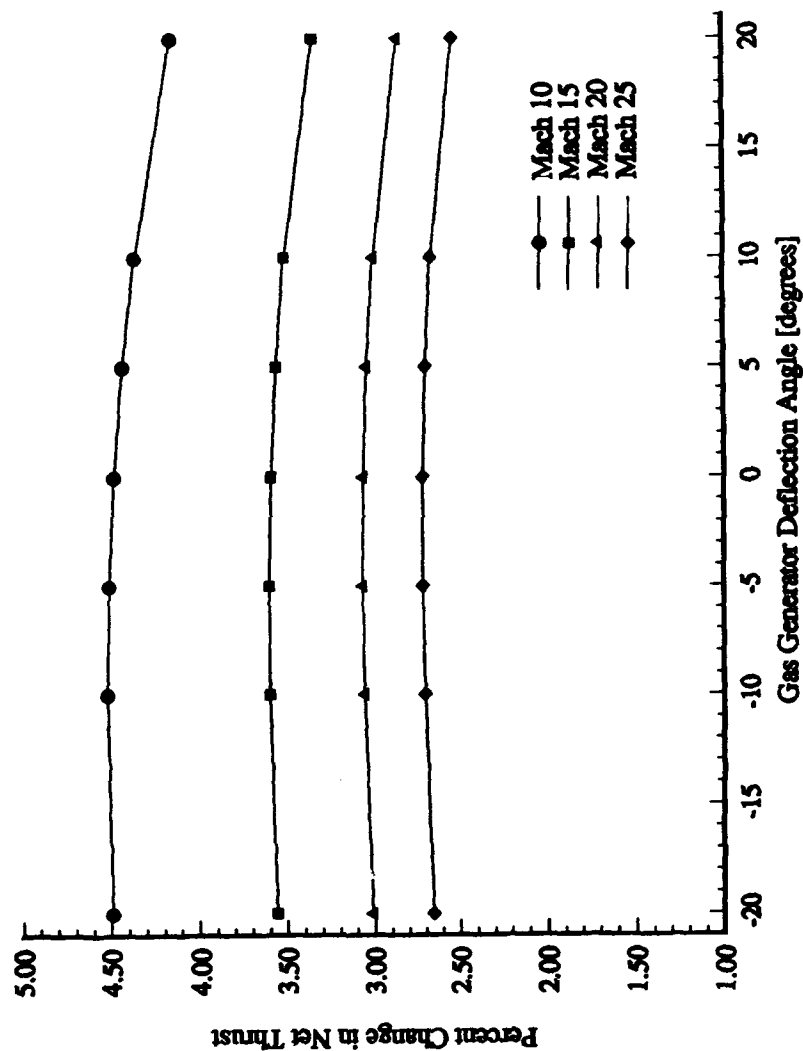


Figure 4-52 Gas Generator Deflection Effects, Nozzle Wall Pressure, Direct Gas Generator, and Nozzle Exhaust Contributions to Net Thrust, Gas Generator Throttle 100%

V. CONCLUSIONS AND RECOMMENDATIONS

5.1 Summary

The proposed improved cowl concept was evaluated for two hypersonic vehicle nozzle/cowl afterbody configurations. The effect of inserting a gas generator into the cowl trailing edge was investigated numerically using an experimentally validated finite volume computational code developed by Wright Laboratory. The two dimensional Navier-Stokes equations were solved assuming laminar flow and a perfect gas equation of state using two flux-split methods. The flowfields were solved using a combination of the explicit formulations of the Van Leer flux-vector splitting and the Roe flux-difference splitting algorithms. The effects of gas generator mass flow increases and thrust vector deflection angles were evaluated in terms of the pressure distribution on the nozzle wall and its effect on overall nozzle performance.

The experimentally evaluated hypersonic nozzle/cowl configuration was analyzed over a range of nozzle pressure ratios for two supersonic off-design Mach numbers. The flowfields were dominated by the initial expansion of the nozzle flow. The extent of the pressure recovery along the nozzle wall was affected by the size and location of the separation regions. Mach number, nozzle pressure ratio, and gas generator throttle setting all had a significant impact on the location and size of the separation regions.

The trends associated with inserting a gas generator into the generic nozzle/cowl afterbody configuration on the high Mach, on-design trajectory were not

as significant as they were for the experimentally validated off-design configuration. For the generic nozzle configuration, the flow was also dominated by the very dramatic initial expansion. Gas generator effects on the nozzle wall pressure recovery were limited to small changes in nozzle wall pressure at the downstream locations. For a majority of the operating envelope, the gas generator actually caused a slight decrease in nozzle wall pressure recovery.

5.2 Conclusions

For the experimental off-design configuration, inserting the gas generator into the end of the cowl increased the pressure through the first separation bubble resulting in a higher pressure recovery along the nozzle. The high pressure boundary created by the gas generator exhaust delayed the internal nozzle flow expansion resulting in a higher overall nozzle wall pressure distribution. Furthermore, the presence of the gas generator tended to minimize the internal nozzle shock attached to the cowl which eliminated the second separation region associated with the low speed, low nozzle pressure ratio off-design flow conditions.

For the experimental off-design configuration, the gas generator throttle setting had a significant impact on the overall nozzle wall pressure recovery. The primary variable affecting the nozzle internal flow was the high pressure boundary created by the gas generator. As the gas generator throttle setting increased, both the gas generator mass flow and exhaust pressure increased. The higher gas generator exhaust pressure resulted in a significantly higher nozzle wall pressure recovery near the first separation bubble.

For the experimental configuration, the gas generator deflection effects were also significant. Deflections towards the wall dramatically increased the nozzle wall pressure recovery while deflections away from the wall only caused relatively small losses. Most of the effects of gas generator deflections were isolated to the upstream locations near the first separation bubble. Gas generator deflections had very little impact on the downstream nozzle wall pressure recovery.

The comparison of gas generator effects to nozzle cowl geometry change effects was promising. The gas generator effectively acts as an aerodynamic cowl extension. The results associated with the addition of the gas generator were very similar to the effects of increasing the length of the cowl. Deflections of the cowl extension effects also follow the same trends associated with the gas generator deflections. An integrated cowl gas generator has the potential of saving overall weight due to a decrease in required cowl length.

For the generic nozzle cowl configuration analyzed over a typical trajectory, the effects of the gas generator on nozzle wall pressure recovery were not very significant in terms of overall nozzle performance. The small changes in nozzle wall pressure recovery were primarily a result of the propagation of pressure differences behind the blunt cowl to the nozzle wall downstream locations. When the gas generator was turned off, the recompression shock behind the blunt trailing edge of the cowl caused a very large pressure rise in this region. Although this pressure rise associated with the blunt cowl increased the downstream nozzle wall pressure recovery slightly, it generated a stronger external flow shock resulting in increased plume drag.

For the generic nozzle/cowl configuration, the overall effects of the gas

generator on nozzle wall pressure recovery were secondary to the net effects of the gas generator on overall nozzle performance. As opposed to the nozzle wall pressure recovery changes, the direct thrust and lift terms associated with the gas generator momentum flux contributed significantly to the overall nozzle performance.

The potential benefits for inserting a gas generator into the cowl of a hypersonic vehicle were demonstrated for both configurations over a wide range of off-design and on-design operating conditions. For the low speed off-design cases, the gas generator made a significant contribution to overall nozzle wall pressure recovery. As proposed, the gas generator demonstrated the potential to act as an aerodynamic cowl extension.

Although the gas generator effects on nozzle wall pressure recovery were minimal for the generic nozzle operating at the high Mach number on-design trajectory points, the gas generator effects on the overall integrated nozzle/cowl/gas generator performance were significant. In particular, the direct thrust term associated with the gas generator contributes significantly to overall performance. The offset location of the gas generator also provides the potential to make a significant contribution to overall vehicle stability and control moment control. Direct moment control could be achieved through any desired combination of gas generator deflections and gas generator mass flow settings. This direct moment control has the potential to reduce the tremendous trim drag penalties associated with conventional control surface deflections typically required for flight vehicles operating at hypersonic speeds.

5.3 Recommendations

Further investigation of the improved cowl concept is warranted. The biggest limitation of the present investigation was that it was limited to an investigation of two-dimensional effects. To gain a thorough understanding of the complex flowfield, a full three dimensional model should be evaluated. Ideally, a three dimensional hypersonic vehicle afterbody point design would be evaluated over an optimized trajectory using a realistic cowl-integrated gas generator.

Short of a full three-dimensional analysis, further refinements to the two-dimensional approach would be beneficial. The incorporation of turbulence into the Wright Laboratory code would help overcome some of the errors associated with the exact shape of the first separation bubble. Additional modifications that would add realism to the code for the high speed, high temperature flows would be the incorporation of chemically dissimilar flowfields with flowfield mixing or the possible incorporation of chemical reactions into the code.

Additional variations on the improved cowl concept should also be explored. Since the gas generator performance is highly dependent on the extent of the internal flow expansion along cowl wall, the on-design, high Mach number performance of a gas generator concept should be evaluated using more realistic nozzle configurations and trajectories.

Finally, a trade study should be done to determine the benefits associated with increasing the gas generator exhaust pressure at the expense of a decrease in exit momentum. This could easily be accomplished by parametrically decreasing the gas generator nozzle expansion ratio.

Bibliography

1. Hyun, Yonghee, *A Comparison of Computational and Experimental Data for a Subscale High Speed Propulsive Nozzle*, MS Thesis, AFIT GAE/ENY/93J-02, School of Engineering, Air Force Institute of Technology (AU), Wright-Patterson AFB, OH, June 1993.
2. Bonaparte, Micheal J., *Nozzle/Cowl Optimization for a Hypersonic Vehicle on a Typical Trajectory*, MS Thesis, AFIT GAE/ENY/92D-10, School of Engineering, Air Force Institute of Technology (AU), Wright-Patterson AFB, OH, December 1992.
3. Anderson, John D. Jr., *Hypersonic and High Temperature Gas Dynamics*, New York: McGraw-Hill Book Company, 1989.
4. Cochran, R. Bruce, *Hypersonic Nozzle/Afterbody Performance at Low Mach Numbers*, MS Thesis, AFIT GAE/ENY/89J-2, School of Engineering, Air Force Institute of Technology (AU), Wright-Patterson AFB, OH, December 1989.
5. Anderson, W. K., Thomas, J. L., and Van Leer, B., "Comparison of Finite Volume Flux Vector Splitting for the Euler Equation," *AIAA Journal* Vol.24, No. 9, September 1986.
6. Gaitonde, Datta, *Computation of Viscous Shock/Shock Hypersonic Interactions with an Implicit Flux Split Scheme*. Final Report for Period September 1989-September 1990. Wright-Patterson AFB, OH: Universal Energy Systems, December 1990, (WRDC-TR-90-3076)
7. Gaitonde, Datta, *The Performance of Flux-Split Algorithms in High-Speed Flows*. AIAA 92-0186, 30th Aerospace Sciences Meeting and Exhibit. Reno, Nevada, January 1992.
8. Gaitonde, Datta, *Hypersonic Flow Simulation with Upwind Methods*, Computational Fluid Dynamics Short Course, Wright-Patterson AFB, OH, 21-24 September 1992.
9. Doty, John H., *Maximum Thrust Planar Supersonic Nozzles Using a Flux-Difference-Splitting Technique*, Ph.D Dissertation. School of Engineering, Purdue University, West Lafayette IN, August 1991.

10. Anderson, Dale A., Tannehill, John C., and Pletcher, Richard H., *Computational Fluid Mechanics and Heat Transfer*, New York: Hemisphere Publishing Corporation, 1984.
11. Anderson, John D. Jr., *Modern Compressible Flow with Historical Perspective*, New York: McGraw-Hill Book Company, 1982.
12. Sutton, George P., *Rocket Propulsion Elements, an Introduction to the Engineering of Rockets*, (Fifth Edition), New York: John Wiley and Sons, 1986.
13. John, James E. Jr., *Gas Dynamics*, Boston: Allyn and Bacon, Inc., 1984.
14. Jameson, Antony, "Computational Algorithm for Aerodynamic Analysis and Design," Contribution to the INRIA 25th Anniversary Conference on Computer Science and Control, Paris, December 1992.
15. Walatka, P. P., Plessel, T., McCabe, R. K., Clucas, J., and Elson, P. A., *FAST User's Manual*, Beta 2.0, NASA RND-91-011, December 1991.
16. Steinbrenner, John P., and Chawner, John R., *The GRIDGEN Version 8 Multiple Block Grid Generation Software*, MDA Engineering Report, MDA Engineering, Inc., December 1992.
17. Steinbrenner, John P., and Chawner, John R., *The GRIDGEN 3D Multiple Block Grid Generation System: Interim Report*, 1 October 1987-1 October 1990, Contract F33615-87-C-3003, Fort Worth Texas: General Dynamics Corporation, April 1991 (WRDC-TR90-3022).
18. Yee, H. C., *A Class of High-Resolution Explicit and Implicit Shock-Capturing Methods*, NASA TM 101088, February 1989.
19. Edwards, A. Thomas, *The Effects of Exhaust Plume/Afterbody Interaction on Installed Scramjet Performance*, NASA TP-1940, 1981.
20. Kumar, Ajay, *Numerical Analysis of the Scramjet-inlet Flow Fields by Using Two-Dimensional Navier-Stokes Equations*, NASA TP-1940, 1981.
21. Van Gretheisen, Valery, Heat Transfer Branch, National-Aerospace Plane System Program Office, Wright-Patterson AFB, OH. Telephone interview. 14 January 1994.

22. **Butler, Mark C., and Rothenflue, James, "Analysis of Second Stage Performance,"** Term project for MENG 530, Air Force Institute of Technology (AU), Wright-Patterson AFB, OH, December 1990.
23. **MacCormack, Robert W., "The Effect of Viscosity in Hypervelocity Impact Cratering,"** AIAA Paper No. 69-354.
24. **Pandolfini, P., *Instructions for Using RAMJET Performance Analysis (RIPA)-IBM-PC Version 1.0*, Contract JHU/APL-NASP-86-2. Laurel MD: The John Hopkins University Applied Physics Laboratory, November, 1986.**

Appendix A: Code Inputs

This appendix contains a sample input file and a description of the inputs for the Wright Laboratory computation fluid dynamics code used in this research. The inputs can be broken down into several categories; algorithm control parameters, geometric parameters, flowfield initial conditions, and basic solution control parameters. The most significant parameters are highlighted in the following tables.

Table A-1 Algorithm Control Parameters

ISWVL	Solution method; Van Leer (3), Roe (4)
NEND	Number of iterations
INS	Flow model; Euler (0), Navier-Stokes (1)
CFLMAX	Maximum allowable CFL
CFL	Initial CFL used to start solution
CFLEXP	Number of iterations before CFL doubles
ICFL	Number of iterations between CFL increases
IMPLT	Numerical formulation; Explicit (0), Implicit (1)

Table A-2 Geometric Parameters

IL, JL	Grid dimensions in ξ and η respectively
INS1, INS2	Grid location defining cowl edge ξ location
JNS1, JNS2	Grid location defining cowl edge η location

Table A-3 Flowfield Conditions

IADBWL	Adiabatic wall (0) or constant temperature wall (1) BC
TWALL	Wall temperature
ALPHA	Freestream angle of attack
RM	Freestream Mach number
REL	Freestream Reynolds number per foot
TINF	Freestream static temperature
GASCONSTANTEXT	Freestream gas constant R
GAMMAEXT	Freestream γ
AINALPHA	Internal flow angle of attack
RINM	Internal flow Mach number
RINEL	Internal flow Reynolds number per foot
TININF	Internal flow static temperature
GASCONSTANTIN	Internal flow gas constant R
GAMMAIN	Internal flow γ
AGGALPHA	Gas generator thrust vector deflection
RGGM	Gas generator Mach number
RGGEL	Gas generator Reynolds number per foot
TGGINF	Gas generator static temperature
GASCONSTGG	Gas generator gas constant R
GAMMAGG	Gas generator γ

Table A-4 Basic Control Parameters

IREAD	Deadstart (0) or Restart (1)
IGRID	Grid Format
IP3DOP	Plot3D output file format
MODPR	Iterations between printing convergence data

The following sample input file represents the Mach 15 flow condition with the gas generator operating at 100% throttle with no deflection.

cnldat

IL, JL, IMETRC
102 72 0

NEND
2000

ICFL, CFLEXP, CFLMAX, CFL
5 1 0.9 0.01

IREST, CFCRHO, CFCEI, CFLPEN, CEXPPEN, INOFRZ
1 5.00 5.00 1 1 1

IMPLT, ILCTST, ISWVL, ILMTR, OMEGA, DELTEP, DELTIL, IENTH, INS, NSWPS
0 1 4 2 1 1.E-10 0.5 2 1 2

IADBWL, ICASE, TWALL, ALPHA, RMINF, REL, RL, TINF, IGRID
0 2 2000.00 0. 9.5347 7.3728E5 1.0 1113.21 2

IREAD, IP3DOP, DGBUG, MODPR, NRST, IFMRTI, IFMRTO, IINT1
1 2 0 10 0 1 1 1

INS1, INS2, JNS1, JNS2
1 52 37 46

TINWALL, AINLPHA, RIMINF, RINEL, RINL, TININF, IGRID
2000.00 0.0 3.4445 2.8701E6 1.0 5511.96 2

AggLPHA, RggMINF, RggEL, RggL, TggINF, GASCONSTgg, GAMMAgg
0. 4.680 0.75723E6 1.0 2158.29 3508.98 1.26059

GASCONSTin GAMMAin GASCONSText GAMMAext
2257.34 1.25 1727.62 1.35

Appendix B: Code Parallelization

This appendix contains an example of parallel processing techniques applied to the solution of a generic nozzle/cowl flowfield at the Mach 15 design condition with a gas generator operating at 100% throttle (Section 3.2). For this example, 1000 Roe iterations were completed. An example of the code modifications are presented for subroutine *L.f*.

B.1 Profile of Non Parallelized Code

This section contains the execution profile of the original code without any parallelization. This output was used to identify the subroutines that consumed the most CPU time and were therefore the best candidates for parallelization. Subroutines *LMTRI*, *LMTRJ*, *FSIROE*, *FSJROE*, *WISEUL*, *VJSEUL*, and *L* were chosen for parallelization based on this breakdown.

Profile listing generated Fri Jan 14 08:07:28 1994 with:
prof -pixie -quit 1% -clock 25 nozzle.exe

```
-----
* -p[rocedures] using basic-block counts;
* sorted in descending order by the number of cycles executed in each
* procedure; unexecuted procedures are excluded
-----
```

130230207604 cycles (5209.2083 seconds at 25.00 megahertz)

	cycles	%cycles	cum %	seconds	cycles /call	bytes /line	procedure (file)
17962368802	13.79	13.79	718.4948	89812	93	lmtrj_ (LMTRJ.f)	
17844680000	13.70	27.50	713.7872	127462	41	fairoe_ (FSIROE.f)	
17517206720	13.45	40.95	700.6883	125123	90	lmtri_ (LMTRI.f)	
17186000000	13.20	54.14	687.4400	85930	40	fajroe_ (FSJROE.f)	
16364936000	12.57	66.71	654.5974	16364936	56	l_ (L.f)	
10890460000	8.36	75.07	435.6184	77789	80	viseul_ (WISEUL.f)	
10375555374	7.97	83.04	415.0222	42	6	sqrtf_ (sqrtf.s)	
9522240000	7.31	90.35	380.8896	21	23	r_sign_ (r_sign.c)	
8616600000	6.62	96.97	344.6640	43083	62	vjseul_ (VJSEUL.f)	
1776125600	1.36	98.33	71.0450	1776126	57	estdt_ (ESTDT.f)	

```
-----
* -p[rocedures] using invocation counts;
* sorted in descending order by number of calls per procedure;
* unexecuted procedures are excluded
-----
```

787998451 invocations total

	calls	%calls	cum%	bytes	procedure (file)
--	-------	--------	------	-------	------------------

453440000	57.54	57.54	112	r_sign (r_sign.c)
247037108	31.35	88.89	248	sqrtf (sqrtf.s)
84420000	10.71	99.61	64	cvmgp_ (CVMGP.f)

* -h[eavy] using basic-block counts;
 * sorted in descending order by the number of cycles executed in each
 * line; unexecuted lines are excluded

procedure (file)	line	bytes	cycles	%	cum %
r_sign (r_sign.c)	11	52	4987840000	3.83	3.83
r_sign (r_sign.c)	10	44	3627520000	2.79	6.62
l_ (L.f)	83	232	3248000000	2.49	9.11
lmtrj_ (LMTRJ.f)	106	344	2435194846	1.87	10.98
lmtri_ (LMTRI.f)	105	344	2425980342	1.86	12.84
l_ (L.f)	39	168	2352000000	1.81	14.65
lmtrj_ (LMTRJ.f)	91	284	1995181060	1.53	16.18
lmtrj_ (LMTRJ.f)	98	272	1907973495	1.47	17.65
lmtrj_ (LMTRJ.f)	94	272	1902484691	1.46	19.11
lmtri_ (LMTRI.f)	88	232	1618924982	1.24	20.35
lmtri_ (LMTRI.f)	96	208	1449538271	1.11	21.46
lmtri_ (LMTRI.f)	92	208	1442205804	1.11	22.57

B.2 Profile of Parallelized Code

This section contains the execution profile for the parallelized code. CPU usage is broken down for the four processors used on the Silicon Graphics 4D/240 machine.

Processor number 1:

Profile listing generated Mon Feb 14 14:16:04 1994 with:
prof -pixie -quit 1% -clock 25 nozzle.exe nozzle.exe.Addr nozzel.exe.Counts12635

```

* -p[rocedures] using basic-block counts;
* sorted in descending order by the number of cycles executed in each
* procedure; unexecuted procedures are excluded

```

50776235875 cycles (2031.0494 seconds at 25.00 megahertz)

	cycles	%cycles	cum %	seconds	cycles /call	bytes /line	procedure (file)
9191735840	18.10	18.10	367.6694	45959	2812	_lmtrj_151_aaad_ (LMTRJ.f)	
8835036657	17.40	35.50	353.4015	63108	406	_lmtri_148_aaad_ (LMTRI.f)	
4761120000	9.38	44.88	190.4448	21	23	r_sign (r_sign.c)	
3336355374	6.57	51.45	133.4542	42	6	sqrtf (sqrtf.s)	
2955960000	5.82	57.27	118.2384	21114	3392	_fsiroe_90_aaac_ (FSIROE.f)	
2920260000	5.75	63.02	116.8104	803	1620	_viseul_54_aaaa_ (VISEUL.f)	
2867600000	5.65	68.67	114.7040	14338	3332	_fsjroe_89_aaac_ (FSJROE.f)	
2268000000	4.47	73.14	90.7200	630	373	_vjseul_57_aaaa_ (VJSEUL.f)	
1776125600	3.50	76.63	71.0450	1776126	57	estdt_ (ESTDT.f)	
1433600000	2.82	79.46	57.3440	28672	1804	_l_227_aaaa_ (L.f)	
1412880000	2.78	82.24	56.5152	5046	912	_fsiroe_64_aaab_ (FSIROE.f)	
1335021836	2.63	84.87	53.4009	1299	24		
mp_master_wait_for_interleaved_loop_completion (mp.c)							
1321600000	2.60	87.47	52.8640	3304	868	_fsjroe_63_aaab_ (FSJROE.f)	
1162771203	2.29	89.76	46.5108	855	16	_mp_simple_sched_ (mp_simple.s)	
1109400000	2.18	91.95	44.3760	5547	1776	_l_149_aaab_ (L.f)	
881160000	1.74	93.68	35.2464	6294	1460	_l_87_aaaa_ (L.f)	
744285429	1.47	95.15	29.7714	744286	45	rest_ (REST.f)	
715600000	1.41	96.56	28.6240	14312	944	_l_252_aaaf_ (L.f)	

```

* -p[rocedures] using invocation counts;
* sorted in descending order by number of calls per procedure;
* unexecuted procedures are excluded

```

353941539 invocations total

	calls	%calls	cum%	bytes	procedure (file)
226720000	64.06	64.06	112	r_sign (r_sign.c)	
79437108	22.44	86.50	248	sqrtf (sqrtf.s)	
21720000	6.14	92.64	64	cvmgp_ (CVMGP.f)	
8024000	2.27	94.90	48	_mp_call_ (aux.s)	
3640000	1.03	95.93	3240	_viseul_54_aaaa_ (VISEUL.f)	
3600000	1.02	96.95	2608	_vjseul_57_aaaa_ (VJSEUL.f)	

```

* -h[eavy] using basic-block counts;
* sorted in descending order by the number of cycles executed in each
* line; unexecuted lines are excluded

```

procedure (file)	line	bytes	cycles	%	cum %
_lmtrj_151_aaad_ (LMTRJ.f)	?	2812	9191735840	18.10	18.10

_lmtri_148_aaad_ (LMTRI.f)	54	2780	8835036657	17.40	35.50
_fsiroe_90_aaac_ (FSIROE.f)	?	3392	2955960000	5.82	41.32
_fsjroe_89_aaac_ (FSJROE.f)	?	3332	2867600000	5.65	46.97
_viseul_54_aaaa_ (VISEUL.f)	?	3104	2796500000	5.51	52.48
r_sign (r_sign.c)	11	52	2493920000	4.91	57.39
_vjseul_57_aaaa_ (VJSEUL.f)	?	2240	1936800000	3.81	61.20
r_sign (r_sign.c)	10	44	1813760000	3.57	64.78
_l_227_aaaa_ (L.f)	?	1804	1433600000	2.82	67.60
_fsiroe_64_aaab_ (FSIROE.f)	?	912	1412880000	2.78	70.38
_fsjroe_63_aaab_ (FSJROE.f)	?	868	1321600000	2.60	72.99
mp_master_wait_for_interleaved_loop_completion (mp.c)		691		40	1311377836 2.58
75.57					
_l_149_aaab_ (L.f)	?	1776	1109400000	2.18	77.75
_l_87_aaaa_ (L.f)	?	1460	881160000	1.74	79.49
_l_252_aaaf_ (L.f)	?	944	715600000	1.41	80.90

Processor number 2:

Profile listing generated Mon Feb 14 14:16:17 1994 with:
prof -pixie -quit 14 -clock 25 nozzle.exe nozzle.exe.Addrns nozzle.exe.Counts12636

```

* -p[rocedures] using basic-block counts;
* sorted in descending order by the number of cycles executed in each
* procedure; unexecuted procedures are excluded

```

47605084663 cycles (1904.2034 seconds at 25.00 megahertz)

	cycles	%cycles	cum %	seconds	cycles /call	bytes /line	procedure (file)
9201032962	19.33	19.33	368.0413		46006	2812	_lmtrj_151_aaad_ (LMTRJ.f)
8863339687	18.62	37.95	354.5336		63310	406	_lmtri_148_aaad_ (LMTRI.f)
4761120000	10.00	47.95	190.4448		21	23	r_sign (r_sign.c)
3626888840	7.62	55.57	145.0756		1519	688	mp_slave_wait_for_work (mp_slave.s)
2867600000	6.02	61.59	114.7040		14338	3332	_fsjroe_89_aaac_ (FSJROE.f)
2842420000	5.97	67.56	113.6968		20303	3392	_fsiroe_90_aaac_ (FSIROE.f)
2807000000	5.90	73.46	112.2800		802	1620	_viseul_54_aaaa_ (VISEUL.f)
2385600000	5.01	78.47	95.4240		42	6	sqrtf (sqrtf.s)
2268000000	4.76	83.23	90.7200		630	373	_vjseul_57_aaaa_ (VJSEUL.f)
1433600000	3.01	86.24	57.3440		28672	1804	_l_227_aaaa_ (L.f)
1358840000	2.85	89.10	54.3536		4853	912	_fsiroe_64_aaab_ (FSIROE.f)
1321600000	2.78	91.87	52.8640		3304	868	_fsjroe_63_aaab_ (FSJROE.f)
1109400000	2.33	94.21	44.3760		5547	1776	_l_149_aaab_ (L.f)
881160000	1.85	96.06	35.2464		6294	1460	_l_87_aaaa_ (L.f)
715600000	1.50	97.56	28.6240		14312	944	_l_252_aaaf_ (L.f)

```

* -p[rocedures] using invocation counts;
* sorted in descending order by number of calls per procedure;
* unexecuted procedures are excluded

```

325364632 invocations total

	calls	%calls	cum%	bytes	procedure (file)
226720000	69.68	69.68		112	r_sign (r_sign.c)
56800000	17.46	87.14		248	sqrtf (sqrtf.s)
21300000	6.55	93.69		64	cvmgp_ (CVMGP.f)
7884000	2.42	96.11		48	_mp_Call_ (aux.s)
3600000	1.11	97.22		2608	_vjseul_57_aaaa_ (VJSEUL.f)
3500000	1.08	98.29		3240	_viseul_54_aaaa_ (VISEUL.f)

```

* -h[eavy] using basic-block counts;
* sorted in descending order by the number of cycles executed in each
* line; unexecuted lines are excluded

```

procedure (file)	line	bytes	cycles	%	cum %
_lmtrj_151_aaad_ (LMTRJ.f)	?	2812	9201032962	19.33	19.33
_lmtri_148_aaad_ (LMTRI.f)	54	2780	8863339687	18.62	37.95
mp_slave_wait_for_work (mp_slave.s)	99	688	3626888840	7.62	45.57
_fsjroe_89_aaac_ (FSJROE.f)	?	3332	2867600000	6.02	51.59
_fsiroe_90_aaac_ (FSIROE.f)	?	3392	2842420000	5.97	57.56
_viseul_54_aaaa_ (VISEUL.f)	?	3104	2688000000	5.65	63.21
r_sign (r_sign.c)	11	52	2493920000	5.24	68.44
_vjseul_57_aaaa_ (VJSEUL.f)	?	2240	1936800000	4.07	72.51
r_sign (r_sign.c)	10	44	1813760000	3.81	76.32
_l_227_aaaa_ (L.f)	?	1804	1433600000	3.01	79.33
_fsiroe_64_aaab_ (FSIROE.f)	?	912	1358840000	2.85	82.19
_fsjroe_63_aaab_ (FSJROE.f)	?	868	1321600000	2.78	84.97
_l_149_aaab_ (L.f)	?	1776	1109400000	2.33	87.30
_l_87_aaaa_ (L.f)	?	1460	881160000	1.85	89.15
_l_252_aaaf_ (L.f)	?	944	715600000	1.50	90.65

Processor number 3:

Profile listing generated Mon Feb 14 14:16:26 1994 with:
prof -pixie -quit 14 -clock 25 nozzle.exe nozzle.exe.Counts12637

* -p[rocedures] using basic-block counts; *
* sorted in descending order by the number of cycles executed in each *
* procedure; unexecuted procedures are excluded *

33454808749 cycles (1338.1923 seconds at 25.00 megahertz)

	cycles	%cycles	cum %	seconds	cycles /call	bytes /line	procedure (file)
12594445500 (mp_slave.s)	37.65	37.65	503.7778		5275	688	_mp_slave_wait_for_work
2842420000	8.50	46.14	113.6968		20303	3392	_fsiroe_90_aaac_ (FSIROE.f)
2807000000	8.39	54.53	112.2800		802	1620	_viseul_54_aaaa_ (VISEUL.f)
2708600000	8.10	62.63	108.3440		13543	3332	_fsjroe_89_aaac_ (FSJROE.f)
2335200000	6.98	69.61	93.4080		42	6	sqrtf (sqrtf.s)
2271800000	6.79	76.40	90.8720		632	373	_vjseul_57_aaaa_ (VJSEUL.f)
1433600000	4.29	80.69	57.3440		28672	1804	_l_227_aaaa_ (L.f)
1358840000	4.06	84.75	54.3536		4853	912	_fsiroe_64_aaab_ (FSIROE.f)
1248800000	3.73	88.48	49.9520		3122	868	_fsjroe_63_aaab_ (FSJROE.f)
1109400000	3.32	91.80	44.3760		5547	1776	_l_149_aaab_ (L.f)
881160000	2.63	94.43	35.2464		6294	1460	_l_87_aaaa_ (L.f)
715600000	2.14	96.57	28.6240		14312	944	_l_252_aaaf_ (L.f)

* -p[rocedures] using invocation counts; *
* sorted in descending order by number of calls per procedure; *
* unexecuted procedures are excluded *

96164634 invocations total

	calls	%calls	cum%	bytes	procedure (file)
55600000	57.82	57.82		248	sqrtf (sqrtf.s)
20700000	21.53	79.34		64	cvmgp_ (CVMGP.f)
7544000	7.84	87.19		48	_mp_call_ (aux.s)
3600000	3.74	90.93		2608	_vjseul_57_aaaa_ (VJSEUL.f)
3500000	3.64	94.57		3240	_viseul_54_aaaa_ (VISEUL.f)
2388001	2.48	97.05		688	_mp_slave_wait_for_work (mp_slave.s)
1028000	1.07	98.12		560	_mp_do_interleaved_sched (mp.c)

* -h(eavy) using basic-block counts; *
* sorted in descending order by the number of cycles executed in each *
* line; unexecuted lines are excluded *

procedure (file)	line	bytes	cycles	%	cum %
_mp_slave_wait_for_work (mp_slave.s)	99	688	12594445500	37.65	37.65
_fsiroe_90_aaac_ (FSIROE.f)	?	3392	2842420000	8.50	46.14
_fsjroe_89_aaac_ (FSJROE.f)	?	3332	2708600000	8.10	54.24
_viseul_54_aaaa_ (VISEUL.f)	?	3104	2688000000	8.03	62.27
_vjseul_57_aaaa_ (VJSEUL.f)	?	2240	1940600000	5.80	68.07
_l_227_aaaa_ (L.f)	?	1804	1433600000	4.29	72.36
_fsiroe_64_aaab_ (FSIROE.f)	?	912	1358840000	4.06	76.42
_fsjroe_63_aaab_ (FSJROE.f)	?	868	1248800000	3.73	80.15
_l_149_aaab_ (L.f)	?	1776	1109400000	3.32	83.47
_l_87_aaaa_ (L.f)	?	1460	881160000	2.63	86.10
_l_252_aaaf_ (L.f)	?	944	715600000	2.14	88.24

Processor number 4:

Profile listing generated Mon Feb 14 14:16:40 1994 with:
prof -pixie -quit 10 -clock 25 nozzle.exe nozzle.exe.Addr nozzel.exe.Counts12638

* -p[rocedures] using basic-block counts;
* sorted in descending order by the number of cycles executed in each
* procedure; unexecuted procedures are excluded

33521020588 cycles (1340.8408 seconds at 25.00 megahertz)

	cycles	%cycles	cum %	seconds	cycles /call	bytes /line	procedure (file)
12807481280 (mp_slave.s)	38.21	38.21	512.2993	5364	688		__mp_slave_wait_for_work
2843400000	8.48	46.69	113.7360	20310	3392		_fsiroe_90_aaac_ (FSIROE.f)
2807000000	8.37	55.06	112.2800	802	1620		_viseul_54_aaaa_ (VISEUL.f)
2710000000	8.08	63.15	108.4000	13550	3332		_fsjroe_89_aaac_ (FSJROE.f)
2318400000	6.92	70.06	92.7360	42	6		sqrtf (sqrtf.s)
2142000000	6.39	76.45	85.6800	630	373		_vjseul_57_aaaa_ (VJSEUL.f)
1433600000	4.28	80.73	57.3440	28672	1804		_l_227_aaaa_ (L.f)
1360800000	4.06	84.79	54.4320	4860	912		_fsiroe_64_aaab_ (FSIROE.f)
1251600000	3.73	88.52	50.0640	3129	868		_fsjroe_63_aaab_ (FSJROE.f)
1109400000	3.31	91.83	44.3760	5547	1776		_l_149_aaab_ (L.f)
881160000	2.63	94.46	35.2464	6294	1460		_l_87_aaaa_ (L.f)
715600000	2.13	96.60	28.6240	14312	944		_l_252_aaaf_ (L.f)

* -p[rocedures] using invocation counts;
* sorted in descending order by number of calls per procedure;
* unexecuted procedures are excluded

95364636 invocations total

	calls	%calls	cum%	bytes	procedure (file)
55200000	57.88	57.88		248	sqrtf (sqrtf.s)
20700000	21.71	79.59		64	cvmgp_ (CVMGP.f)
7344000	7.70	87.29		48	_mp_call_ (aux.s)
3500000	3.67	90.96		3240	_viseul_54_aaaa_ (VISEUL.f)
3400000	3.57	94.53		2608	_vjseul_57_aaaa_ (VJSEUL.f)
2388001	2.50	97.03		688	_mp_slave_wait_for_work (mp_slave.s)
1028000	1.08	98.11		560	_mp_do_interleaved_sched (mp.c)

* -h[eavy] using basic-block counts;
* sorted in descending order by the number of cycles executed in each
* line; unexecuted lines are excluded

procedure (file)	line	bytes	cycles	%	cum %
_mp_slave_wait_for_work (mp_slave.s)	99	688	12807481280	38.21	38.21
_fsiroe_90_aaac_ (FSIROE.f)	?	3392	2843400000	8.48	46.69
_fsjroe_89_aaac_ (FSJROE.f)	?	3332	2710000000	8.08	54.77
_viseul_54_aaaa_ (VISEUL.f)	?	3104	2688000000	8.02	62.79
_vjseul_57_aaaa_ (VJSEUL.f)	?	2240	1829200000	5.46	68.25
_l_227_aaaa_ (L.f)	?	1804	1433600000	4.28	72.53
_fsiroe_64_aaab_ (FSIROE.f)	?	912	1360800000	4.06	76.59
_fsjroe_63_aaab_ (FSJROE.f)	?	868	1251600000	3.73	80.32
_l_149_aaab_ (L.f)	?	1776	1109400000	3.31	83.63
_l_87_aaaa_ (L.f)	?	1460	881160000	2.63	86.26
_l_252_aaaf_ (L.f)	?	944	715600000	2.13	88.39

B.3 Parallelization of Subroutine L_f

```

C*****
SUBROUTINE L
C   INCLUDE 'gcommon.f'
   PARAMETER (ILD = 102, JLD = 72, ILDMX = 103, IVMAX = 103)
   PARAMETER (IPC = 2)
   PARAMETER (ILDP1 = 103, JLDP1 = 73)
   PARAMETER (PI=3.1415926)
   COMMON /DGDEL/FLOWVR(103,73,4,4)
   COMMON /CVGN/XNORM,RESID,PRESID,TRESID,QRESID,FRSTRD,RLIFTJ,DRAGI
   COMMON /CFLVL/ICFL,CFLXP,CFLMAX,CFL,CFLDG1,CFCRHO,CFCEI,
1    CFLPEN,CEXPEN,IFREEZE,INOFREZ,IREST,
   RDG2,TDG2,UDG2,VDG2,CONSTT,R2BR1,CDG2,CUDG2,SHKAN,SLOPE,
2    IUNST,IUNEN,ISDST,ISDEN
   COMMON /CONS/RHO(102,72,2), RHOU(102,72,2), RHOV(102,72,2), E(102,
X   72,2)
   COMMON /GASD/U(102,72), V(102,72), EI(102,72), P(102,72)
   COMMON /MSHPT/X(103,73), Y(103,73), VOL(103,73)
   COMMON /GASP/GAMMA,GM1,GGM1,CV,PR,CVISC1,CVISC2,IMETRC,RC
   COMMON /MESHV/IL,JL,ILM1,JLM1,IGRID,INS1,INS2,INS3,INS4,
$    JNS1,JNS2,JNS3,JNS4
   COMMON /GTEMP/N, M, SX, SY, IP3D, IADD, JADD, FS1V(103,4,3),
X    NSTART, NI, II, JJ, CFLTMP, ICFLAG
   COMMON /GTIME/NADV, NEND, DT, TIME, DTDG(103,73)
   COMMON /ALG/IMPLT,ILCTST,ISWVL,ILMTR,OMEGA,DELTEP,
C    IENTH,INS,DELTIL,NSWPS
   COMMON /FLPRM/IADBWL,EIWall,RL,UINF,VINF,TINF,RHOINF,CINF,
C    RM,CHARTIM,REL,TWALL,PINF,ICASE,CHARLEN,RMUINF,
$    ALPHA,CAPUINF,RCAPUINF,REINF,
$    TINWALL,AINLPHA,RINM,RINEL,RINL,TININF,
$    EINIWALL,CININF,CINAPUINF,UININF,VININF,RINMUINF,
$    RINHOINF,RINCAPUINF,PININF,RINEINF,
$    AGGLPHA,RGGM,RGGEL,RGGL,TGGINF,
$    CGGINF,CGGAPUINF,UGGINF,VGGINF,RGGMUINF,
$    RGGHOINF,RGGCAPUINF,PGGINF,RGGEINF,
$    xmcbr,xmcbrg
   COMMON /CHNG/DU(102,72,4), DUS(102,72,4)
   COMMON /GAUSS/G11(103), G12(103), G13(103), G14(103), G21(103),
X    G22(103), G23(103), G24(103), G31(103), G32(103), G33(103)
X    ), G34(103), G41(103), G42(103), G43(103), G44(103)
   CHARACTER*20 NORBCON,GRANDFL,TRANF,NORBLIN,STATFL,FGRID,FDAT
X    ,FMONT,FFLWIN,FFLWOT,P3DGRD,P3DFLW,CVGFL
   COMMON /SYSGN/ISYS,IUNNRB,IUNGRN,IUNTRN,IUNNL,IUNSTF,IUNGRD,IUNDAT,
C    IUNMT,IUNFIN,IUNFOT,IUNP3G,IUNP3F,IUNCVG,
C    NORBCON,GRANDFL,TRANF,NORBLIN,STATFL,FGRID,FDAT,
C    FMONT,FFLWIN,FFLWOT,P3DGRD,P3DFLW,CVGFL
   COMMON /IOXX/IREAD,IP3DOP,IDGBUG,ITRANP,
C    MODPR,WRST,IFMRTI,IFMRT0,IINTI
   INTEGER I11, I12, I13, I14, I15, I16, I17, I18, I19, I110, I111,
X    I112, I113, I114
   DO 20 N=1,2
   RLIFTJ = 0.
   DRAGI = 0.
   M = 3 - N
   I12 = JLM1
   DO 51 I11=2,I12
   IF (ISWVL.EQ. 1) THEN
   CALL STEGI (I11)
   ELSE
   IF (ISWVL.EQ. 3) THEN
   CALL FIVLVC (I11)
   ELSE
   IF (ISWVL.EQ. 4) THEN
   CALL FSIROE (I11)
   END IF
   END IF
   END IF
cmcb_Comenting out solid boundary fluxes on step (cowl lip)
cmcb_will force the use of the conditions specified in initl.f and bc.f
C    RESET FLUXES ON STEP

cmcb      IF ((J.GE. JNS1).AND. (J.LE. JNS2-1)) THEN
cmcb      SX=+(Y(INS2,J+1)-Y(INS2,J))
cmcb      SY=-(X(INS2,J+1)-X(INS2,J))
cmcb      PIJJ=P(INS2,J)
cmcb      FS1V(INS2-1,1,1)=0.0
cmcb      FS1V(INS2-1,2,1)=PIJJ*SX

```

```

cncb          FS1V(INS2-1,3,1)=PIJJ*SY
cncb          FS1V(INS2-1,4,1)=0.0
cncb          ENDIF
cncb_endmod

      IF (INS .EQ. 1) THEN
        CALL VISEUL (II1)
      ENDIF
C$MP_SCHEDTYPE=INTERLEAVE
C$DOACROSS SHARE (ILM1,II1,DTDG,VOL,DU,FS1V),LOCAL(DTV,II11,KDMY,I)
      DO 3 KDMY=1,4
        II11 = MOD (ILM1 - 1, 4)
        DO 2 I=2,II11+1
          DTV = DTDG(I,II1) / VOL(I,II1)
          DU(I,II1,KDMY) = -DTV * (FS1V(I,KDMY,1) - FS1V(I-1,
X          KDMY,1))
2          CONTINUE
          DO 3 I=II11+2,ILM1,4
            DTV = DTDG(I,II1) / VOL(I,II1)
            DU(I,II1,KDMY) = -DTV * (FS1V(I,KDMY,1) - FS1V(I-1,
X            KDMY,1))
            DTV = DTDG(I+1,II1) / VOL(I+1,II1)
            DU(I+1,II1,KDMY) = -DTV * (FS1V(I+1,KDMY,1) - FS1V(I,
X            KDMY,1))
            DTV = DTDG(I+2,II1) / VOL(I+2,II1)
            DU(I+2,II1,KDMY) = -DTV * (FS1V(I+2,KDMY,1) - FS1V(I+1
X            ,KDMY,1))
            DTV = DTDG(I+3,II1) / VOL(I+3,II1)
            DU(I+3,II1,KDMY) = -DTV * (FS1V(I+3,KDMY,1) - FS1V(I+2
X            ,KDMY,1))
3          CONTINUE
51        CONTINUE
        DO 1011 I=2,ILM1
          IF (ISWVL .EQ. 1) THEN
            CALL STEGJ(I)
          ELSE
            IF (ISWVL .EQ. 3) THEN
              CALL FJVLVC(I)
            ELSE
              IF (ISWVL .EQ. 4) THEN
                CALL FSJROE(I)
              END IF
            END IF
          END IF
        END IF
C      FOR NOZZLE FLOW: J=1 has now been modified to be a solid surface
        SX = -(Y(I+1,2) - Y(I,2))
        SY = (X(I+1,2) - X(I,2))
        FS1V(1,1,1) = 0.
        FS1V(1,2,1) = P(I,1) * SX
        FS1V(1,3,1) = P(I,1) * SY
        FS1V(1,4,1) = 0.
C      Also for lip - lower surface
        IF ((I .GE. INS1) .AND. (I + 1 .LE. INS2)) THEN
          SX = -(Y(I+1,JNS1) - Y(I,JNS1))
          SY = (X(I+1,JNS1) - X(I,JNS1))
          FS1V(JNS1-1,1,1) = 0.
          FS1V(JNS1-1,2,1) = P(I,JNS1-1) * SX
          FS1V(JNS1-1,3,1) = P(I,JNS1-1) * SY
          FS1V(JNS1-1,4,1) = 0.
C      UPPER LIP
          SX = -(Y(I+1,JNS2) - Y(I,JNS2))
          SY = (X(I+1,JNS2) - X(I,JNS2))
          FS1V(JNS2-1,1,1) = 0.
          FS1V(JNS2-1,2,1) = P(I,JNS2) * SX
          FS1V(JNS2-1,3,1) = P(I,JNS2) * SY
          FS1V(JNS2-1,4,1) = 0.
        ENDIF
        IF (INS .EQ. 1) THEN
          CALL VJSEUL(I)
        ENDIF
C$MP_SCHEDTYPE=INTERLEAVE
C$DOACROSS SHARE (JLM1,I,DTDG,VOL,DU,FS1V),LOCAL(DTV,II12,KDMY,II1)
      DO 5 KDMY=1,4
        II12 = MOD (JLM1 - 1, 4)
        DO 4 II1=2,II12+1
          DTV = DTDG(I,II1) / VOL(I,II1)
          DU(I,II1,KDMY) = DU(I,II1,KDMY) - DTV * (FS1V(II1,KDMY
X          ,1) - FS1V(II1-1,KDMY,1))
4          CONTINUE

```



```

DO 5 I11=I112+2,JLM1,4
  DTV = DTDG(I,I11) / VOL(I,I11,
  DU(I,I11,KDMY) = DU(I,I11,KDMY) - DTV * (FS1V(I11,KDMY
X ,1) - FS1V(I11-1,KDMY,1))
  DTV = DTDG(I,I11+1) / VOL(I,I11+1)
  DU(I,I11+1,KDMY) = DU(I,I11+1,KDMY) - DTV * (FS1V(I11+
X 1,KDMY,1) - FS1V(I11,KDMY,1))
  DTV = DTDG(I,I11+2) / VOL(I,I11+2)
  DU(I,I11+2,KDMY) = DU(I,I11+2,KDMY) - DTV * (FS1V(I11+
X 2,KDMY,1) - FS1V(I11+1,KDMY,1))
  DTV = DTDG(I,I11+3) / VOL(I,I11+3)
  DU(I,I11+3,KDMY) = DU(I,I11+3,KDMY) - DTV * (FS1V(I11+
X 3,KDMY,1) - FS1V(I11+2,KDMY,1))
5 CONTINUE
1011 CONTINUE
C FOR NOZZLE FLOW, BLANK OUT LIP - Eliminated
  I17 = INS2 - 1
  I18 = JNS2 - 1
C$MP SCHEDTYPE=INTERLEAVE
C$DOACROSS IF((INS2 - INS1) * (JNS2 - JNS1) .GT. 31),SHARE(JNS1,I18,I17,
C$4 INS1,DU),LOCAL(I113,KDMY,I11,I)
  DO 7 KDMY=1,4
    DO 7 I11=JNS1,I18
      I113 = MOD (I17 - INS1 + 1, 4)
      DO 6 I=INS1,I113+INS1-1
        DU(I,I11,KDMY) = 0.
6 CONTINUE
      DO 7 I=I113+INS1,I17,4
        DU(I,I11,KDMY) = 0.
        DU(I+1,I11,KDMY) = 0.
        DU(I+2,I11,KDMY) = 0.
        DU(I+3,I11,KDMY) = 0.
7 CONTINUE
      IF ((IREST .EQ. 1) .AND. (N .EQ. 1)) CALL REST
      IF (IMPLT .EQ. 1) THEN
        CALL LIMP
      ELSE
        IF (IMPLT .NE. 0) THEN
          PRINT *, 'WIERD VALUE OF IMPLT ', IMPLT
          STOP
        END IF
      END IF
C FOR NOZZLE FLOW, BLANK OUT LIP - Eliminated
  I19 = INS2 - 1
  I110 = JNS2 - 1
C$MP SCHEDTYPE=INTERLEAVE
C$DOACROSS IF((INS2 - INS1) * (JNS2 - JNS1) .GT. 31),SHARE(JNS1,I110,I19
C$4 ,INS1,DU),LOCAL(I114,KDMY,I11,I)
  DO 9 KDMY=1,4
    DO 9 I11=JNS1,I110
      I114 = MOD (I19 - INS1 + 1, 4)
      DO 8 I=INS1,I114+INS1-1
        DU(I,I11,KDMY) = 0.
8 CONTINUE
      DO 9 I=I114+INS1,I19,4
        DU(I,I11,KDMY) = 0.
        DU(I+1,I11,KDMY) = 0.
        DU(I+2,I11,KDMY) = 0.
        DU(I+3,I11,KDMY) = 0.
9 CONTINUE
    RN=N
    RNM1 = RN - 1.
    RESID = 0.
    IF (IDGBUG .EQ. 0) THEN
C
C Added parallel construct by hand - pfa does not know how to use
C reduction variables - mcb
C
C$MP SCHEDTYPE=INTERLEAVE
C$DOACROSS REDUCTION(RESID),LOCAL(I,JX,J,RHOOLD,DRHO,RUOLD,DRHOU,RVOLD,
C$4 DRHOV,REOLD,DEVL)
  DO 10 I=2,I1M1
    DO 10 JX=2,JLM1
      RHOOLD = RHO(I,(JL-JX+1),1)
      RHO(I,(JL-JX+1),M) = (RNM1 * RHO(I,(JL-JX+1),M) + RHO(
X I,(JL-JX+1),N) + DU(I,(JL-JX+1),1)) / RN
      DRHO = RHO(I,(JL-JX+1),M) - RHOOLD
      RUOLD = RHOU(I,(JL-JX+1),1)
      RHOU(I,(JL-JX+1),M) = (RNM1 * RHOU(I,(JL-JX+1),M) +

```

```

X RHO(I, (JL-JX+1), N) + DU(I, (JL-JX+1), 2)) / RN
DRHO = RHO(I, (JL-JX+1), M) - RUOLD
RVOLD = RHOV(I, (JL-JX+1), 1)
RHOV(I, (JL-JX+1), M) = (RNM1 * RHOV(I, (JL-JX+1), M) +
X RHOV(I, (JL-JX+1), N) + DU(I, (JL-JX+1), 3)) / RN
DRHOV = RHOV(I, (JL-JX+1), M) - RVOLD
REOLD = E(I, (JL-JX+1), 1)
E(I, (JL-JX+1), M) = (RNM1 * E(I, (JL-JX+1), M) + E(I, (JL-
X JX+1), N) + DU(I, (JL-JX+1), 4)) / RN
DEVL = E(I, (JL-JX+1), M) - REOLD
RESID = RESID + ((DRHO / RHOINF) ** 2 + (DRHO /
X RHOV(I, (JL-JX+1), M) + DU(I, (JL-JX+1), 3)) / RN
RESID = RESID + ((DRHO / RHOINF) ** 2 + (DRHOV /
X RHOV(I, (JL-JX+1), M) + DU(I, (JL-JX+1), 3)) / RN
RESID = RESID + ((DRHOV / RHOINF) ** 2 + (DEVL / REINF) ** 2)
X / (DTDG(I, (JL-JX+1)) * DTDG(I, (JL-JX+1)))
10 CONTINUE
C$MP SCHEDTYPE=INTERLEAVE
C$DOACROSS SHARE (ILM1, JLM1, JL, U, M, RHO, RHO, V, RHOV, EI, E, P, GM1), LOCAL(I, JX
C$ )
DO 11 I=2, ILM1
DO 11 JX=2, JLM1
U(I, (JL-JX+1)) = RHO(I, (JL-JX+1), M) / RHO(I, (JL-JX+1)
X ,M)
V(I, (JL-JX+1)) = RHOV(I, (JL-JX+1), M) / RHO(I, (JL-JX+1)
X ,M)
EI(I, (JL-JX+1)) = E(I, (JL-JX+1), M) / RHO(I, (JL-JX+1), M
X ) - 0.5 * (U(I, (JL-JX+1)) * U(I, (JL-JX+1)) + V(I, (JL-JX+1)) * V(
X I, (JL-JX+1)))
P(I, (JL-JX+1)) = GM1 * RHO(I, (JL-JX+1), M) * EI(I, (JL-
X JX+1))
11 CONTINUE
ELSE
C
C Commented out max accumulation code - just used for output and
C difficult to parallelize - mcb
C
Cmcb RESMX=0.0
Cmcb IRSDMX=2
Cmcb JRSDMX=2
C$MP SCHEDTYPE=INTERLEAVE
C$DOACROSS REDUCTION(RESID), LOCAL(I, JX, J, RHOOLD, DRHO,
C$ RUOLD, DRHO, RVOLD, DRHOV, REOLD, DEVL, TERM)
DO 12 I=2, ILM1
DO 12 JX=2, JLM1
RHOOLD = RHO(I, (JL-JX+1), 1)
RHO(I, (JL-JX+1), M) = (RNM1 * RHO(I, (JL-JX+1), M) + RHO(
X I, (JL-JX+1), N) + DU(I, (JL-JX+1), 1)) / RN
DRHO = RHO(I, (JL-JX+1), M) - RHOOLD
RUOLD = RHO(I, (JL-JX+1), 1)
RHO(I, (JL-JX+1), M) = (RNM1 * RHO(I, (JL-JX+1), M) +
X RHO(I, (JL-JX+1), N) + DU(I, (JL-JX+1), 2)) / RN
DRHO = RHO(I, (JL-JX+1), M) - RUOLD
RVOLD = RHOV(I, (JL-JX+1), 1)
RHOV(I, (JL-JX+1), M) = (RNM1 * RHOV(I, (JL-JX+1), M) +
X RHOV(I, (JL-JX+1), N) + DU(I, (JL-JX+1), 3)) / RN
DRHOV = RHOV(I, (JL-JX+1), M) - RVOLD
REOLD = E(I, (JL-JX+1), 1)
E(I, (JL-JX+1), M) = (RNM1 * E(I, (JL-JX+1), M) + E(I, (JL-
X JX+1), N) + DU(I, (JL-JX+1), 4)) / RN
DEVL = E(I, (JL-JX+1), M) - REOLD
TERM = ((DRHO / RHOINF) ** 2 + (DRHO / RHOV(I, (JL-JX+1), M) + DU(I, (JL-JX+1), 3)) / RN
X + (DRHOV / RHOV(I, (JL-JX+1), M) + DU(I, (JL-JX+1), 3)) / RN
X + (DEVL / REINF) ** 2) / (DTDG(I, (JL-
X JX+1)) * DTDG(I, (JL-JX+1)))
Cmcb IF (RESMX .LE. TERM) THEN
Cmcb RESMX=TERM
Cmcb IRSDMX=I
Cmcb JRSDMX=J
Cmcb ENDIF
RESID=RESID+TERM
12 CONTINUE
C$MP SCHEDTYPE=INTERLEAVE
C$DOACROSS SHARE (ILM1, JLM1, JL, U, M, RHO, RHO, V, RHOV, EI, E, P, GM1), LOCAL(I, JX
C$ )
DO 13 I=2, ILM1
DO 13 JX=2, JLM1
U(I, (JL-JX+1)) = RHO(I, (JL-JX+1), M) / RHO(I, (JL-JX+1)
X ,M)
V(I, (JL-JX+1)) = RHOV(I, (JL-JX+1), M) / RHO(I, (JL-JX+1)
X ,M)
EI(I, (JL-JX+1)) = E(I, (JL-JX+1), M) / RHO(I, (JL-JX+1), M
X ) - 0.5 * (U(I, (JL-JX+1)) * U(I, (JL-JX+1)) + V(I, (JL-JX+1)) * V(

```

```

X I, (JL-JX+1)))
      P(I, (JL-JX+1)) = GM1 * RHO(I, (JL-JX+1), M) * EI(I, (JL-
X      JX+1))
13      CONTINUE
      PRINT *, 'MAX RESID ', SORT (RESMX), 'OCCURS AT ', IRSDMX,
X      JRSDMX
      ENDIF
      RESID = SORT (RESID) / ((ILM1 - 1) * (JLM1 - 1))
      CALL BC
20 CONTINUE
RETURN
END

```

Appendix C: Pressure and Mach Number Contours

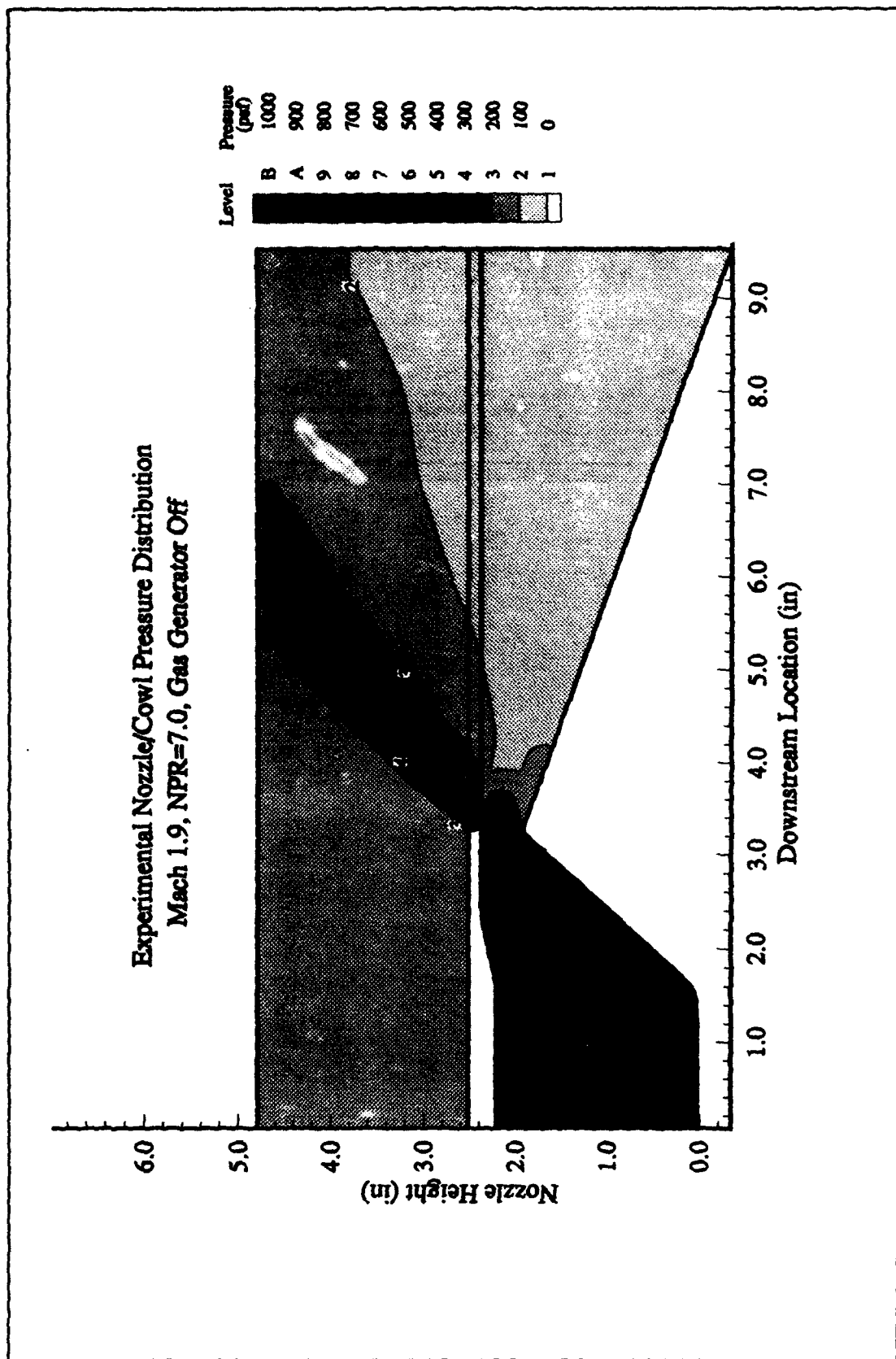


Figure C-1 Pressure Contours, Mach 1.9, Gas Generator Off

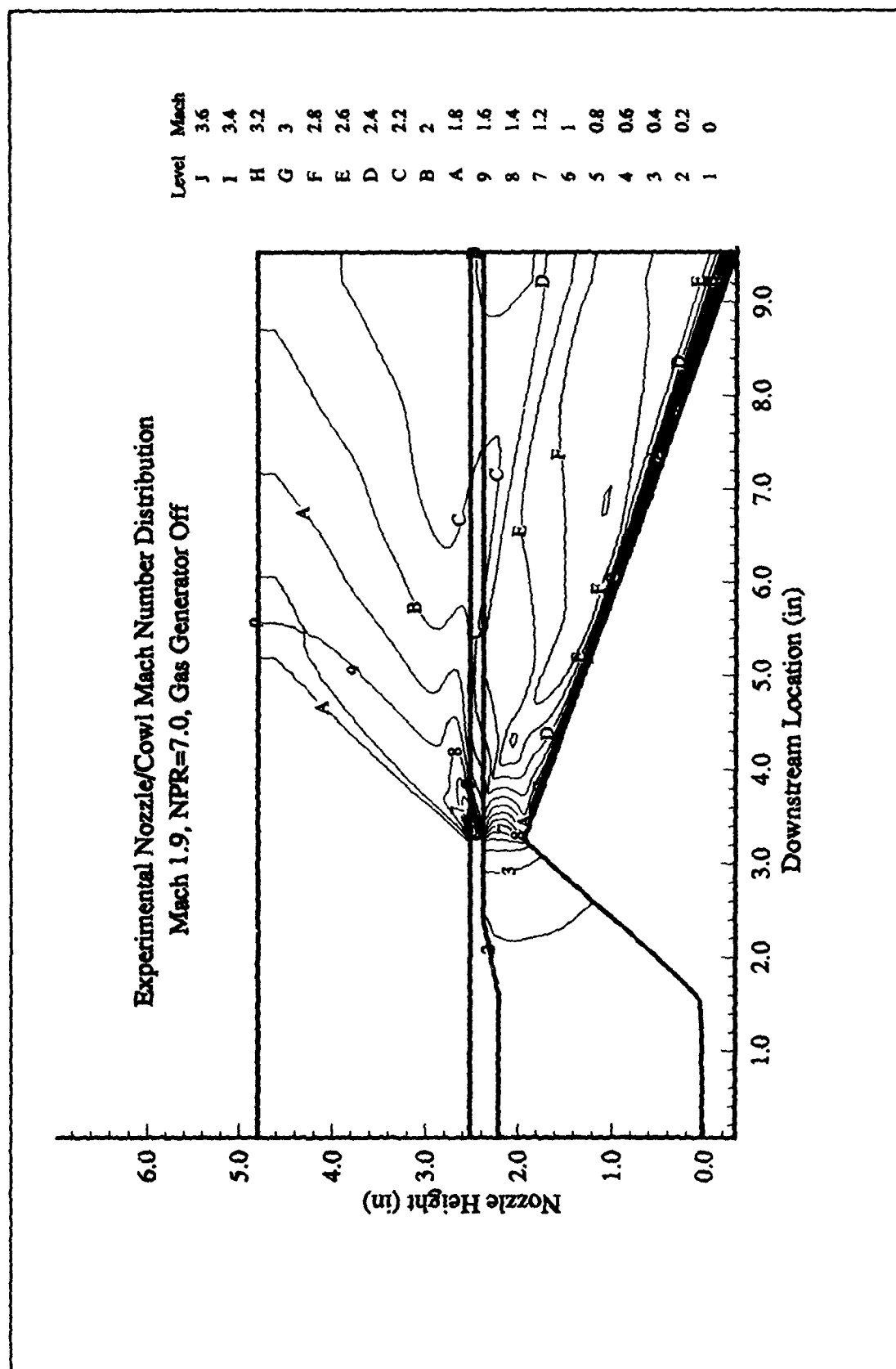


Figure C-2 Mach Number Contours, Mach 1.9, Gas Generator Off

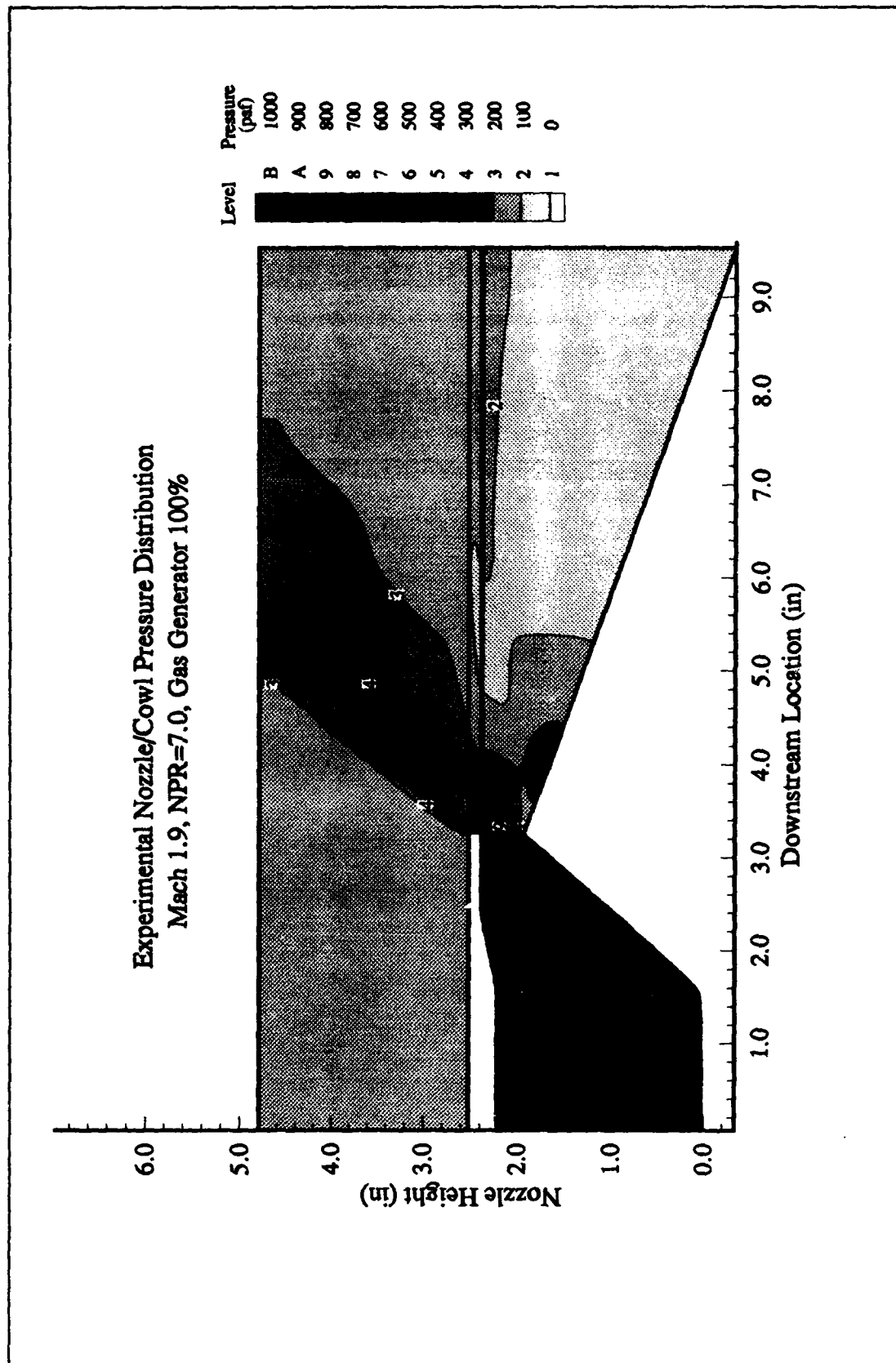


Figure C-3 Pressure Contours, Mach 1.9, Gas Generator 100%

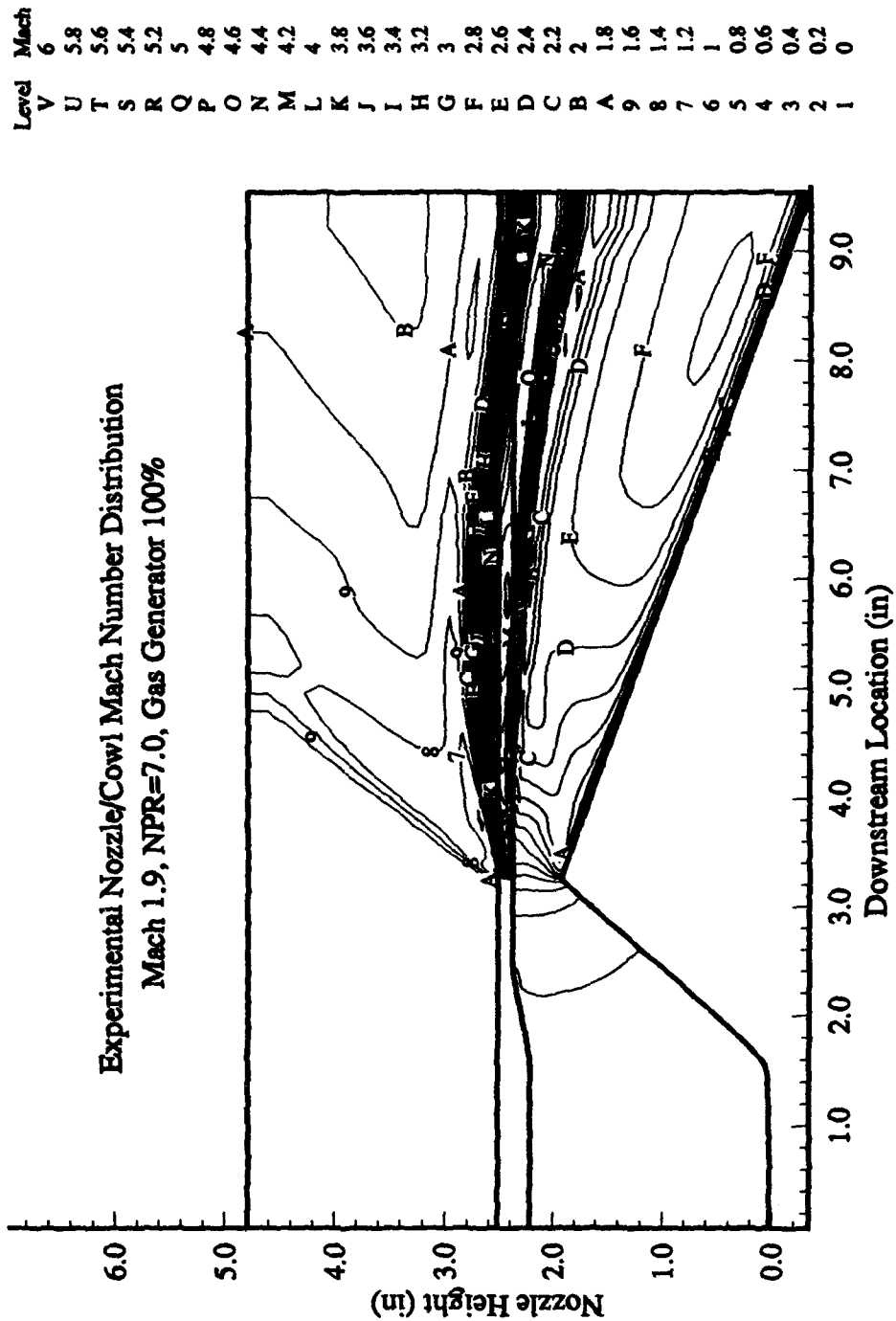


Figure C-4 Mach Number Contours, Mach 1.9, Gas Generator 100%

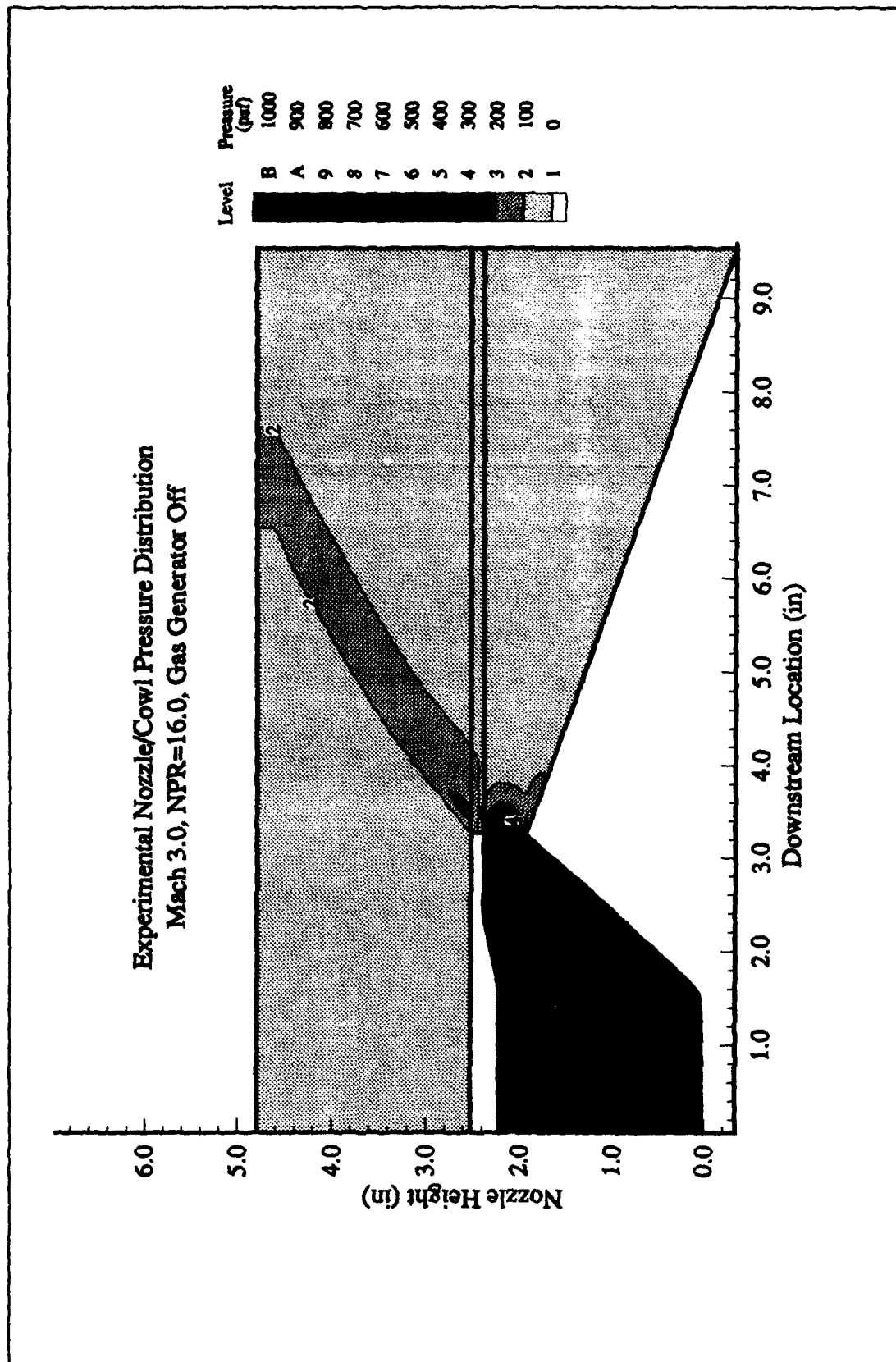


Figure C-5 Pressure Contours, Mach 3.0, Gas Generator Off

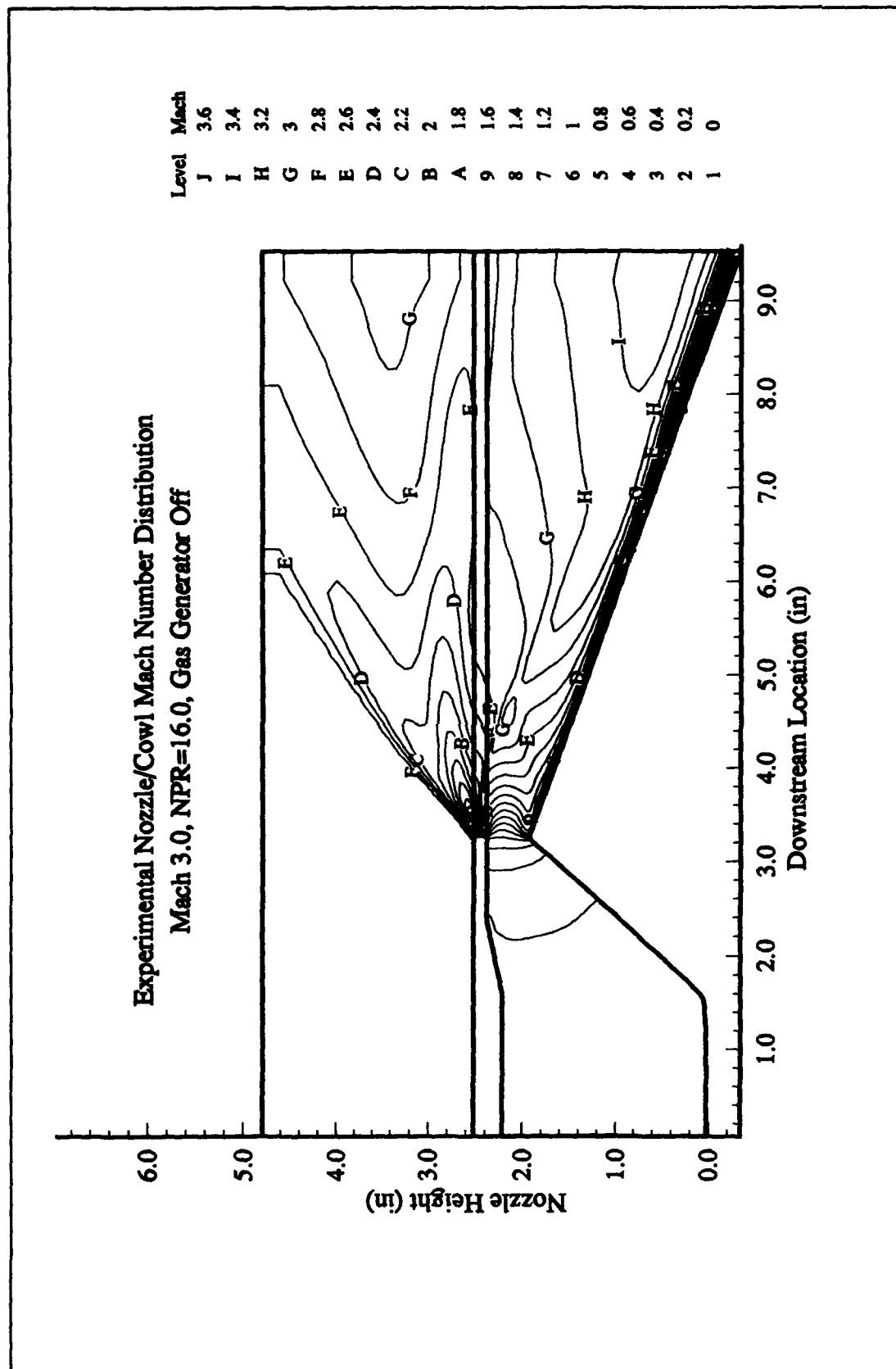


Figure C-6 Mach Number Contours, Mach 3.0, Gas Generator Off

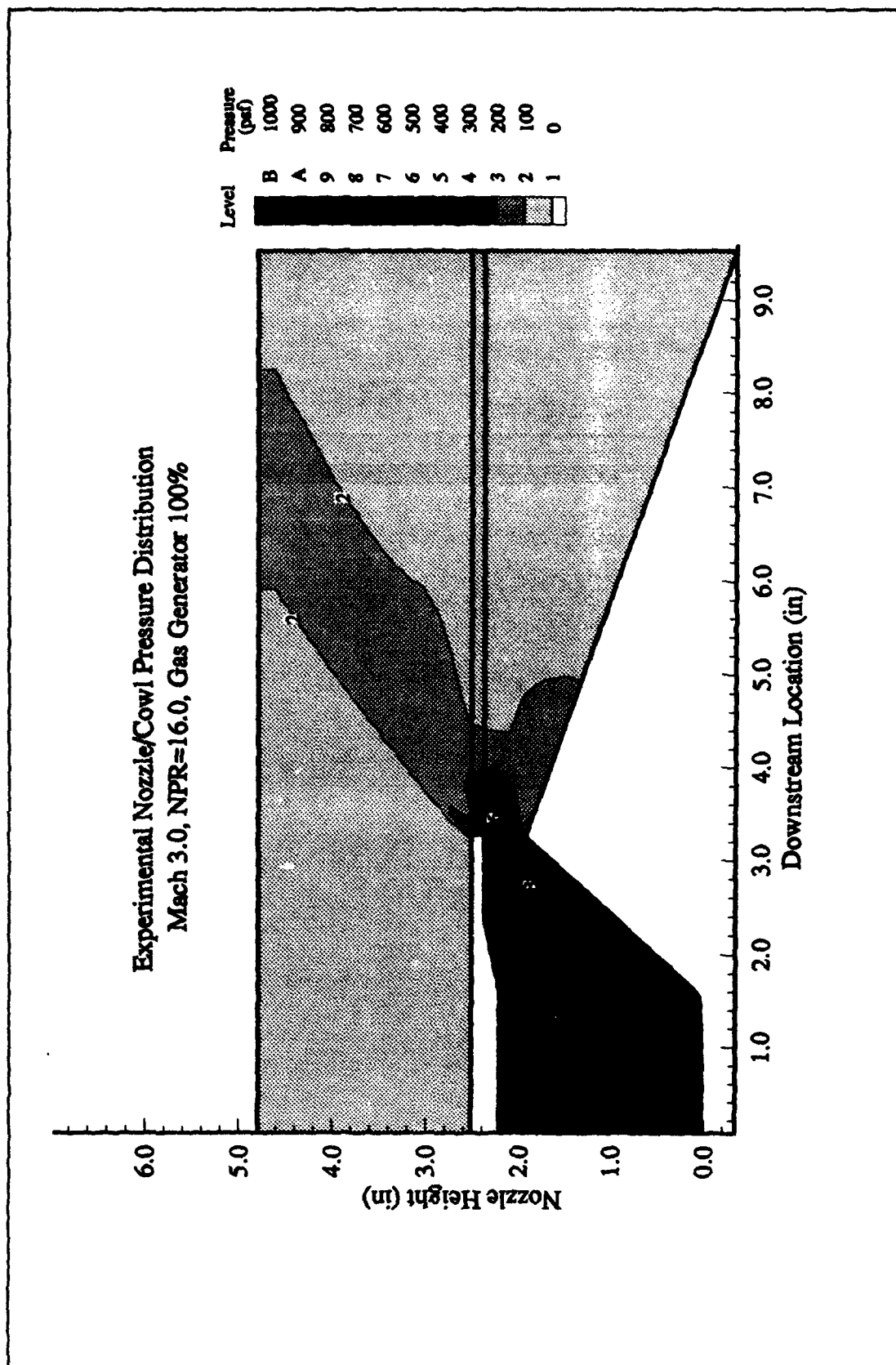


Figure C-7 Pressure Contours, Mach 3.0, Gas Generator 100%

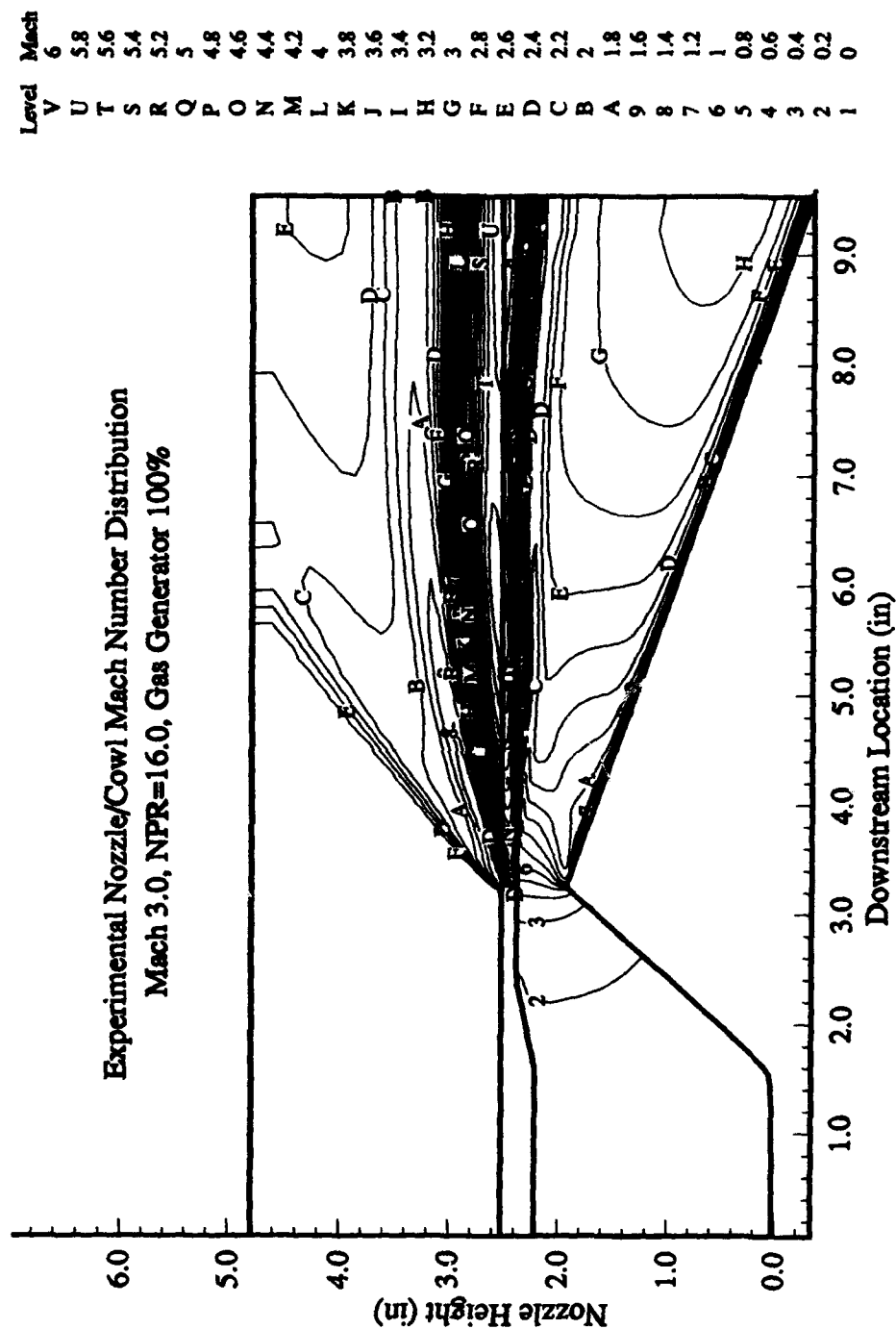


Figure C-8 Mach Number Contours, Mach 3.0, Gas Generator 100%

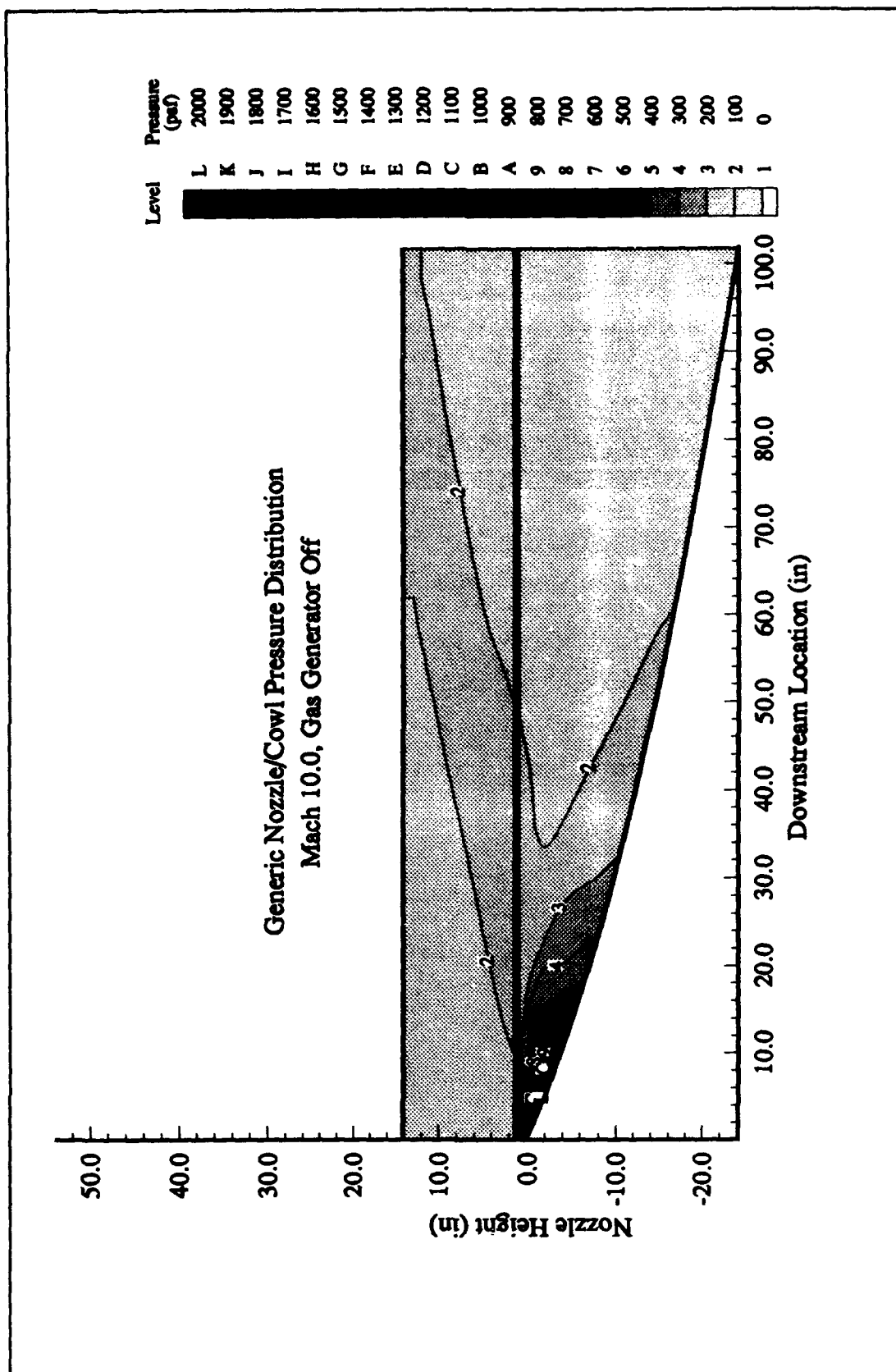


Figure C-9 Pressure Contours, Mach 10, Gas Generator Off

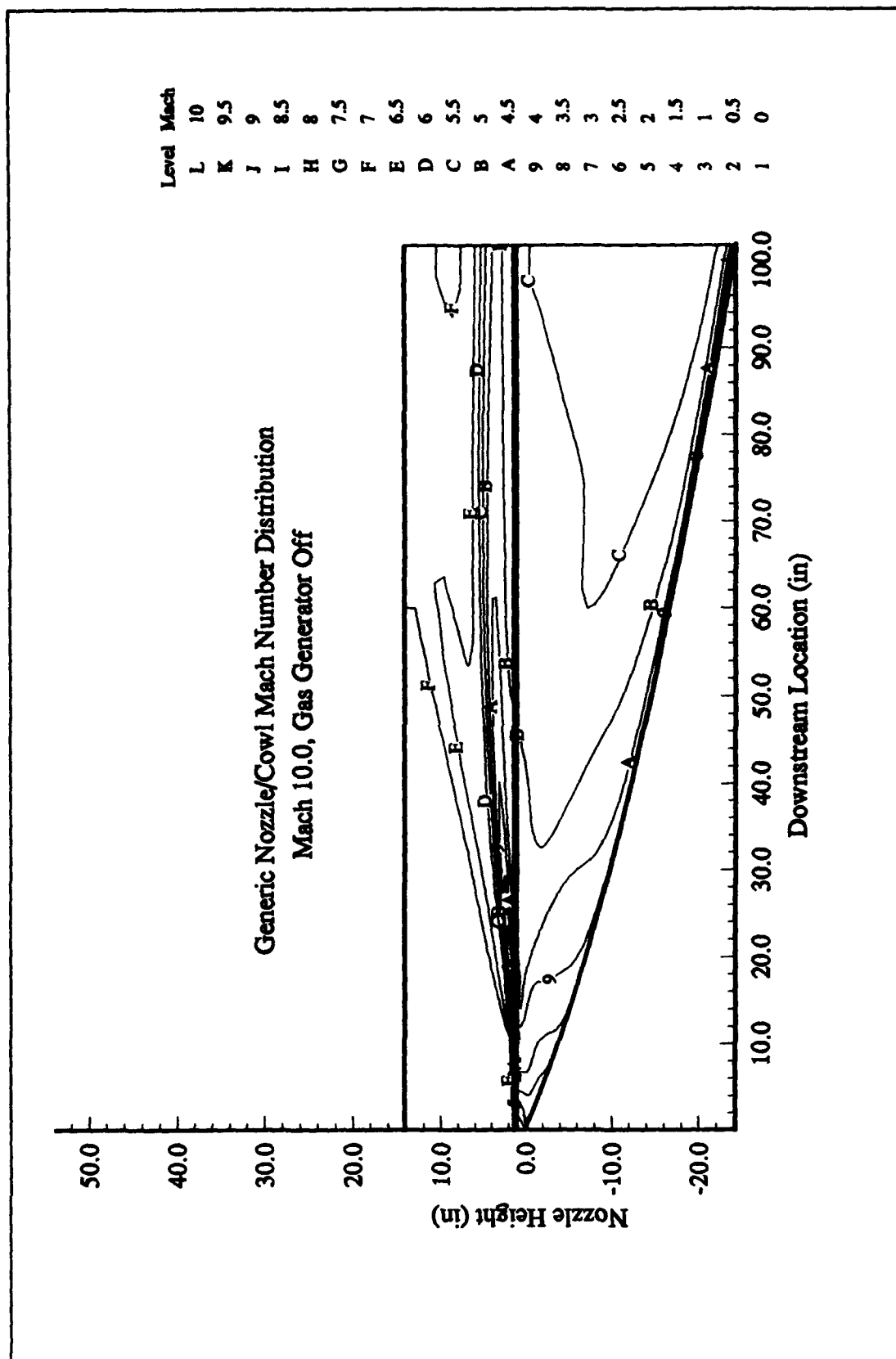


Figure C-10 Mach Number Contours, Mach 10, Gas Generator Off

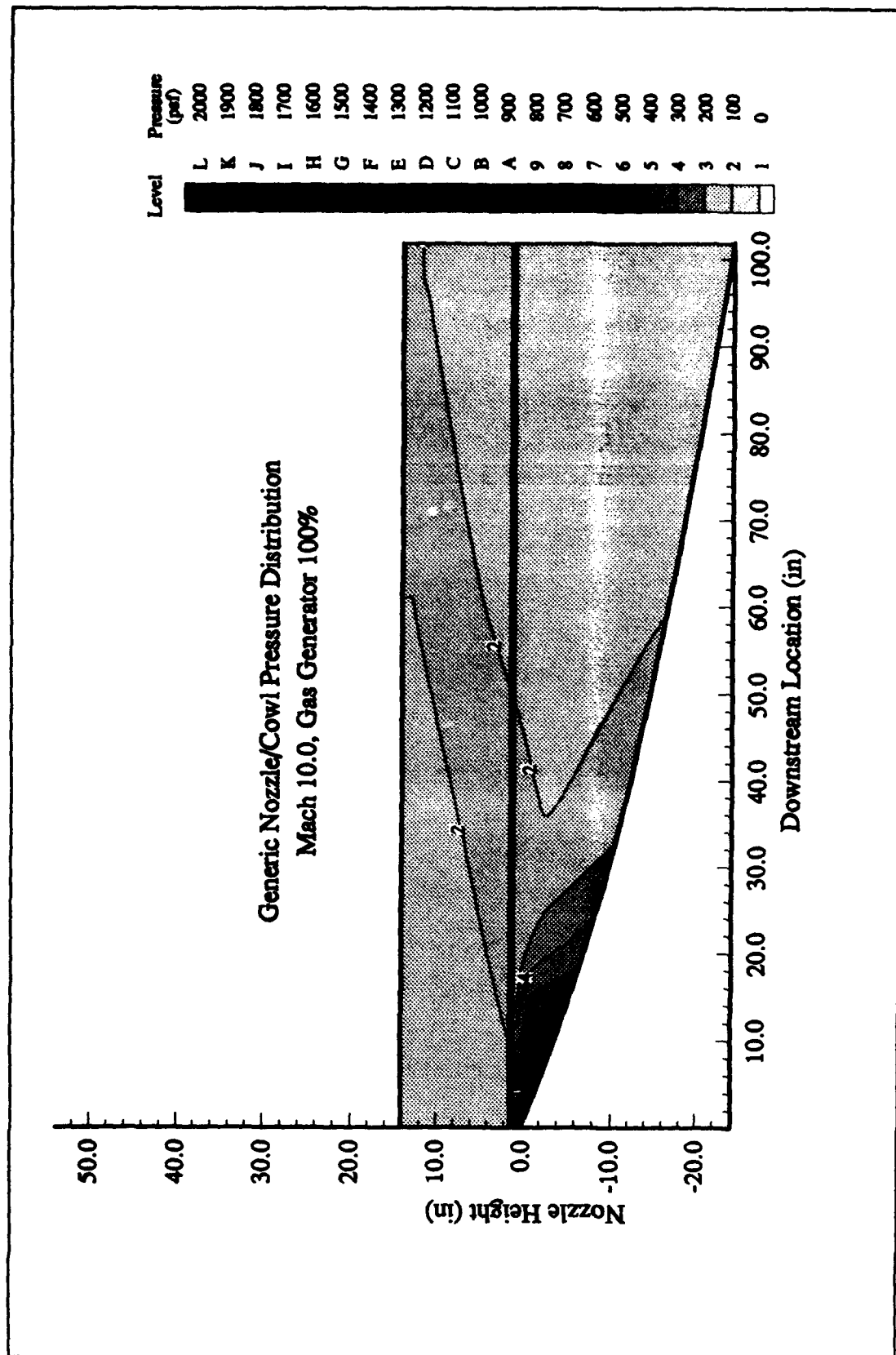


Figure C-11 Pressure Contours, Mach 10, Gas Generator 100%

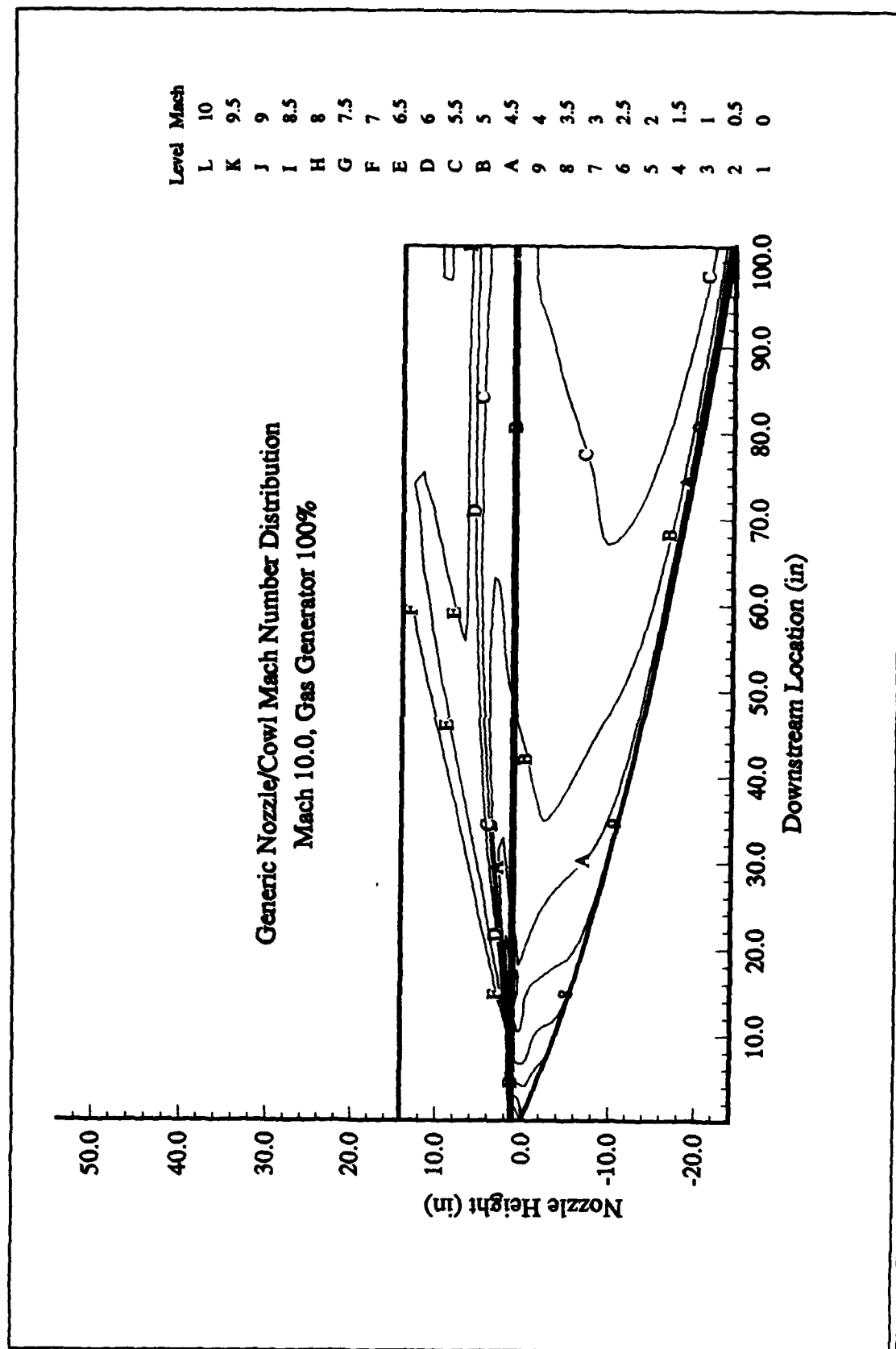


Figure C-12 Mach Number Contours, Mach 10, Gas Generator 100%

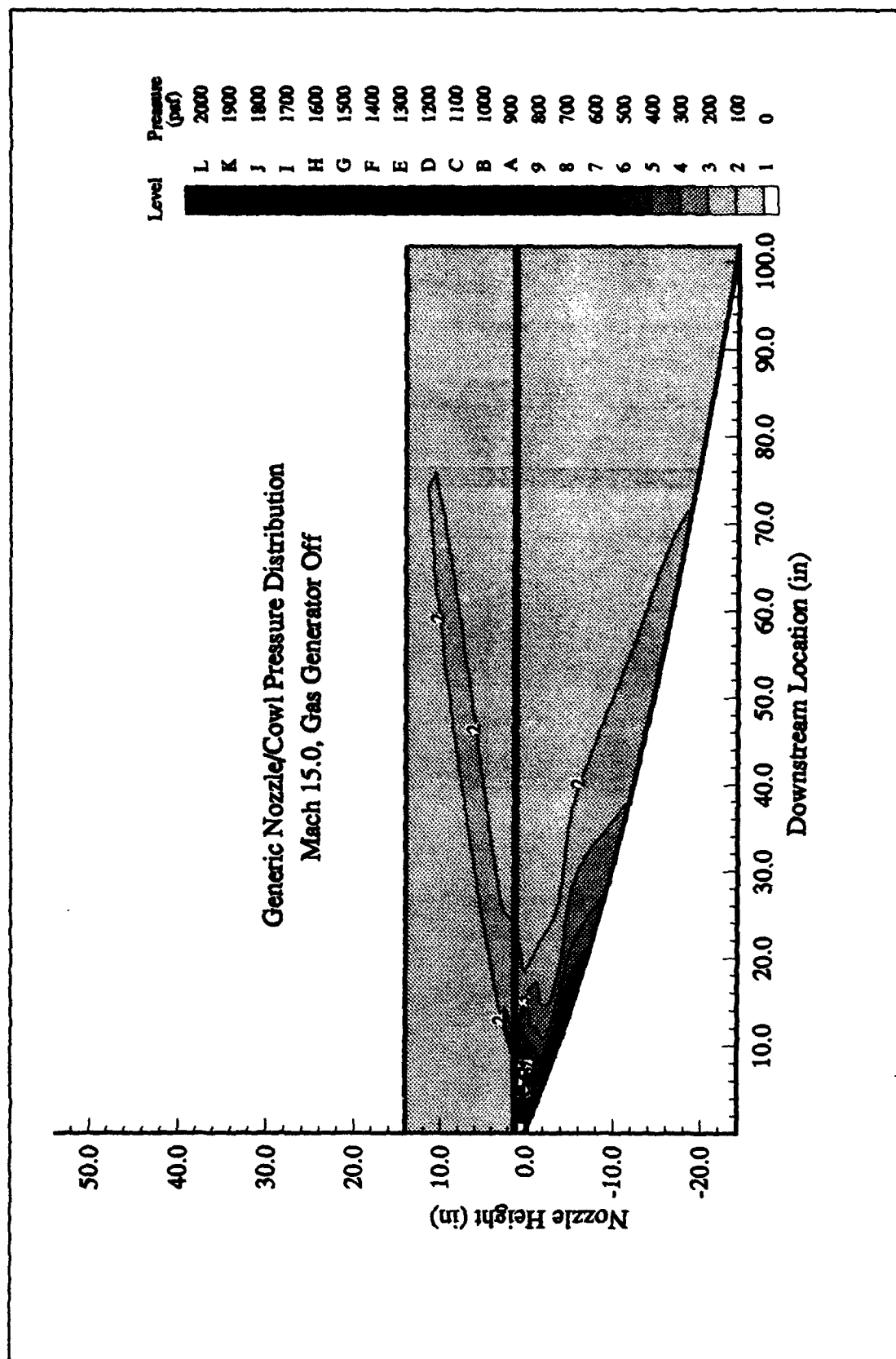


Figure C-13 Pressure Contours, Mach 15, Gas Generator Off

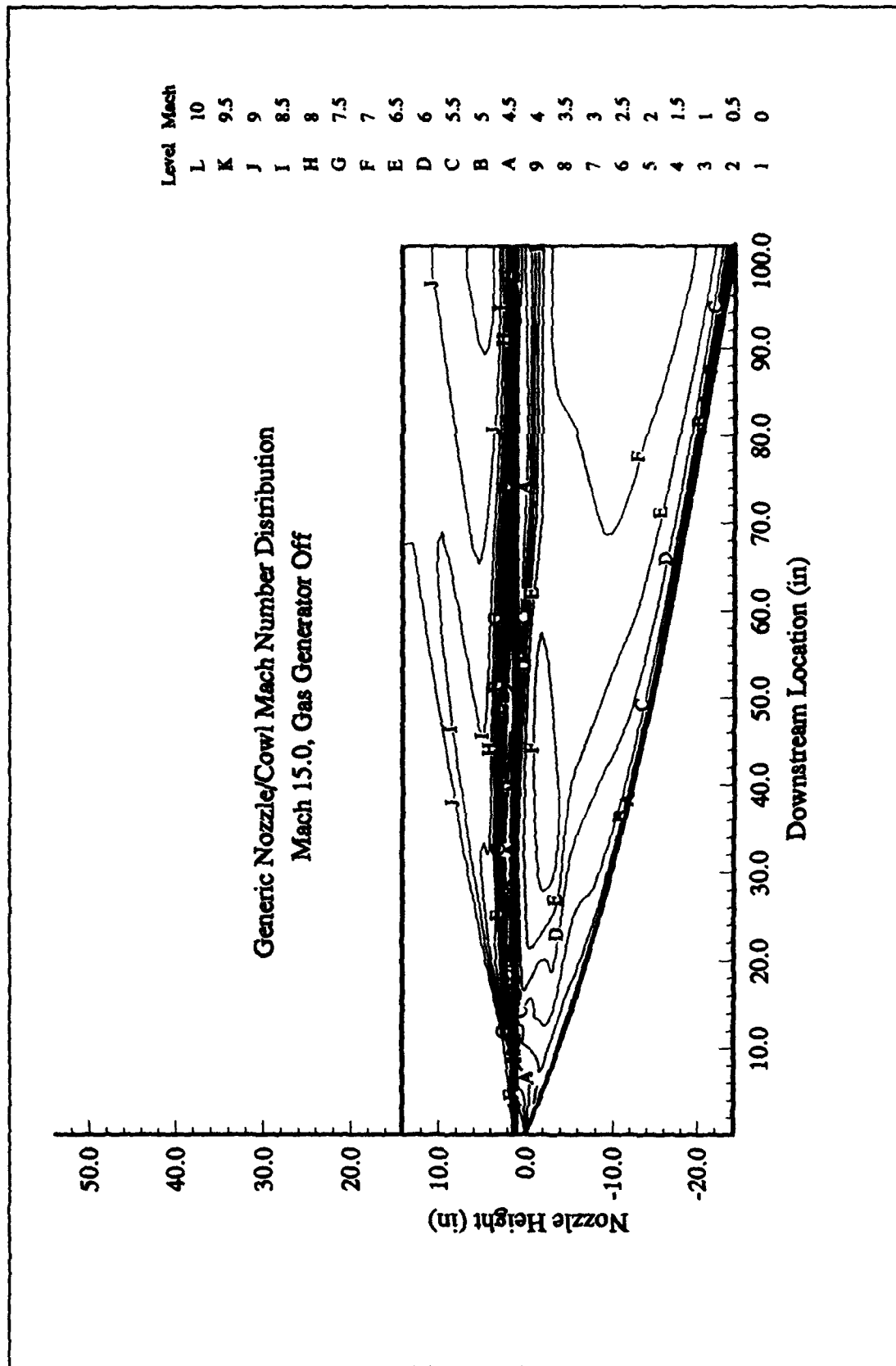


Figure C-14 Mach Number Contours, Mach 15, Gas Generator Off

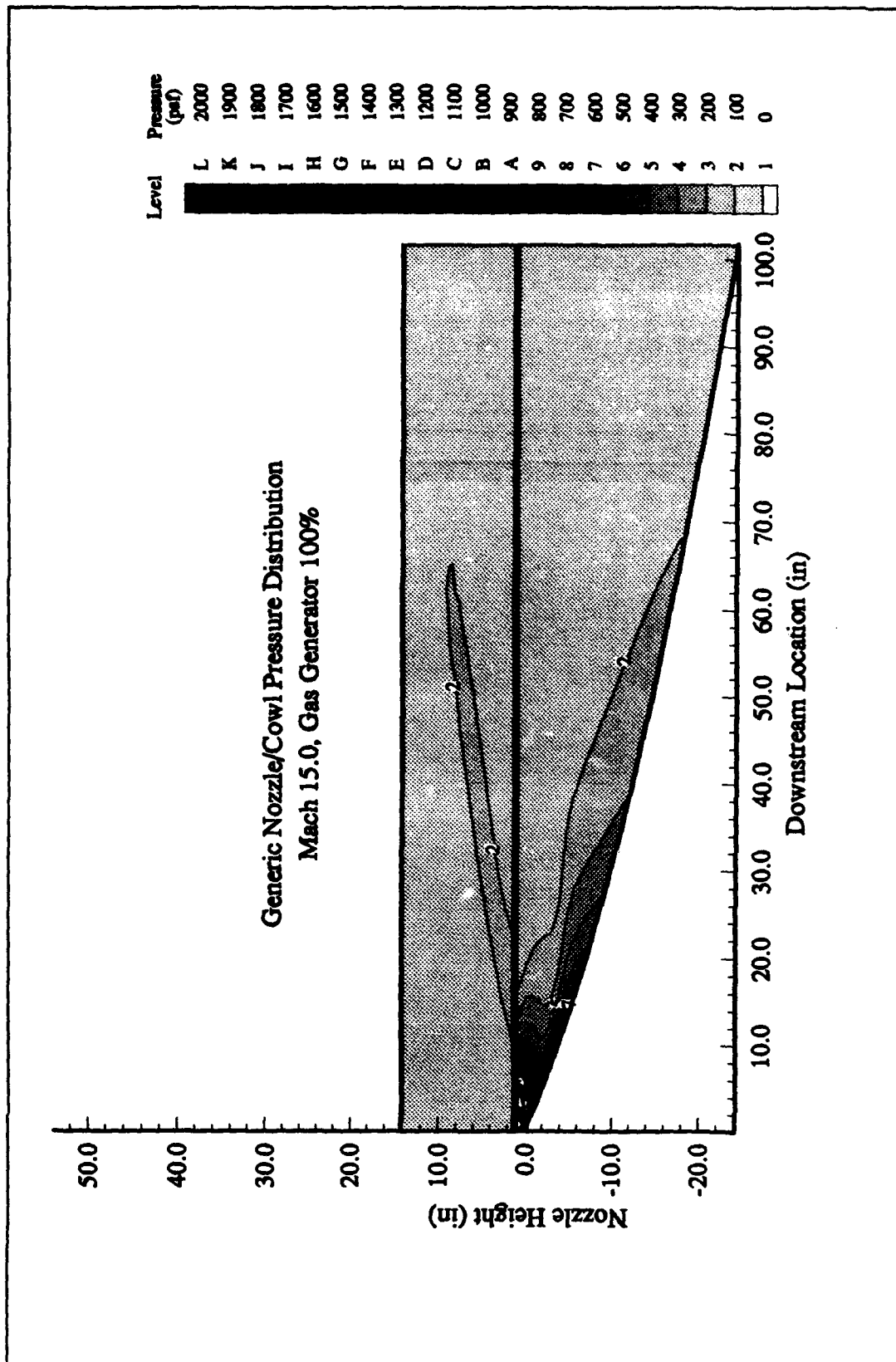


Figure C-15 Pressure Contours, Mach 15, Gas Generator 100%

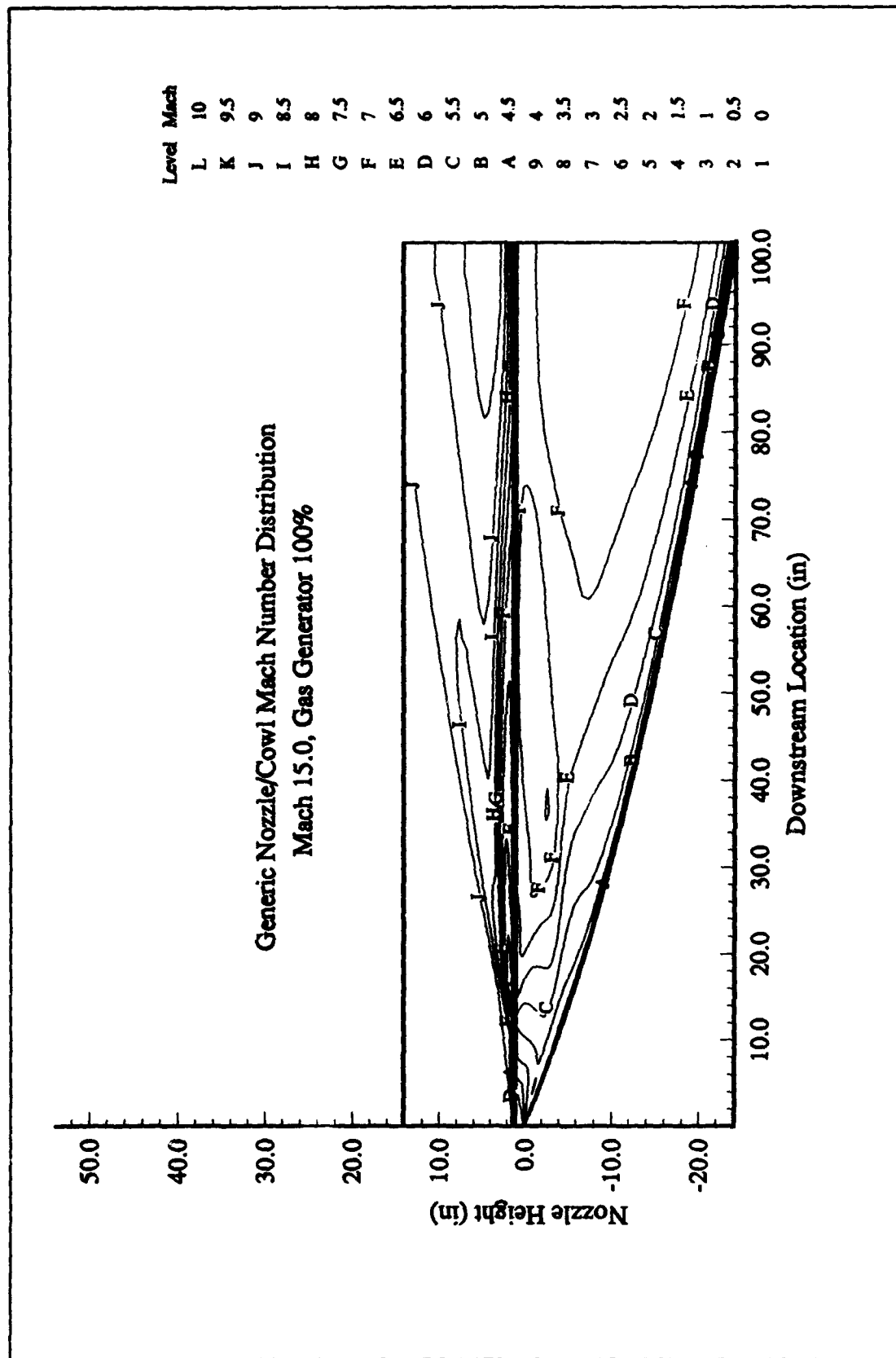


Figure C-16 Mach Number Contours, Mach 15, Gas Generator 100%

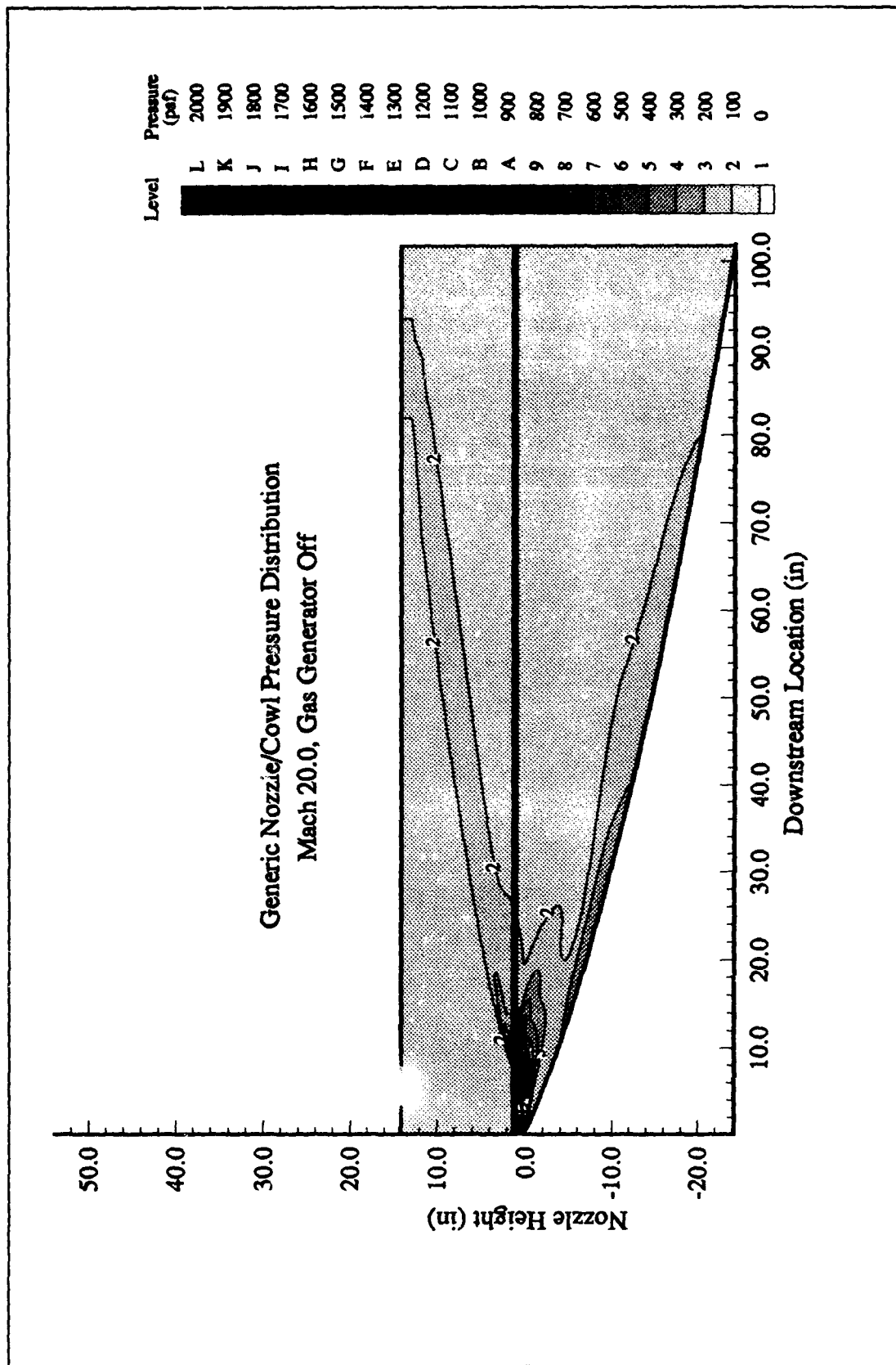


Figure C-17 Pressure Contours, Mach 20, Gas Generator Off

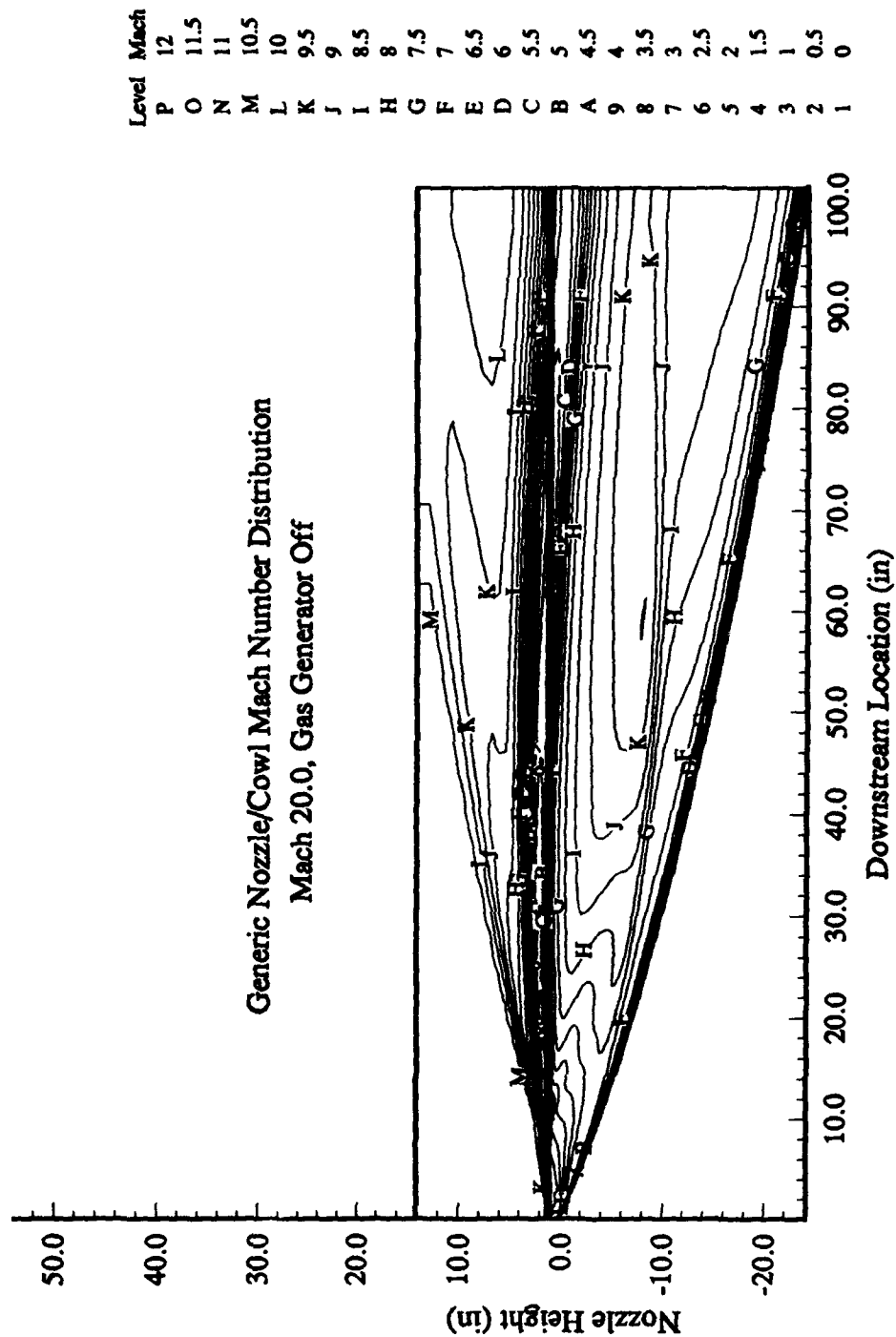


Figure C-18 Mach Number Contours, Mach 20, Gas Generator Off

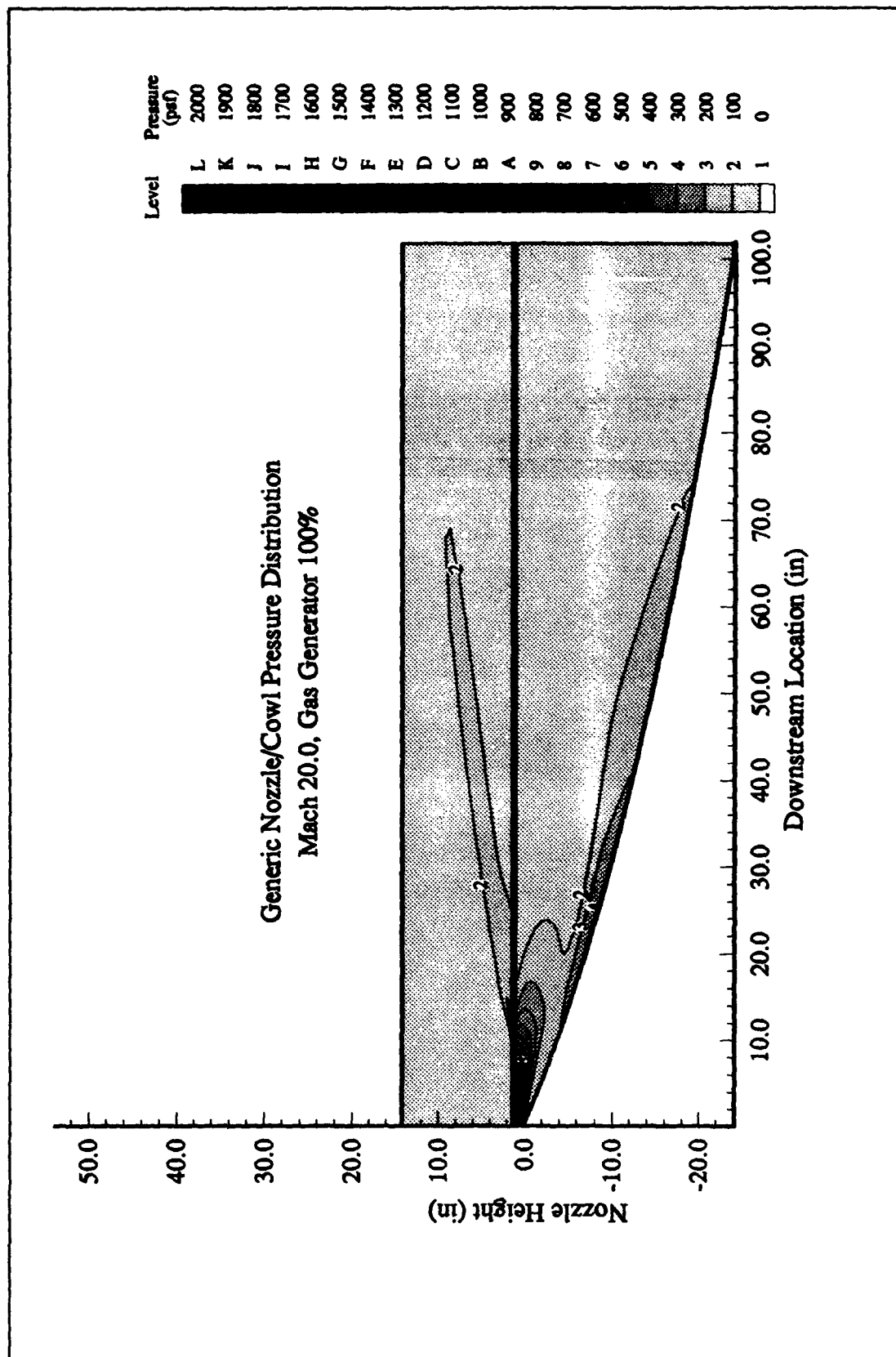


Figure C-19 Pressure Contours, Mach 20, Gas generator 100%

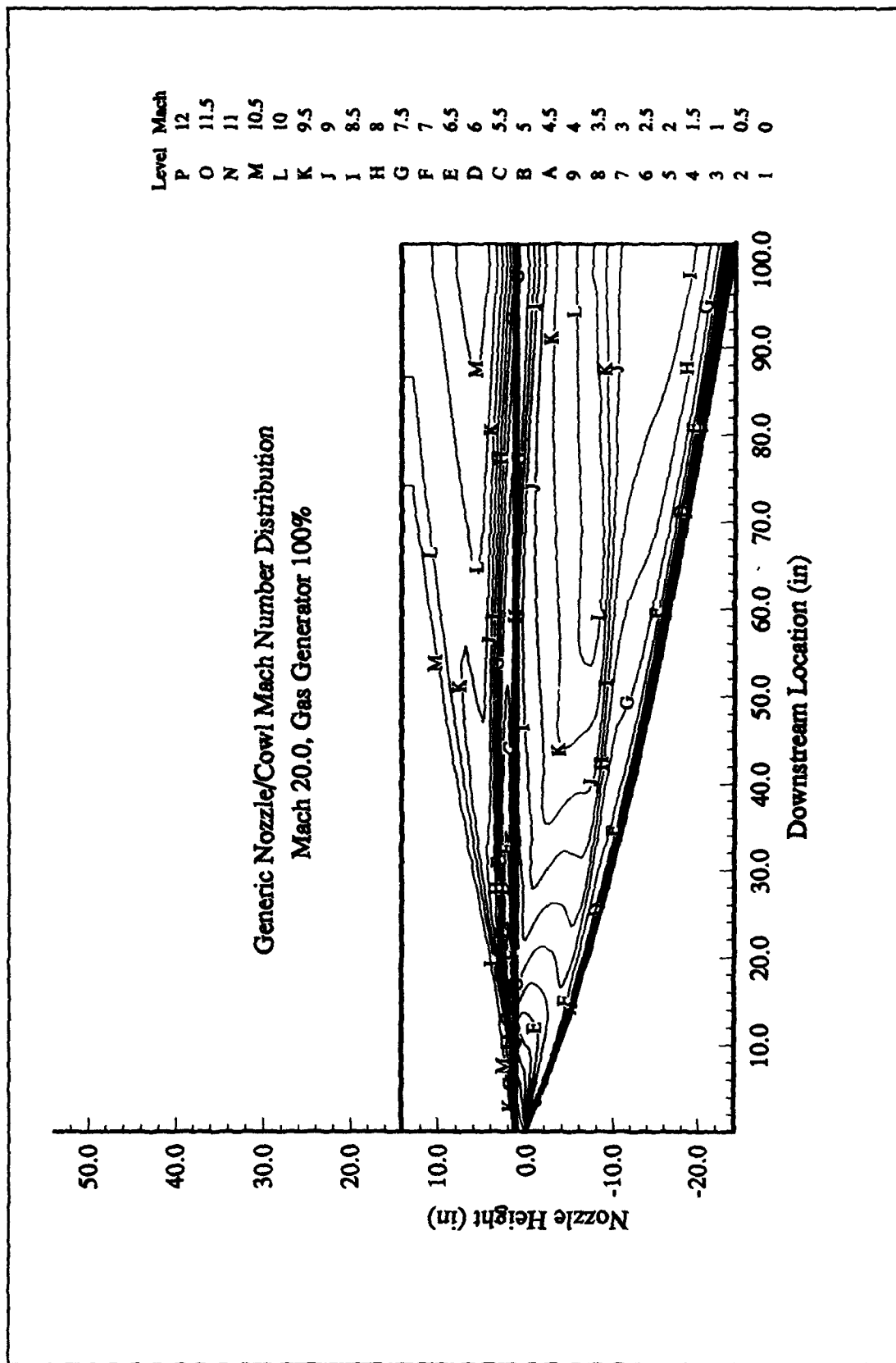


Figure C-20 Mach Number Contours, Mach 20, Gas Generator 100%

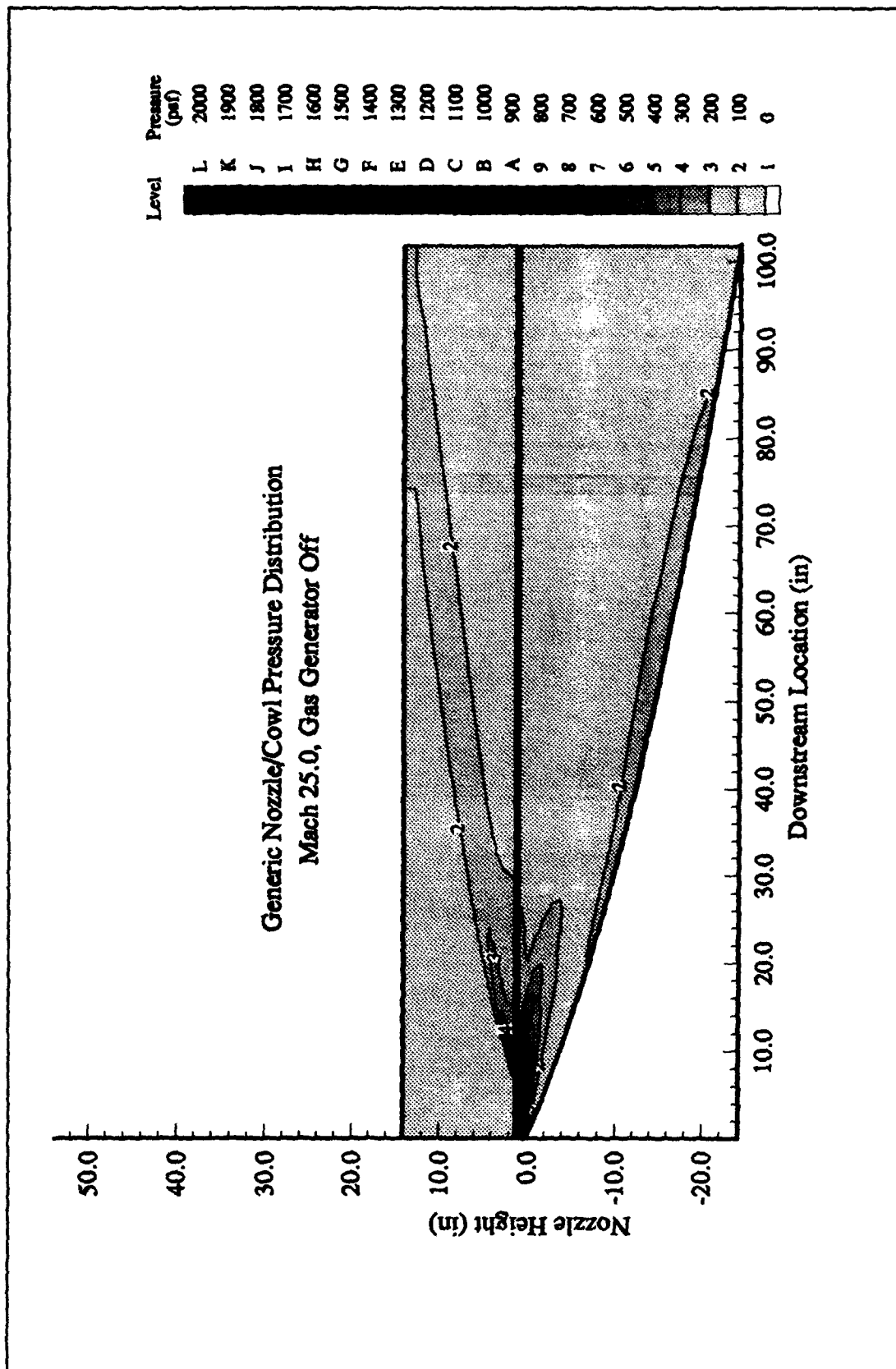


Figure C-21 Pressure Contours, Mach 25, Gas Generator Off

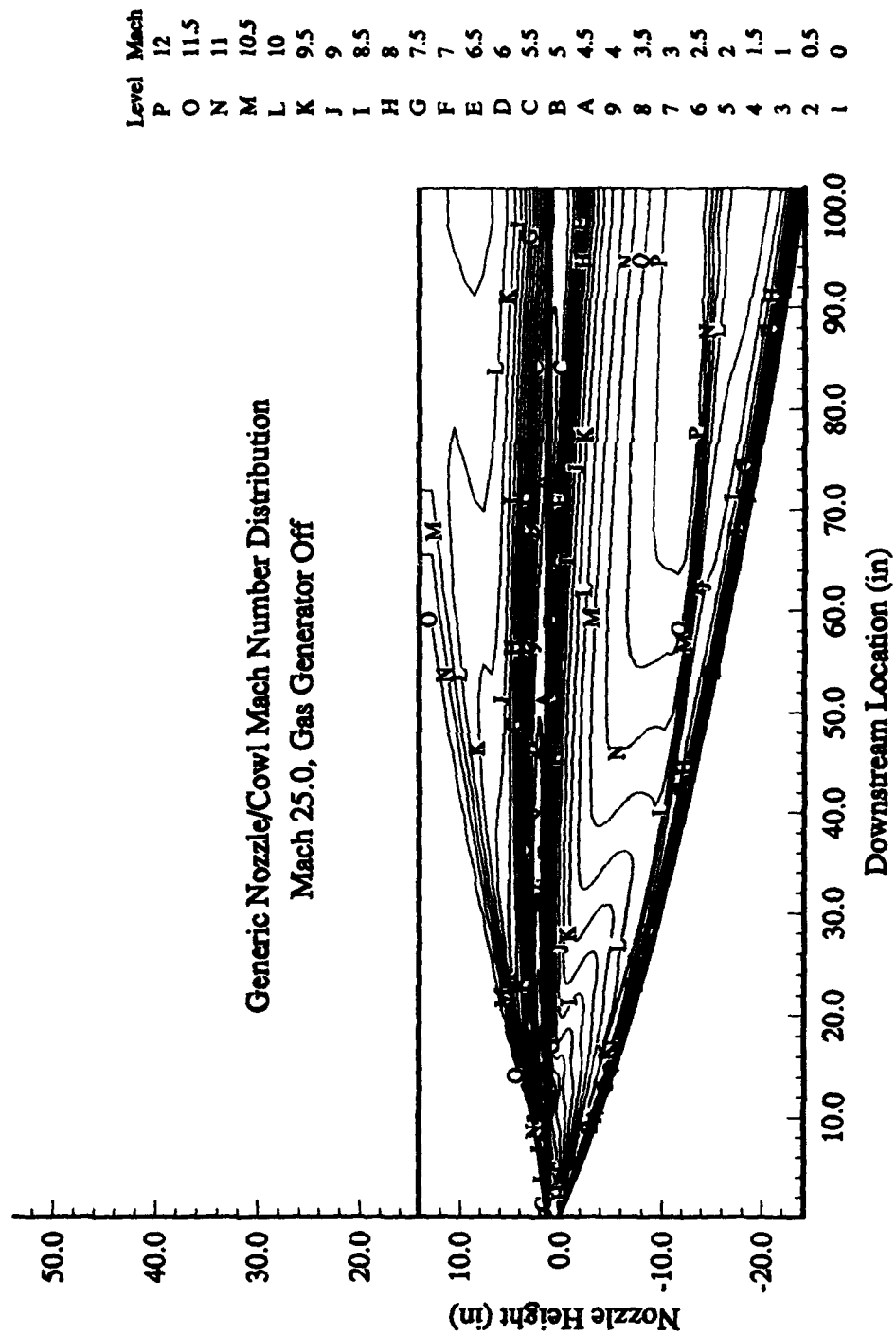


Figure C-22 Mach Number Contours, Mach 25, Gas Generator Off

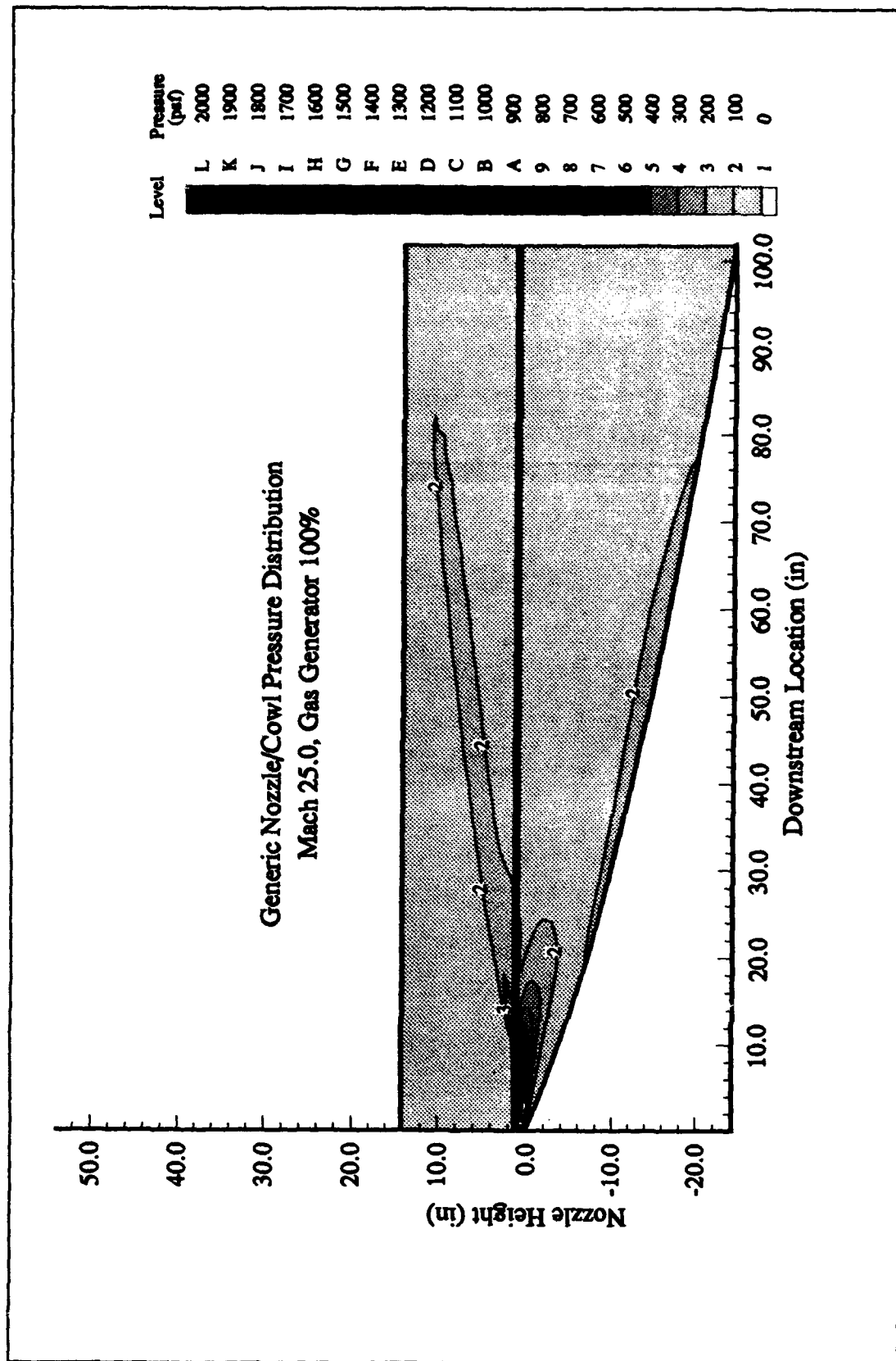


Figure C-23 Pressure Contours, Mach 25, Gas Generator 100%

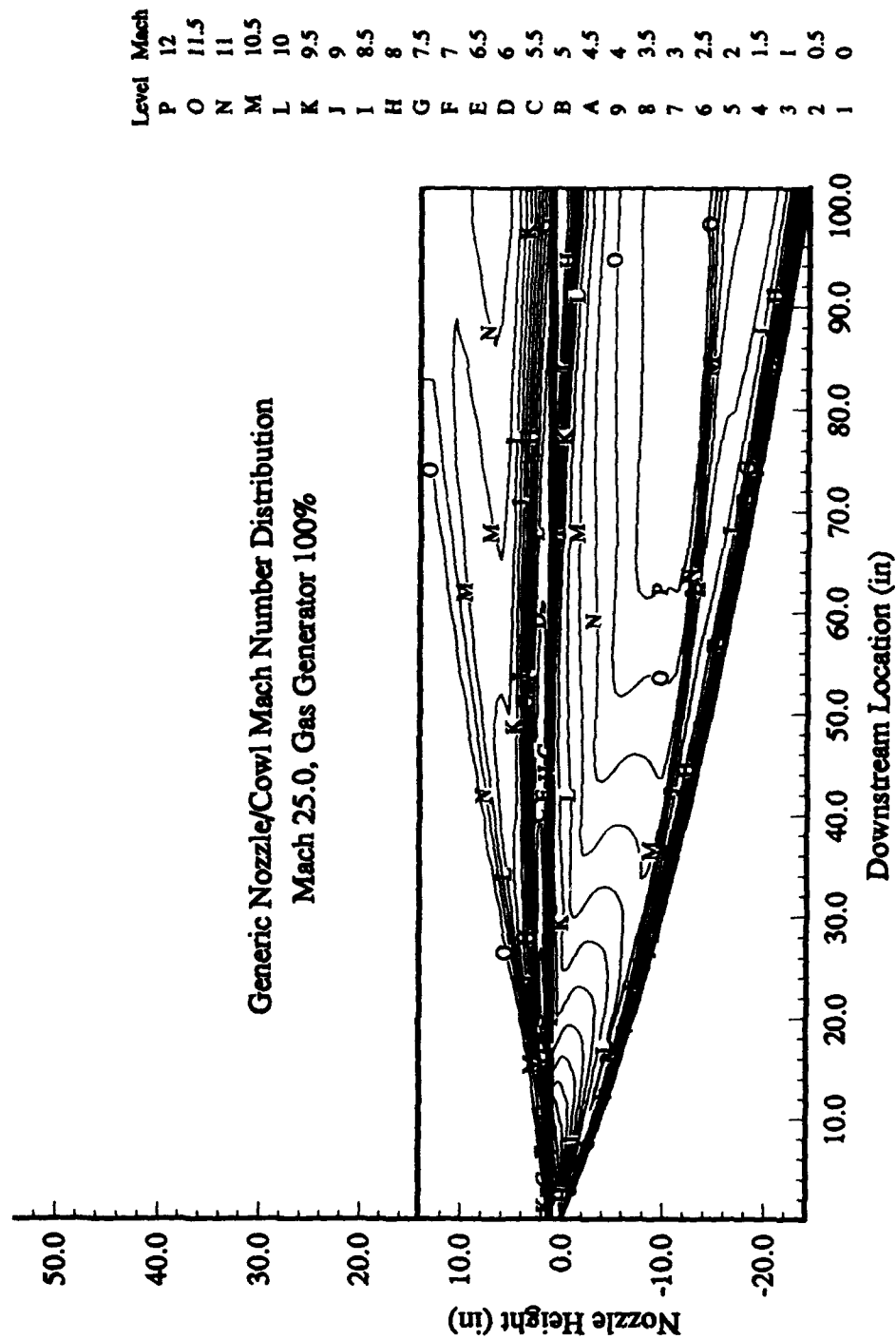


Figure C-24 Mach Number Contours, Mach 25, Gas Generator 100%

Vita

Mark C. Butler was born on 4 May 1966, in Elizabeth, New Jersey. He was raised in Solon, Ohio where he graduated from Solon High School in 1984. From there, he went on to attend the University of Cincinnati in Cincinnati, Ohio where he received a Bachelor of Science Degree in Aerospace Engineering in 1989. While he attended the University of Cincinnati he worked at Lockheed Georgia Company in Marietta, Georgia and at General Electric Aircraft Engines in Evendale, Ohio as a cooperative education student. After graduation, he accepted a civilian position with the National Air Intelligence Center (then Foreign Technology Division), Wright-Patterson AFB, Ohio where he is currently employed as a combat effectiveness analyst in the Aerodynamic Systems Division, Engagement Analysis Branch. He is currently the program manager for the high fidelity, pilot-in-the-loop, Threat Fighter Simulation Program. He entered the Air Force Institute of Technology's graduate program in Aeronautical Engineering on a part-time basis in September, 1989.

REPORT DOCUMENTATION PAGE			Form Approved OMB No. 0704-0188	
Public reporting burden for this collection of information is estimated to average 1 hour per response, including the time for reviewing instructions, searching existing data sources, gathering and maintaining the data needed, and completing and reviewing the collection of information. Send comments regarding this burden estimate or any other aspect of this collection of information, including suggestions for reducing this burden, to Washington Headquarters Services, Directorate for Information Operations and Reports, 1215 Jefferson Davis Highway, Suite 1204, Arlington, VA 22202-4302, and to the Office of Management and Budget, Paperwork Reduction Project (0704-0188), Washington, DC 20503				
1. AGENCY USE ONLY (Leave blank)	2. REPORT DATE June, 1994	3. REPORT TYPE AND DATES COVERED Master's Thesis		
4. TITLE AND SUBTITLE COMPUTATIONAL INVESTIGATION OF AN IMPROVED COWL CONCEPT FOR HYPERSONIC PROPULSIVE NOZZLES			5. FUNDING NUMBERS	
6. AUTHOR(S) Mark C. Butler				
7. PERFORMING ORGANIZATION NAME(S) AND ADDRESS(ES) Air Force Institute of Technology Wright-Patterson AFB, OH 45433-7765			8. PERFORMING ORGANIZATION REPORT NUMBER AFIT/GAE/ENY/94J-1	
9. SPONSORING/MONITORING AGENCY NAME(S) AND ADDRESS(ES) Mr. R. Bruce Cochran ASC/ENFT 2335 7th Street, Suite 3, Bldg 125 Wright-Patterson AFB, OH 45433			10. SPONSORING/MONITORING AGENCY REPORT NUMBER	
11. SUPPLEMENTARY NOTES				
12a. DISTRIBUTION/AVAILABILITY STATEMENT Approved for public release; distribution unlimited			12b. DISTRIBUTION CODE	
13. ABSTRACT (Maximum 200 words) The effects of placing a gas generator into the cowl of a hypersonic nozzle/afterbody were investigated computationally. Gas generator mass flow and deflection angle effects were analyzed for two nozzle/cowl geometries; an experimentally validated nozzle/cowl configuration evaluated at off-design conditions and a generic hypersonic propulsive nozzle evaluated at more realistic on-design conditions. A combination of Van Leer flux-vector splitting and Roe flux-difference splitting finite volume computational algorithms were used to solve the unsteady two-dimensional Navier-Stokes equations based on planar, laminar flow, perfect gas equation of state assumptions. For the low speed off-design cases analyzed, gas generator effects on nozzle wall pressure recovery were similar to geometric cowl extension and deflection effects. Nozzle wall pressure recovery increased with increased mass flow. Gas generator deflections towards the nozzle wall provided dramatic improvements in pressure recovery and only small penalties were paid for deflections away from the wall. As the combustor exit pressure and trajectory Mach number increased, the nozzle flow became increasingly dominated by large initial expansions which minimized the overall effects of the gas generator and tended to push the gas generator effects on nozzle wall pressure recovery further downstream.				
14. SUBJECT TERMS Hypersonic Nozzle, Navier-Stokes Solutions, Laminar, Unsteady Flow, Flux-Vector Splitting, Flux Difference Splitting.			15. NUMBER OF PAGES 187	
			16. PRICE CODE	
17. SECURITY CLASSIFICATION OF REPORT Unclassified	18. SECURITY CLASSIFICATION OF THIS PAGE Unclassified	19. SECURITY CLASSIFICATION OF ABSTRACT Unclassified	20. LIMITATION OF ABSTRACT UL	